Title

Investigation of Coupled Processes and Impact of High Temperature Limits in Argillite Rock: FY17 Progress

Authors

Zheng, L
Rutqvist, J
Xu, H
et al.

Publication Date

2017-06-23

Peer reviewed

Investigation of Coupled Processes and Impact of High Temperature Limits in Argillite Rock: FY17 Progress

Spent Fuel and Waste Disposition

Prepared for
U.S. Department of Energy
Integrated Waste Management System
Liange Zheng, Jonny Rutqvist, Hao xu, Kunwhi Kim, Marco Voltolini, Xiaoyuan Cao
Lawrence Berkeley National Laboratory
June 23, 2017
SFWD-SFWST-2017-000040
LBNL No. XXXXXX

SFWD Working Document: External Release

This page is intentionally left blank.

Revision 3
10/01/2016

APPENDIX E

FCT DOCUMENT COVER SHEET [1]

Name/Title of Deliverable/Milestone/Revision No.	Investigation of Coupled Processes and Impact of High Temperature Limits in Argillite Rock: FY17 Progress
Work Package Title and Number	Argillite Disposal R&D – LBNL/Argillite International Collaboration – LBNL
Work Package WBS Number	SF-17LB01030105 / SF-17LB01030106
Responsible Work Package Manager	Liange Zheng (signature on file)
	(Name/Signature)

Date Submitted **6/23/2017**

Quality Rigor Level for Deliverable/Milestone[2]	☐ QRL-1 Nuclear Data	☐ QRL-2	☐ QRL-3	☒ QRL 4 Lab-specific

This deliverable was prepared in accordance with Lawrence Berkeley National Laboratory (LBNL)
(Participant/National Laboratory Name)

QA program which meets the requirements of
☒ DOE Order 414.1 ☐ NQA-1 ☐ Other

This Deliverable was subjected to:

☐ Technical Review

Technical Review (TR)

Review Documentation Provided

☐ Signed TR Report or,
☐ Signed TR Concurrence Sheet or,
☒ Signature of TR Reviewer(s) below

Name and Signature of Reviewers

Patrick Dobson (signature on file)
Mengsu Hu (signature on file)
Pierre Jeanne (signature on file)

☐ Peer Review

Peer Review (PR)

Review Documentation Provided

☐ Signed PR Report or,
☐ Signed PR Concurrence Sheet or,
☐ Signature of PR Reviewer(s) below

Name and Signature of Reviewers

NOTE 1: *Appendix E should be filled out and submitted with each deliverable. Or, if the PICS:NE system permits, completely enter all applicable information in the PICS:NE Deliverable Form. The requirement is to ensure that all applicable information is entered either in the PICS:NE system or by using the FCT Document Cover Sheet.*

- *In some cases there may be a milestone where an item is being fabricated, maintenance is being performed on a facility, or a document is being issued through a formal document control process where it specifically calls out a formal review of the document. In these cases, documentation (e.g., inspection report, maintenance request, work planning package documentation or the documented review of the issued document through the document control process) of the completion of the activity, along with the Document Cover Sheet, is sufficient to demonstrate achieving the milestone.*

NOTE 2: *If QRL 1, 2, or 3 is not assigned, then the QRL 4 box must be checked, and the work is understood to be performed using laboratory specific QA requirements. This includes any deliverable developed in conformance with the respective National Laboratory / Participant, DOE or NNSA-approved QA Program.*

This page is intentionally left blank.

CONTENTS

This page is intentionally left blank.

LIST OF FIGURES

LIST OF TABLES

ACRONYMS

AET	aqueous extract tests
ALS	Advanced Light Source (at LBNL)
BBM	Barcelona Basic Model
BExM	Barcelona Expansive Clay Model
BGR	Bundesanstalt für Geowissenschaften und Rohstoffe
BGS	British Geological Survey
CDM	continuum damage mechanics
CEA	Commission for Atomic Energy and Alternative Energies
CNSC	Canadian Nuclear Safety Commission
COx	callovo-oxfordian claystone
DECOVALEX	DEvelopment of COupled Models and their VAlidation against EXperiments
DOE	Department of Energy
DRZ	disturbed rock zone
DSID	Deviatoric Stress Induced Damage
EBS	engineered barrier system
EDZ	excavation damaged zone
FE	full-scale emplacement
FEBEX	full-scale engineered barrier experiment
FEBEX-DP	full-scale engineered barrier experiment dismantling project
FY	fiscal year
H2	Heater 2
HLW	high-level radioactive waste
HM	hydro-mechanical
I/S	Illite/Smectite
IRSN	Institut de Radioprotection et de Sûreté Nucléaire
KAERI	Korea Atomic Energy Research Institute
LBNL	Lawrence Berkeley National Laboratory
MC	mechanical-chemical
MCC	modified cam clay
MHM	Meuse/Haute-Marne
NBS	natural barrier system
NS	natural system

PA	performance assessment
PWR	pressurized water reactor
R&D	Research & Development
SEM	scanning electron microscopy
SFWST	Spent Fuel and Waste Science and Technology
SI	saturation index
SNL	Sandia National Laboratory
STP	standard temperature and pressure
SXR-μCT	synchrotron x-ray microCT
TH	thermal-hydrological
THC	thermo-hydro-chemical
THM	thermo-hydro-mechanical
THMC	thermal-hydrological-mechanical-chemical
UDM	user defined constitutive model
UFD	Used Fuel Disposition
UfZ	Helmholtz-Centre for Environmental Research
UPC	Universitat Politècnica de Catalunya
URLs	underground research laboratories

This page is intentionally left blank.

1. INTRODUCTION

Shale and argillite geological formations have been considered as potential host rock for geological disposal of high-level radioactive waste throughout the world because of their low permeability, low diffusion coefficient, high retention capacity for radionuclides, and capability to self-seal fractures. The low permeability of clay and shale rock are well-known in the hydrogeology community where these rock types represent aquitards that severely limit groundwater movement, and in petroleum geology, where they act as caprocks limiting the rise of buoyant petroleum fluids. While fractures can occur, argillite and shale often demonstrate the tendency to self-seal fractures, which reduces the effects of fractures on bulk permeability. Other favorable characteristics of argillite /shale are the strong sorptive behavior for many radionuclides, reducing conditions because of the lack of oxygen transport from the surface, and chemical buffering of introduced materials.

Engineered barrier system (EBS) with bentonite backfill is also a critical component in most repository concepts. A large body of information concerning the behavior of argillite/shale geologic environments using bentonite backfill for nuclear waste disposal has been developed through the repository programs with underground research laboratories in Switzerland, France, Belgium, and Japan. In this report we document modeling of tests conducted at Mont Terri underground rock laboratory and Grimsel underground rock laboratory in Switzerland, and the Bure underground research laboratory in France.

The focus of research within the Spent Fuel and Waste Science and Technology (SFWST) (formerly called Used Fuel Disposal) Campaign is on repository-induced interactions that may affect the key safety characteristics of EBS bentonite and an argillaceous rock. These include thermal-hydrological-mechanical-chemical (THMC) process interactions that occur as a result of repository construction and waste emplacement. Some of the key questions addressed in this report include the development of fracturing in the excavation damaged zone (EDZ) and THMC effects on the near-field argillaceous rock and buffer materials and petrophysical characteristics, particularly the impacts of temperature rise caused by waste heat.

Within the SFWST Campaign at the Department of Energy's (DOE) Office of Nuclear Energy LBNL's research activities have focused on understanding and modeling the evolution of the EBS and EDZ and the associated coupled processes and impacts of high temperature on parameters and processes relevant to performance of an argillite repository, including to establish the technical base for the maximum allowable temperature. This report documents results from some of these activities. These activities address key Features, Events, and Processes (FEPs), which have been ranked in importance from medium to high, as listed in Table 7 of the Used Fuel Disposition Campaign Disposal Research and Development Roadmap (FCR&D-USED-2011-000065 REV0) (Nutt, 2011). Specifically, they address FEP 2.2.01, Excavation Disturbed Zone, for clay/shale, by investigating how coupled processes affect EDZ evolution; FEP 2.2.05, Flow and Transport Pathways; and FEP 2.2.08, Hydrologic Processes, and FEP 2.2.07, Mechanical Processes, and FEP 2.2.09, Chemical Process—Transport, by studying near-field coupled THMC processes in clay/shale repositories. The activities documented in this report also address a number of research topics identified in Research & Development (R&D) Plan for Used Fuel Disposition Campaign Natural System Evaluation and Tool Development (Wang, 2011), including Topics S3, Disposal system modeling – Natural System; P1, Development of discrete fracture network (DFN) model; P14, Technical basis for thermal loading limits; and P15 Modeling of disturbed rock zone (DRZ) evolution (clay repository).

This report documents the following research activities:

- Section 2 presents THM model developments and validation, including modeling of underground heater experiments at Mont Terri and Bure underground research laboratories (URLs). The heater experiments modeled are the Mont Terri FE (Full-scale Emplacement) Experiment, conducted as

part of the Mont Terri Project, and the TED in heater test conducted in Callovo-Oxfordian claystone (COx) at the Meuse/Haute-Marne (MHM) underground research laboratory in France. The modeling of the TED heater test is one of the Tasks of the DEvelopment of COupled Models and their VAlidation against EXperiments (DECOVALEX)-2019 project.

- Section 3 presents the development and application of thermal-hydrological-mechanical-chemical (THMC) modeling to evaluate EBS bentonite and argillite rock responses under different temperatures (100 °C and 200 °C). Model results are presented to help to understand the impact of high temperatures on the properties and behavior of bentonite and argillite rock. Eventually the process model will support a robust GDSA model for repository performance assessments.
- Section 4 presents coupled THMC modeling for an *in situ* test conducted at Grimsel underground laboratory in Switzerland in the Full-Scale Engineered Barrier Experiment Dismantling Project (FEBEX-DP). The data collected in the test after almost two decades of heating and two dismantling events provide a unique opportunity of validating coupled THMC models and enhancing our understanding of coupled THMC process in EBS bentonite.
- Section 5 presents a planned large in-situ test, "HotBENT," at Grimsel Test Site, Switzerland. In this test, bentonite backfilled EBS in granite will be heated up to 200 °C, where the most relevant features of future emplacement conditions can be adequately reproduced. Lawrence Berkeley National Laboratory (LBNL) has very actively participated in the project since the very beginning and have conducted scoping calculations in FY17 to facilitate the final design of the experiment.
- Section 6 presents present LBNL's activities for modeling gas migration in clay related to Task A of the international DECOVALEX-2019 project. This is an international collaborative activity in which DOE and LBNL gain access to unique laboratory and field data of gas migration that are studied with numerical modeling to better understand the processes, to improve numerical models that could eventually be applied in the performance assessment for nuclear waste disposal in clay host rocks and bentonite backfill.
- Section 7 summarizes the main research accomplishments for FY17 and proposes future work activities.

2. TOUGH-FLAC AND MODELING OF HEATER EXPERIMENTS AT MONT TERRI AND BURE URLS

In this section, we present Lawrence Berkeley National Laboratory's (LBNL) activities related to THM model developments and validation, including modeling of underground heater experiments at Mont Terri and Bure underground research laboratories (URLs). The heater experiments modeled are the Mont Terri FE (Full-scale Emplacement) Experiment, conducted as part of the Mont Terri Project, and the TED in heater test conducted in Callovo-Oxfordian claystone (COx) at the Meuse/Haute-Marne (MHM) underground research laboratory in France. The modeling of the TED heater test is one of the Tasks of the DEvelopment of COupled Models and their VAlidation against EXperiments (DECOVALEX)-2019 project.

The DOE SFWST objectives for participating in these international activities are to develop expertise and test advanced models of coupled processes in clay-based backfill in interaction with clay host rock. Through participation in modeling these field experiments, the models will be developed and experience will be gained for a range of different backfill materials (e.g., bentonite pellets and sand/bentonite mixture), as well as different host rocks (e.g., Opalinus clay and mudstone).

The main software developed and used for these simulations is the numerical simulator TOUGH-FLAC (Rutqvist et al. 2002; 2011; 2014b). For nuclear waste isolation, TOUGH-FLAC provides SFWST with a model framework for modeling coupled THM processes in the Engineered Barrier System (EBS) and host rock and their interactions using state-of-the-art macroscopic constitutive models for bentonite, crushed rock salt backfill, clay, salt and crystalline host rocks. For rigorous modeling of the THM behavior of bentonite-based (swelling) buffer and back-fill materials, the BBM (Barcelona Basic Model) and BExM (Barcelona Expansive Model) have been implemented into TOUGH-FLAC (Rutqvist et al., 2011; 2014b; Vilarrasa et al., 2016). Modeling of the *in situ* heater experiments provides a unique opportunity to validate and test the models at realistic, large-scale, in-situ conditions, including the interactions between the host rock and EBS. Finally, through the numerical modeling of these experiments and being at the forefront of modeling coupled THMC processes our goal is also to advance the state-of-the-science internationally in the field of coupled processes modeling of clay barriers.

In the following Subsection 2.1, the modeling approach and the status of model development will be summarized, and in Subsection 2.2, the implementation of a continuum damage model into TOUGH-FLAC will be described. The continuum damage model was implemented with the goal of applying it for modeling of the evolution of the disturbed rock zone (DRZ) around emplacement tunnels. Then the modeling of the Mont Terri FE experiment and TED heater experiment at Bure will be presented in Subsections 2.3 and 2.4, respectively. Finally, in Subsection 2.5, the status and plans for THM modeling will be summarized.

2.1 TOUGH-FLAC simulator for modeling nuclear waste disposal in clay host rocks

TOUGH-FLAC simulator developed at LBNL is the primary analysis tool. The simulator has the required capabilities to model a large variety of problems associated with nuclear waste disposal for various engineering and natural systems. TOUGH-FLAC can simulate coupled THM processes under multiphase flow conditions through a sequential coupling of the TOUGH2 multiphase flow simulator with the FLAC3D geomechanical code (Rutqvist et al., 2002; Rutqvist, 2011). TOUGH-FLAC was originally developed for modeling coupled THM process associated with nuclear waste disposal in welded Tuff (Rutqvist et al., 2002), but has recently been modified for applications related with to bentonite-backfilled repositories in clay host formations (Rutqvist et al., 2014b).

The TOUGH-FLAC simulator (Rutqvist, 2011), is based on linking the TOUGH2 multiphase flow and heat transport simulator (Pruess et al., 2012) with the FLAC3D geomechanical simulator (Itasca, 2011). In this approach, TOUGH2 (Pruess et al., 2012) is used for solving multiphase flow and heat transport equations, whereas FLAC3D (Itasca, 2011) is used for solving geomechanical stress-strain equations. The two codes are sequentially coupled so that a TOUGH-FLAC simulation runs seamlessly.

For analysis of coupled THM problems, TOUGH2 and FLAC3D are executed on compatible numerical grids and linked through a coupled THM model (Figure 2-1) with coupling functions to pass relevant information between the field equations that are solved in the respective codes. In the coupling scheme between TOUGH2 and FLAC3D, the TOUGH2 multiphase pressures, saturation, and temperature are provided to update temperature, and pore pressure to FLAC3D (Figure 2-1). After data transfer, FLAC3D internally calculates thermal expansion, swelling, and effective stress. Conversely, element stress or deformation from FLA3D is supplied to TOUGH2 to correct element porosity, permeability, and capillary pressure for the fluid-flow simulation in TOUGH2. The corrections of hydraulic properties are based on material-specific functions.

In a TOUGH-FLAC simulation, the calculation is stepped forward in time with the transient multiphase fluid flow analysis in TOUGH2, and at each time step or at the TOUGH2 Newton iteration level, a quasi-static mechanical analysis is conducted with FLAC3D to calculate stress-induced changes in porosity and intrinsic permeability (Figure 2-2). In this scheme, the fluid-flow sequence is solved first under fixed stress, and the resulting pressure and temperature are prescribed in the mechanical sequence. This corresponds to so-called stress-fixed iterations in the sequential scheme, in which the solution becomes unconditionally stable. The resulting THM analysis may be explicit sequential, meaning that the porosity and permeability is evaluated only at the beginning of each time step, or the analysis may be implicit sequential, with permeability and porosity updated on the Newton iteration level towards the end of the time step using an iterative process.

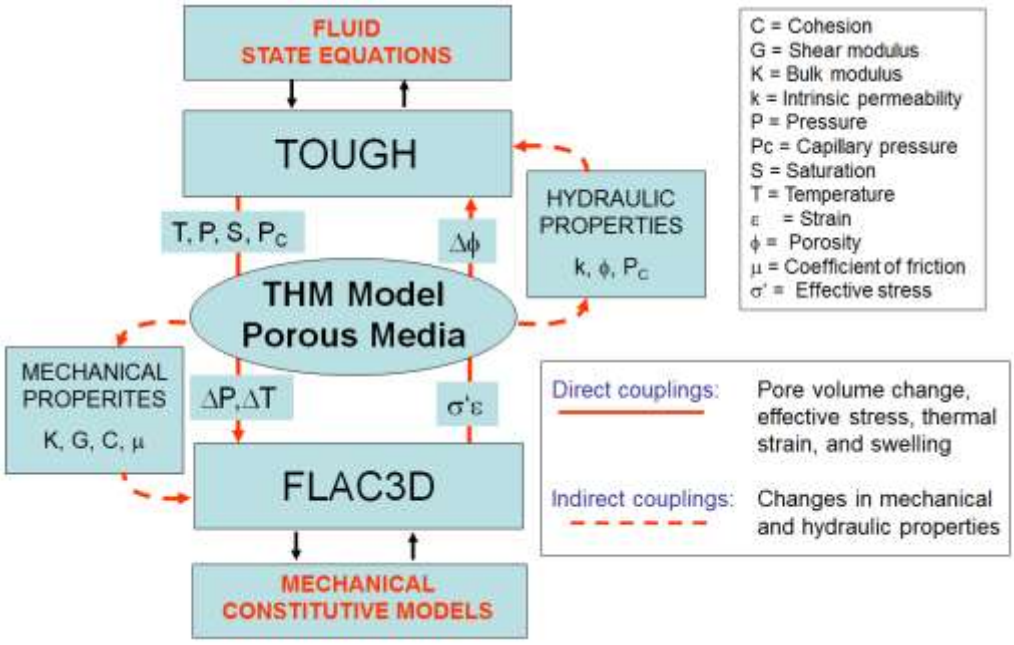

Figure 2-1. Schematic of linking of TOUGH2 and FLAC3D in a coupled TOUGH-FLAC simulation.

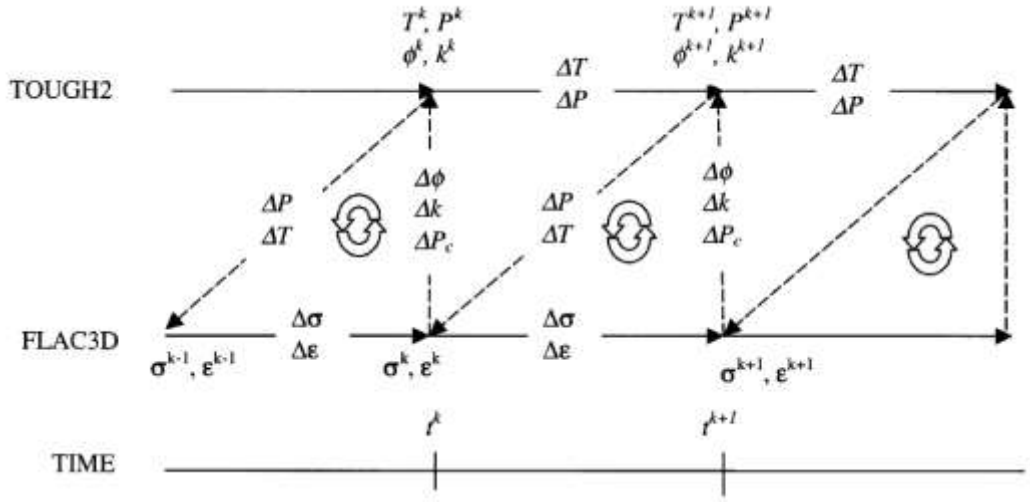

Figure 2-2. Numerical procedure of a linked TOUGH2 and FLAC3D simulation with subscript k signifying time step

A great advantage with TOUGH-FLAC is that both TOUGH2 and FLAC3D are continuously developed and widely used in both academia and industry. In TOUGH2, a large number of fluid equation-of-state modules are available, while in FLAC3D, a large number of geomechanical constitutive models are available. This means that the simulator can be easily extended to new application areas.

The TOUGH-FLAC simulator in recent years has been extended and applied to issues related to nuclear waste disposal with bentonite backfilled tunnels (Rutqvist et al., 2011; 2014b). This includes implementation of the (BBM) (Alonso et al., 1990), for the mechanical behavior of unsaturated soils, which was applied for modeling of bentonite backfill behavior (Rutqvist et al., 2011). The BBM was first developed and presented in the early 1990s as an extension of the Modified Cam Clay (MCC) model to unsaturated soil conditions (Alonso et al., 1990). The model can describe many typical features of unsaturated-soil mechanical behavior, including wetting-induced swelling or collapse strains, depending on the magnitude of applied stress, as well as the increase in shear strength and apparent preconsolidation stress with suction (Gens et al., 2006). More details about the BBM model are given in Section 2.2.1.

The BBM was used for modeling bentonite-buffer behavior in various national nuclear waste programs in Europe and Japan. For example, the BBM was successfully applied to model the coupled THM behavior of unsaturated bentonite clay associated with the FEBEX *in situ* heater test at the Grimsel Test Site, Switzerland (Gens et al., 2009). The BBM has also been applied to other types of bentonite-sand mixtures based on MX-80, considered as an option for an isolating buffer in the Swedish KBS-3 repository concept (Kristensson and Åkesson 2008). As part of the UFD program, the BBM was also used by Rutqvist et al. (2014b), for modeling of coupled THM processes around a generic repository in a clay host formation.

In the last few years, as part of the UFD EBS program, the BBM was extended to a dual structure model, corresponding to the Barcelona Expansive Model (BExM). In a dual-structure model, the material consists of two structural levels: a microstructure in which the interactions occur at the particle level, and a macrostructure that accounts for the overall fabric arrangement of the material comprising aggregates and macropores (Figure 2-3) (Gens et al., 2006, Sánchez et al., 2005, Gens and Alonso, 1992). A dual-structure model has important features for modeling the mechanical behavior of a bentonite buffer, such

as irreversible strain during suction cycles. However, most importantly, a dual-structure model provides the necessary link between chemistry and mechanics, enabling us to develop a coupled THMC model for the analysis of long-term EBS behavior. This approach enables mechanistic modeling of processes important for long-term buffer stability, including effects of pore-water salinity on swelling (loss of swelling), conversion of smectite to nonexpansive mineral forms (loss of swelling), and swelling pressure versus exchangeable cations. Details of the development, testing and applications of the dual structure model, were presented in the FY2014 milestone report titled "Investigation of Coupled THMC Processes and Reactive Transport: FY14 Progress" (Rutqvist et al. 2014a) and have been published in a journal paper (Vilarrasa et al., 2016).

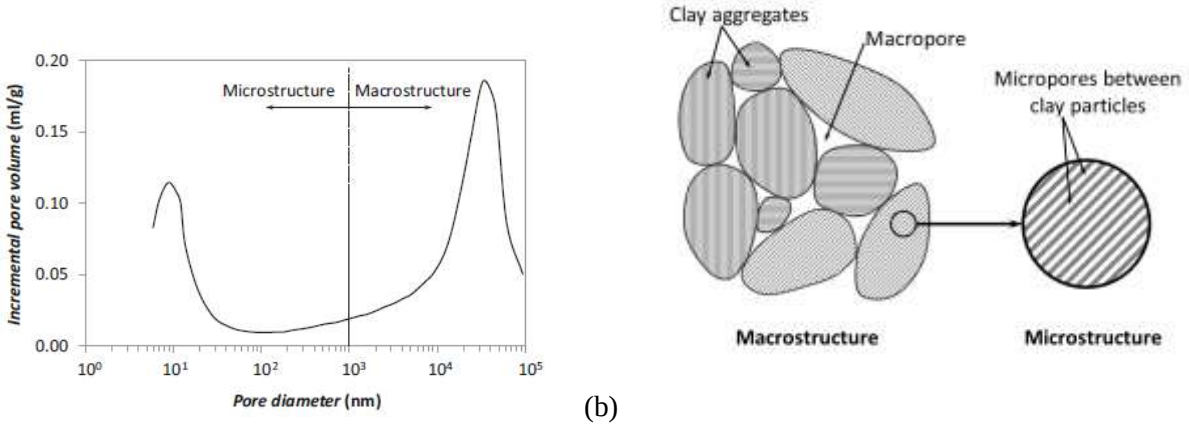

Figure 2-3. (a) Pore size distribution and (b) schematic representation of the two structural levels considered in the dual structure model. Clay particles are represented by the gray lines (Vilarrasa et al., 2016).

The dual structure model is implemented into FLAC3D using the UDM option. The model implementation have been validated by modeling one swelling pressure test on Boom clay pellets, two cyclic wetting-drying tests on one type of expansive clay and two tests with combination of loading paths on compacted bentonite samples. Based on the simulation results, the model is capable to reproduce the observed behavior of expansive clays during experiments associated with suction changes. The computation results we obtained with BExM agree well with the experiment data, and also follow the same tendency of results presented by BExM developers. It was concluded that the implementation of dual- structure model, BExM, on FLAC3D was validated and can be used for more complicated cases including THM or THMC processes for clays in a repository environment.

2.2 Implementation of continuum damage model into TOUGH-FLAC

2.2.1 Description of continuum damage model

Cracking can be originated by various THM processes inducing microstructure changes. Application of damage in porous media may be found in the design of nuclear waste disposals (Tsang et al., 2005) and geothermal systems (Brandl, 2006). The non-uniform distribution of micro-cracking makes it difficult to upscale flaw evolution. Continuum Damage Mechanics (CDM) avoids to model cracks at the micro-scale, as opposed to micro-mechanics. Damage effects were analyzed at the scale of Representative Elementary Volume REV). In this section, we first present the outline of a continuum damage model developed in research (Xu and Arson, 2014; Xu and Prévost, 2016), then the model is implemented into FLAC3D, and verified with two material tests against the other two codes.

2.2.1.1 Constitutive equations of the skeleton

The proposed anisotropic damage model named Deviatoric Stress Induced Damage (DSID) model is hyper-elastic, i.e., the stress-strain relationship derives from the expression of a thermodynamic potential. The free energy utilized in this model is Gibbs free energy, whose general form was introduced into Continuum Damage Mechanics with the concept of effective stress to account for the reduction of undamaged areas (Chaboche, 1992). Hayakawa and Murakami (1997) formulated a different expression, which is linearly dependent on damage variable $\boldsymbol{\Omega}$, and a modified stress tensor is proposed to represent closure effects of microcracks. DSID model is based on the energy expression Shao et al. (2005) proposed, which is similar as Hayakawa and Murakami's. However, this equation depends on Cauchy stress tensor, so it avoids discontinuous differential in integration process (Shao et al., 2005).

$$\begin{aligned} G_s = \; & \frac{1+\nu_0}{2E_0}\mathrm{Tr}(\boldsymbol{\sigma}^2) - \frac{\nu_0}{2E_0}(\mathrm{Tr}\boldsymbol{\sigma})^2 + a_1\,\mathrm{Tr}(\boldsymbol{\Omega})(\mathrm{Tr}\boldsymbol{\sigma})^2 + a_2\,\mathrm{Tr}(\boldsymbol{\sigma}\cdot\boldsymbol{\sigma}\cdot\boldsymbol{\Omega}) \\ & + a_3\,\mathrm{Tr}(\boldsymbol{\sigma})\mathrm{Tr}(\boldsymbol{\Omega}\cdot\boldsymbol{\sigma}) + a_4\,\mathrm{Tr}(\boldsymbol{\Omega})\mathrm{Tr}(\boldsymbol{\sigma}\cdot\boldsymbol{\sigma}) \end{aligned} \tag{2.1}$$

where E_0 and ν_0 is the initial Young's modulus and Poisson's ratio respectively; $\boldsymbol{\sigma}$ is the Cauchy stress; $\boldsymbol{\Omega}$ is the damage tensor, defined as the second-order crack density tensor (Kachanov, 1958); and a_i are material parameters for the free energy. The damage driving force is obtained by deriving G_s by the damage tensor:

$$\mathbf{Y} = \frac{\partial G_s}{\partial \boldsymbol{\Omega}} = a_1(\mathrm{Tr}\boldsymbol{\sigma})^2\,\boldsymbol{\delta} + a_2\boldsymbol{\sigma}\cdot\boldsymbol{\sigma} + a_3\mathrm{Tr}(\boldsymbol{\sigma})\boldsymbol{\sigma} + a_4\mathrm{Tr}(\boldsymbol{\sigma}\cdot\boldsymbol{\sigma})\boldsymbol{\delta} \tag{2.2}$$

The total elastic strain $\boldsymbol{\epsilon}^E$ is obtained by deriving G_s by the Cauchy stress $\boldsymbol{\sigma}$:

$$\begin{aligned} \boldsymbol{\epsilon}^E = \frac{\partial G_s}{\partial \boldsymbol{\sigma}} = \; & \frac{1+\nu_0}{E_0}\boldsymbol{\sigma} - \frac{\nu_0}{E_0}(\mathrm{Tr}\boldsymbol{\sigma})\boldsymbol{\delta} + 2a_1\,[\mathrm{Tr}(\boldsymbol{\Omega})(\mathrm{Tr}\boldsymbol{\sigma})]\boldsymbol{\delta} + a_2\,(\boldsymbol{\sigma}\cdot\boldsymbol{\Omega} + \boldsymbol{\Omega}\cdot\boldsymbol{\sigma}) \\ & + a_3[\mathrm{Tr}(\boldsymbol{\sigma}\cdot\boldsymbol{\Omega})\boldsymbol{\delta} + (\mathrm{Tr}\boldsymbol{\sigma})\boldsymbol{\Omega}] + 2a_4(\mathrm{Tr}\boldsymbol{\Omega})\boldsymbol{\sigma} \end{aligned} \tag{2.3}$$

and it contains two parts:

$$\boldsymbol{\epsilon}^E = \boldsymbol{\epsilon}^{el} + \boldsymbol{\epsilon}^{ed} \tag{2.4}$$

in which $\boldsymbol{\epsilon}^{el}$ is the purely elastic strain, which would be recovered by unloading, and $\boldsymbol{\epsilon}^{ed}$ is the additional elastic strain induced by the degradation of stiffness. Therefore, total strain $\boldsymbol{\epsilon}$ can be decomposed as

$$\boldsymbol{\epsilon} = \boldsymbol{\epsilon}^E + \boldsymbol{\epsilon}^{id} = \boldsymbol{\epsilon}^{el} + \boldsymbol{\epsilon}^{ed} + \boldsymbol{\epsilon}^{id} \tag{2.5}$$

$\boldsymbol{\epsilon}^{id}$ is the irreversible strain, induced by residual crack openings existing in a sample after a release of loading stress (additional compression is needed to close the cracks and to get back to a state of zero deformation) (Abu Al-Rub and Voyiadjis, 2003).

2.2.1.2 Damage function

The expression of the damage function is written in the following form:

$$f_d = \sqrt{J^*} - \alpha I^* - k \tag{2.6}$$

J^* and I^* are defined as

$$J^* = \frac{1}{2}(\mathbb{P}_1 : \mathbf{Y} - \frac{1}{3}I^*\boldsymbol{\delta}) : (\mathbb{P}_1 : \mathbf{Y} - \frac{1}{3}I^*\boldsymbol{\delta}), \quad I^* = (\mathbb{P}_1 : \mathbf{Y}) : \boldsymbol{\delta} \tag{2.7}$$

where $\mathbb{P}_1$ is a fourth-order projection tensor defined as

$$\mathbb{P}_1(\boldsymbol{\sigma}) = \sum_{p=1}^{3}\left[H(\sigma^{(p)}) - H(-\sigma^{(p)})\right]\mathbf{n}^{(p)} \otimes \mathbf{n}^{(p)} \otimes \mathbf{n}^{(p)} \otimes \mathbf{n}^{(p)} \tag{2.8}$$

in which $H(\cdot)$ is the Heaviside distribution function, $\boldsymbol{\sigma}^{(p)}$ is the p^{th} eigenvalue of the stress tensor, $\mathbf{n}^{(p)}$ is the vector aligned with the p^{th} principal direction of stress, and α is a material parameter accounting for the aperture of the cone in the $\mathbb{P}_1:\mathbf{Y}$ space. The threshold k in Eq. 2.6 is defined as a linear function of damage:

$$k = C_0 + C_1 \mathrm{Tr}(\boldsymbol{\Omega}) \tag{2.9}$$

where C_0 is the initial threshold of damage, and C_1 controls the damage hardening.

2.2.1.3 Damage potential

In order to enforce the constraint on the eigenvalues of damage tensor to be non-negative, it is proposed to define the damage potential as a homogeneous function of degree one in $\mathbf{Y}$:

$$g_d = \sqrt{\frac{1}{2}(\mathbb{P}_2:\mathbf{Y}):(\mathbb{P}_2:\mathbf{Y})} - C_2 \tag{2.10}$$

The projection tensor, $\mathbb{P}_2$, is introduced to represent both "crossing" and "splitting" effects (Xu and Arson, 2014; Xu, 2014):

$$\mathbb{P}_2 = \sum_{p=1}^{3} H\left[\sigma^{(p)} - \min_{q=1}^{3}(\sigma^{(q)})\right] \mathbf{n}^{(p)} \otimes \mathbf{n}^{(p)} \otimes \mathbf{n}^{(p)} \otimes \mathbf{n}^{(p)} \tag{2.11}$$

2.2.1.4 Flow rule

Damage evolution law is obtained by calculating

$$\mathrm{d}\boldsymbol{\Omega} = \lambda \frac{\partial g}{\partial \mathbf{Y}} \tag{2.12}$$

where λ is the Lagrange Multiplier accounting for the magnitude of the damage increment. Analytical solutions for elementary mechanical tests shows that the irreversible strain $\boldsymbol{\epsilon}^{id}$ is better predicted when derived from a non-associated flow rule:

$$\mathrm{d}\boldsymbol{\epsilon}^{id} = \lambda \frac{\partial f_d}{\partial \boldsymbol{\sigma}} = \lambda \frac{\partial f_d}{\partial \mathbf{Y}} \frac{\partial \mathbf{Y}}{\partial \boldsymbol{\sigma}} \tag{2.13}$$

2.2.2 Implementation

The damage model was implemented with the Cutting-Plane Algorithm solving for Lagrange Multiplier. Through this method, we can have a stable method to get results for the simulation. All these implementations are based on the strain-controlled strategy, which is typically utilized in the programming of constitutive modeling. A trial calculation is tested with a new strain increment based on elastic assumption. If the yield condition is reached, the cutting-plane algorithm is utilized to drive the stress status back to the yield surface; if the yield condition is not reached, state variables are updated using the elastic solution.

2.2.2.1 Cutting-Plane Algorithm

The Cutting-Plane Algorithm, first proposed in reference (Simo and Ortiz, 1985), is one type of return mapping algorithm and follows in a straightforward manner from the theory of operator splitting applied to nonlinear constitutive relations. Following the procedure of the algorithm summarized in the work (Simo and Hughes, 1998), we can derive all the equations for DSID model.

The damage function at next step can be linearized at the current iteration step:

$$f_{n+1}^{(i+1)} \approx f_{n+1}^{(i)} + \partial_{\boldsymbol{\sigma}} f_{n+1}^{(i)} : \left[\boldsymbol{\sigma}_{n+1}^{(i+1)} - \boldsymbol{\sigma}_{n+1}^{(i)}\right] + \partial_{\boldsymbol{\Omega}} f_{n+1}^{(i)} : \left[\boldsymbol{\Omega}_{n+1}^{(i+1)} - \boldsymbol{\Omega}_{n+1}^{(i+1)}\right] = 0 \tag{2.14}$$

From the above equation, two increment terms are needed to update. The stress can be discretizing as

$$\boldsymbol{\sigma}_{n+1}^{(i+1)} - \boldsymbol{\sigma}_{n+1}^{(i)} = -\lambda_{n+1}^{(i)} \mathbb{S}_{n+1}^{-1} : \left[\partial_{\boldsymbol{\sigma}} f_{n+1}^{(i)} + \boldsymbol{\sigma}_{n+1}^{(i)} : \partial_{\boldsymbol{\Omega}} \mathbb{S}_{n+1}^{(i)} : \partial_{\mathbf{Y}} g_{n+1}^{(i)} \right] \tag{2.15}$$

The flow rule (Eq. 2.12) indicates that the damage increment can be discretized as

$$\boldsymbol{\Omega}_{n+1}^{(i+1)} - \boldsymbol{\Omega}_{n+1}^{(i)} = \lambda_{n+1}^{(i)} \partial_{\mathbf{Y}} g_{n+1}^{(i)} \tag{2.16}$$

Taking equations 2.15 and 2.16 into equation 2.14, we obtain an equation for computing Lagrange Multiplier:

$$\lambda_{n+1}^{(i)} = \frac{f_{n+1}^{(i)}}{\partial_{\boldsymbol{\sigma}} f_{n+1}^{(i)} : \mathbb{S}^{-1} : \left[\partial_{\boldsymbol{\sigma}} f_{n+1}^{(i)} + \boldsymbol{\sigma}_{n+1}^{(i)} : \partial_{\boldsymbol{\Omega}} \mathbb{S}_{n+1}^{(i)} : \partial_{\mathbf{Y}} g_{n+1}^{(i)} \right] - \partial_{\boldsymbol{\Omega}} f_{n+1}^{(i)} : \partial_{\mathbf{Y}} g_{n+1}^{(i)}} \tag{2.17}$$

The discretization reveals that this algorithm is based on a forward integration of the rate equations. The updated damage function will be updated with new Lagrange Multiplier and checked for convergence.

2.2.3 Improvement and validation of the damage model in TOUGH-FLAC

The damage model was implemented into TOUGH-FLAC using the User Defined Constitutive Model (UDM) option in FLAC3D, including C++ coding and dynamic link libraries. The new model can be utilized in the simulator TOUGH-FLAC3D (Rutqvist, 2011) to study anisotropic damage evolution in host rocks. In this section, we present two material tests, one uniaxial compression test and one uniaxial tension test to validate the model implementation. The numerical analyses are launched with the set of material parameters calibrated by the model development team against laboratory experiments from published literature.

2.2.3.1 Uniaxial compression test

The results simulated with FLAC3D were compared with two different codes (Dynaflow and ABAQUS/UMAT). A set of parameters of DSID model for granite is used for the simulation. The values are listed in Table 2-1. In uniaxial compression test, a deviatoric strain $\Delta\epsilon_{33} = -2\%$ is applied in the vertical direction. Figure 2-4 shows the stress-strain relationship of uniaxial compression simulated by these three codes. Because the sample is compressed in the vertical direction (3-direction), the horizontal damage (Ω_{11} and Ω_{22}) will be generated after damage thereshold is reached. Before $\epsilon_{33} - \epsilon_{11} = 0.15\%$ (corresponding to $\sigma_{33} - \sigma_{11} = 85$MPa), the stress-strain relationship is linear elastic (Figure 2-4), and no damage occurs ($\Omega_{11} = 0$). After this point, cracks due to damage are generated. As the result of that, the material modulus decreases, damage component Ω_{11} increases, and the stress-strain relationship becomes non-linear. The magnitude of final differential stress $\sigma_{33} - \sigma_{11}$ computed by FLAC3D and ABAQUS/UMAT is slightly higher (about 1.4%) than Dynaflow.

Table 2-1. Parameters in DSID model for material tests.

Elastic parameters		Free Energy				Damage function		
E_0	ν_0	a_1	a_2	a_3	a_4	C_0	C_1	$\alpha(-)$
MPa	-	MPa^{-1}	MPa^{-1}	MPa^{-1}	MPa^{-1}	MPa	MPa	-
6.8×10^4	0.21	1.26×10^{-7}	3.94×10^{-5}	-1.26×10^{-6}	2.51×10^{-6}	0.11	2.2	0.231

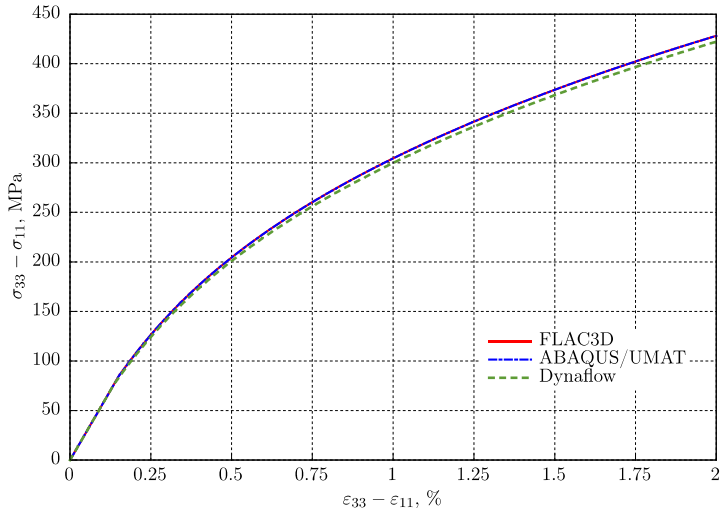

Figure 2-4. Comparison of different codes for stress-strain curves in uniaxial compression test.

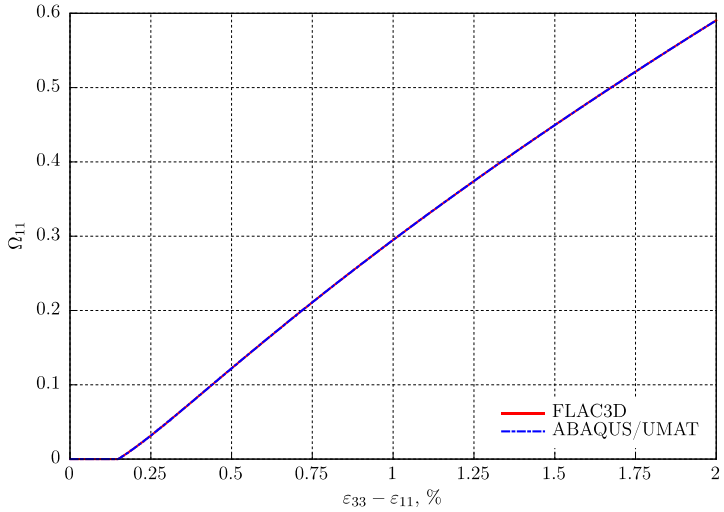

Figure 2-5. Comparison of different codes for damage components in uniaxial compression test. The damage components by Dynaflow are not available for printing out.

2.2.3.2 Uniaxial tension test

The same parameters in Table 2-1 are used for uniaxial tension test. In this test, a deviatoric strain $\Delta\epsilon_{33} = 2\%$ is applied in the vertical direction. Figure 2-6 shows the stress-strain relationship of uniaxial compression simulated by three codes. Because the sample is stretched in the vertical direction (3-direction), the vertical damage (Ω_{33}) will be generated after damage thereshold is reached. Before $\epsilon_{33} - \epsilon_{11} = -0.078\%$ (corresponding to $\sigma_{33} - \sigma_{11} = -43$MPa), the stress-strain relationship is linear elastic (Figure 2-6), and no damage occurs ($\Omega_{33} = 0$, Figure 2-7). After this point, cracks due to damage are generated. As the result of that, the material modulus decreases, damage component Ω_{33} increases, and the stress-strain relationship becomes non-linear. The final differential stress $\sigma_{33} - \sigma_{11}$ computed by FLAC3D and ABAQUS/UMAT is slightly higher (about 0.87%) than Dynaflow.

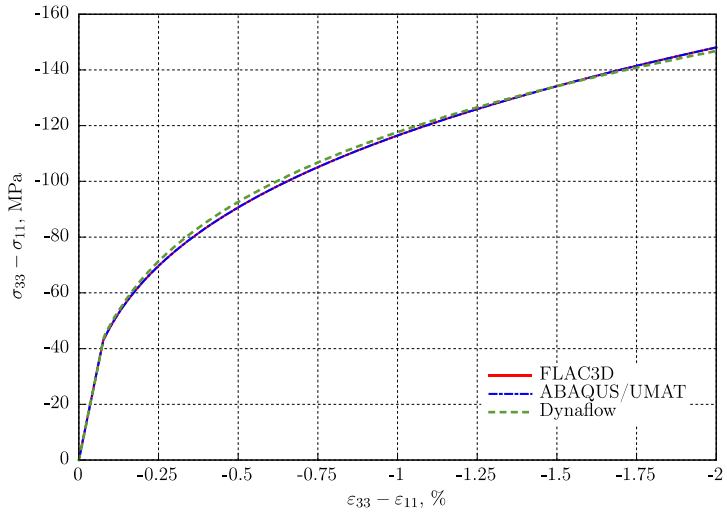

Figure 2-6. Comparison of different codes for stress-strain curves in uniaxial tension test.

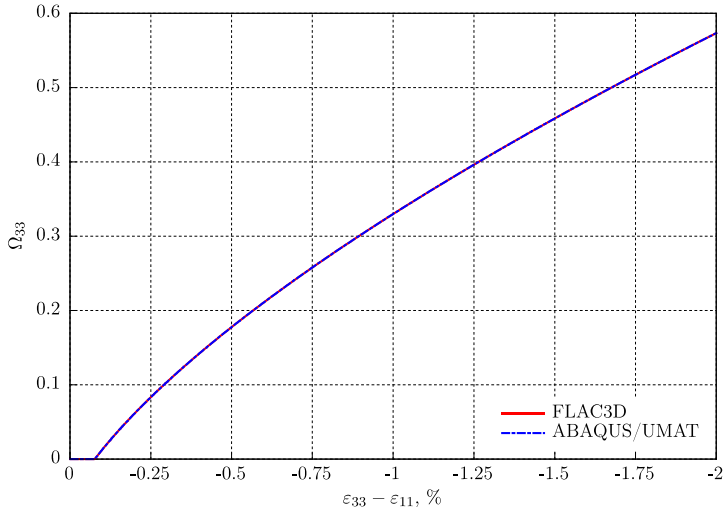

Figure 2-7. Comparison of different codes for damage components in uniaxial tension test. The damage components by Dynaflow are not available for printing out.

The model implementation has been validated by modeling one uniaxial compression test and one uniaxial tension test on granite and by comparing computation results with different codes. The agreements on simulation results prove the damage model is implemented correctly in FLAC3D and is capable to reproduce the same non-linear mechanical behavior due to damage propagation. The model on FLAC3D can be utilized for host rocks in a repository environment.

2.3 FE Experiment at the Mont Terri Site (Mont Terri Project)

In this section, we present the status of the FE Experiment at Mont Terri and updated TOUGH-FLAC modeling of the experiment. In particular, in FY2017 we have extended the modeling for comparison with up to two years of field data from the experiment at additional monitoring points within the bentonite buffer. In the following we first provided a description and status of the FE Experiment and then present the current THM modeling.

2.3.1 Description and status of the Mont Terri FE experiment

The Mont Terri FE experiment is undertaken by NAGRA, Switzerland as an ultimate test for the performance of geologic disposal in Opalinus Clay, with focus on both the EBS components and the host-rock behavior. It will be one of the largest and longest-duration heater tests worldwide, with focus on both the EBS components and the host-rock behavior. The FE experiment is conducted in a side tunnel at Mont Terri, excavated along the claystone bedding planes for this purpose, extending 50 m in length and about 2.8 m in diameter (Figure 2-8). Heating from emplaced waste will be simulated by three heat-producing canisters of 1500 W maximum power. The temperature is expected to exceed 100°C, with a target temperature 125 to 135°C at the inner parts of the buffer. A sophisticated monitoring program was implemented, including dense instrumentation of the bentonite buffer and host rock, and extensive geophysical monitoring.

The experiment will provide data useful for the validation of THM coupling effects regarding the processes in the host rock, while correctly accounting for (and examining) the conditions in the emplacement tunnel (temperature, saturation, and swelling pressure). Due to the 1:1 scale of the experiment, it will be possible to achieve realistic temperature, saturation, and stress gradients. It will also be possible to test backfilling technology with granular bentonite, as well as lining technology with shotcrete, anchors, and steel ribs. Processes examined in the test cover many aspects of repository evolution, such as creation and desaturation of the EDZ during tunnel excavation and operation (including ventilation for about one year), as well as reconsolidation of the EDZ, resaturation, thermal stresses, and thermal pore-pressure increase after backfilling and heating (heating and monitoring period > 10 years).

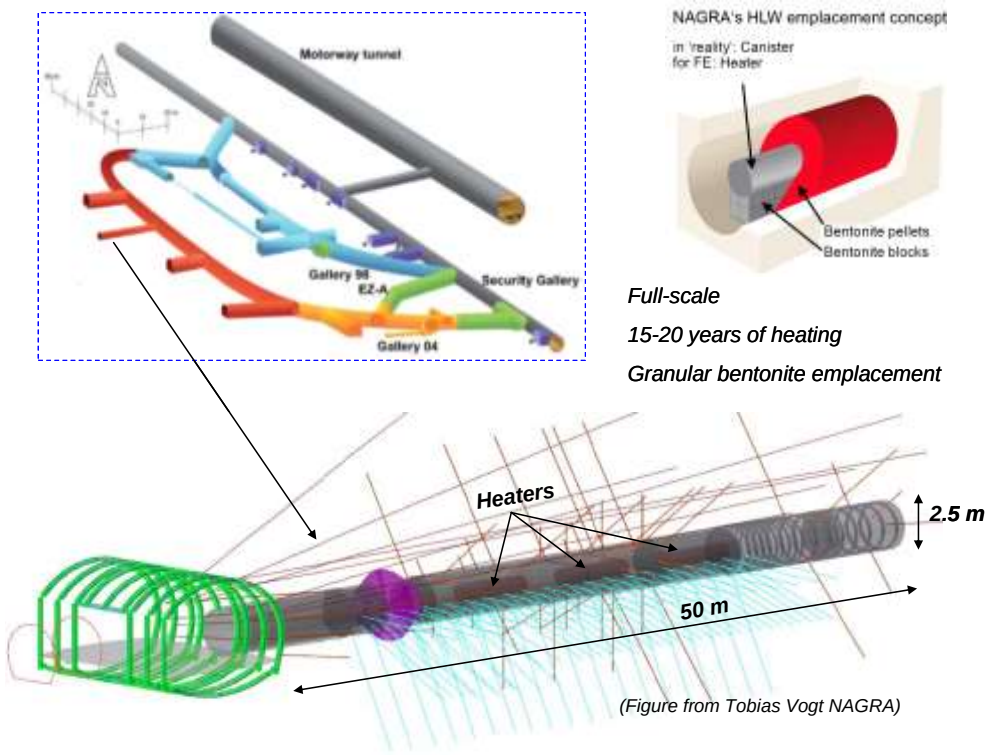

Figure 2-8. Plan view of FE experiment setup and borehole layout.

In 2011, a niche in front of the FE tunnel was constructed, followed by a first phase of instrumentation of the rock mass surrounding the tunnel, using boreholes from the niche. The FE tunnel was then excavated by road-header in 2012; this was followed by another phase of instrumentation. The tunnel was open for a

one-year ventilation period. This was followed by the emplacement of the heaters, bentonite buffer, and a concrete plug, after which the heating was gradually turned on during the fall of 2014 and early 2015, with full heat power of 1350 W at all three heaters (H1, H2, H3) from February 18, 2015 (Figure 2-9). The heating is then expected to go on for at least 15 years, with continuous monitoring of THM processes in both the bentonite buffer and surrounding rock.

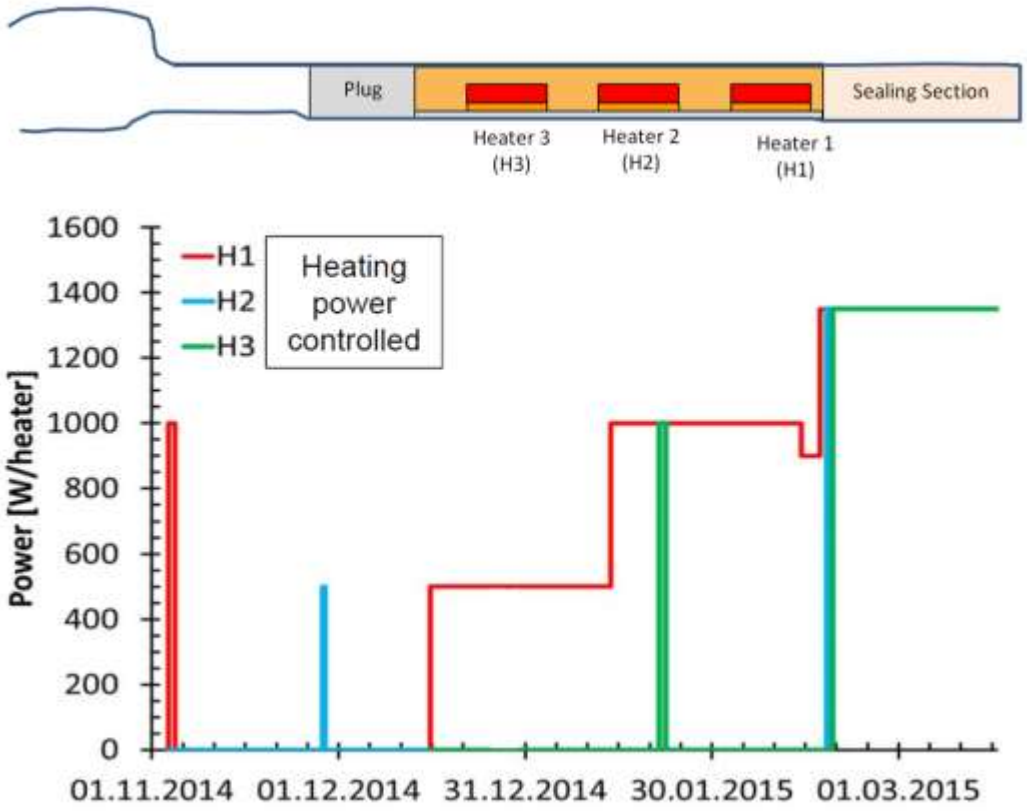

Figure 2-9. Heat power applied to heater 1, 2 and 3 during the start-up of the heating at the Mont Terri FE experiment.

2.3.2 FE-E experiment modeling tasks

DOE is one of the experimental partners for the FE heater experiment, and LBNL is one of the modeling teams. In addition to LBNL, six other modeling teams are currently involved in the Mont Terri FE experiment from Germany (2 teams), U.K., Spain, Switzerland, and Canada.

The THM modeling program includes three types of computations:

1. Scoping calculations and bench Marking
2. Predictive modeling
3. Interpretative modeling

The scoping calculations include brainstorming on potential ongoing processes, evaluating their significance and parameter range, comparing simulation results and input parameters derived by each team, and lessons learned (parameter range, importance, expected response). The benchmarking uses well-defined geometry problems with exact parameter values given to the teams, focusing on process

modeling with precise comparison of codes. In the predictive calculations, likely parameters values and the as-built information of the experiment will be frozen.

Each modeling team develops its conceptual models and material properties using available literature (papers and reports) on lab experiments and previous Mont Terri *in situ* tests, etc. Moreover, this is complemented with a restricted benchmark test for code comparison, in which properties and model geometry are set by NAGRA. In the FY2013 UFD milestone report (Houseworth et al., 2013), we presented results on the scoping calculations and the benchmarking which was completed in April 2014. We also made a first full THM 3D simulation of the FE heater test, including the BBM model for calculating the mechanical responses. These were scoping and preliminary predictions with the material properties available at the time, though in some cases including a different kind of bentonite.

In the FY2015 UFD milestone report (Zheng et al., 2015b), we presented simulation results related to the thermal evolution for different heat power schemes. This included a staged heating during the first few months of the experiment. A staged heating schedule was also adopted in the real experiment to be able to use early data for determining the maximum heat load so that temperatures would not exceed certain limits. For example, the maximum temperature should not exceed 150°C as such high temperature could potentially damage the monitoring system. The modeling presented in the FY15 UFD milestone report indeed showed that temperature could increase about 150°C in the maximum heat power of 1500 W would be applied on each of the heaters. It was decided by NAGRA, to limit the maximum heat power to 1350 W to be well below 150°C in maximum temperature.

In the FY2016 UFD milestone report (Zheng et al., 2016), we presented initial interpretative modeling of the FE experiment with comparison to field data for the first year of heating. The approach was to use the previously developed 3D model of the FE experiment but with THM properties updated and determined from the modeling of the smaller scale HE-E experiment. In the modeling we obtained a good agreement with monitored evolution of temperature and relative humidity when using an effective diffusivity that was lowered used a tortuosity factor as low as 0.14 (Zheng et al., 2016).

In this report we present updated model simulations with comparison to monitoring data extended to more than two years, including additional comparison for monitoring points located at other sections along the tunnel, i.e., comparisons made at monitoring sections located at all three heaters.

2.3.3 TOUGH-FLAC model of the Mont Terri FE Experiment

For the modeling of the FE experiment, we have developed a conceptual model and modeling approach that was presented and used for model simulations in previous milestone reports (Houseworth et al., 2013; Zheng et al., 2014; 2015b; 2016). The host rock is modeled using TOUGH-FLAC with anisotropic properties considering bedding planes of the Opalinus Clay. To accurately model anisotropic thermal and hydrological behavior, we created an inclined TOUGH2 mesh. Anisotropic mechanical material behavior is simulated using the FLAC3D ubiquitous joint model, with initial properties of those derived from the excavation design analysis of the experimental tunnels. In the ubiquitous joint model, weak planes are assumed along the bedding planes of the Opalinus Clay in which the shear strength properties are different along bedding versus across bedding (Housworth et al. 2013). For the bentonite, we started with the BBM model as applied by the CINEMAT and UPC (Garitte and Gens, 2012), and derived specific input material parameters for the MX-80 bentonite pellets that is used as the emplaced bentonite buffer around the heaters. With this modeling approach, we are able to simulate THM processes in both the bentonite and host rock, as well as their interactions.

Figure 2-10 presents the 3D TOUGH-FLAC numerical grid of the FE experiment. This model grid includes all vital material components for the modeling of the FE experiment, including layered Opalinus Clay host rock, excavation disturbed zone, tunnel, three heaters, bentonite buffer, concrete liner, and concrete plug. The initial conditions for the model simulation are 2 MPa pore-fluid pressure and 15°C

temperature for the host rock. The 2 MPa pore pressure is not under hydrostatic conditions, and the process is affected by the existing tunnel system at the site. In our simulations, we first run a simulation with an open tunnel at atmospheric pressure for one year, creating a pressure drop and hydraulic gradient around the tunnel. Thereafter, we assume instantaneous emplacement of the heater and buffer, and start our heating simulation.

The thermal and hydraulic material properties for modeling the FE experiment are given in Table 2-2. These properties are based on the modeling studies of several other smaller scale heater experiments at the Mont Terri laboratory, including the HE-D and HE-E experiments described in previous reports (Zheng et al., 2015b; 2016). The intrinsic permeability of gas flow in the bentonite is about six orders of magnitude higher than the intrinsic permeability for liquid flow and this is simulated in TOUGH2 using a high value of the Klinkenberg parameter. The initial saturation in granular bentonite and bentonite block are different that in the previous HE-E experiment and is for the FE experiment set to 16.5% for granular bentonite and to 75% for bentonite blocks.

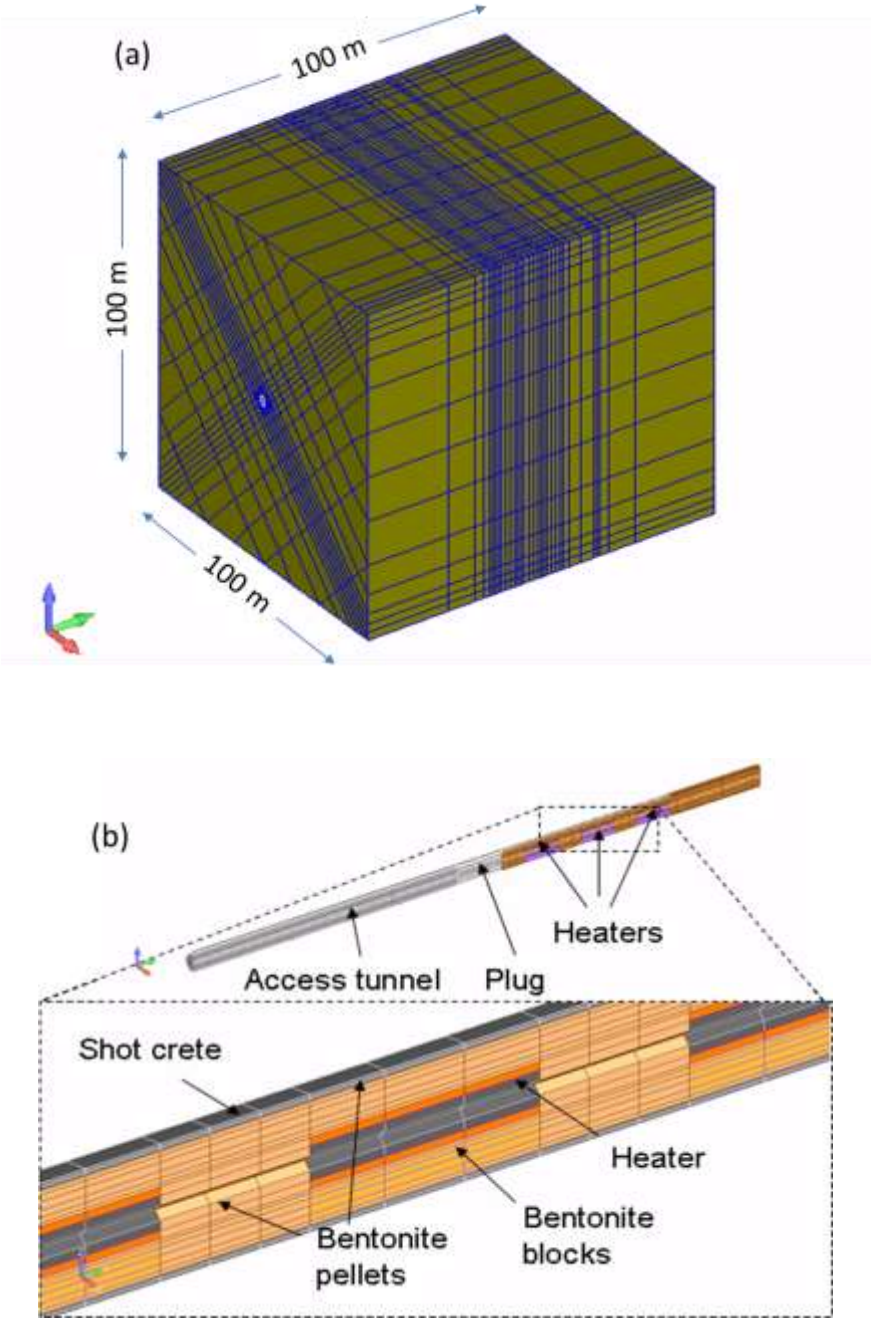

Figure 2-10. TOUGH-FLAC 3D numerical grid of the FE experiment, (a) entire model and (b) details of the materials and gridding of the EBS.

Table 2-2. Parameters used in the modeling of the Mont Terri FE experiment.

Parameters	Symbol	Opalinus Clay	Granular Bentonite	Bentonite blocks	Concrete (shotcrete and plugs)	Unit
Grain density	ρ_g	2.7×10^3	2.7×10^3	2.7×10^3	2.7×10^3	kg/m^3
Porosity	$\emptyset$	0.15	0.46	0.389	0.15	-
Intrinsic permeability	k	5.0×10^{-20}	5.0×10^{-21}	2.0×10^{-21}	3.5×10^{-21}	m^2
Liquid relative permeability (van Genuchten, 1980) $k_{lr}(S_l)=\left(\frac{S_l-S_{lr}}{S_{ls}-S_{lr}}\right)^A$	A	-	5	3	-	-
Liquid relative permeability (van Genuchten, 1980) $k_{lr}(S_l)=\left(\frac{S_l-S_{lr}}{S_{ls}-S_{lr}}\right)^{1/2}\left[1-\left\{1-\left(\frac{S_l-S_{lr}}{S_{sl}-S_{lr}}\right)^{1/m}\right\}^m\right]^2$	m	0.52	-	-	0.52	-
Capillary curve (van Genuchten, 1980) $\psi(S_l)=P0\left\{\left(\frac{S_l-S_{lr}}{S_{ls}-S_{lr}}\right)^{-1/m}-1\right\}^{1-m}$	P_0	1.09×10^7	1.0×10^7	3.0×10^7	1.09×10^7	Pa
	M	0.29	0.4	0.32	0.29	-
	S_{ls}	1.0	1.0	1.0	1.0	-
	S_{lr}	0.01	0.0	0.0	0.01	-
Thermal conductivity (wet)	λ_{sat}	1.7	1.3	1.0	1.7	W/m°K
Thermal conductivity (dry)	λ_{dry}	1.06	0.3	0.5	1.06	W/m°K
Grain specific heat	C	800	950	950	800	J/kg°K

2.3.4 TOUGH-FLAC simulation results with comparison to monitored data

Here we focus on the simulation and monitored data for the evolution of temperature and relative humidity in the bentonite buffer. At this early stage, a few years after emplacement of the bentonite buffer, no significant swelling stress has developed in the buffer. A conceptual model of the evolution of moisture content is shown in Figure 2-11. The figure shows the creation of a thermal gradient due to the heating. Near the heater, liquid evaporates to vapor in the gas phase that is then transported outwards by diffusion towards cooler regions where some of the vapor is condensed to liquid. At the same time, liquid water infiltrates from the rock into the bentonite buffer. The wetting of the outer parts of the buffer and the drying of the inner parts causes a gradient in liquid saturation and capillary pressure that will results in liquid fluid flow from the outer parts towards the inner dryer parts of the buffer.

The outward vapor diffusion is modeled in TOUGH2 using the following equation;

$$\mathbf{i}_g^w = -\rho_g \phi S_g \tau D_g^w \mathbf{I} \nabla X_g^w \tag{2.18}$$

where $\mathbf{i}_g^w$ is diffusion of water component in the gas phase, ρ_g is density of gas, ϕ is porosity, S_g is gas saturation, τ is flow tortuosity factor, D_g^w is water vapor diffusion coefficient, and X_g^w is mass fraction of water in the gas phase. The vapor diffusion is from areas of high mass fraction of water vapor in the gas phase (near the heater) towards outer regions of the buffer of lower mass fraction of water vapor in the gas phase. An effective vapor diffusion for the partially saturated porous media, includes the effects of porosity, gas saturation and the flow tortuosity factor (see also Figure 2-11).

The liquid flux from the outer parts of the buffer towards the inner parts is governed by the following equation:

$$\mathbf{q}_l^w = -\rho_l X_l^w \frac{\mathbf{k} k_{rl}}{\mu_l}\left(\nabla P_l - \rho_l \mathbf{g} \nabla z\right) \tag{2.19}$$

where $\mathbf{q}_l^w$ is the liquid water mass flux, ρ_l is density of liquid, X_l^w is mass fraction of water in liquid phase, **k** is intrinsic permeability, k_{rl} is relative permeability for liquid flow, μ_l is dynamic fluid viscosity, P_l is liquid pressure, ***g*** is acceleration from gravity, and z is elevation. The liquid flux is driven by the liquid pressure gradient, which in turn is strongly dependent on the capillary pressure and the water retention curve. At emplacement, there is a strong suction (high capillary pressure) within the partially saturated buffer and this suction becomes higher near the heater due to drying by evaporation. The flux also depends on the liquid flow mobility, including effects of intrinsic permeability and relative permeability for liquid flow.

The key parameters affecting the early time evolution of the moisture content are the water retention curve, absolute permeability and relative permeability, and the effective vapor diffusion coefficient for the partially saturated porous media. These parameters are usually determined from various laboratory experiments. The material parameters for the bentonite at the FE heater experiment have been determined by a number of experiments (both on granular bentonite samples and compacted bentonite blocks). Another key parameter is also the saturation dependent thermal conductivity of the bentonite. The thermal conductivity impacts the temperature evolution and the thermal gradient and will therefore also impact the evolution of the moisture in the bentonite buffer.

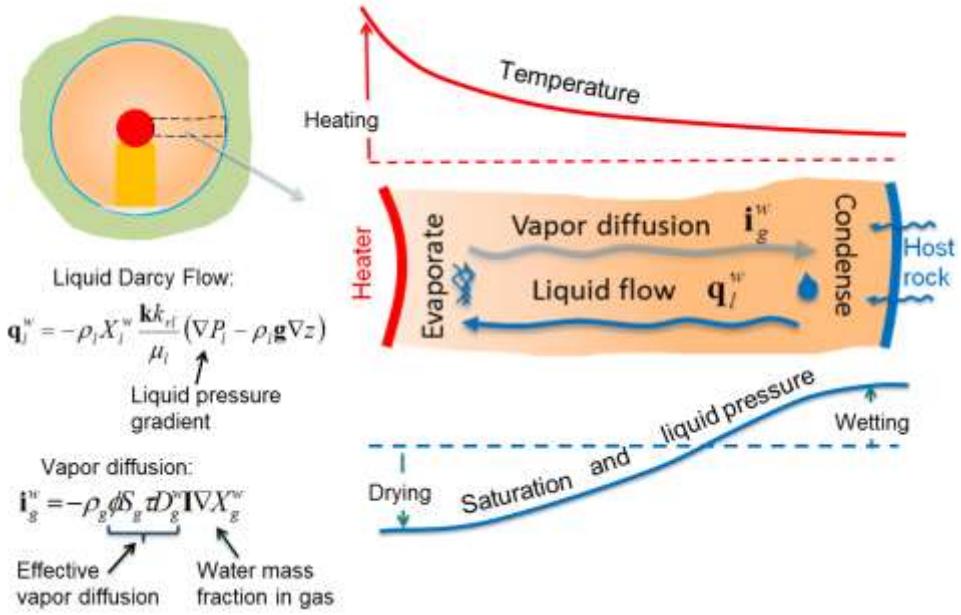

Figure 2-11. Conceptual model of the evolution of moisture in the heated bentonite buffer and equations for vapor diffusion in the gas phase and for liquid Darcy flow along the gradient of liquid pressure (capillary driven).

In the FY2016 milestone report (Zheng et al., 2016), the simulation results with comparison to one year was presented. One of the main results reported was the fact that a tortuosity parameter as low as $\tau = 0.14$ was applied in order to obtain good match for the evolution of relative humidity in the buffer. Example of the results of temperature and relative humidity evolution for the FY2016 model at Heater 2 (H2) is shown in Figure 2-12. In FY2016 milestone report it was shown that if using a higher tortuosity factor, e.g., $\tau = 1.0$, the modeling with predict too much drying near the heater compared to that observed in the measurements.

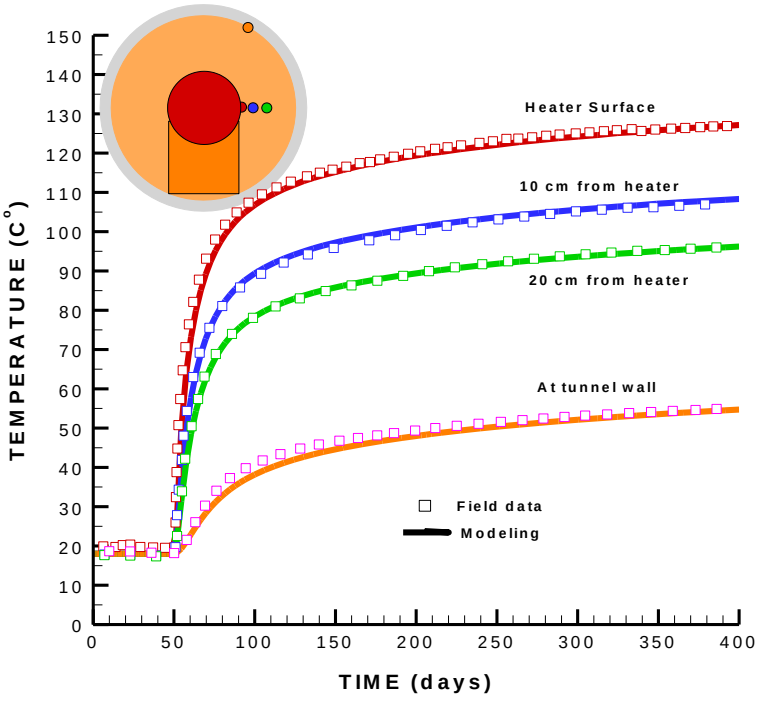

(a)

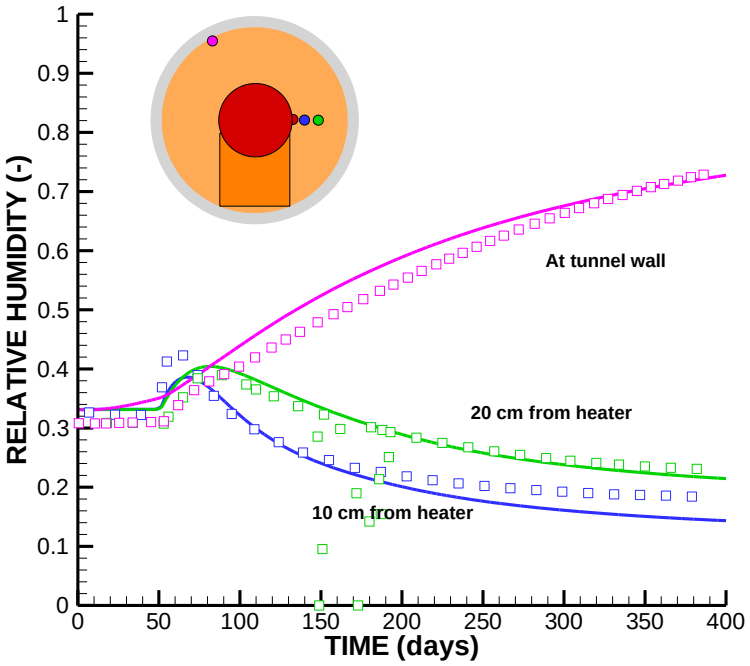

(b)

Figure 2-12. Comparison of modeled (lines) and measured (symbols) evolutions of (a) temperature and (b) relative humidity at monitoring point located in granular bentonite at H2 as presented in FY2016 milestone report (Zheng et al., 2016).

In FY2017, we have expanded the analysis with comparison to more than two years of field data and made a comparison at monitoring points at all heaters H1, H2 and H3. This includes a more accurate placement monitoring points for extracting simulation results from the numerical modeling. In the FY2016 milestone report, only approximate locations in the buffer were used, e.g., at 10 cm and 20 cm (e.g., Figure 2-12 results). However, in the field data the location of the monitoring points where not exactly at 10 and 20 cm, and the exact location can have a substantial impact on the extracted output results.

The FY2017 updated numerical results to date with comparison to measured data are shown in Figures 2.13 to 2.18. The time zero in these figures are at 12/28/2014, which is just after the start of the heating at H1. The material parameters used in the modeling here are exactly the same as that in the FY2016 milestone report. For example, we still apply a tortuosity factor of 0.14.

Overall, the results shown in Figures 2-13 to 2-18 confirm a continuous excellent agreement in buffer temperature evolution and a good agreement in the evolution of relative humidity. Some disagreements can be noted related to (1) the relative humidity evolution in the bentonite blocks (Figures 2-14b, 2-16b, and 2-18b), (2) relative humidity evolution near the rock wall (Figure 2-17b), as well as (3) some minor discrepancies in temperature evolution at a few locations (e.g., Figure 2-15a)

The simulation overestimates the relative humidity in the bentonite blocks close to all three of the heaters (Figures 2.14b, 2.16b, and 2.18b). This might be surprising considering that a good agreement was obtained in the FY2016 milestone report (Zheng et al., 2016). The explanation is that the more accurate locations have been defined in the numerical output data. In the FY2016 report, the standard distance of 10 cm was used, while the accurate locations are at 14 to 18 cm from the heater. At that distance, the calculated drying effect from the evaporation and vapor diffusion is smaller. This result indicates that the application of the tortuosity factor as low as 0.14 is good for the granular bentonite, but does suppress the vapor diffusion too much in bentonite blocks. Thus, a better match will likely be achieved by increasing the tortuosity factor for the bentonite blocks.

The simulated evolution of relative humidity near the tunnel wall is generally in good agreement with measurements, but some disagreement can be observed for the results at heater 3 (Figure 2-17b), where the measurements shows a more rapid increase. However, it is noted that the rate of wetting is very sensitive to how far from the rock wall the monitoring point is located. In the modeling, the tunnel is simulated as a perfect circle, while in the field the shape of the tunnel is not perfectly circular (Figure 2-19). Also in the modeling, the shotcrete is modeled with a certain uniform thickness, which might be different from the heterogeneous shotcrete thickness in the field. Overall, the rate of inflow from the rock and the relative humidity evolution is well captured. In general, the rate of inflow to saturate the buffer is small due to the low permeability of the host rock.

Some minor discrepancies in the temperature evolution can be noted close to H1. The calculated temperature at H1 is generally smaller than the measured. In fact, the calculations show that the heater in the middle (H2) has about 2°C higher maximum temperature than at H1 and H3. In the field on the other hand, H1 has a slightly higher maximum temperature than H2 and H3. The higher temperature at H1 could be due to a heterogeneous buffer in which the buffer density affects the local thermal conductivity. Another factor that can affect the temperature in the buffer close to the heater is the fact that the heater is not exactly centered at the tunnel axis, but displaced slightly to the right in Figure 2-19.

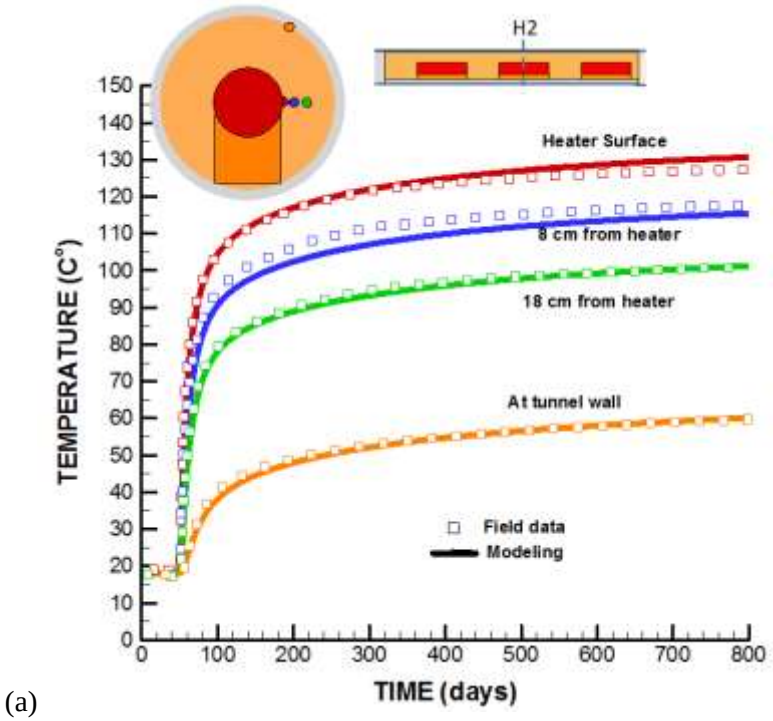

(a)

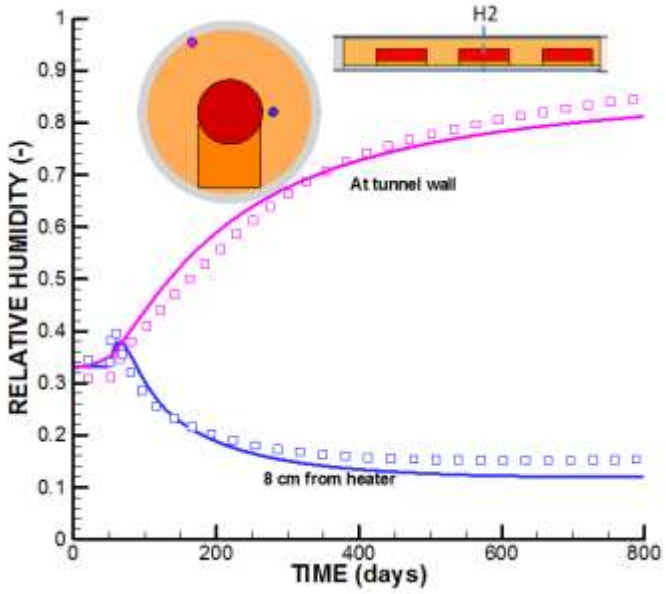

(b)

Figure 2-13. Comparison of modeled (lines) and measured (symbols) evolutions of (a) temperature and (b) relative humidity at monitoring point located in granular bentonite at H2 for over two years of monitoring data.

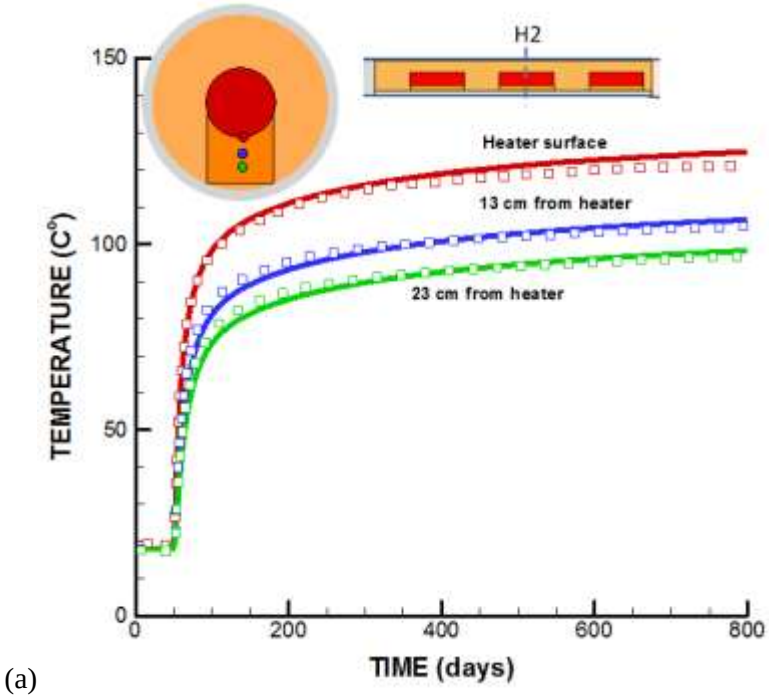

(a)

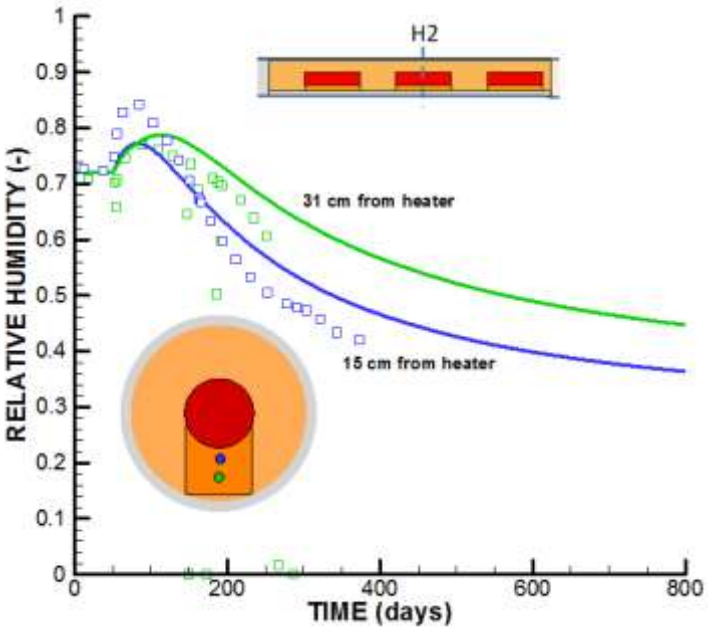

(b)

Figure 2-14. Comparison of modeled (lines) and measured (symbols) evolutions of (a) temperature and (b) relative humidity at monitoring point located in bentonite blocks at H2 for over two years of monitoring data.

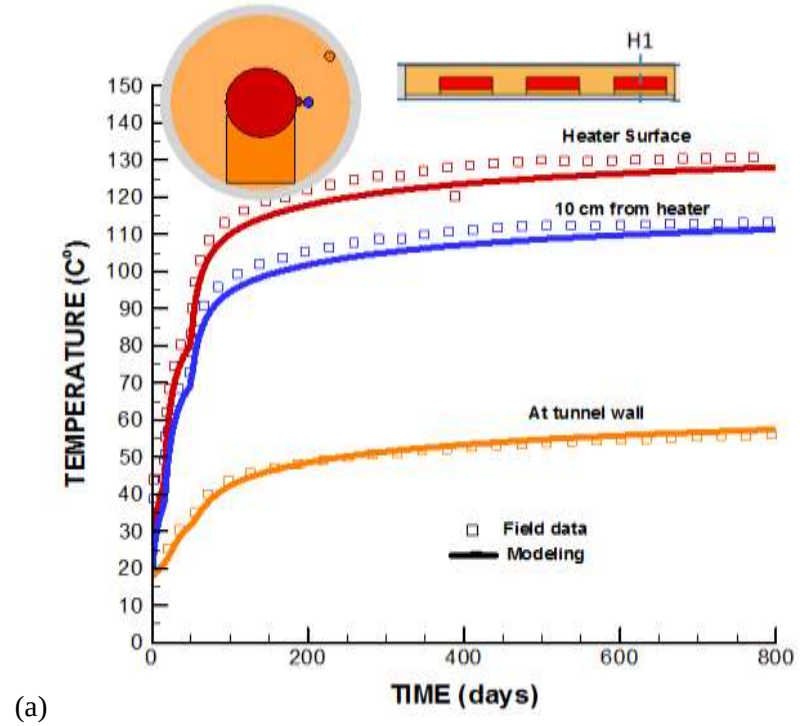

(a)

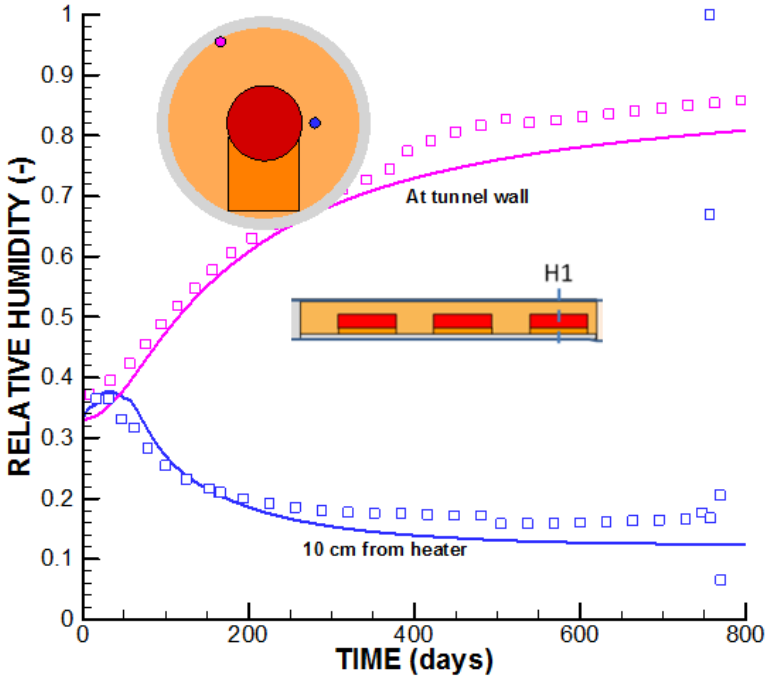

(b)

Figure 2-15. Comparison of modeled (lines) and measured (symbols) evolutions of (a) temperature and (b) relative humidity at monitoring point located in granular bentonite at H1 for over two years of monitoring data.

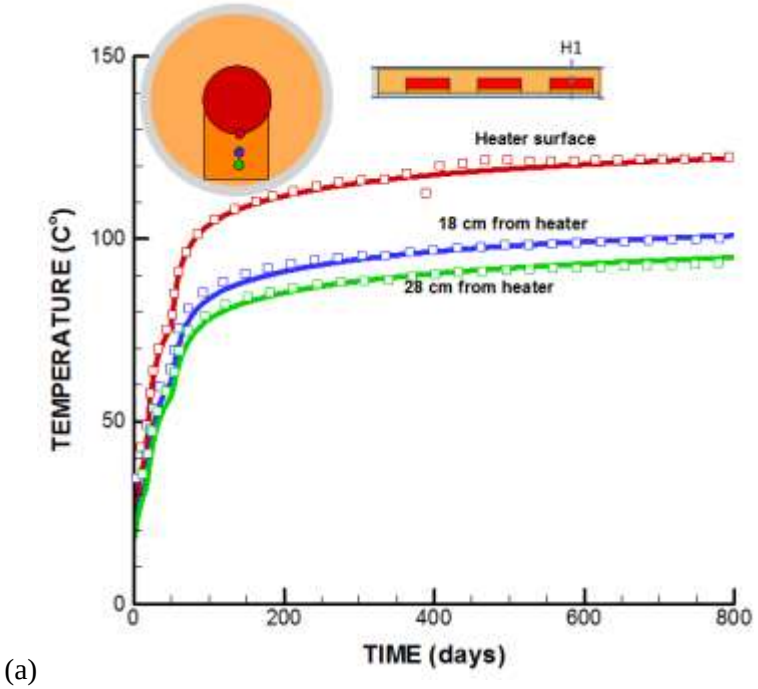

(a)

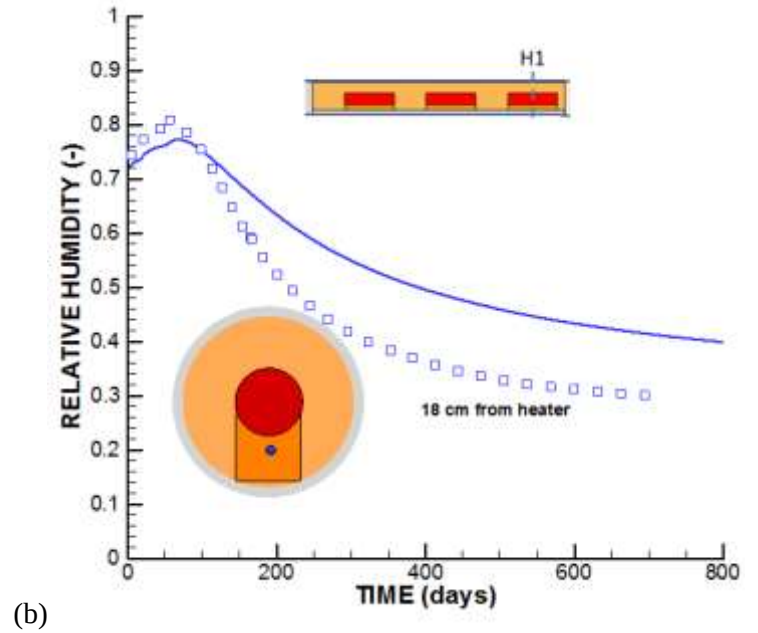

(b)

Figure 2-16. Comparison of modeled (lines) and measured (symbols) evolutions of (a) temperature and (b) relative humidity at monitoring point located in bentonite blocks at H1 for over two years of monitoring data.

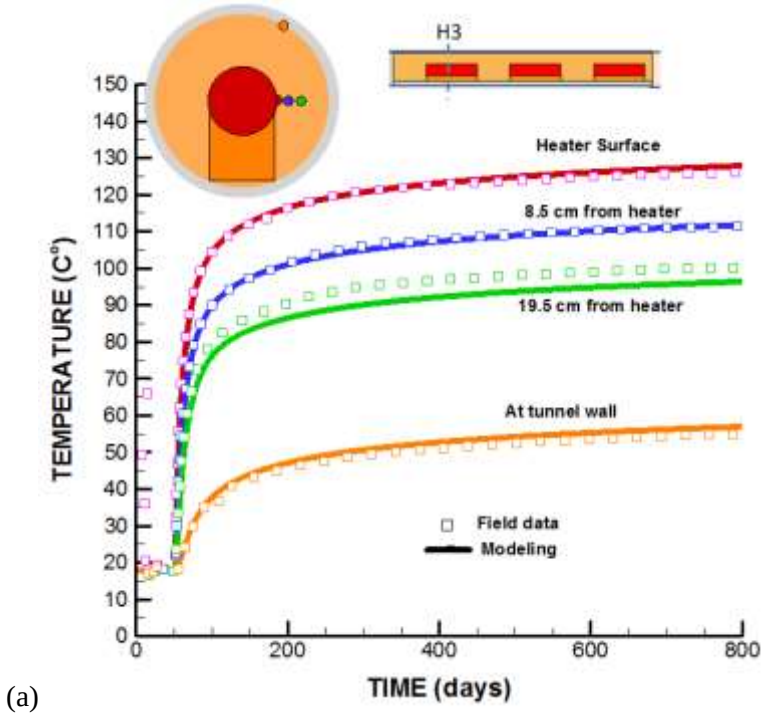

(a)

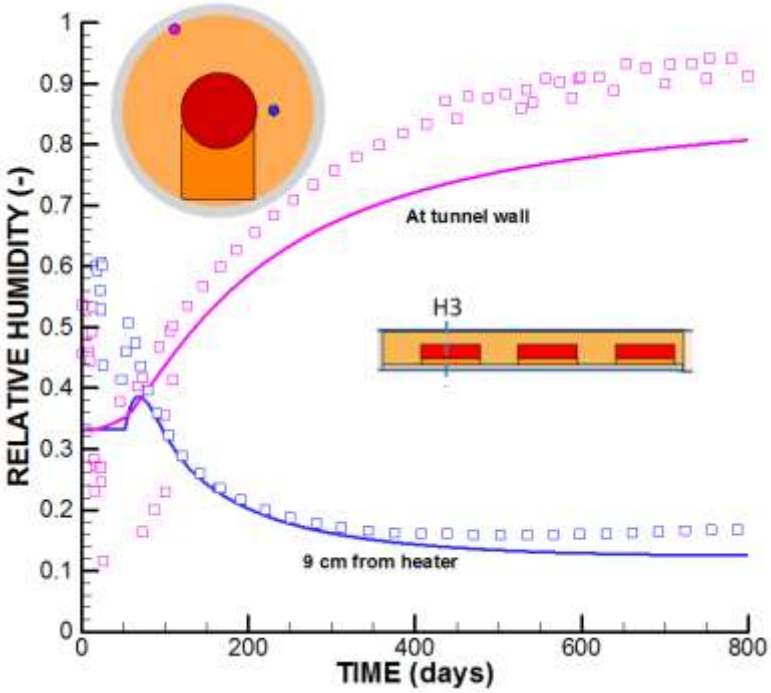

(b)

Figure 2-17. Comparison of modeled (lines) and measured (symbols) evolutions of (a) temperature and (b) relative humidity at monitoring point located in granular bentonite at H3 for over two years of monitoring data.

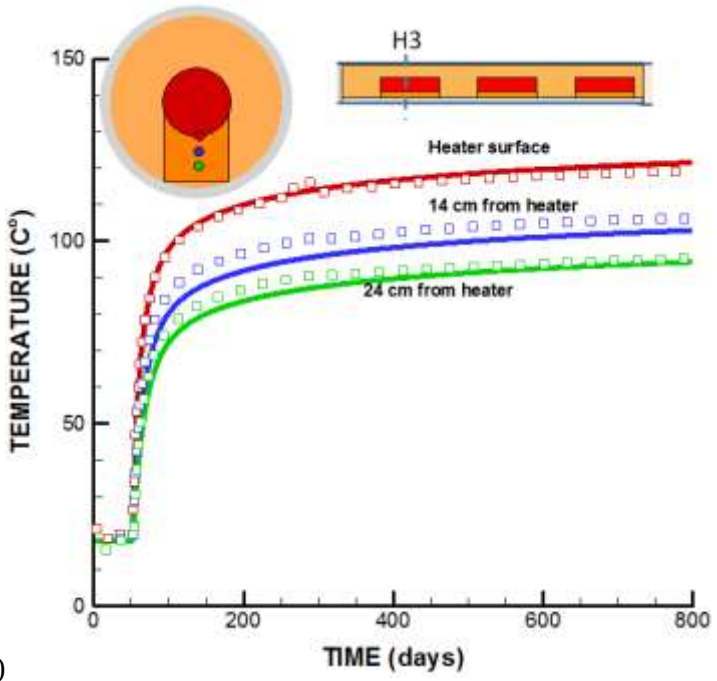

(a)

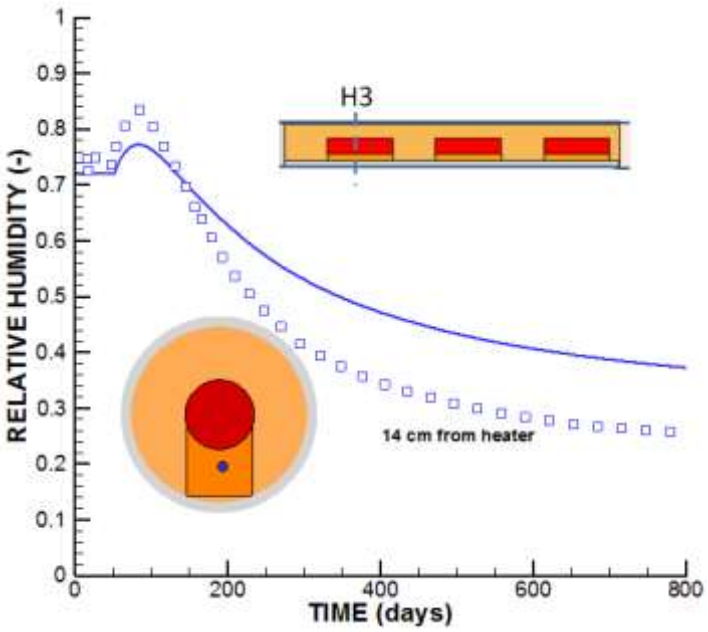

(b)

Figure 2-18. Comparison of modeled (lines) and measured (symbols) evolutions of (a) temperature and (b) relative humidity at monitoring point located in bentonite blocks at H1 for over two years of monitoring data.

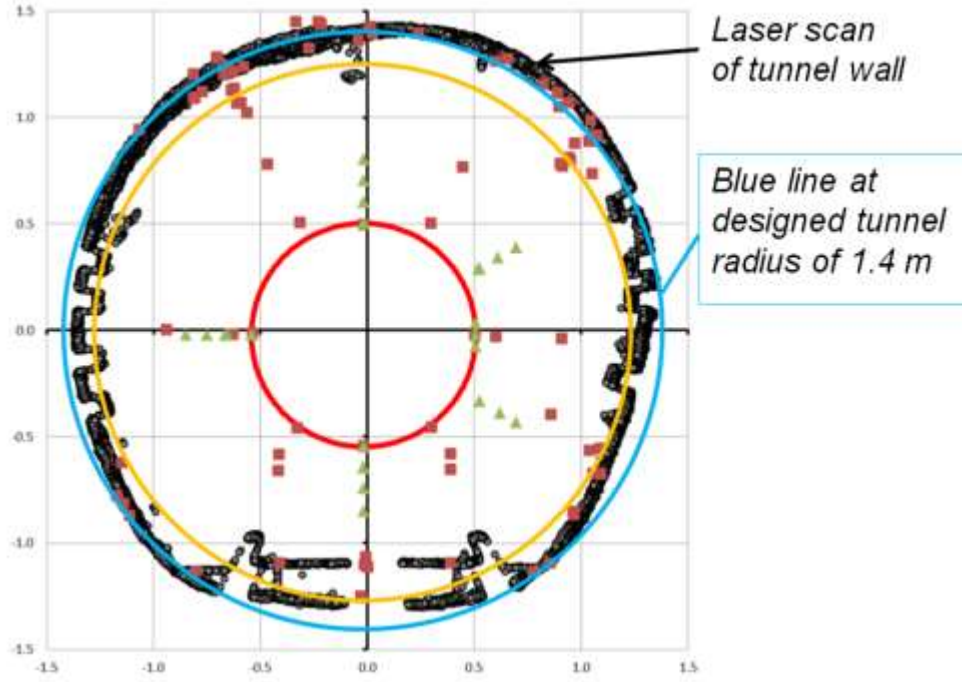

Figure 2-19. Laser scan of experimental tunnel with comparison to perfectly circular tunnel design as used in the modeling. The red circle in the middle is the heater. Squares and triangles indicates locations of some of the monitoring sensors. Axis units are in meters.

2.3.5 Summary and status the FE experiment modeling

As a modeling team in the Mont Terri FE experiment, we have conducted various types of modeling over the past few years, including benchmarking, heating design modeling, model predictions and interpretative modeling. Currently, we have interpreted temperature and relatively humidity data up to two years of heating. We have completed comparison of the basic temperature and relative humidity evolution in both granular bentonite and bentonite blocks. Some finding and lessons learned from this:

- A good agreement between modeled and measured evolutions in buffer temperature and relative humidity was achieved at the FE experiment based on a model prediction using properties of bentonite and Opalinus Clay determined associated with the previous Mont Terri HE-E experiment.
- A value of the effective vapor diffusion coefficient (and medium tortuosity factor) could be precisely calibrated against measured relative humidity evolution in the granular bentonite, but the value was much lower than used for previous modeling of the HE-E experiment. This difference and the potential role of enhanced thermal diffusion of the early time TH response in the buffer are open questions that warrant further studies.
- New comparison with exact location of output points revealed that the low medium tortuosity factor does not apply to the bentonite blocks, as the current model does not capture the degree of drying that is observed in the measurement.

Future modeling will in more detail study the difference in the evolution of relative humidity between granular bentonite and bentonite blocks. A higher effective diffusion (higher value of medium tortuosity) should results in better agreement for the relative humidity evolution in the bentonite blocks.

2.4 TED Experiment at Bure URL (DECOVALEX-2019 Project)

In this section, we present TOUGH-FLAC modeling results related to the TED *in situ* heater experiment conducted in Callovo-Oxfordian claystone (COx) at the MHM underground research laboratory in Bure, France. The modeling of the TED heater test is one of the Tasks of the DEvelopment of COupled Models and their VAlidation against EXperiments (DECOVALEX)-2019 project. In the following, we first provide a description of the DECOVALEX-2019 Task E and international modeling teams associated with this task; then provide a description of the TED experiment and current TOUGH-FLAC simulation results with comparison to experimental data.

2.4.1 DECOVALEX-2019 Task E and international modeling teams

DECOVALEX-2019, Task E is a study addressing important issues related to repository design and safety calculation: "How to go from sample to a repository scale?" Thermally induced pore pressure build-up and stress changes around a repository are important issues studied in this task. The task is coordinated by ANDRA in France and involves modeling of two *in situ* tests performed at the underground research laboratory in Bure (France):

- The TED experiment, a small-scale heating experiment focused on the claystone THM behavior of the undisturbed rock mass in the far field
- The ALC experiment, a one-to-one scale heating experiment especially focused on the interaction between the surrounding rock and the support (steel casing in this case) in the near field

Following the modeling of the two *in situ* tests, the impact of the behavior at the repository scale (considering several parallel cells) will be modeled. This application should address some key technical challenges, such as the variability of the THM parameters over such a surface and the determination of appropriate boundary conditions when 2D modeling is used to represent a series of parallel cells.

DECOVALEX-2019, Task E is conducted by a systematic approach, from small-scale to full-scale study (Figure 2-20). It is structured into four main steps and includes a benchmark test (step 1), an interpretive exercise (step 2), a blind prediction (step 3a) and an application (step 4):

- Step 1: Simple 3D THM modeling benchmark
- Step 2: Interpretative modeling of the TED experiment (back analysis)
- Step 3: Modeling of the ALC experiment
    - Step 3a: Predictive modeling of the ALC experiment using the reference values for the rock mass parameters determined in step 2
    - Step 3b: Interpretative modeling of the ALC experiment
    - Step 3c: Interpretative modeling of the ALC experiment focus on the support of the micro tunnel
- Step 4: Prediction at the repository scale/ modeling of an area with several high level waste cells

Participating Groups in the DECOVALEX-2019, Task E are

- France: Andra
- Germany: BGR (UFZ Leipzig)
- UK: RWM (Quintessa Ltd.)
- USA: DOE, LBNL

Currently, Step 1 has been completed related to 3D THM modeling benchmark and Step 2 is ongoing related to interpretative modeling of the TED experiment at Bure. The modeling of the ALC experiment should be started before the next DECOVALEX-2019 workshop that on which will be held in October 2017.

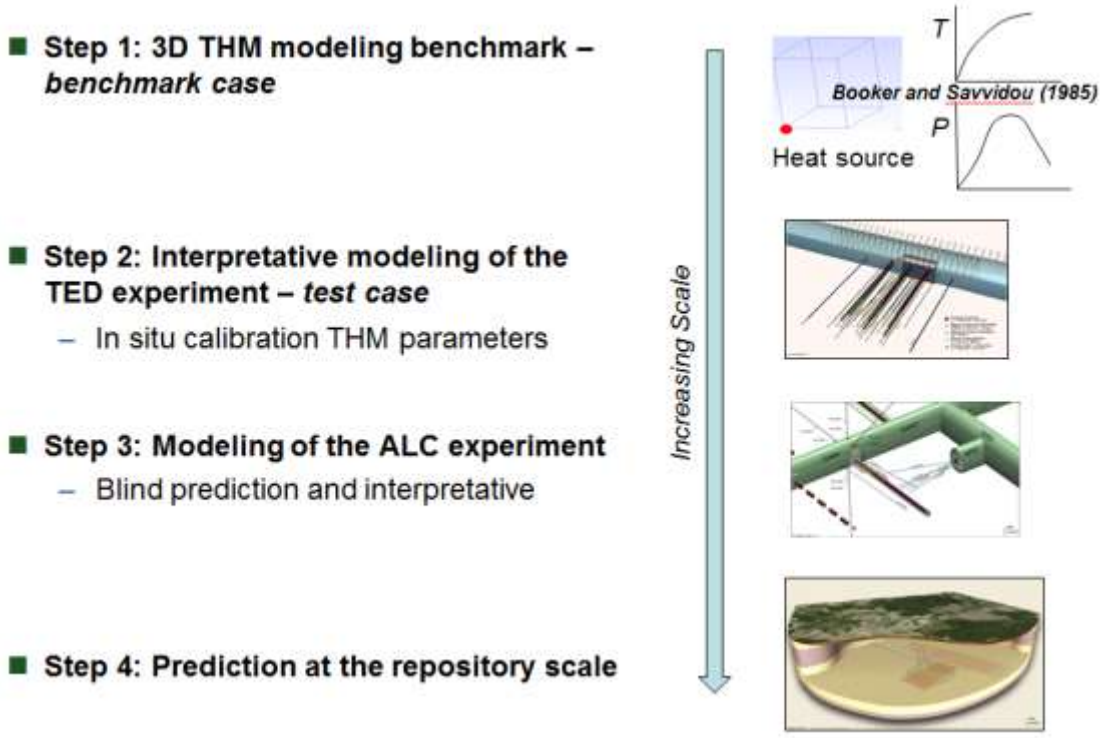

Figure 2-20. Overview of DECOVALEX-2019 Task E with steps of increasing scale.

2.4.2 Description of TED Experiment at Bure

The TED experiment lasted three years between 2010 and 2013. It involved three heaters at a depth of 490 m, in three parallel boreholes at a separation of about 2.7 m (Figure 2-21). The three heaters were 4 m long and were installed at the end of 160 mm diameter and 16 m long boreholes, drilled from a main drift and parallel to the maximum horizontal stress. This arrangement represented a similar configuration to high-level nuclear waste cells with parallel micro tunnels, but at a smaller scale. The TED experiment was heavily instrumented with 108 temperature sensors in the rock mass, 69 temperature sensors in the 3 heater boreholes, 18 piezometers, 2 extensometers and inclinometers, and 10 temperature sensors recording the temperature at the level of the main drift. The temperature measurements made during the TED experiment showed that the rock has an anisotropic thermal conductivity; at the same distance from the heater, the temperature increase is higher in the bedding plane than in the perpendicular direction. Observations of pore pressure also showed that its evolution depended on the location with respect to the bedding plane; following a power increase, the pore pressure increased faster in the direction parallel to bedding than in perpendicular direction.

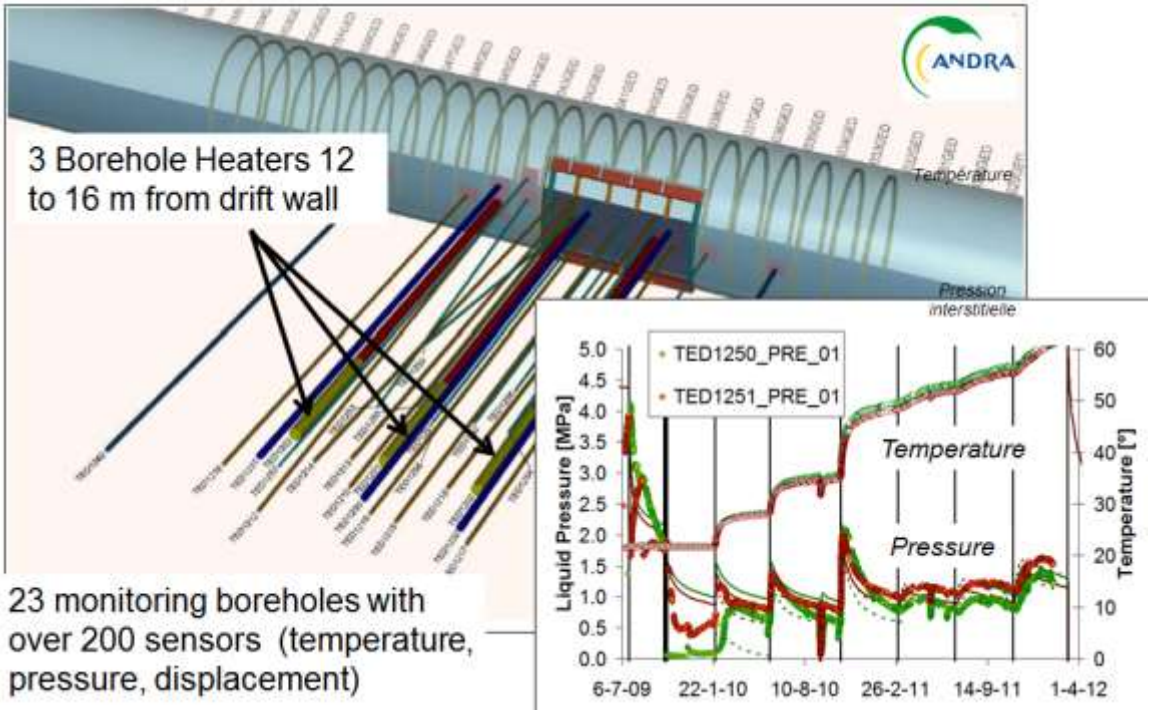

Figure 2-21. The TED experiment at Bure with insert of pressure and temperature evolution that are used by modeling teams in DEOVALEX-2019, Task E, for interpretative modeling.

2.4.3 TOUGH-FLAC simulation results with comparison to experimental data

2.4.3.1 Step 1 - 3D THM modeling benchmark

The step 1 of Task E is a basic benchmark test considering the consolidation of an infinite homogeneous saturated porous medium around a constant point heat input. Booker and Savvidou (1985) provided the analytical solution for this problem with the hypothesis that the pore water and the solid grains are incompressible. The analytical solution showed that, with a heat source located at the origin, temperature T, pore pressure p, and displacement u at a point (x, y, z) can be given by (with $i, j = x, y, z$):

$$T = \frac{Q}{4\pi\lambda R} f\left(\frac{\kappa t}{R^2}\right) \tag{2.20}$$

$$p = \frac{X}{1-c_v/\kappa}\frac{Q}{4\pi\lambda R}\left[f\left(\frac{\kappa t}{R^2}\right) - f\left(\frac{c_v t}{R^2}\right)\right] \tag{2.21}$$

$$u_i = \alpha_u i \frac{Q}{4\pi\lambda R} g^* \tag{2.22}$$

where λ is the thermal conductivity of porous medium; t is the time; and κ is the thermal diffusivity of the porous medium given by

$$\kappa = \frac{\lambda}{\rho C_p} \tag{2.23}$$

in which ρ is the density of the porous medium and C_p is its specific heat capacity.

c_v is the coefficient of consolidation, defined as

$$c_v = K_H(\lambda_L + 2G_L)/\gamma_w \tag{2.24}$$

where K_H is the hydraulic conductivity; λ_L and G_L are the Lame constants of the soil skeleton; and γ_w is the specific weight of water.

a_u is the volumetric thermal expansion coefficient of porous medium given by

$$\alpha_u = \alpha_s(1-\phi) + \alpha_w\phi \tag{2.25}$$

in which ϕ is the porosity and α_w and α_s are respectively the volumetric thermal expansion coefficients of pore water and solid grains.

R is the distance to the heat source:

$$R = \sqrt{x^2 + y^2 + z^2} \tag{2.26}$$

the functions f, g, f^* and g^* defined such as:

$$f\left(\frac{\kappa t}{R^2}\right) = \operatorname{erfc}\left(\frac{R}{2\sqrt{\kappa t}}\right) \tag{2.27}$$

$$g\left(\frac{\kappa t}{R^2}\right) = \frac{\kappa t}{R^2} + \left(\frac{1}{2} - \frac{\kappa t}{R^2}\right)\operatorname{erfc}\left(\frac{R}{2\sqrt{\kappa t}}\right) - \sqrt{\frac{\kappa t}{\pi R^2}}\exp\left(-\frac{R^2}{4\pi t}\right) \tag{2.28}$$

$$f^* = Yf\left(\frac{\kappa t}{R^2}\right) - Zf\left(\frac{c_v t}{R^2}\right) \tag{2.29}$$

$$g^* = Yg\left(\frac{\kappa t}{R^2}\right) - Zg\left(\frac{c_v t}{R^2}\right) \tag{2.30}$$

with X, Y, and Z such as

$$X = \alpha_u(\lambda_L + 2G_L) - b' \tag{2.31}$$

$$Y = \frac{1}{\lambda_L + 2G_L}\left(\frac{X}{(1 - c_v/\kappa)\alpha_u} + \frac{b'}{\alpha_u}\right) \tag{2.32}$$

$$Z = \frac{1}{\lambda_L + 2G_L}\frac{X}{(1 - c_v/\kappa)\alpha_u} \tag{2.33}$$

Simulator

We use the simulator TOUGH-FLAC for modeling of coupled THM processes in the heater test. The fundamental theory developed in this simulator is based on thermoporoelasticity, which extends thermoelasticity to porous continua. This extension is reached by considering an underlying thermoelastic skeleton. The stress in solid skeleton can be expresses as

$$\mathrm{d}\boldsymbol{\sigma} = \mathbb{C}\colon \mathrm{d}\boldsymbol{\epsilon} - \mathbf{b}\mathrm{d}p - \mathbb{C}\colon \boldsymbol{\alpha}\mathrm{d}T \tag{2.34}$$

where $\boldsymbol{\sigma}$ is the Cauchy stress; $\mathbb{C}$ is the tensor of skeleton tangent elastic stiffness modulus; $\boldsymbol{\epsilon}$ is the strain tensor; $\mathbf{b}$ is the Biot's tangent tensor; p is the pore pressure; $\boldsymbol{\alpha}$ is the tensor of skeleton tangent thermal dilation coefficients; and T is the absolute temperature.

The fluid continuity equation is

$$\frac{\mathrm{d}m_f}{\rho_f} = \mathbf{b}\colon \mathrm{d}\boldsymbol{\epsilon} + \frac{1}{M}\mathrm{d}p - 3\alpha_m \mathrm{d}T \tag{2.35}$$

where m_f is the fluid mass content; ρ_f is the fluid density; $\frac{1}{M} = \frac{1}{N} + \frac{\phi}{K_f}$; N is the Biot's tangent modulus linking the pressure variation and the porosity variation; ϕ is the porosity; K_f is the fluid tangent bulk

modulus; $\alpha_m = \alpha_\phi + \phi\alpha_f$; $3\alpha_\phi$ is the volumetric thermal dilation coefficient related to the porosity; and $3\alpha_f$ is the fluid tangent coefficient of volumetric thermal dilation.

In the analytical solution from Booker and Savvidou (1985), they assume that the fluid is incompressible, so the term $1/M\,\mathrm{d}p$ in equation is ignored. Because of that, the variation of fluid mass is only due to mechanical deformations and thermal expansion of the porous media. Moreover, in order to be consistent with the analytical solution, the density of fluid is modified to be only dependent on the temperature, and the viscosity of fluid is fixed in TOUGH.

Sequential Coupling of Thermo-hydraulics (TOUGH) and mechanics (FLAC)

We use a sequential coupling scheme named fixed stress-split method. This method is developed by Kim et al. (2011) to couple TOUGH and FLAC, and the solution by this method is unconditionally stable. In fixed stress-split method, flow problems are solved first under fixed stress; then pressure, temperature are passed to FLAC and prescribed during mechanical simulations. A porosity correction $\Delta\Phi_c$ is derived from the constitutive equations of solid skeleton for this scheme implementation:

$$\mathrm{d}\Phi = \left(\frac{b^2}{K} + \frac{b-\phi}{K_s}\right)\mathrm{d}p + \phi\alpha_s \mathrm{d}T - \Delta\Phi_c \tag{2.36}$$

where K is the bulk modulus of porous medium, and K_s is the bulk modulus of solid skeleton. The porosity correction $\Delta\Phi_c$ is calculated as

$$\Delta\Phi_c = -\frac{b}{K}\mathrm{d}\sigma_v = -\frac{b}{K}(K\mathrm{d}\epsilon_v - b\mathrm{d}p - K\alpha\mathrm{d}T) \tag{2.37}$$

Model setup

The 3D model is a cube of 15m×15m×15m that is generated with FLAC as Figure 2-22 shows. Considering the symmetric planes, only one eighth of the model is simulated. Due to the limitation of the temperature in the module EOS1 in TOUGH, we need to assign a bigger size for heat source with high thermal conductivity to lower the temperature inside heat source. Therefore, the heat source is represented by a 1/8 cylinder with 2.5 cm radius centered at origin point and is refined with smaller meshes. Additional, we also decrease the heat power from suggested 700 W to 14 W to reduce the highest temperature inside the heater.

The initial temperature, pore pressure and stresses are set to 0 °C and 0 Pa. Regarding thermal and hydraulic conditions and considering symmetric conditions, the three symmetry planes are impermeable and adiabatic. At far field, the temperature and pore pressure is set to 0 °C and 0 Pa. At the heat source,the constant heat power of Q=14 W is instantaneously applied at t=0. Regarding mechanical conditions, all the boundaries are free except the symmetry planes where null displacement conditions are applied normal to the boundaries.

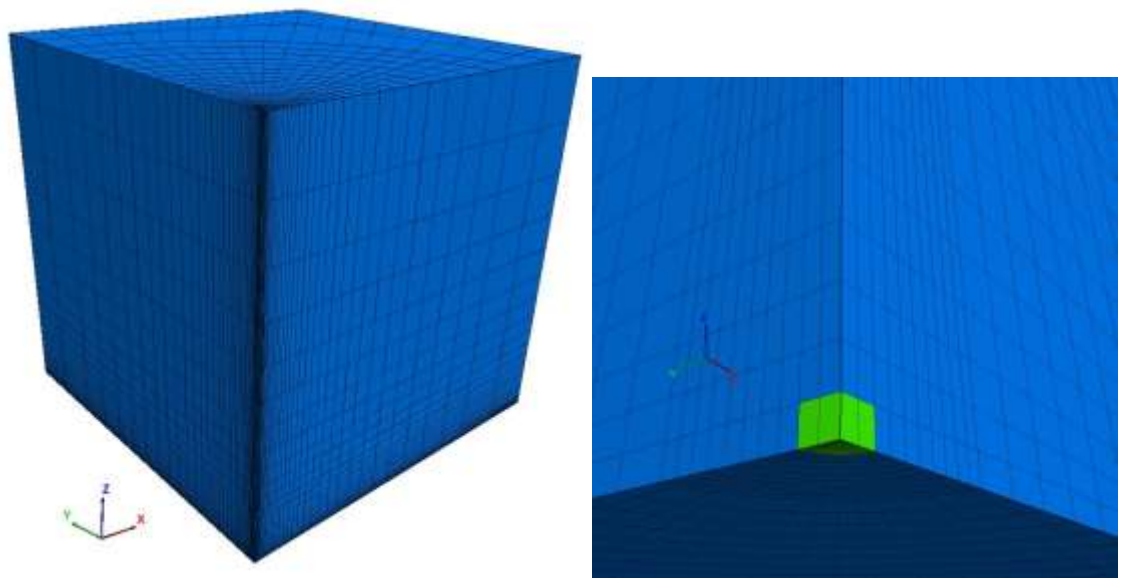

a) b)

Figure 2-22. a) Geometry of the simulation domain, b) the heater source (green elements) is a 1/8 cylinder with 2.5cm radius.

A homogenous and isotropic material is considered. The model parameters are listed in Table 2-3. It can be noted that the table includes the THM parameters of the two components (solid phase and pore water).

Table 2-3. Model parameters of step 1.

Parameters	Values
Porosity	$\phi = 0.15$
Equivalent thermal conductivity [W/m/K]	$\lambda = 1.7$
Equivalent density [kg/m^3]	$\rho = 2400$
Equivalent heat capacity [J/kg/K]	$C_p = 1000$
Permeability [m^2]	$k = 4.5 \times 10^{-20}$
Young modulus [MPa]	$E = 4500$
Poisson's ratio	$\nu = 0.3$
Density of solid grains [kg/m^3]	$\rho_s = 2700$
Heat capacity of solid grains [J/kg/K]	$C_{ps} = 773$
Volumetric coefficient of thermal expansion of solid grains [1/K]	$\alpha_s = 4.2 \times 10^{-5}$
Density of water [kg/m^3]	$\rho_w = 1000$
Compressibility of water [1/Pa]	$c_w = 0^*$
Heat capacity of water [J/kg/K]	$C_{pw} = 4180$
Dynamic viscosity of water [Pa×s]	$\mu_w = 1 \times 10^{-3}$
Volumetric coefficient of thermal expansion of water [1/K]	$\alpha_w = 4 \times 10^{-4}$

*Note: the analytical solution in (Booker and Savvidou, 1985) assumes the water is incompressible, indicating $c_w = 0$.

For comparison between modeling results and analytical solution, temperature, pressure, displacements (u_x, u_y, u_z) evolution up to 365 days at the following points are plotted in Table 2-4:

Table 2-4. Points for numerical results for step 1.

Points	(x, y, z) coordinates	Quantity
P1	(0.35, 0, 0)	Temperature, pressure
P2	(0.5, 0, 0)	Temperature, pressure
P3	(1.5, 0, 0)	Temperature, pressure
P4	(0.35, 0.5, 0.6)	Temperature, pressure, displacements

The simulation results of temperature are shown in Figure 2-23 as well as the analytical solutions. The calculated temperature at points P1 and P2 is slightly lower than the analytical solution, which is due to the size effects of the heat sources. As the result of the finite size and higher thermal conductivity of the heater, the peak value of the temperature inside the heater decreases, inducing the small amount reduction of the temperature at the points close to the heater. Except for these differences at point P1 and P2, an overall good agreement is obtained on the temperature evolution between numerical simulations and analytical solutions.

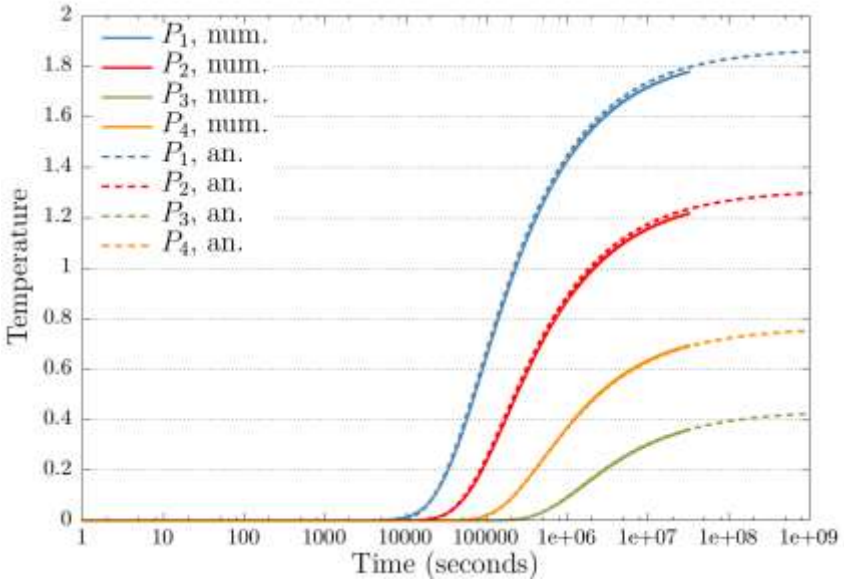

Figure 2-23. Simulation results of temperature at different points.

The same as temperature results, a good agreement on pore pressure is achieved as well. The differences between the model computation and analytical solution is due to the strategy of sequential coupling with TOUGH and FLAC. At each time step, TOUGH simulates the porosity change based on the current pore pressure and temperature, but the porosity correction is calculated from previous stress status ($d\sigma_v$), which is one-step before flow transport. Consequently, pore pressure does not contain the current stress status. One disadvantage of sequential coupling is when larger time increments are utilized in the simulation, this delayed effect is amplified, and the difference between model computation and analytical solution is larger. For the simplicity, the result is not presented here.

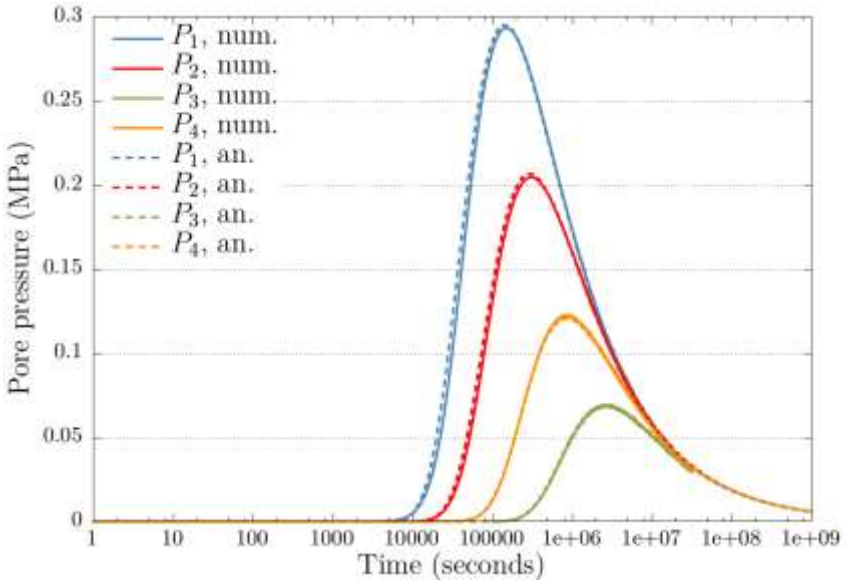

Figure 2-24. Simulation results of pore pressure at different points.

Figure 2-25 displays the displacement (u_x, u_y, u_z) evolutions at point P4. Generally, all displacements increase since the materials under the heat load. After about 10^6 seconds, all displacements start to decrease. The displacement in z-direction is larger than displacements in other two directions. The numerical results match the analytical solution well, although there are slight differences for each displacement.

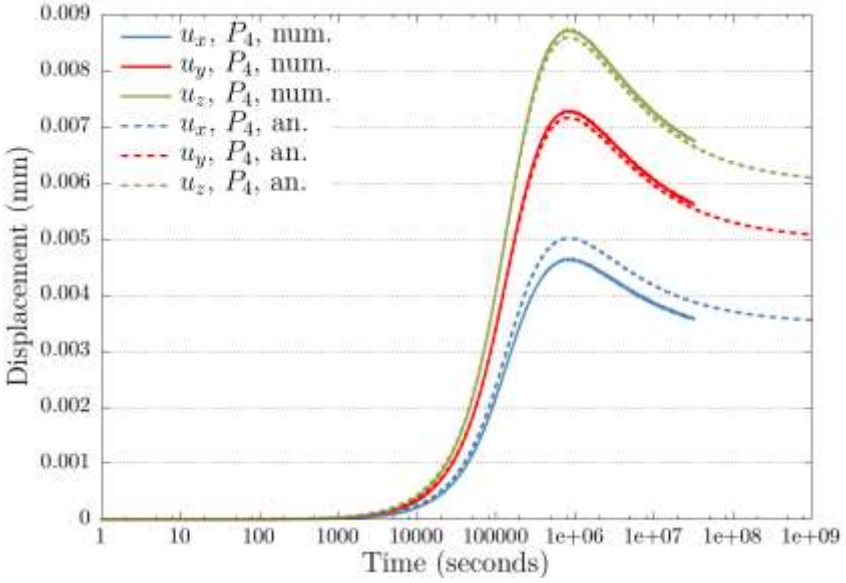

Figure 2-25. Simulation results of displacements at point P4.

To conclude, in order to simulate the THM problem analyzed in Booker and Savvidou (1985), first, we modified the simulator to match all theoretical assumptions as theirs. In addition to the modification, we also need to reduce the heat power to decrease the temperature inside the heater. As a result, the temperature does not exceed the limit of TOUGH requirements. In this way, a good agreement between

numerical simulations by TOUGH-FLAC and analytical solutions is obtained, which verifies the correctness of the THM models' computation in TOUGH-FLAC.

Water properties

In the previous section, we present an ideal case with saturated incompressible water in the porous media. To achieve the goal, we did some modification including changing the computation on water properties in the source code of TOUGH. Usually, water properties (density, specific enthalpy, viscosity) are calculated from the steam table equations (IFC-1976) in TOUGH. If this option is utilized for calculation, we can obtain the simulation results as follows.

The temperature evolutions at four points are shown in Figure 2-26. Compared with Figure 2-23, there are no obvious differences after the water properties are changed with temperature and fluid pressure.

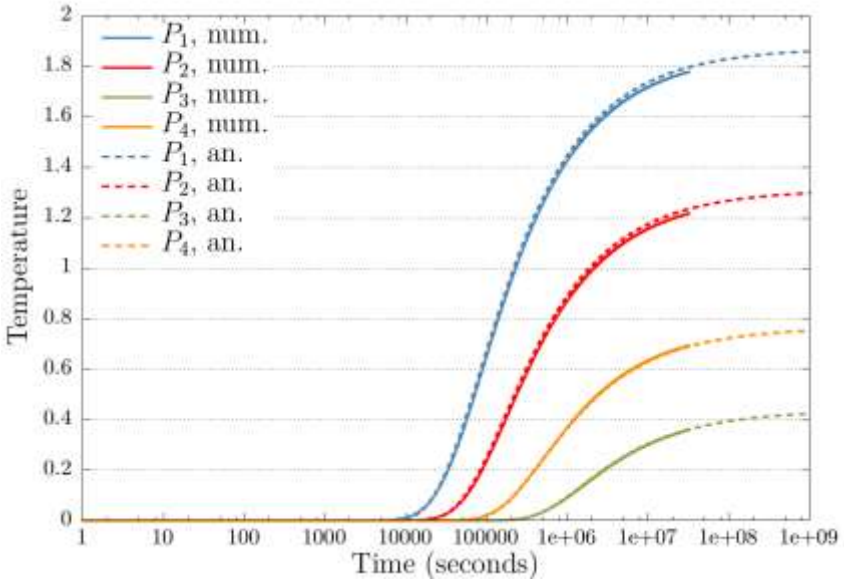

Figure 2-26. Temperature evolutions simulated with the water properties calculated form steam table equations.

However, not the same as temperature, all pore pressures reduce to about half of the previous results. With the changes on water properties, water becomes less stiff since the compressibility of water is non-zero in this case. Thus, pore pressures do not accumulate as high as before.

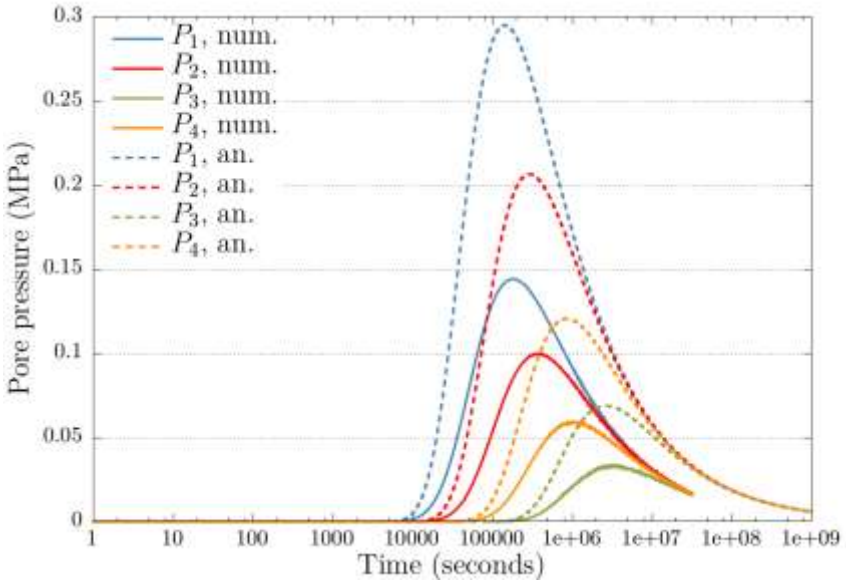

Figure 2-27. Pore pressure results simulated with the water properties calculated form steam table equations.

Figure 2-28 displays the displacement (u_x, u_y, u_z) evolutions at point P4. The peak values of displacements decrease and the reductions after 10^6 seconds are slower. For u_z, although the path of displacement evolution changes in this case, the trend shows the final displacement converges to the same value (about 0.0062mm) as the previous case. The same phenomenon can be found for u_x and u_y. The displacement in induced by effective stress, which is total stress minus pore pressure. As Figures 2-24 and 2.27 show, the pore pressure will dissipate to zero, indicating the heat loads will generate the same stress status in the end. Therefore, the corresponding displacements in both cases will become the same finally.

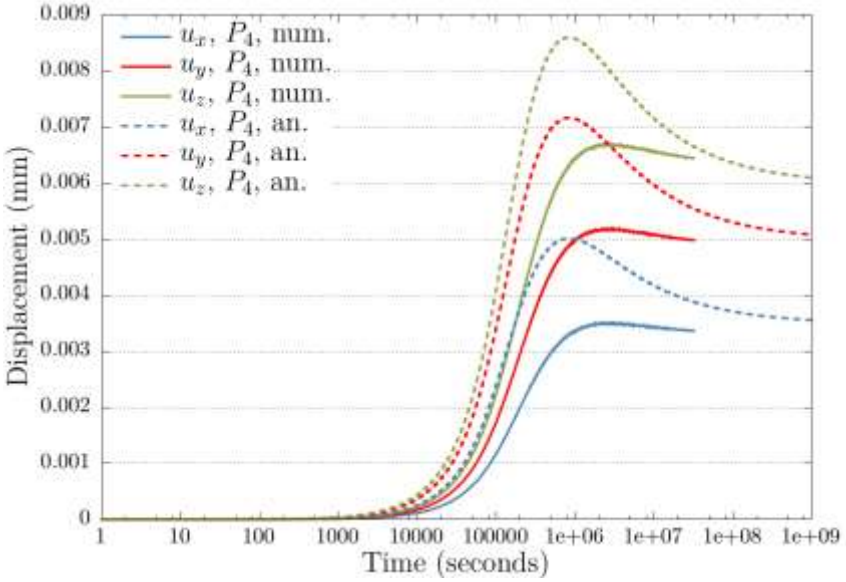

Figure 2-28. Displacement results at point P4 simulated with the water properties calculated form steam table equations.

2.4.3.2 Step 2 – TED experiment

The purpose of the step 2 is to model the THM response of Callovo-Oxfordian claystone in the TED experiment and to calibrate the numerical models against experimental data. This modeling of the TED experiment will help to increase understanding of the physical phenomena observed.

Model setup

The geometry simulated by the models is a cube with a side length of 50 m centered in height at z = 0, i.e., almost exactly the GED drift center at the depth of 490 m. The model represents only half of the GED drift (Figure 2-29). Three heaters are embed at the center of the domain with surrounded refined grids. For the modeling, it is assumed that the whole domain is saturated and remains saturated during the experiment. The boundary conditions are summarized in Table 2-5.

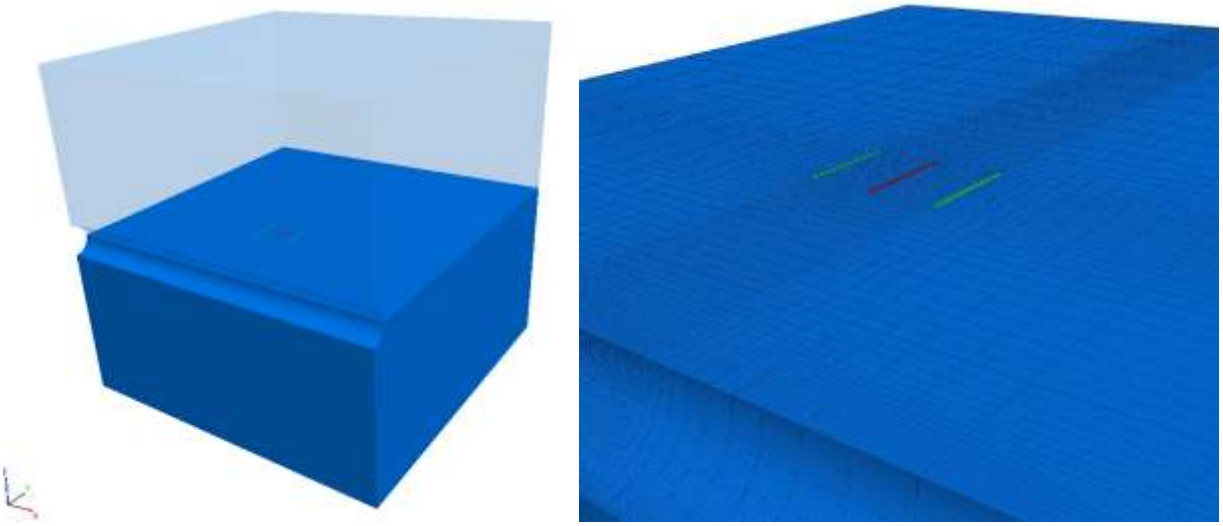

a) b)

Figure 2-29. a) The model setup. Heaters are embedded at the center of the domain, b) heater 1 (red) and heaters 2 and 3 (green) surrounded by refined meshes.

Table 2-5. THM boundary conditions of TED experiment modeling for step 2

Boundary	Thermal condition	Hydraulic condition	Mechanical condition
External faces (except top and bottom)	No heat flux	No water flux	No normal displacements
Top surface	*In situ* temperature T = 21 °C	4.7 MPa	Vertical geostatic stress $\sigma_v = 12.7$ MPa
Bottom	*In situ* temperature T = 23 °C	4.7 MPa	No normal displacements
GED drift wall	Temperature measurements in the GED drift (Figure 2-31)	Draining condition: atmospheric pressure	No normal displacements
TED1230 and TED1231 boreholes (extensometers)*	No heat flux	Draining condition: atmospheric pressure	No normal displacements
Heater boreholes	History of applied power (Figure 2-30)	Draining condition: atmospheric pressure	

**Note: the current simulation does not explicitly model these boreholes.*

The heating phase ran for about 1251 days, and the heat power input was divided into several stages. Heater 1 was turned on at the beginning of experiment. It took three steps to reach the planned heat power (600W). After the heater 1 working for 400 days, heaters 2 and 3 started to heat the domain, which includes three steps as well as heater 1. The heat power used in computation is simplified as Figures 2.30 a) and b) show.

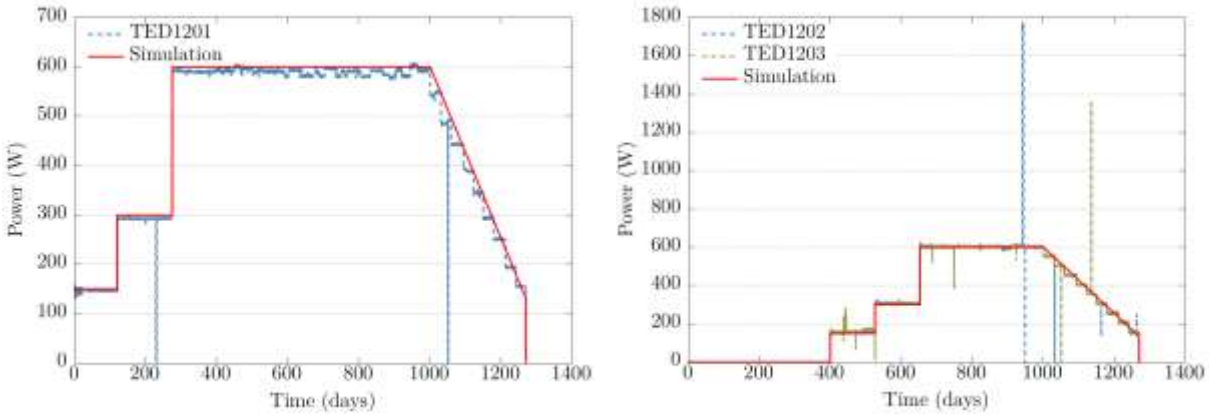

(a) (b)

Figure 2-30. a) Heat power used for heater 1, b) heat power used for heaters 2 and 3.

During the heating stage, the temperature at the GED tunnel is measured, which is considered as the temperature boundary conditions in the simulation domain. In TOUGH, one layer of boundary elements is added into the GED tunnel to calibrate the temperature changes during the heating phase. The calibrated temperature evolution (Figure 2-31) displays a good match for this boundary condition.

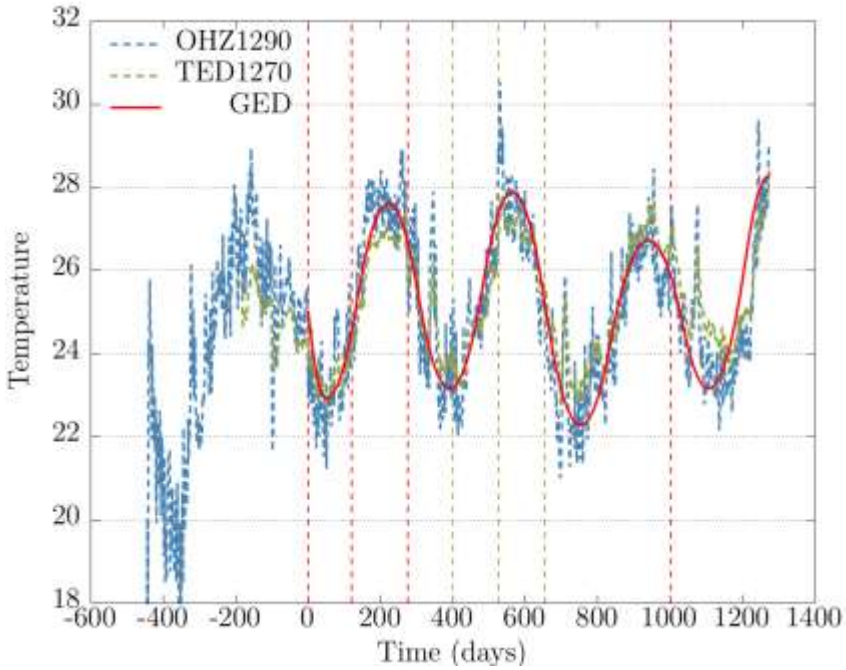

Figure 2-31. Temperature boundary conditions at GED tunnel.

Calibration of thermal conductivity

Six sensors were placed at different boreholes near heaters to measure the temperature evolution during the heating stage. The collected data were used as a basis for calibration of thermal properties. We calibrated thermal conductivities by using TOUGH only since the thermal transport is not affected much by hydro-mechanical processes. First, we launched a case with the reference value of thermal conductivity parallel/perpendicular to bedding plane suggested by the experimenters. TH parameters used for this work are listed in Table 2-6.

Table 2-6. TH parameters of step 2: used for calibration on thermal conductivities.

Parameters	Values
Porosity	$\phi = 0.15$
Equivalent thermal conductivity parallel to bedding [W/m/K]	$\lambda = 1.96$
Equivalent thermal conductivity perpendicular to bedding [W/m/K]	$\lambda = 1.26$
Equivalent density [kg/m^3]	$\rho = 2400$
Equivalent heat capacity [J/kg/K]	$C_p = 1000$
Density of solid grains [kg/m^3]	$\rho_s = 2600$
Heat capacity of solid grains [J/kg/K]	$C_{ps} = 800$
Water properties (ρ_w, c_w, C_{pw}, μ_w, α_w),	IFC-1967

The results of temperature changing with time together with the experimental data are plotted in Figure 2-32. All simulated temperatures are predicted higher than observed values, indicating the thermal energy

transfers are slower than expected. Then we re-calibrate the thermal conductivities by testing different values and an optimal set of values is obtained. The calibrated values are provided in Table 2-7.

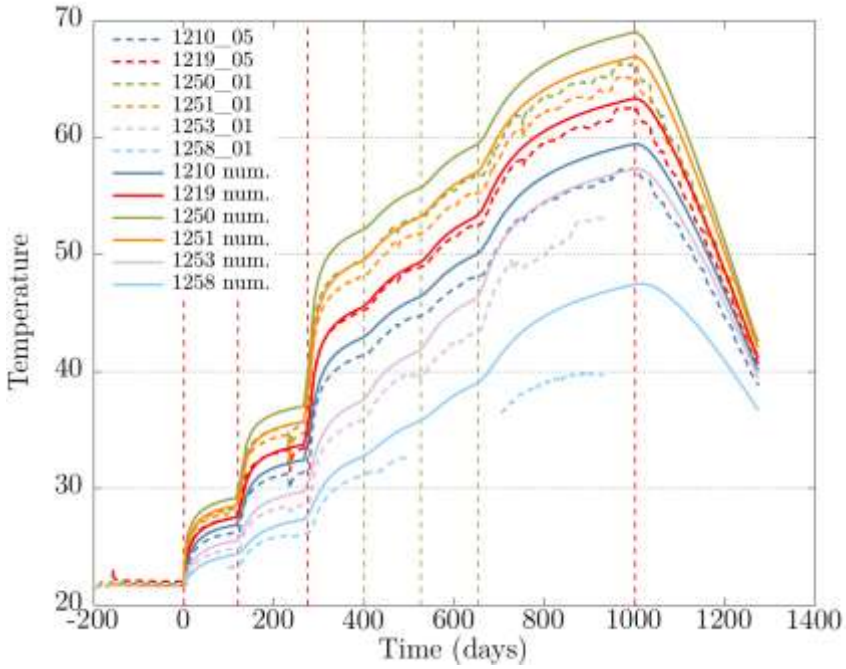

Figure 2-32. Temperature evolution simulated with reference thermal conductivities at measuring points.

Table 2-7. Calibrated values of thermal conductivities.

Parameters	Values
Equivalent thermal conductivity parallel to bedding [W/m/K]	$\lambda = 2.23$
Equivalent thermal conductivity perpendicular to bedding [W/m/K]	$\lambda = 1.21$

Figure 2-33 displays the new temperature results with calibrated thermal conductivities. As the figure shows, a good agreement on the temperature at boreholes 1210, 1219, 1250, and 1251 is achieved between the model prediction and the experimental data. While at the two farther points from the heater, boreholes 1253 and 1258, model overestimates the temperature about 3 ~ 5 degrees. However, these two sensors are reported as unreliable, so the calibration on the thermal transport is acceptable.

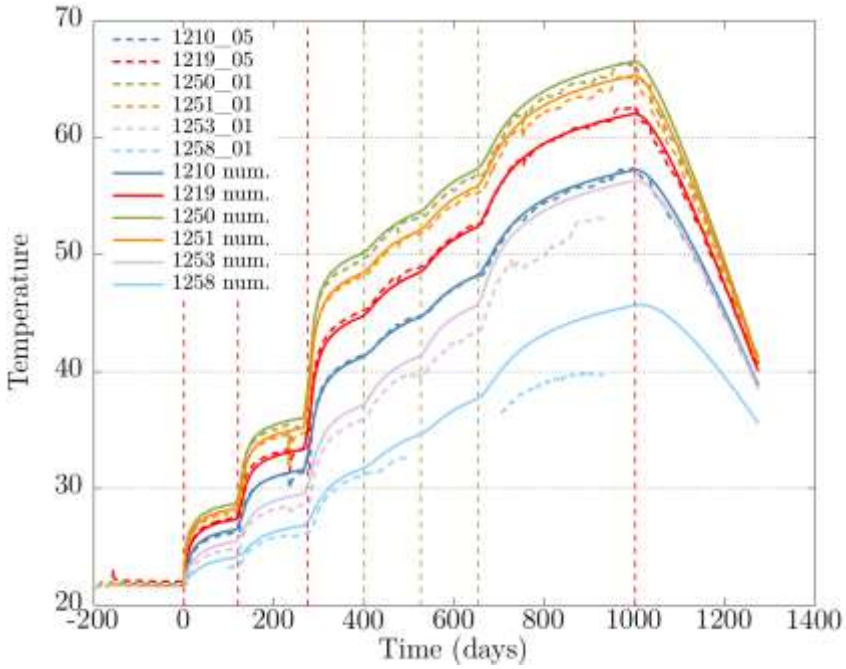

Figure 2-33. Temperature evolution simulated with calibrated thermal conductivities at measuring points.

Calibration of mechanical properties

The experiment team carries out laboratory tests, such as triaxial compression test and triaxial extension test, on rock samples. To account for the effects of anisotropic properties, in the same test, the deviatoric load is imposed to be parallel or perpendicular to the bedding plane. A transversely isotropic model is chosen for the rock. This model assumes the moduli parallel to bedding plane $E_1 = E_2 = E_{\parallel}$ are different from the modulus perpendicular to bedding plane $E_3 = E_{\perp}$. The mechanical properties are calibrated to match the observed stress-strain curves from laboratory experiments. Then we found the optimal parameters for the rock samples, summarized in Table 2-8.

Table 2-8. Calibrated mechanical parameters of rock samples.

Parameters	Values
Young's modulus parallel to bedding plane [GPa]	$E_1 = E_{\parallel} = 2.9$
Young's modulus perpendicular to bedding plane [GPa]	$E_3 = E_{\perp} = 4.5$
Poisson's ratio inside the bedding plane [-]	$\nu_{12} = 0.27$
Poisson's ratio between in bedding plane and out-of-plane [-]	$\nu_{13} = 0.32$

THM simulations

The THM computation is using the simulator TOUGH-FLAC. The only change from step 1 is the water properties are calculated from the steam table equations (IFC-1967), which can represent the water behavior in reality.

Table 2-9. THM parameters of step 2: used for THM simulations.

Parameters	Values
Porosity	$\phi = 0.15$
Equivalent thermal conductivity parallel to bedding [W/m/K]	$\lambda = 2.23$
Equivalent thermal conductivity perpendicular to bedding [W/m/K]	$\lambda = 1.21$
Equivalent density [kg/m^3]	$\rho = 2400$
Density of solid grains [kg/m^3]	$\rho_s = 2600$
Heat capacity of solid grains [J/kg/K]	$C_{ps} = 800$
Permeability parallel to bedding [m^2]	$K_{\parallel} = 6 \times 10^{-20}$
Permeability perpendicular to bedding [m^2]	$K_{\perp} = 3 \times 10^{-20}$
Biot coefficient	$b = 0.7$
Volumetric coefficient of thermal expansion of solid grains [1/K]	$\alpha_s = 4.2 \times 10^{-5}$
Young's modulus parallel to bedding [GPa]	$E_1 = E_{\parallel} = 2.9$
Young's modulus perpendicular to bedding [GPa]	$E_3 = E_{\perp} = 4.5$
Poisson's ratio inside the bedding plane [-]	$\nu_{12} = 0.27$
Poisson's ratio between in bedding plane and out-of-plane [-]	$\nu_{13} = 0.32$
Water properties (ρ_w, c_w, C_{pw}, μ_w, α_w)	IFC-1967

The pore water pressure is considered uniform at 4.7 MPa in the entire domain. The stress values follows the anisotropic state of stress. For the calculation, the stresses are proposed as the major horizontal stress σ_H is set to 16.1 MPa, and the horizontal minor stress σ_h and the lithostatic stress σ_v are set respectively to 12.4 MPa and 12.7 MPa.

The pore pressure at the beginning of the heating phase depends on the final status of excavation phase, so we shift the pore pressure to match the value at $t = 0$ (starting point at heating phase). The results are marked as "shifted" to indicate this change in figures. Figure 2-36 a) represents the simulation results of pore pressure at the sensor positions in boreholes 1253 and 1258. Compared with experimental data, the increase of pore pressure at borehole 1258 is underestimated, while the one at borehole 1253 is overestimated. Moreover, the observed date at borehole 1253 decreases during the heating phase, which is the opposite of the model prediction.

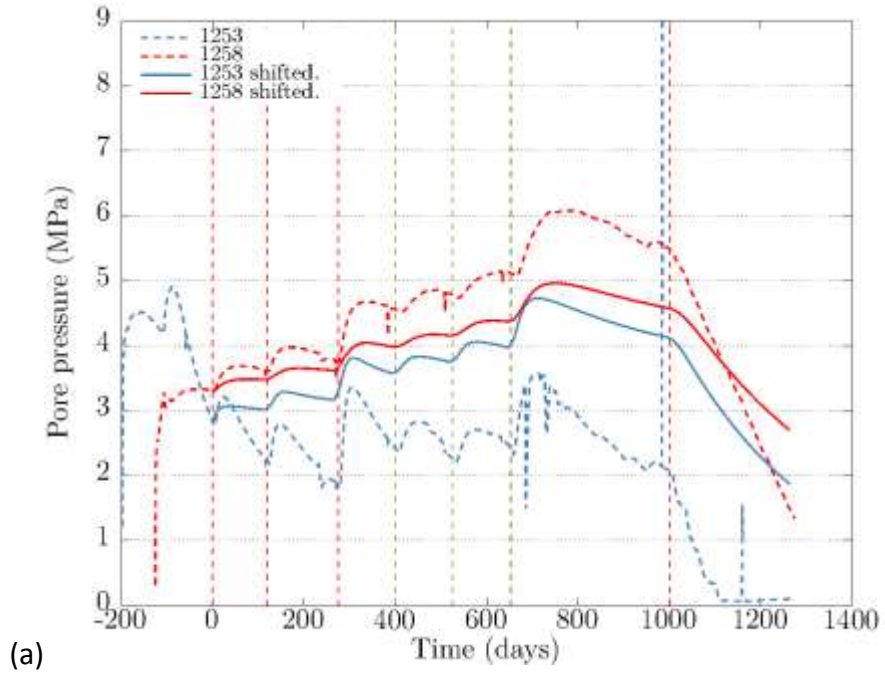

(a)

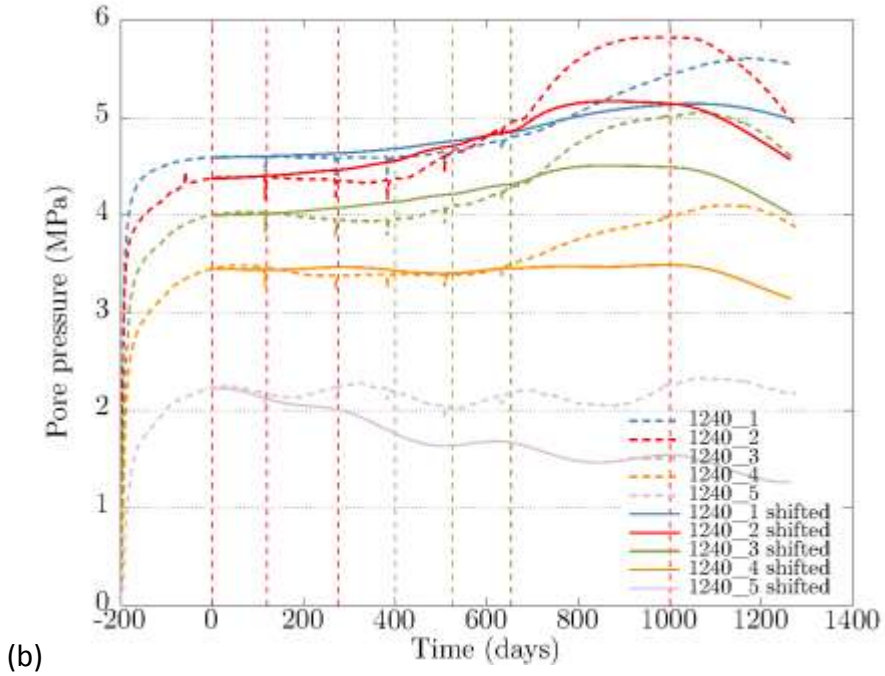

(b)

Figure 2-34. a) Pore pressure evolution at boreholes 1253 and 1258, b) pore pressure evolutions at boreholes 1240.

In Figure 2-34 b), the magnitudes of pore pressure increase at other measuring points in borehole 1240 are also smaller than the observed data. Therefore, for better prediction, we need to adjust some material parameters in our model. The fluid flow is calculated with diffusion equations in the simulator. For this question, the coefficient of water diffusion is expressed as

$$c_v = \frac{KK_s}{u_w} \tag{2.37}$$

Based on the previous results, the lower pore pressure indicates faster water diffusion. As the result of that, the diffusion coefficient should be reduced to drive the pore pressure increase. As the equation 2.37 illustrates, if the mechanical properties (K_s) and viscosity of water (u_w) keep constant, the permeability should be decreased. Therefore, we re-calibrate permeabilities; the optimal values are listed in Table 2-10.

Table 2-10. Calibrated permeabilities of rock samples.

Parameters	Values
Permeability parallel to bedding [m^2]	$K_{\parallel} = 1.5 \times 10^{-20}$
Permeability perpendicular to bedding [m^2]	$K_{\perp} = 1 \times 10^{-20}$

The new simulation is launched with calibrated permeabilities, and the pore pressure results are plotted in Figure 2-35. Figure 2-35 a) represents the results at the sensor positions in boreholes 1253 and 1258. Compared with experimental data, the increase of pore pressure in borehole 1258 matches the observed values well, while the one at borehole 1253 is still overestimated. The trend of pore pressure change at borehole 1253 is the opposite of the observed date. In the TED experiment, one extensometers borehole exists near the borehole 1253, where the draining condition is applied. Therefore, the drainage causes the pore pressure to decrease at the monitoring point in borehole 1253. So far, this condition is not imposed in the current model and results in this error in the simulation. The drainage condition will be added to the model in the future works.

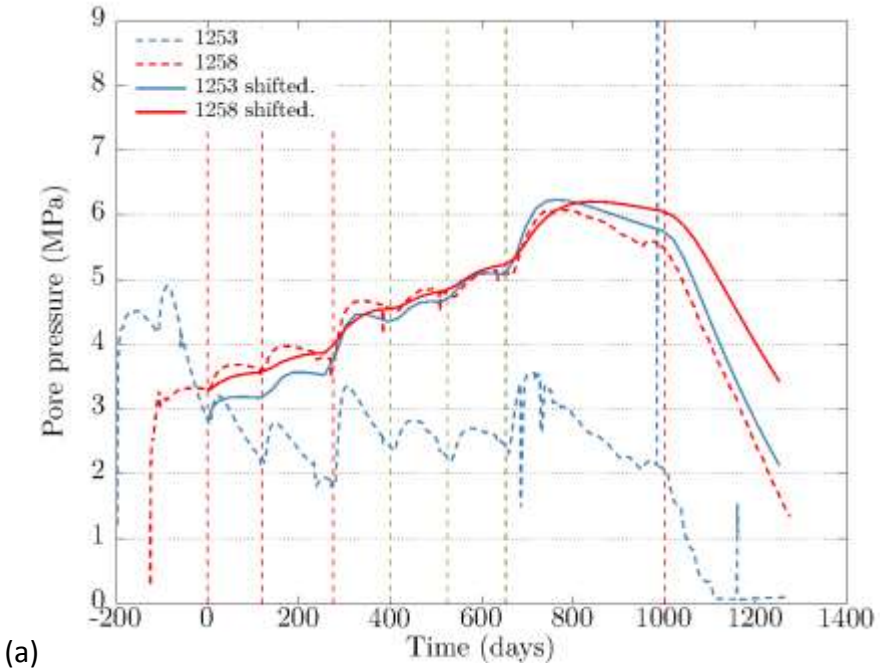

(a)

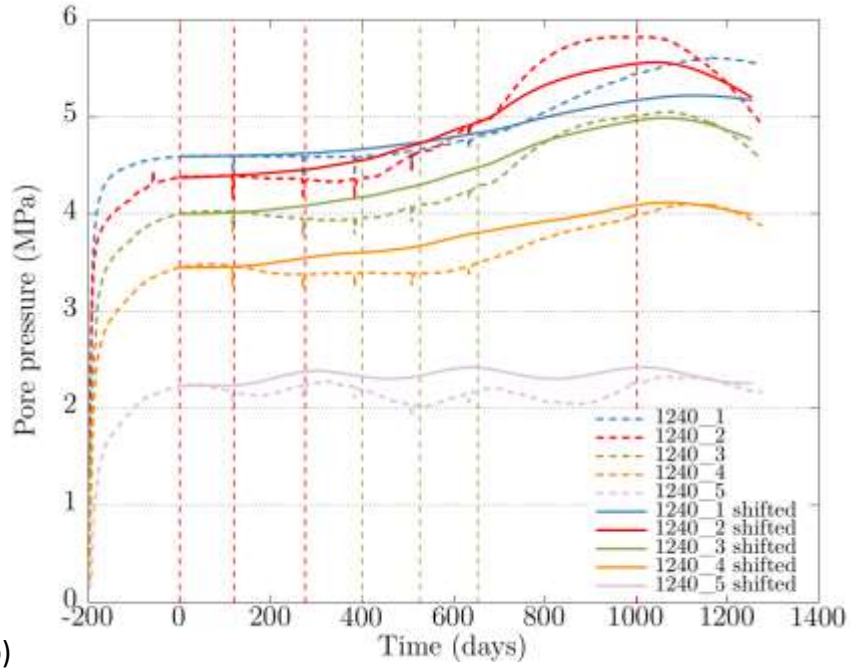

(b)

Figure 2-35. Simulation results with calibrated permeabilities, a) Pore pressure evolution at boreholes 1253 and 1258, b) pore pressure evolution at boreholes 1240.

Figure 2-35 b) presents the updated results of pore pressure at different positions in borehole 1240. Compared with the previous results in the figure, the trends of all pore pressure evolutions have been well captured by the simulation with calibrated parameters.

The stress results are shown as well in Figure 2-36. The plots show the stresses increase as the heat powers increase, decrease when the heaters cool down. Therefore, the shape of each stress evolution is similar with the temperature changes. Since no measured data on stresses provided, comparison between model results and experimental data is not available.

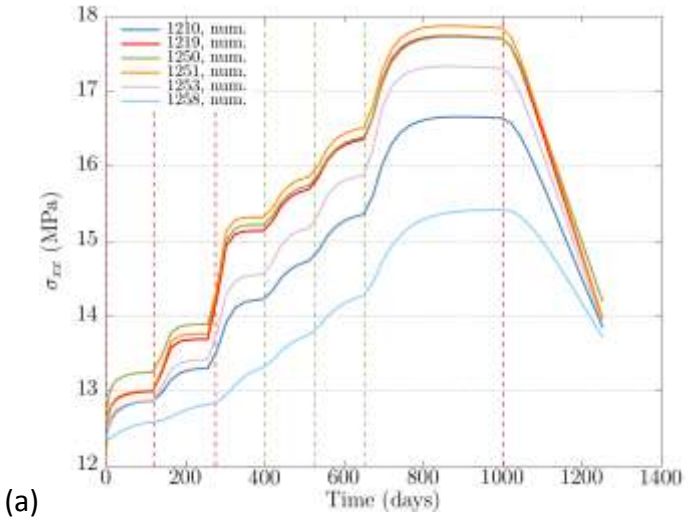

(a)

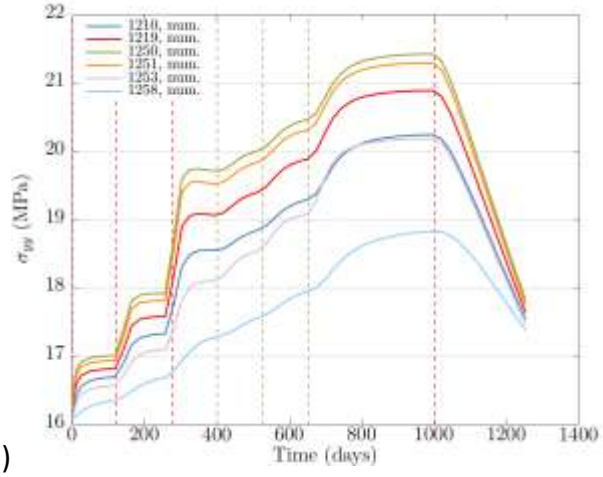

(b)

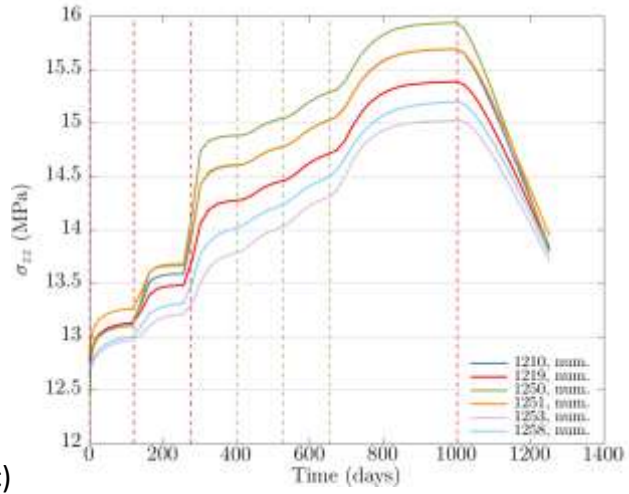

(c)

Figure 2-36. Stress evolution at measuring points, a) σ_{xx} evolutions, b) σ_{yy} evolutions, c) σ_{zz} evolutions.

2.4.4 Summary and status TED experiment modeling

In the past year, as Task E in the DECOVALEX-2019 project, we have validated our model with theoretical solutions on a consolidation problem in which the material is subjected to a heat load, and conducted modeling of coupled THM processes in a small-scale *in situ* heating test performed in Callovo-Oxfordian claystone. The current progress on this task is:

- For step 1, we have modified the source code of TOUGH to follow the assumptions in analytical solutions. A sequential coupling method between Thermo-hydrological simulator and geomechanical simulator was utilized with fixed stress-split method, and implemented through a porosity correction to account for coupled THM modeling. Through a simple 3D THM modeling benchmark, a good agreement was achieved between our model simulation and theoretical solutions.
- For step 2, we have determined THM parameters of claystone from TED experiment, including calibration on thermal conductivities to match the temperature evolution on heating phase, calibration on mechanical properties to match the triaxial compression and extension experimental data, and a back analysis on the simulation results to correct permeabilities. The TED experiment during heating phase has been simulated with TOUGH-FLAC for coupled THM modeling with good match to experimental data.

2.5 Status of THM Modeling and Future Work

DOE and LBNL greatly benefit from participating in these international activities for developing expertise and testing advanced models for coupled THM processes to be used for predicting long-term THM evolution of a multibarrier nuclear waste repository system, involving backfilled emplacement tunnels in argillite host formations. FY2017 work has been focused on modeling of FE experiment at Mont Terri in Opalinus clay and the TED experiment at Bure URL in Cox clay stone. Participating in these two international activities provides experience and model validation for two different clay stone host rocks and for two different repository design concept; the emplacement in horizontal tunnels (Swiss concept) and emplacement in micro-tunnels, extended from the walls of larger tunnels (French concept).

For the rest of remainder of FY2017 we plan to improve the interpretative modeling of the FE experiment related to the relative humidity evolution in the bentonite blocks. We will also review the current evolution of the stress in the buffer, to determine if swelling stress is starting to develop and can be used for model validation. Related to the modeling of the heater experiments at Bure, the modeling of the TED experiment will be improved by considering excavation effects on absolute pressure. Moreover, we will initiate modeling of the larger scale ALC experiment.

The FY2018 work on the Mont Terri FE experiment will focuse on modeling of the mechanical evolution of the buffer and host rock, including the application of the BExM model at a large scale. It will be a great opportunity to apply and test the BExM at the larger scale on the FE experiment. In particular, because one the other international modeling teams is the University of Catalonia group in Barcelona, Spain that is the origin of the BExM model and they will apply BExM for the modeling of the Mont Terri FE experiment, but using a different numerical simulator. At the same time, we will continue to validate and gain experiences in the use of the BExM. We will also expand the analysis with more comparison of the host rock behavior, including the excavation-disturbed zone.

The FY2018 work on the heater experiments at Bure will focuse on the modeling of the large-scale ALC experiment. This will first involve a predictive analysis of the coupled THM behavior, using the model and THM parameters that were calibrated against the smaller scale TED experiment. This will involve comparison to the modeling results of other international modeling teams within the DEOCOVALEX-2019 project.

This page is intentionally left blank.

3. INVESTIGATION OF THE IMPACTS OF HIGH TEMPERATURE LIMITS WITH THMC MODELING

3.1 Introduction

Radioactive waste from spent fuel emanates a significant amount of thermal energy due to decay processes, which causes temperature increases in the surrounding environment particularly in the early stages of waste emplacement. The temperature to which the EBS (engineered barrier system) and natural rock can be exposed is one of the most important design variables for a geological repository, because it determines waste package spacing, distance between disposal galleries, and therefore the overall size (and cost) of repository for a given amount of heat-emanating waste (Horseman and McEwen, 1996). This is especially important for a clay repository, because argillaceous rocks have relatively small heat conductivity. Temperature governs chemical alteration and the subsequent changes in mechanical properties of the EBS. A high temperature could result in chemical alteration of buffer and backfill materials (bentonite) within the EBS through illitization and cementation, which compromise the function of these EBS components by reducing their plasticity and capability to swell when wetting (Pusch and Karnland, 1996; Pusch et al., 2010; Wersin et al., 2007). The swelling capability of clay minerals within the bentonite is important for sealing gaps between bentonite blocks, between bentonite and other EBS components, and between the EBS and the surrounding host rock. Chemical alteration may also occur in the near-field host rock, which could reduce the clay capability for self-sealing within the excavation damaged zone (EDZ). Because the permeability of clay rock is low, a high temperature may induce significant pore pressure build-up (through pore water expansion and vaporization) in the near field, which could generate adverse mechanical deformation (such as fracturing), damaging the integrity of the host rock (Horseman and McEwen, 1996).

All disposal concepts throughout the world, despite their differences in design, unanimously impose a temperature limit of about 100^{o}C (Hicks et al., 2009). However, Wersin et al. (2007), after reviewing a number of data sets, concluded that the criterion of 100^{o}C for the maximum temperature within the bentonite buffer is overly conservative. Their conclusion was based on their findings that no significant changes in bentonite hydraulic properties occur at temperatures of up to 120^{o}C under wet conditions and that bentonite is chemically stable to much higher temperature under dry conditions. The impact of high temperature on bentonite and clay host rock behavior, and consequences on repository performance, remain largely an open question for a clay repository system. While various studies have shed light on certain aspects of this question, there is no study that integrates the relevant THMC processes while considering the interaction between EBS and host rock.

In this chapter, the first part is about coupled THMC model to evaluate the chemical alteration and mechanical changes in EBS bentonite and the NS (natural system) clay formation under various scenarios, attempting to provide necessary information for decisions on temperature limits. Two scenarios were simulated for comparison: (1) a case in which the peak temperature in the bentonite near the waste canister is about 200 ^{o}C and, (2) a case in which the temperature in the bentonite near the waste canister peaks at about 100^{o}C. In these simulations, it was assumed that the host rock properties were representative of Opalinus Clay (Bossart, 2011; Lauber et al., 2000) and the EBS bentonite was Kunigel-VI bentonite (Ochs et al., 2004) or FEBEX bentonite (ENRESA, 2000). Model results (Liu et al., 2013; Zheng et al., 2014; 2015b; 2016) found out the illitization is enhanced at high temperature. However, the magnitude of illitization varies a great deal and has to be evaluated case by case. In general, illitization leads to reduction in swelling stress but the degree of reduction varies with the type of bentonite.

The coupling between chemical and mechanical processes is the key part of THMC model that allow us to evaluate the direct impact of chemical changes on mechanical behavior. In previous THMC model (e.g., Zheng et al., 2015b), the coupling between chemical and mechanical processes was carried out via

an extended linear swelling model, which is simple and key parameters are relatively easy to be calibrated. However, such model does not accurately describe the transient state of swelling, neglect the history of mechanical change and is unable to account for the impact of cations exchange on the swelling. In FY17, THMC models uses double structure Barcelona Expansive Clay Model (BExM) (Sánchez et al., 2005) to link mechanical process with chemistry. As a result, the model can simultaneously incorporate the effects of exchangeable cations, ionic strength of pore water and abundance of swelling clay on the swelling stress of bentonite. In this report, we first summarize the key findings from previous modeling work (Liu et al., 2013; Zheng et al., 2014; 2015b; 2016) which set the stage for the simulations conducted in FY17; second, we discuss the coupled THMC model using BExM and the chemical effect on stress.

In the second part of this chapter, we report a prediction of bentonite alteration based on a THMC model for full-scale field test. One of the findings from the coupled THMC model for generic cases reported in the first part of the report is that illitization is affected by many chemical factor and is therefore a site-specific issue. Even though for a specific site, a model has to be calibrated based on data, and then extend the modeling time to predict evolution of THMC properties for the time that is required by the performance assessment. A coupled THMC has been developed and validated against the FEBEX (Full-scale Engineered Barrier EXperiment) *in situ* test (see Section 4 of this report). This model provides a unique opportunity to make long-term prediction of the bentonite alteration. Therefore, in FY17, we extend the simulation time of the THMC model for FEBEX *in situ* test to 100,000 years and modify the boundary condition for the canister—instead of fixing at 100 °C, a heat release function was prescribed—to predict the illitization in the bentonite.

3.2 Model Development

Because the model used in this report is similar to that in previous years (Liu et al., 2013; Zheng et al., 2014; 2015b; 2016), we briefly describe each element of the THMC model here, focusing on the updates in FY16. Additional details on the THMC model are presented in Liu et al. (2013).

3.2.1 Simulator

A review of simulators that could conduct coupled THMC model were given in Zheng et al. (2016). Although there are several simulators that are able to simulate THMC processes, successful application are seldom report, which reflects that it is very challenging to conduct such simulations. The numerical simulations in this study are conducted with TOUGHREACT-FLAC3D, which sequentially couples the multiphase fluid flow and reactive transport simulator, TOUGHREACT (Xu et al., 2011), with the finite-difference geomechanical code FLAC3D (Itasca, 2009). The coupling of TOUGHREACT and FLAC3D was initially developed in Zheng et al. (2012) to provide the necessary numerical framework for modeling fully coupled THMC processes. It included a linear elastic swelling model (Zheng et al., 2012; Rutqvist et al., 2014b) to account for swelling as a result of changes in saturation and pore-water composition and the abundance of swelling clay (Liu et al., 2013; Zheng et al., 2014). The model was also equipped with dual structural BExM, which will be discussed with more detailed later.

3.2.2 Modeling Scenario

The model scenario is still the same as in Liu et al. (2013) and Zheng et al. (2014). The model is applied to a hypothetical bentonite-backfilled nuclear waste repository in clay rock, a repository example that involves a horizontal nuclear waste emplacement tunnel at 500 m depth (Figure 3-2) (Rutqvist et al., 2013). The Z-axis is set as vertical, while the horizontal Y- and X-axes are aligned parallel and perpendicular to the emplacement tunnel, respectively (Figure 3-2) in this 2-D model. Note that while the canister is modeled as a heat source with mechanical properties of steel, the THC changes in the canister and their interactions with EBS bentonite are not considered here for the sake of simplicity.

An initial stress field is imposed by the self-weight of the rock mass. Zero normal displacements are prescribed on the lateral boundaries of the model. Zero stress is applied to the top and vertical displacements are prevented at the bottom. An open boundary is applied to the liquid pressure at top and bottom and initially the model domain is in a hydrostatic state. The initial temperature at the top is about 11 ^{o}C, with a thermal gradient of 27 ^{o}C/km; the initial temperature at the bottom is 38 ^{o}C. The model simulation was conducted in a nonisothermal mode with a time-dependent heat power input (Rutqvist et al., 2014b). The power curve in Figure 3-2 was adopted from representative heating data from the U.S. DOE's Used Fuel Disposition campaign for pressurized water reactor (PWR) used fuel. This heat load is then scaled in the 2D model to represent an equivalent line load, which depends on the assumed spacing between individual waste packages along an emplacement tunnel. The heat load for the "low-T" case corresponds to an initial thermal power of 3144 W for a 4-PWR-element waste package after aging for 60 years, a 50-m spacing between emplacement tunnels, and 3-m spacing between the 5-m long packages. The heat load for the "high T" case represents similar waste package and spacing, except with only 20 years of aging. Initially the EBS bentonite has a water saturation of 65% and the clay formation is fully saturated. From time zero, the EBS bentonite undergoes simultaneously re-saturation, heating, chemical alteration, and stress changes.

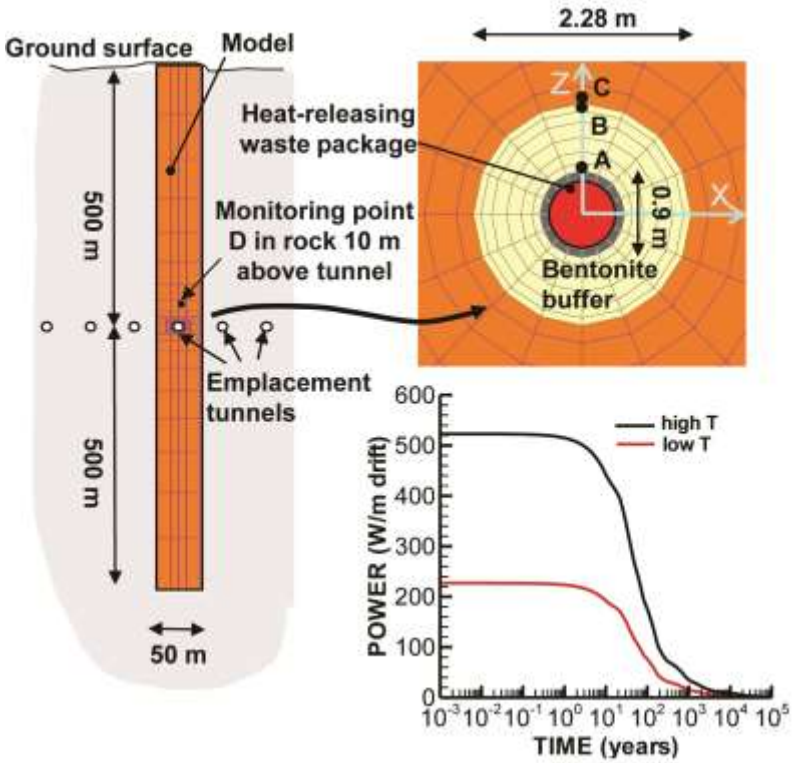

Figure 3-1. Domain for the test example of a bentonite back-filled horizontal emplacement drift at 500 m (Rutqvist et al., 2014b). Modeling monitoring points: A: inside the bentonite near the canister, B: inside the bentonite and near the EBS-NS interface, C: inside the clay rock formation and near the EBS-NS interface, D: inside the clay rock formation at a distance of 10 m from the canister. (Perhaps need to add a little more information on the power curves) "High T": 200 ºC; "Low T": 100ºC.

3.2.3 Mechanical Model

3.2.3.1 Double structure model

In previous modeling works (e.g., Zheng et al., 2015b; 2016), extended linear swelling model was used to describe the mechanical behavior of bentonite. In this report, we primarily used a dual structure model, Barcelona Expansive Clay Model (BExM).

In the dual structure model, the macrostructure is considered with a constitutive model for unsaturated soils, such as the Barcelona Basic Model (BBM). The microstructure is incorporated to extend BBM to a dual structure model, which enables simulating the behavior of expansive soils, such as the dependency of swelling strains and swelling pressures on the initial stress state and on the stress path, strain accumulation upon suction cycles and secondary swelling. Thus, in the dual structure model, the total volume (V), the total void ratio (e), and porosity (ϕ), of the material are divided into a micro-structural part and a macro-structural part. The microstructure can swell to invade the macro-porosity, depending on the mechanical confinement and load level. This is relevant when considering permeability changes during the soil swelling, because fluid flow takes place mostly through the macro-porosity, which is not proportional to the total strain and deformation of the expansive soil. Equations to describe the mechanical behavior of micro-structural and macro-structural levels and the interaction between structural levels are given in Section 2.

We develop a one-way coupling approach, in which chemical changes affect mechanical behaviors of bentonite through the evolution of volume fraction of smectite, exchangeable cation concentration, and ionic strength (via osmotic suction). In this report, these effects are taken into account using a dual-structure model (BExM). The mathematical formulations for CM coupling are summarized below.

The original BExM predicts the micro-strains induced by the effective stress for the whole microstructure, ignoring the effects of smectite. When the material is hydrated, instead of the whole microstructure, only the parts of the smectite within the microstructures that interact with the water invasion swell. Here, we introduce the volume fraction of smectite, f_s, into the microstructure in BExM for C-M coupling. The swelling capacity of the material should decreases with the reduction of the volume fraction of smectite. Thus, the micro-structural volumetric strains is assumed to depend on the change in the microstructural effective stress as follows:

$$\mathrm{d}\varepsilon_{vm}^{e} = \frac{f_s}{K_m}\mathrm{d}\hat{p} \tag{3.1}$$

where $\hat{p} = p + s_m$, $\hat{p}$ is the effective mean stress, p is the total mean stress, and s_m is the microstructural suction. The total suction, s_m, contains two components, matric suction, s, and osmotic suction, s_o, i.e., $s_m = s + s_o$. The effect of ionic strength of the pore water on microstructural strain is carried out via the osmotic suction. It is computed as:

$$s_o = -10^{-6}\frac{RT}{V_w}\ln a_w \tag{3.2}$$

where V_w is the molar volume of water (in m^3/mol), and a_w is the activity of water. a_w is calculated in TOUGHREACT (Xu et al., 2011) as follows:

$$\ln a_w = -\Phi m^{*}\frac{1}{55.51} \tag{3.3}$$

where Φ is osmotic coefficient of the solution and m^* is the sum of the molalities of all species in solution.

In equation 3.4, K_m is calculated as

$$K_m = \frac{e^{\alpha_m \hat{p}}}{\alpha_A \beta_m} \quad 3.4$$

where α_m is the material parameter; α_A is a coefficient to adjust β_m based on the mechanical experiments. The effect of exchangeable cations is linked to mechanics through the dependence of β_m (Equation 3.5) on exchangeable cation concentration as shown in the following equation (Gens, 2010):

$$\beta_m = \sum_i \beta_m^i x_i \quad 3.5$$

Gens (2010) and Guimarães et al. (2013) proposed that β_m^i is proportional to the ionic hydrated radius and inversely, proportional to its valence, and typically $\beta_m^{Li} > \beta_m^{Na} > \beta_m^K$. Thus, Na-smectite, which contains exclusively Na in the interlayer space should swell more than Ca-smectite, provided that other conditions are the same.

3.2.3.2 Calibration of parameters of BExM model for FEBEX bentonite

When coupled THMC model using BExM model to link chemistry with mechanics was first tested in FY16, parameters for mechanical model were taken from published values and the parameters for mechanical-chemical (MC) coupling such as f_s was taken directly from chemical model. The mechanical model with MC coupling was not aligned or adjusted to a known reference conditions. However, based on the studies by Sánchez et al. (2012), when BExM was calibrated from the laboratory experiments, a few parameters vary several orders of magnitude due to chemical reactions in comparison to values obtained without considering chemical reactions. It turns out when MC coupling was incorporated into BExM, the whole set of parameters should be calibrated such that BExM can accurately describe the reference state of bentonite. In FY17, we have calibrated the parameters for BExM based on the swelling pressure experiments to make sure the model results are aligned with the reference state (fully saturated bentonite with a volume fraction of 0.6164 for smectite) such that the model predicts the material swelling pressure in reasonable ranges.

The parameters of BExM utilized in last year's studies are calibrated based on compacted bentonite by Lloret et al. (2003), and are used in the numerical analysis for Mock-up test by Sánchez et al. (2012). To account for size effects, and keep macro-structural bulk modulus of bentonite stay in reasonable ranges, we modified the parameters related to macro-structural bulk modulus, κ, but keep the same ratio of $\frac{\kappa}{\kappa_s}$ as Lloret et al. (2003) and Sánchez et al. (2012b) used in their simulations. The void ratios e_{micro} and e_{macro} are recalculated based on the experiment data. Then, we launched some simulations on swelling pressure test to investigate the swelling capacity of bentonite. This swelling pressure test was operated under constant volume conditions, while the suction (s) was controlled as external loading changes. The experiment includes two loading steps. It started with an initial suction of 80 MPa and a low vertical stress. First, a wetting path was followed up by decreasing the suction to 0.01 MPa. In the second step, the sample was subjected to drying, up to a maximum suction of 0.4 MPa.

For the simplicity, we only modify f_s in each simulation to account for the effects of volume fraction of smectite on swelling pressure of bentonite. f_s ranges from 0 to 0.6164, the volume fraction smectite in the original FEBEX bentonite, is used as a reference value from experiments. The experiment indicates the swelling pressure of FEBEX bentonite is around 5 MPa (Figure 3-2). However, the previous set of

parameters used in FY16 model led to a maximum swelling pressure that is less than 0.014 MPa, a quite unreasonable value.

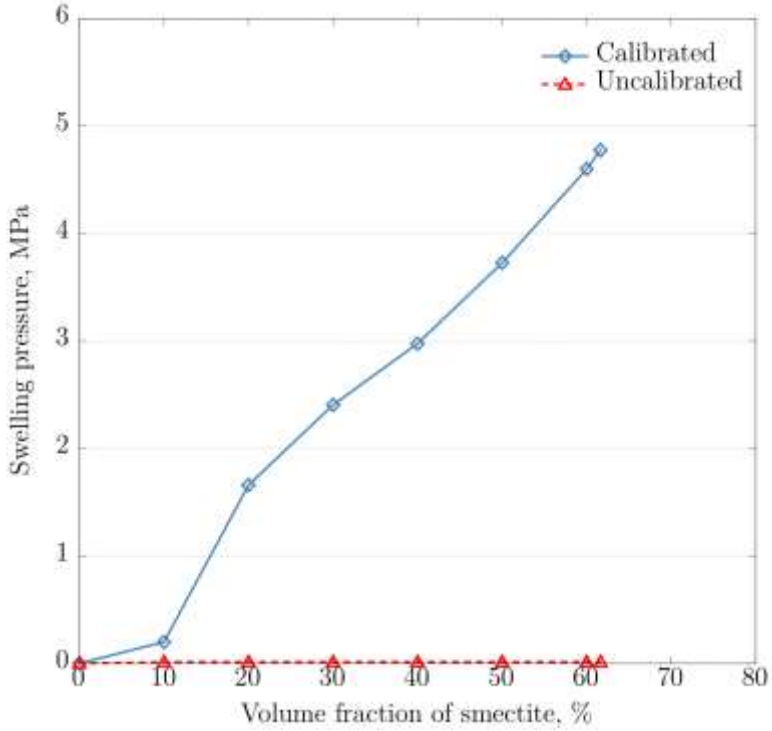

Figure 3-2. Simulation results of swelling pressure with respect to volume fraction of smectite using two sets of parameters for BExM model, respectively. The "uncalibrated" set of parameters was what used in FY16 models.

Using simulations on swelling pressure experiments, parameters of BExM model are calibrated and the optimal parameters are listed in Table 3.1. Swelling pressures dependent on volume fraction of smectite is plotted in Figure 3-2, in which the relationship is approximately linear. The calibrated parameters lead to the swelling pressure between 0 and 5 MPa, such that the reference state (fully saturated bentonite with 61.64% volume fraction of smectite) has a swelling pressure of about 4.8 MPa stress, and zero volume fraction of smectite ($f_s = 0$) corresponds to zero swelling pressure.

Table 3-1. Parameters of BExM model for FEBEX bentonite.

Parameters defining the Barcelona basic model for macrostructural behavior						
$\kappa = 0.018$	$\kappa_s = 0.0036$	$\lambda(0) = 0.08$	$p_c = 0.5$ MPa	$r = 0.90$	$\zeta = 1$ MPa^{-1}	$p_0^* = 6.5$ MPa
$\alpha_a = 0.5$	$\alpha_0 = 1 \times 10^{-5}$°C					
Parameters defining the law for microstructural behavior						
$\alpha_m = 2.1 \times 10^{-2}$ MPa^{-1}	$\chi = 1$	$\alpha_A = 1000$				
Interaction functions						
$f_{ci} = 1 + 0.9 \tanh\left[20\left(\frac{p_r}{p_0} - 0.25\right)\right]$		$f_{si} = 0.8 - 1.1 \tanh\left[20\left(\frac{p_r}{p_0} - 0.25\right)\right]$				
Initial conditions						
$e_{macro} = 0.21$	$e_{micro} = 0.48$	$f_s = 0.6164$	$s_o = 0.777$ MPa	$\beta_m = 2.74 \times 10^{-12}$ MPa^{-1}		

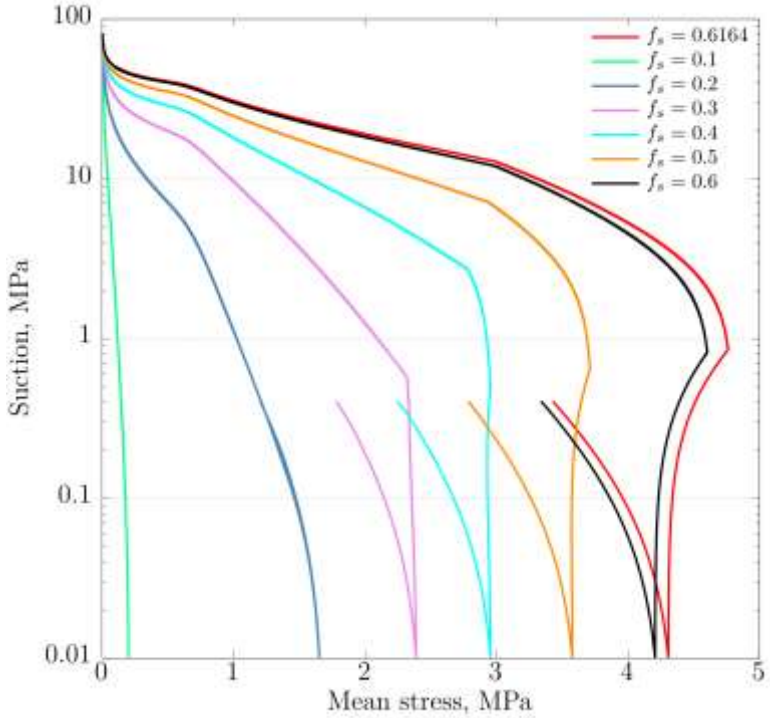

Figure 3-3. Simulated stress paths for different volume fractions of smectite using the model calibrated based on swelling pressure experiments.

The micro- and macro-structural bulk moduli are also displayed in Figures 3-4 and 3-5 respectively. Subjected to hydration, bentonite swells, inducing stress increases in bentonite (Figure 3-3). With the rising of total stress, micro-structural bulk modulus, K_m, decreases as Figure 3-4 illustrates. Equation 3.4 describes the dependence of K_m on the effective stress, $\hat{p}$, which includes two factors, suction s_m and mean stress p at the micro-scale. In this case, the mean stress p ranges from 0.01 MPa to 4.8 MPa, which is less than the magnitude of suction (ranges from 0.01 MPa to 80 MPa). Although mean stress increases during the bentonite swelling, the reduction of suction is dominant in the experiment, which results in the drop of micro-structural bulk modulus.

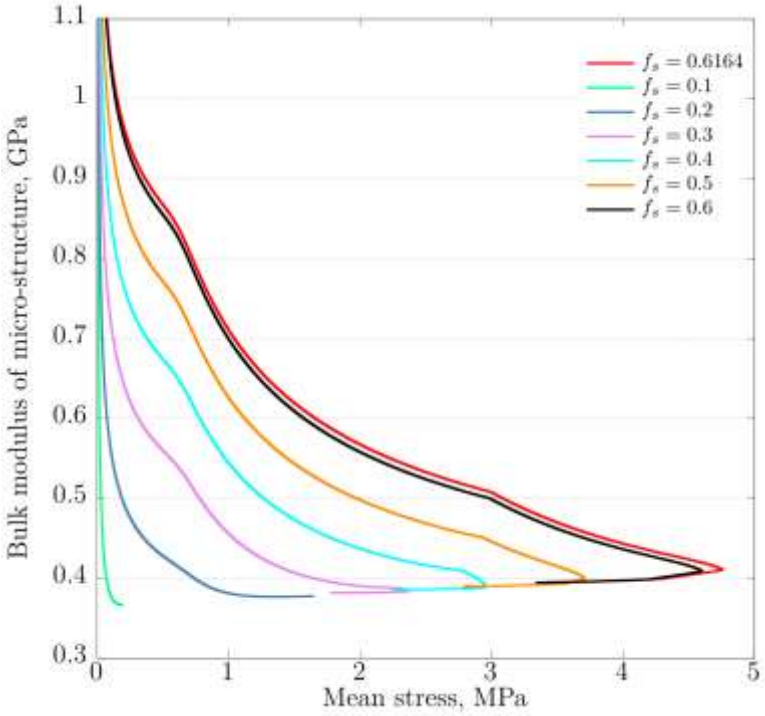

Figure 3-4. Micro-structural bulk modulus evolutions versus stress with different volume fractions of smectite.

The macro-structural bulk modulus K is linearly dependent on mean stress. Thus, with the growth of mean stress, K increases until the maximum swelling pressure is achieved. This evolution is presented in Figure 3-5.

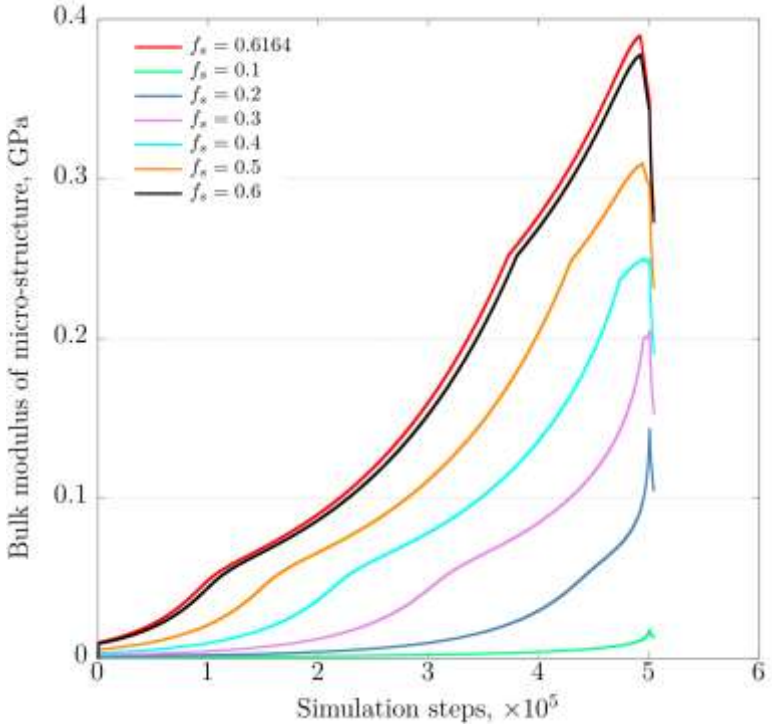

Figure 3-5. Macro-structural bulk modulus evolutions versus simulation steps with different volume fractions of smectite.

3.2.4 Chemical Model

In previous models for generic cases, it is assumed that that the host rock properties are representative of Opalinus Clay (Bossart, 2011; Lauber et al., 2000). Two cases are used for the EBS backfill: one is Kunigel-VI bentonite (Ochs et al., 2004) and the other is FEBEX bentonite (ENRESA, 2000). The mineral compositions of the bentonite and clay formation are listed in Table 3-2. Mineral dissolution/precipitation is kinetically controlled. Details about the how mineral dissolution/precipitation is calculated was given in Zheng et al. (2016).The pore-water compositions of the Kunigel-VI bentonite (Sonnenthal et al., 2008), FEBEX bentonite (Fernández et al., 2001) and the clay formation (Fernández et al., 2007) are listed in Table 3-3.

In this report, we focus on the model for a case using FEBEX bentonite as EBS backfill and Opalinus Clay as host rock. Table 3-3 lists the thermal and hydrodynamic parameters used in the model

Table 3-2. Mineral volume fraction (dimensionless, ratio of the volume for a mineral to the total volume of medium) of the Kunigel-VIbentonite (Ochs et al., 2004), FEBEX bentonite (ENRESA, 2000; Fernández et al., 2004; Ramírez et al., 2002) and Opalinus Clay (Bossart 2011; Lauber et al., 2000).

Mineral	EBS Bentonite: Kunigel-VI	EBS Bentonite: FEBEX	Clay formation: Opalinus Clay
Calcite	0.016	0.0065	0.093
Dolomite	0.018	0.0	0.050
Illite	0.000	0.0	0.273
Kaolinite	0.000	0.0	0.186
Smectite	0.314	0.6	0.035
Chlorite	0.000	0.0	0.076
Quartz	0.228	0.026	0.111
K-Feldspar	0.029	0.0065	0.015
Siderite	0.000	0.0	0.020
Ankerite	0.000	0.0	0.045
Pyrite	0.000	0.01	0.000
Greenrust	0.000	0.000	0.000
Magnetite	0.000	0.000	0.000
Hematite	0.000	0.000	0.000
Goethite	0.000	0.000	0.000
Fe(oh)3(s)	0.000	0.000	0.000
Fe(oh)2	0.000	0.000	0.000
Vermiculites	0.000	0.000	0.000
Berthierine(Fe^{+2})	0.000	0.000	0.000
Berthierine(Fe^{+3})	0.000	0.000	0.000
Saponite(Fe, Ca)	0.000	0.000	0.000
Saponite(Fe,K)	0.000	0.000	0.000
Saponite(Fe, Na)	0.000	0.000	0.000
Saponite(Fe, Mg)	0.000	0.000	0.000

Table 3-3. Pore-water composition (mol/kg water, except pH) of Kunigel-VIbentonite (Sonnenthal et al., 2008), FEBEX bentonite (Fernández et al., 2001) and Opalinus Clay (Fernández et al., 2007).

	EBS Bentonite: Kunigel-VI	EBS Bentonite: FEBEX	Clay formation: Opalinus Clay
pH	8.40	7.72	7.40
Cl	1.50E-05	1.60E-01	3.32E-01
SO_4^{-2}	1.10E-04	3.20E-02	1.86E-02
HCO_3^-	3.49E-03	4.1E-04	5.18E-03
Ca^{+2}	1.37E-04	2.2E-02	2.26E-02
Mg^{+2}	1.77E-05	2.3E-02	2.09E-02
Na^+	3.60E-03	1.3E-01	2.76E-01
K^+	6.14E-05	1.7E-03	2.16E-03
Fe^{+2}	2.06E-08	2.06E-08	3.46E-06
SiO_2(aq)	3.38E-04	1.1E-04	1.10E-04
AlO_2^-	1.91E-09	1.91E-09	3.89E-08
O_2(aq)	2.57e-4	2.57e-4	1.2E-51

Table 3-4. Thermal and hydrodynamic parameters.

Parameter	Clay formation: Opalinus Clay	EBS Bentonite
Grain density [kg/m^3]	2700	2700
Porosity ϕ	0.162	0.33
Saturated permeability [m^2]	2.0×10^{-20}	2.0×10^{-21}
Relative permeability k_{rl}	m = 0.6, S_{rl} = 0.01	$K_{rl} = S^3$
Van Genuchten α [1/Pa]	6.8×10^{-7}	3.3×10^{-8}
Van Genuchten m	0.6	0.3
Compressibility β [1/Pa]	3.2×10^{-9}	5.0×10^{-8}
Thermal expansion coeff. [1/^{o}C]	1.0×10^{-5}	1.5×10^{-4}
Dry specific heat [J/kg-^{o}C]	860	800
Thermal conductivity [W/m-^{o}C] dry/wet	1.48/1.7*	1.1/1.5
Tortuosity for vapor phase	$\phi^{1/3}S_g^{10/3}$	$\phi^{1/3}S_g^{10/3}$
Bulk modulus (GPa)	4.17	0.02
Shear modulus (GPa)	1.92	0.0067

*from http://www.mont-terri.ch/internet/mont-terri/en/home/geology/key_characteristics.html

3.3 Model Results

In this multiple years' effort of studying bentonite alteration using coupled THMC model, the simulator was upgraded, more constitutive relationships were tested and more scenarios were analyzed. While previous model mostly employed an extended linear elastic model for mechanical behavior, models in this report featured with using BExM for mechanical behavior. In order to set the stage for discussing the model results from the FY17 modeling effort, in the following sections, we first briefly summarize the key findings from previous modeling work in Sections 3.3.1 and 3.3.2, and then present new model results from FY17 effort in Section 3.3.3.

3.3.1 Key Findings from Previous Models using Extended Linear Elastic Model

In the generic cases we used to study the effect of high temperature on the THMC evolution in bentonite and clay formation. Two bentonites have been simulated: Kunigel-VI and FEBEX bentonite, and two scenarios were simulated for comparison. A case in which the temperature in the bentonite near the waste canister can reach about 200 ^{o}C and a case in which the temperature in the bentonite near the waste canister peaks at about 100 ^{o}C. All these simulations used extended linear elastic model to link chemistry with mechanics. In this section, we summarize the key findings from Liu et al. (2013), Zheng et al. (2014), Zheng et al. (2015b) and Zheng et al. (2016).

3.3.1.1 Enhancement of Illitization under Higher Temperature

The very first question we were attempting to answer by this series of simulations was whether illitization would occur in the EBS bentonite and host clay formation. Illitization, the transformation of smectite to illite, has caught great attention of researchers because it results in a loss of smectite, which in turn causes a loss in the swelling capacity. Illitization is evident in geological systems (Wersin et al., 2007), as

exemplified by several natural analogue studies (Pusch and Madsen, 1995; Kamei et al., 2005; Cuadros, 2006; Casciello et al., 2011). Illite/smectite mixed-layer clay is commonly observed in clayey sediments, and deep formations typically contain more illite than shallow formations (Cuadros, 2006), which leads to a conclusion that smectite is gradually transformed to illite during diagenesis and become of the basis for assuming the illitization would occur in EBS bentonite. Liu et al. (2013) did an extensive review of laboratory experiments (e.g., Mosser-Ruck and Cathelineau, 2004; Pacovsky et al., 2005) and field tests (Pusch et al., 2010) and modeling studies (e.g., Montes-H et al., 2005), and found out there was no conclusive evidence that illitization will occur and swelling capacity will be lower in bentonite. While various studies shed light on certain aspects of this question, there is no study that integrates the relevant THMC processes and considers the interaction between EBS and host rock. One of the key findings from our simulations is that illitization does occur in the two bentonites we tested: Kunigel-VI (Ochs et al., 2004) and FEBEX (ENRESA 2000) bentonite and is enhanced at higher temperature, as shown in Figure 3-6. In addition, we also have the following observations:

- The quantity of illitization, expressed as the smectite volume fraction change, is affected by many chemical factors and as a result varies over a wide range. The most important chemical factors for illitization are the concentration of K and dissolution rate of K-feldspar.
- The geochemical interaction between EBS bentonite and the clay formation has a strong effect on long-term illitization in bentonite.
- Illitization is more pronounced for Kunigel-VI bentonite than FEBEX bentonite (Figure 3-7) due to their difference in chemical properties, indicating illitization in EBS bentonite has to be evaluated case by case.
- In additions to illitization, other chemical alterations include the dissolution of K-feldspar and calcite, and the precipitation of quartz, chlorite, and kaolinite. In addition, precipitation of quartz could affect the mechanical property of bentonite.
- Illitization also occurs in clay formation and is significantly enhanced under higher temperature (see Figure 3-6).

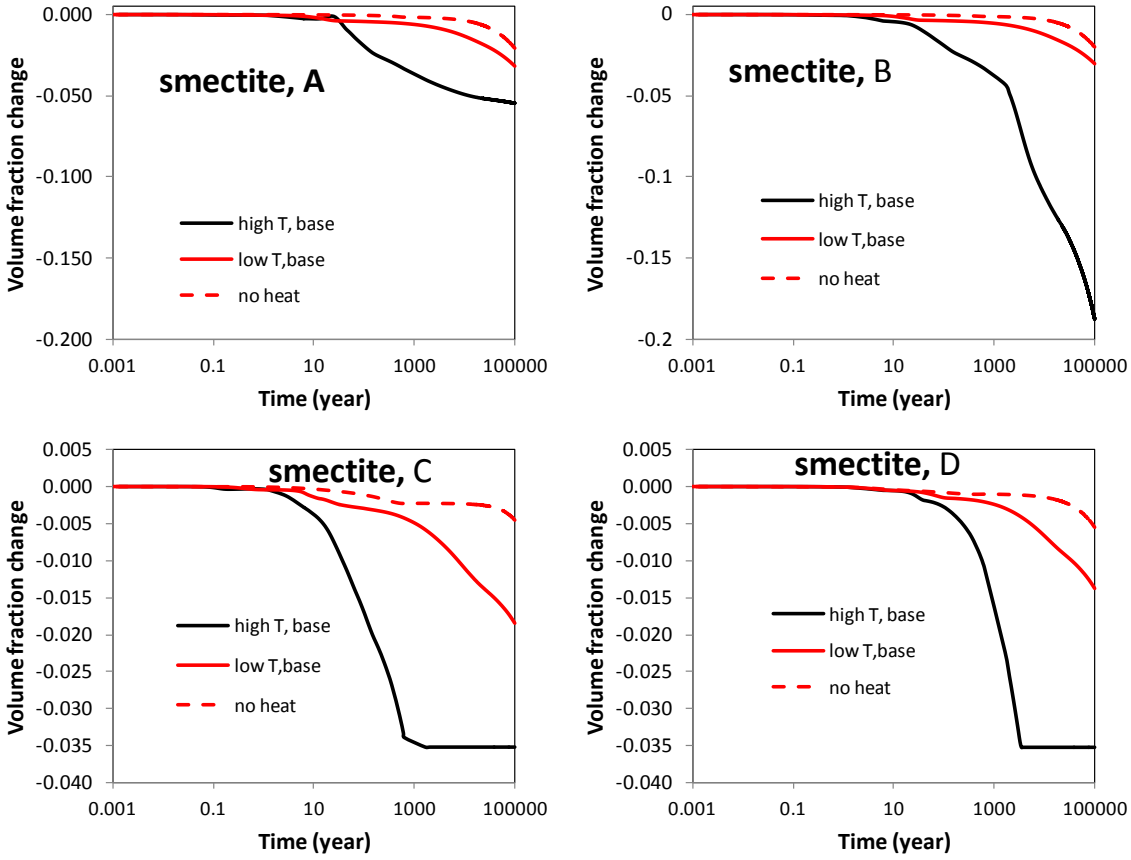

Figure 3-6. The temporal evolution of smectite volume fraction at points A, B, C, and D for the "high T" and "low T" cases; and a simulation that assumes no heat release from the waster package (A: inside the bentonite near the canister, B: inside the bentonite and near the EBS-NS interface, C: inside the clay rock formation and near the EBS-NS interface, D: inside the clay rock formation at a distance of 10 m from the canister).

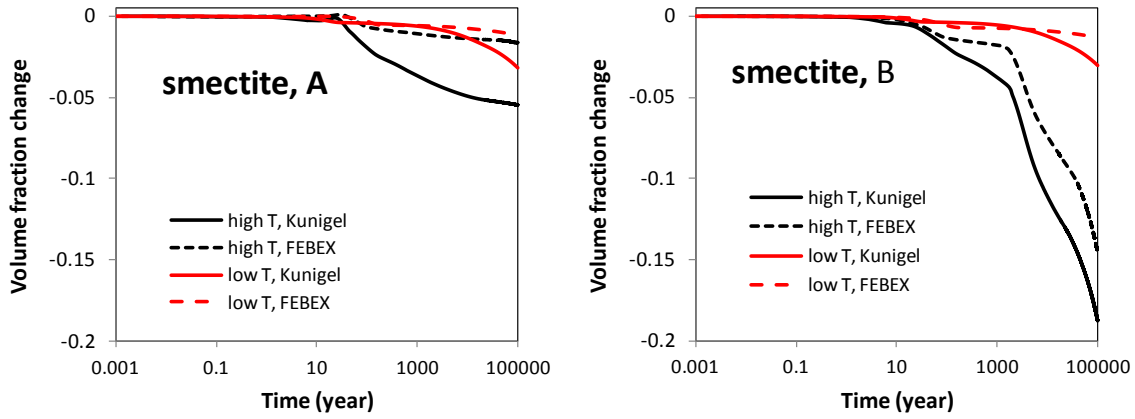

Figure 3-7. The temporal evolution of smectite volume fraction at points A and B for Kunigel and FEBEX bentonite.

3.3.1.2 Impact of Illitization on Swelling Stress

The mechanical-chemical coupling implemented in the model allows us to evaluate how the chemical changes may affect the mechanical behavior of the EBS bentonite in terms of swelling and total stress. Because of the extended linear swelling model used in the model, we limit our analysis to the effects of ion concentration and illitization on swelling and do not include other potential effects of chemical changes on mechanics, such as changes in mechanical properties due to cementation.

Several processes combine to drive stress up in bentonite and peak at around 100 years, and then decrease and stabilized after 20,000-30,000 years. Reasons for the stress increase include the increase in pore pressure due to hydration and thermal pressurization (a processes caused by the difference in thermal expansion of the fluid and solid host rock), bentonite swelling, and thermal expansion. The stronger thermal pressurization in the "high T" case leads to much higher stress in the bentonite than the "low T" case. For both the "high T" and "low T" cases, the major contribution to total stress within the buffer is pore pressure, with smaller contributions from swelling and thermal stresses.

The constitutive relationship described by extended linear swelling model provides an opportunity to evaluate the effect of chemical changes on swelling stress. The swelling stress reduced by ion concentration and smectite dissolution for both Kunigel-Vi and FEBEX bentonite are listed in Table 3-5.

Table 3-5. The geochemically induced swelling stress for Kunigel-VI and FEBEX bentonite at points A and B for "high T" scenario. Stress reduction by ion concentration is the difference between the swelling stress obtained with "σ=f(Sl)" and "σ=f(Sl,C)," and the stress reduction by smectite dissolution is the difference between the swelling stress obtained with "σ=f(Sl,C)" and "σ=f(Sl,C,Ms)" (see Figure 3-7), where the relative amount (%) use the results from "σ=f(Sl)" as the basis.

	Kunigel-VI bentonite				FEBEX bentonite			
	Stress reduction by ion concentration		Stress reduction by smectite dissolution		Stress reduction by ion concentration,		Stress reduction by smectite dissolution	
	MPa	%	MPa	%	MPa	%	MPa	%
Point A	0.07	7%	0.09	9%	0.006	0.1%	0.17	3.4%
Point B	0.08	8%	0.45	45%	0.06	1.1%	0.6	12%

In terms of the effect of chemical changes on swelling stress for bentonite, the modeling results (Zheng et al., 2015b) leads to the following observations:

- More swelling stress reduction take place near the near the EBS-NS interface as more illitization occurs in this area, expressed as the smectite volume fraction change.
- High temperature leads to higher reduction in swelling stress. Although Kunigel-VI and FEEBEX bentonite undergo similar magnitude reduction in swelling stress in absolute values (as in MPa), relative to their corresponding swelling capacity, it is a much minor reduction for FEBEX bentonite because FEBEX bentonite has a swelling capacity about five folds of that of Kunigel-VI bentonite. Using EBS bentonite with higher swelling capacity could alleviate the negative consequence of illitization.

- Despite the swelling stress is noticeably affected by illitization, the total stress is much less affected by the chemical change because swelling stress only accounts for a relatively small proportion of total stress.

3.3.2 THMC Results with the Dual-Structure Model

As described in section 3.2.3, the chemical-mechanical coupling is achieved through the dual-structure model. It allows us to evaluate how the chemical changes may affect the mechanical behavior of the EBS bentonite in terms of effective/net and total stress. The effects considered in the model come from three components: volume fraction of smectite, exchangeable cation concentration, and osmotic suction.

Here, to illustrate the effects of chemical reactions on stress change, we simulated a series of generic repository cases (described in Figure 3-1). For the simplicity, we only present high temperature ("high T") cases in this section. The results of low temperature ("low T") cases show similar behaviors as "high T" cases, while the magnitudes of stress are different. The computation contains five different simulations to account for the effect of each chemical component. The first one is the reference case, which is conducted without MC coupling. Thus, the mechanical behavior of bentonite only depends on TH processes and this case is marked as "THM" case. Since the coupling is one-way, i.e., the mechanical behavior does not affect the fluid, thermal transports or chemical reactions. The evolution of temperature, liquid saturation and pore pressure is the same for "THM" case and other cases computed with MC coupling, which helps to distinguish the chemical effect on stress when comparing other cases with the reference one. The second case only accounts for the effect of volume fraction of smectite through C-M coupling, so it is referred as "THMC(f_s)." Similarly, the simulation refereed as "THMC(β_m)" only takes into account the effect of exchangeable cations and the simulation refereed as "THMC(s_o)" only takes into account the effect of ionic strength via osmotic suction. The simulation considered the effect of all three chemical components is marked as "THMC (f_s, β_m, s_o)."

3.3.2.1 Effects of Volume Fraction of Smectite

As previous section explains, the "THMC(f_s)" case computes the THMC processes with C-M coupling only through the smectite volume fraction. Figure 3-8 shows the evolution of the volume fraction of smectite at points A and B. The current model predicts dissolution of smectite, which leads to decrease in the volume fraction of smectite. While Figure 3-8 shows the relative changes in smectite volume fraction to initial values, Figure 3-6 displays the smectite volume fraction at each time, f_s decreases from 61% to 60% at Point A, while it decreases from 61% to 47% at Point B.

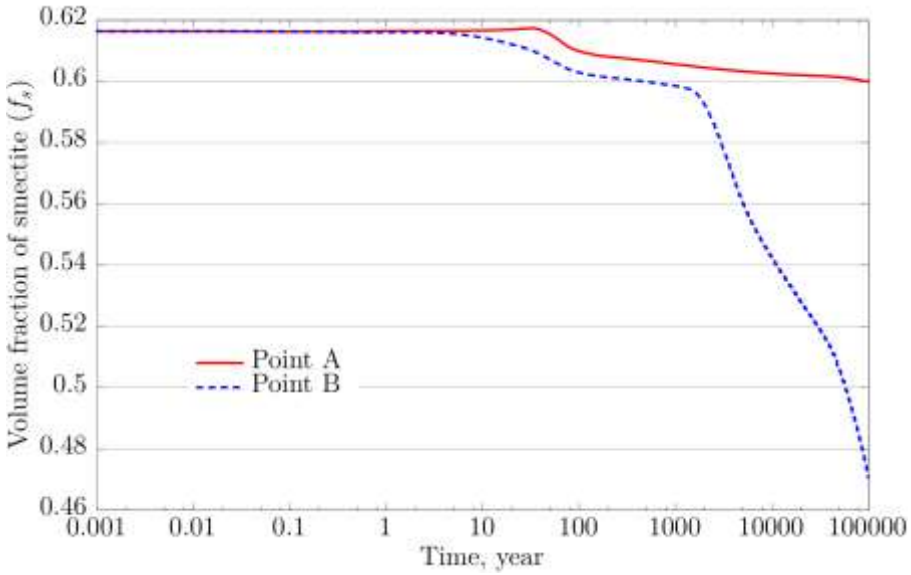

Figure 3-8. The evolution of the volume fraction of smectite at points A and B with FEBEX bentonite for the "high T" scenario.

The calculated stresses for "THMC(f_s)" and "THM" case at Points A and B are plotted in Figures 3-9 and 3-10 respectively. Since smectite is the mineral phase in bentonite to induce swelling due to hydration, the swelling capacity of bentonite tends to decrease as smectite volume fraction decreases. However, the reduction of total mean stress at points A and B is negligible when compared "THMC(f_s)" case with "THM" case (Figures 3-9 and 3-10). The possible reason is the elastic micro-structural strain, which accounts for swelling of bentonite, is quite small due to large magnitude of micro bulk modulus, and the induced pressurization by this strain is small as well. Moreover, the swelling due to smectite is overshadowed by thermal pressurization and hydraulic pressurization. Therefore, the stress change due to dissolution of smectite is not significant in current model.

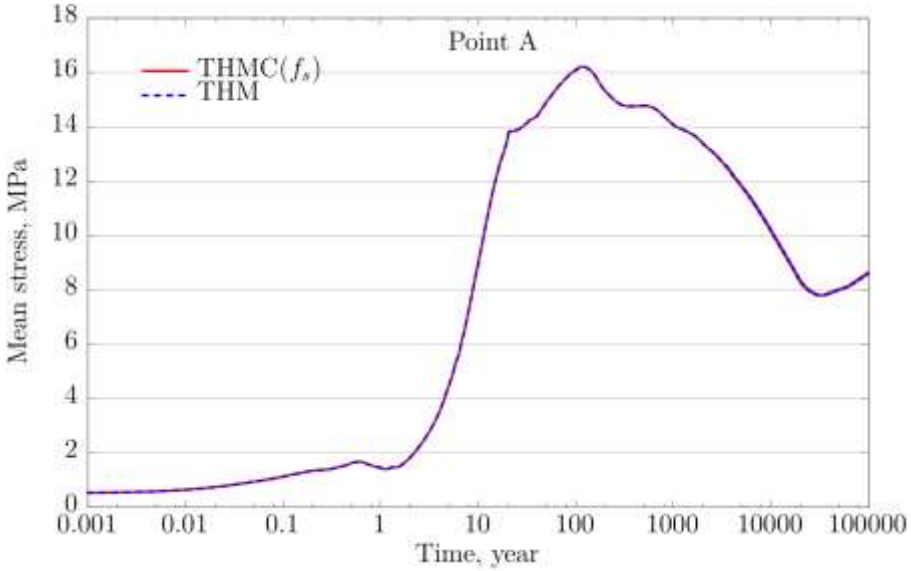

Figure 3-9. Simulation results of mean total stress at point A with FEBEX bentonite for the "THMC(f_s)" and "THM" scenarios, respectively.

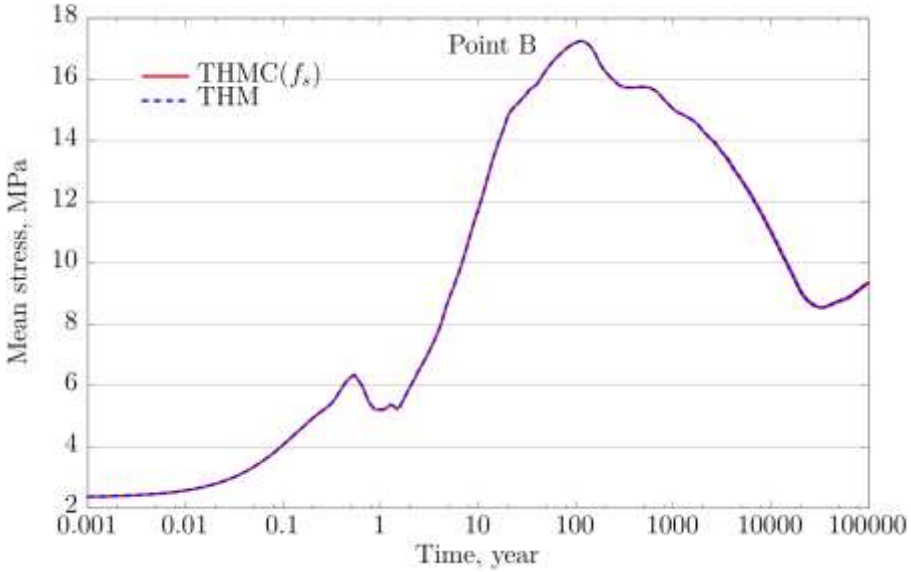

Figure 3-10. Simulation results of mean total stress at point B with FEBEX bentonite for the "THMC(f_s)" and "THM" scenarios, respectively.

3.3.2.2 Effects of Exchangeable Cation Concentration

The "THMC(β_m)" case computes the THMC processes with MC coupling only through the exchangeable cation concentration, which is represented by β_m. Figure 3-10 shows the evolution of β_m at points A and B. In the current model, β_m depends on the concentration of the exchangeable Na, K, Ca and Mg, the enrichment of exchangeable sodium in the interlayer leads to the increase of β_m (Figure 3-11), which tends to increase stress. In Figure 3-11, β_m increases from 2.74×10^{-12} to 4.54×10^{-12} at both points A and B with slight different growing paths, in which β_m drops at around 8 years at point A.

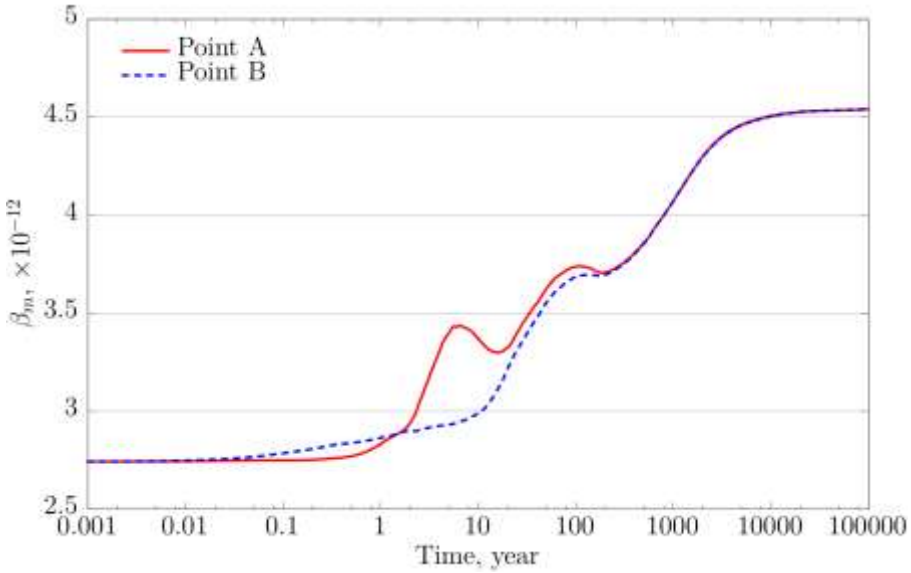

Figure 3-11. Simulation results of the evolution of β_m at points A and B with FEBEX bentonite for the "high T" scenario.

The calculated stresses for "THMC(β_m)" and "THM" case at Points A and B are plotted in Figures 3-12 and 3-13 respectively. The rising of β_m tends to increase the swelling capacity of bentonite. At point A the total mean stress in "THMC(β_m)" case is higher than the stress in "THM" case, and the maximum difference is about 0.6 MPa at around 15 years. As the rise of β_m reaches a plateau after 2000 years at Point A, of the stress difference between "THMC(β_m)" and "THM" case is suppressed. However, the similar behavior is not clear at Point B. The stress difference between "THMC(β_m)" and "THM" case is negligible, which may be due to the high confinement of host rock in the repository. Point B is close to the boundary between ESB and host rock, so the large modulus of host rock and high magnitude of stress inside rocks suppress the swelling of bentonite. Therefore, the stress change due to alteration of exchangeable cation cannot manifest in current model.

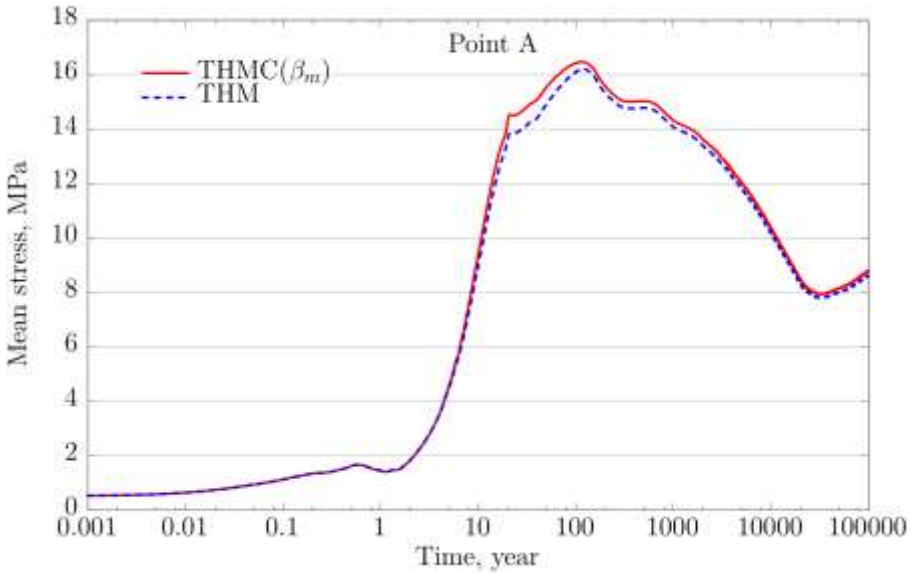

Figure 3-12. Simulation results of mean total stress at point A with FEBEX bentonite for the "THMC(β_m)" and "THM" scenarios, respectively.

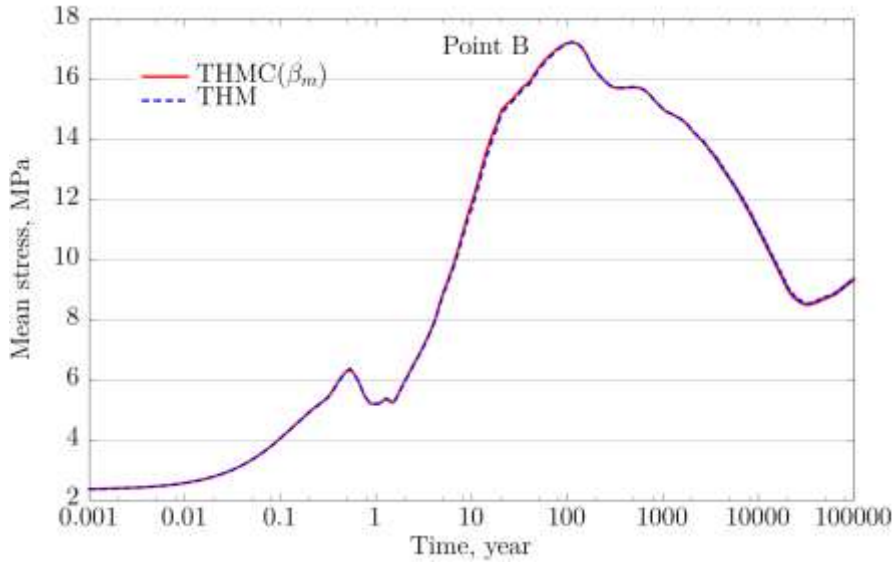

Figure 3-13. Simulation results of mean total stress at point B with FEBEX bentonite for the "THMC(β_m)" and "THM" scenarios, respectively.

3.3.2.3 Effects of Ionic Strength

The "THMC(s_o)" case computes the THMC processes with the effect of ionic strength via osmotic suction. Figure 3-14 shows the evolution of osmotic suction at points A and B. For point A, the osmotic suction increases from the beginning of simulation and peaks at 3.5 MPa at around two years, then starts to decrease until the end of simulation. Similar behavior can be found for point B as well, except that the peak magnitude 2.8 MPa is reached at around 80 years. The osmotic suction reduces to 1.7 MPa at both points by the end of the simulation. The increase in osmotic suction tends to suppress the swelling of bentonite whereas, the reduction of osmotic suction makes bentonite swell more.

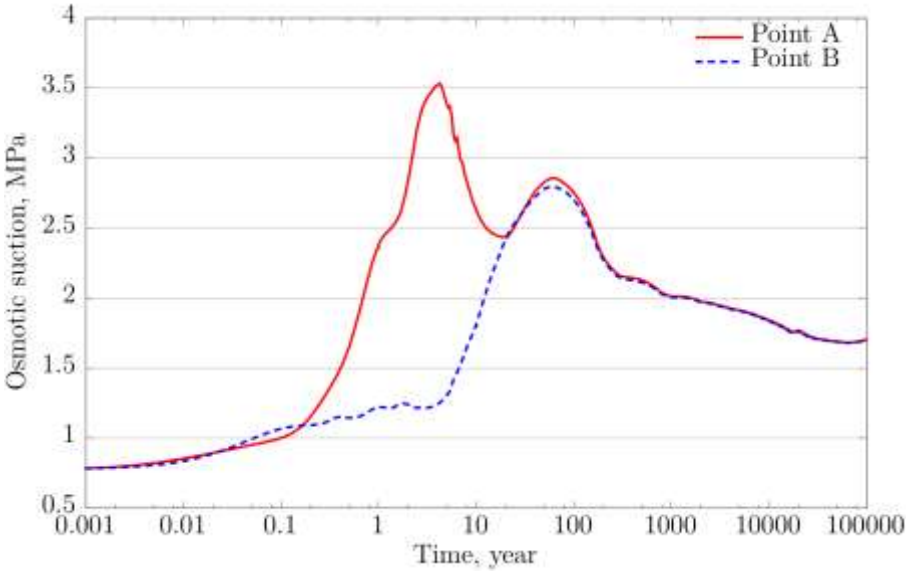

Figure 3-14. Simulation results of osmotic suction evolutions at points A and B with FEBEX bentonite.

The calculated stresses for "THMC(s_o)" and "THM" case at points A and B are plotted in Figures 3-15 and 3-16 respectively. With the osmotic suction effects, the stress at points A and B both decrease when compared with the "THM" case. The total mean stress at point A in "THMC(s_o)" case is about 1.5 MPa lower than that in the "THM" case at around 100 years. After that, although the osmotic suction decreases continuously, the stress difference between "THMC(s_o)" and "THM" case are maintained roughly at the same magnitude with slight fluctuation. For example, near 20000 years, the stress in "THMC(s_o)" becomes 2 MPa less than the corresponding stress in "THM" case. The similar behavior is observed at point B as well (Figure 3-16). The total mean stress at point B in "THMC(s_o)" case is about 1 MPa lower than that in the "THM" case at around 100 years, and the stress in "THMC(s_o)" is 0.6 MPa less than the corresponding stress in "THM" case at 20,000 years. It is fairly clearly that increase osmotic suction lead to the decrease in stress due to the suppression of swelling by osmotic pressure, but quantitatively the decrease in stress is not necessarily proportional to the change in osmotic pressure due to interference of other factors that could alter stress such as pore water pressure, temperature.

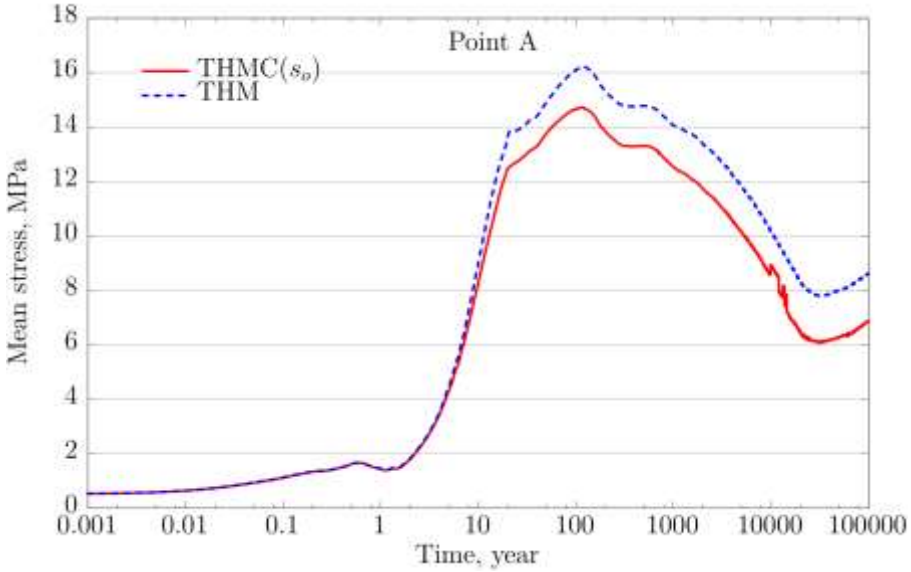

Figure 3-15. Simulation results of mean total stress at point A with FEBEX bentonite for the "THMC(s_o)" and "THM" scenarios, respectively.

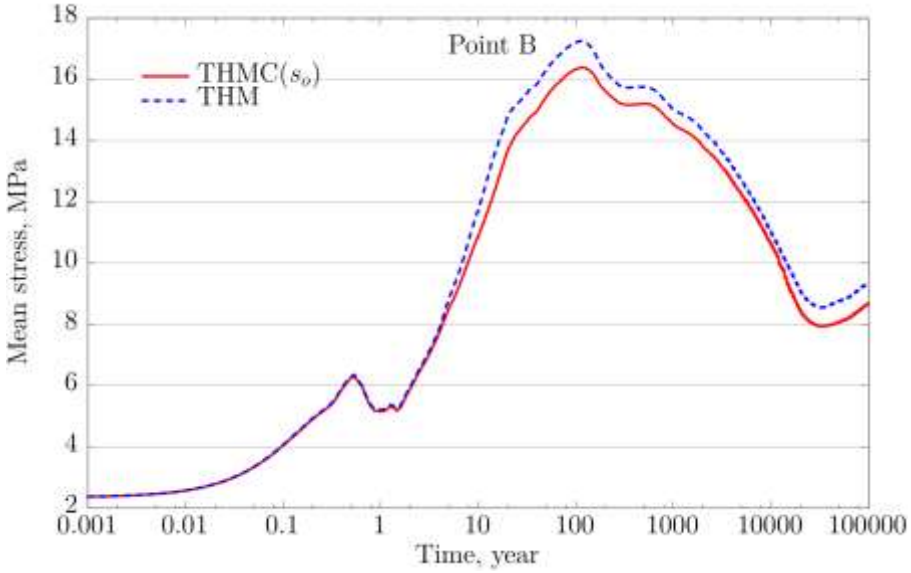

Figure 3-16. Simulation results of mean total stress at point B with FEBEX bentonite for the "THMC(s_o)" and "THM" scenarios, respectively.

3.3.2.4 Combined Effects of all Chemical Reactions

The "THMC(f_s, β_m, s_o)" case takes into account the alteration of mechanical behavior by all three chemical factors: the change in the volume fraction of smectite, change in exchangeable cations and ionic strength contribute. This simulation provides the combination of these three effects and determines whether chemical change enhances or suppresses the stress.

Figures 3-17 and 3-18 show the evolutions of mean total stress at points A and B for "THMC(f_s, β_m, s_o)" case and "THM" case and clearly demonstrate the effect of chemical change on stress. At Point A, peak stresses in bentonite are 15 MPa for the "THMC(f_s, β_m, s_o)" case and 16.2 MPa for the "THM" case both

at around 100 years. Then the total stresses decrease until 30,000 years, after when the stresses increase again to reach the hydrostatic status. The difference in stresses between "THM" and "THMC" cases is 1.2 MPa at around 100 years, and becomes 1.5 MPa in the long term. Apparently chemical changes in bentonite lead to lower total stresses at point A, indicating that the swelling capacity of the bentonite is reduced. At point B, the behavior is similar. Peak stresses in bentonite at point B are 16.5 MPa for the "THMC(f_s, β_m, s_o)" case and 17.3 MPa for the "THM" case at around 100 years. The final stress at point B in "THMC(f_s, β_m, s_o)" case is 0.6 MPa less than that in "THM" case.

Swelling stress cannot be easily extracted from simulation with the dual-structure model, because the micro-swelling strain is calculated directly in the framework of the model. Moreover, the non-linear plasticity induced from both micro- and macro-structures increases the difficulty to distinguish the swelling stress from the total stress. In addition to total mean stress, $\bar{\sigma}$, we present the mean effective/net stress, noted as "$\hat{\sigma}$," (mean net stresses for unsaturated bentonite, and mean effective stress for fully saturated bentonite) in Figures 3-17 and 3-18 as well to illustrate the accumulation of stress in the solid skeleton of bentonite. The difference between mean stress $\bar{\sigma}$ and effective/net stress $\hat{\sigma}$ is pore pressure. At the beginning of the simulation, bentonite is unsaturated. During unsaturated phase, $\hat{\sigma}$ is net stress and it goes up to the peak stress at around 20 years until the bentonite becomes fully saturated, and then $\hat{\sigma}$ become effective stress for the saturated phase. At point A, mean effective/net stresses peak at about 8.5 MPa in "THMC(f_s, β_m, s_o)" case and 9 MPa in "THM" case at around 20 years, then the stresses decrease to 4.5 MPa and 5.5 MPa, respectively. "THMC(f_s, β_m, s_o)" case always has lower stress than the "THM" cases. Similar behaviors can be found with point B, where the mean effective/net stresses reach the highest stress 8 MPa in "THMC(f_s, β_m, s_o)" case and 9 MPa in "THM" case. Then, after the bentonite is fully saturated, the effective/net stresses at point B decrease to 5.8 MPa in "THMC(f_s, β_m, s_o)" case and 6.3 MPa in "THM" case finally.

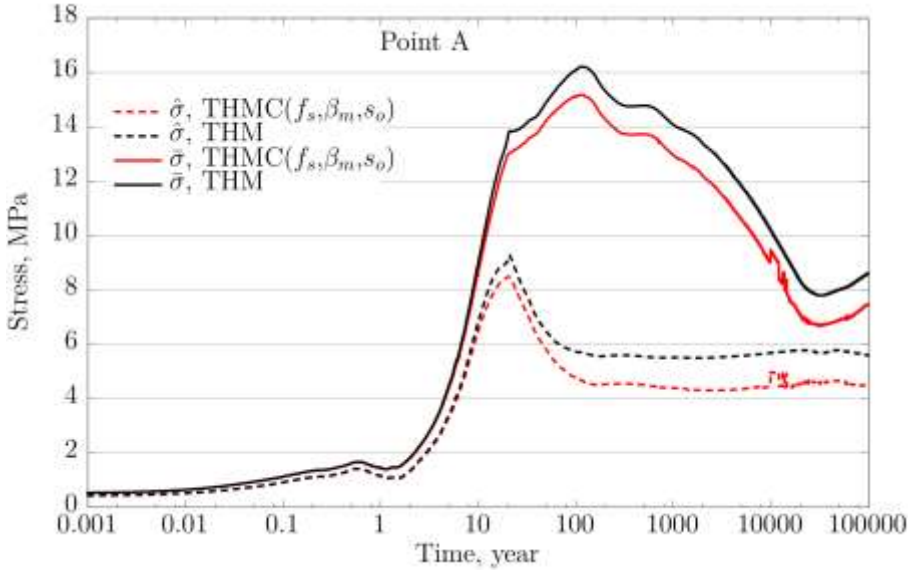

Figure 3-17. Simulation results of mean effective/net stress, $\hat{\sigma}$, and total mean stress, $\bar{\sigma}$, at point A with FEBEX bentonite for the "THMC(f_s,β_m,s_o)" and "THM" scenarios, respectively.

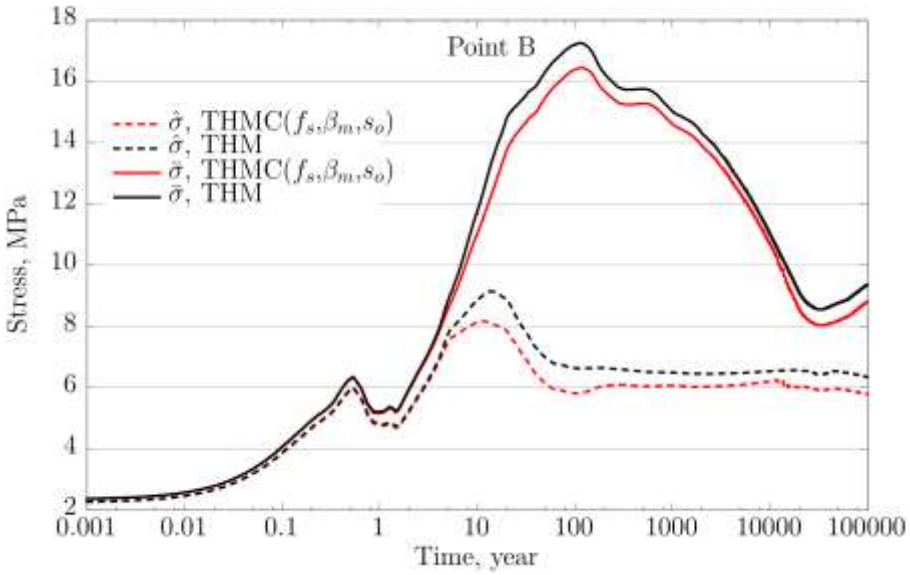

Figure 3-18. Simulation results of stress evolutions at point B with FEBEX bentonite for the "THMC(f_s,β_m,s_o)" and "THM" scenarios, respectively.

Figure 3-19 shows the total stress evolution at point A for "high T" cases with different MC coupling schemes. Overall, chemical effect leads to lower stress. It is found that the stress calculated without any MC coupling ("THM") almost overlaps with the one with only the effect of volume fraction of smectite ("THMC(f_s)"), indicating that changes in volume fraction of smectite has only minimal effect on stress. The stress computed with only exchanged cation concentration ("THMC(β_m)") is higher than the "THM," which reveals that exchanged cations have positive effect on stress. The water infiltration from host rock leads to an increase of ionic strength of pore water in bentonite barrier, which in turn causes the increase in osmotic suction. As a result, the swelling capacity of bentonite decreases, which is manifested by the reduction of the total stress for the case of "THMC(s_o)," i.e., a negative effect. Eventually, the negative effect of ionic strength via osmotic suction on stress outplays the positive effect of exchanged cations on stress, and consequently chemical changes result in lower stress overall. Chemical effects as a whole lead to lower stress than the "THM" model, which is because that the effect of osmotic suction dominates whereas the effects induced by f_s and β_m are smaller. The stress evolutions of all cases at Point B are plotted in Figure 3-18, in which similar observation can be obtained. However, the difference between results by "THM," "THMC(f_s)" and "THMC(β_m)" are negligible, resulting in the result of "THMC(f_s,β_m,s_o)" case is close to the result of "THMC(s_o)" case at Point B. As a result, in terms of chemical effect on stress, point A and B exhibit the some behavior: chemical effect as a whole leads to lower stress than the "THM" computation.

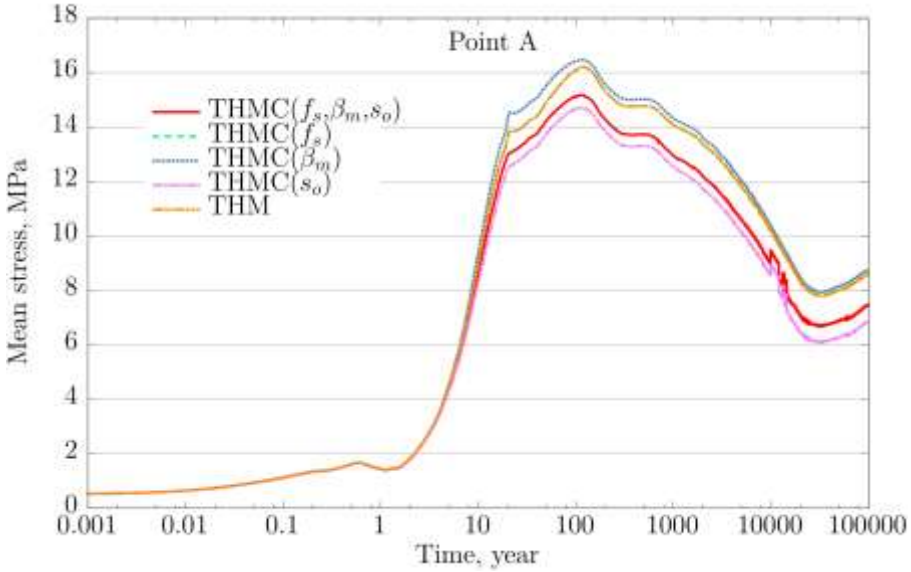

Figure 3-19. Simulation results of mean total stress at point A with FEBEX bentonite. Different MC couplings are considered and computed.

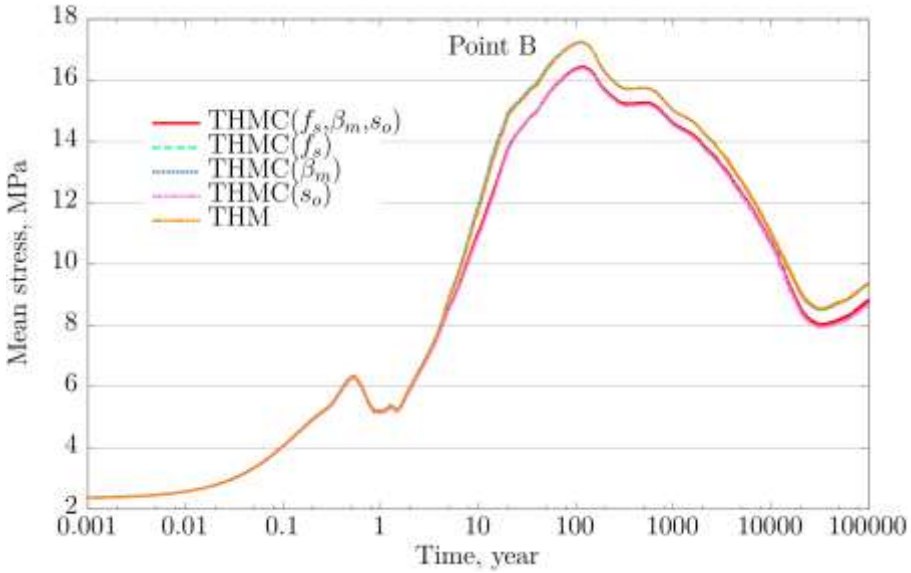

Figure 3-20. Simulation results of mean total stress at point B with FEBEX bentonite. Different MC couplings are considered and computed.

3.4 Long Term Predictions Based on the Model for FEBEX *In Situ* Test

Evaluating the illitization and its impact of the mechanical properties of bentonite is a very challenging because the model is very complicated. In addition to the complex coupling between THMC processes, illitization itself is the result of a very complex reaction networks and eventually how these reaction network play out depends on the local chemical conditions. After Zheng et al. (2015b) simulate the

illitization and its impact on swelling stress using a generic case in which the EBS bentonite properties is based on the Kunigel-VI bentonite and properties host argillite is based on Opalinus Clay, Zheng et al. (2016) conducted another model simulation which is similar to the model developed in Zheng et al. (2015b) except the EBS bentonite properties is based FEBEX bentonite, attempting to find out if those findings revealed by the model in Zheng et al. (2015b) still holds in the scenarios simulated in Zheng et al. (2016). The conclusion is that illitization in bentonite is a site-specific issue and has to be evaluate based on the conditions encountered at a particular repository.

Models in Zheng et al. (2015b; 2016) was developed based on extensive literature review, up-to-date modeling approach and newlydeveloped constitutive relationships. Coupled THMC model (Zheng et al., 2015b; 2016) involves a lot of parameters, and the most plausible values were used based on extensive review of similar modeling work, laboratory experiment and field tests. However, the most plausible values for the key parameters do not mean the combination of these parameters in the THMC model lead to most plausible results. The model, if can be used to make predictions, has to be calibrated based on data, and then extend the modeling time to predict evolution of THMC properties for the time that required by the performance assessment, usually 100,000 years or even a million years. However, model validation was difficult due to lack of THMC data from long-term, large-scale experiments. The FEBEX (Full-scale Engineered Barrier EXperiment) *in situ* test provides a unique opportunity of validating coupled THMC models. Over the course of FEBEX *in situ* test and after the final dismantling of the test, extensive THMC data were collected. A 1-D coupled THMC model has been successfully reproduced all THMC data (see Chapter 4 of this report). Although the chemical part in the THMC model needs to be fine-tuned to catch the evolution of redox conditions and canister-bentonite interaction, this model has been calibrated to an extend that long term prediction is doable. We therefore extend the running time of the 1-D THMC model for FEBEX *in situ* test to 100,000 years and modify the boundary condition for the canister—instead of fixing at 100 °C, a heat release function was prescribed—to evaluate the illitization in the bentonite.

3.4.1 A Brief Description of the FEBEX *In Situ* Test and Calibrated THMC Model

Section 4 of this report has the details of the FEBEX *in situ* test and the calibration of coupled THMC model. Here we just very briefly describe the text and model calibration, hoping reader might not have to refer to Section 4 to understand the model results presented in the next section.

FEBEX *in situ* is a full-scale reproduction of the Spanish disposal concept: waste package will be horizontal emplaced in the tunnel of granite and the space between waste canister and tunnel wall is filled with bentonite. Figure 3-21 shows the configuration of the test, two heaters were installed. The heating started in 1997 and maintained by 100 °C. In 2002, heater #1 was dismantled, the buffer and all components were removed up to a distance of 2 meters from heater #2 to minimize disturbance of the non-dismantled area. After the dismantling of heater #1, the tunnel was plugged with shotcrete and heater #2 was maintained a constant 100 ^{o}C until 2015 when the final dismantling occurred.

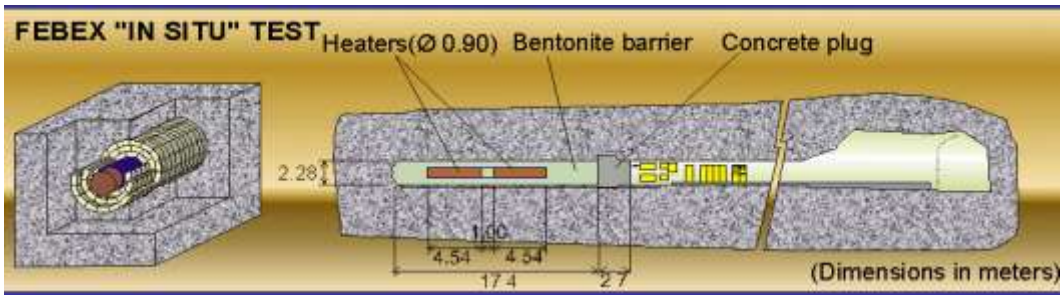

Figure 3-21. The configuration of FEBEX *in situ* test conducted at Grimsel, Switzerland.

In the FEBEX *in situ* test, some data were collected real time by the sensors installed in the bentonite block including temperature, relative humidity and stress, which were used to test the model via the temporal evolution of these variables at several radial distance from the axis of the tunnel; and some of data were measured in the laboratory using the bentonite sample that were taken after dismantling of test sections, including water content, dry density, concentration of ions in pore water and mineralogical composition. Because of the two dismantling events, we therefore have the spatial distribution of these variables at the snapshot; one is at 5.3 years (after the dismantling of heater #1) and the other is at 18.3 years (after the dismantling of heater #2). A 1-D axi-symmetrical THMC model were developed for the "hot" sections that locate crosscutting the middle of heater. All these data were used to calibrate the model and reasonable match between model results and data have been achieved (see Section 4.3).

3.4.2 Prediction Results

To use the model for FEBEX *in situ* test to predict the long-term alteration of bentonite, we have made two changes to the model. The first one is obvious: the simulation time has been extended to 100,000 years. The second one is about the thermal boundary condition for the canister. In the model for the FEBEX *in situ* test, the heater was maintained at a constant 100 ^{o}C according to the test condition. However, considering the decay of heat emanation, it is unrealistic to assume a constant temperature at the canister surface; we therefore use the power curves shown in Figure 3-1. Those curves lead to two simulations: one will have temperature peak of 100 °C at canister surface and the other will have temperature summit of 200 °C at canister surface. The numerical simulations for the case with temperature summit of 200 °C is ongoing, here we only shows the model results for the case with temperature peak of 100 °C at canister surface. Figure 3-22 shows the temporal evolution at several locations. Note that bentonite barrier is from radial distance of 0.45 to 1.13 m. Bentonite is under higher than 30 °C for about 200 years. After about 2000 years, bentonite is just under the ambient condition. Model results also showed that bentonite becomes fully saturated in about 30 years.

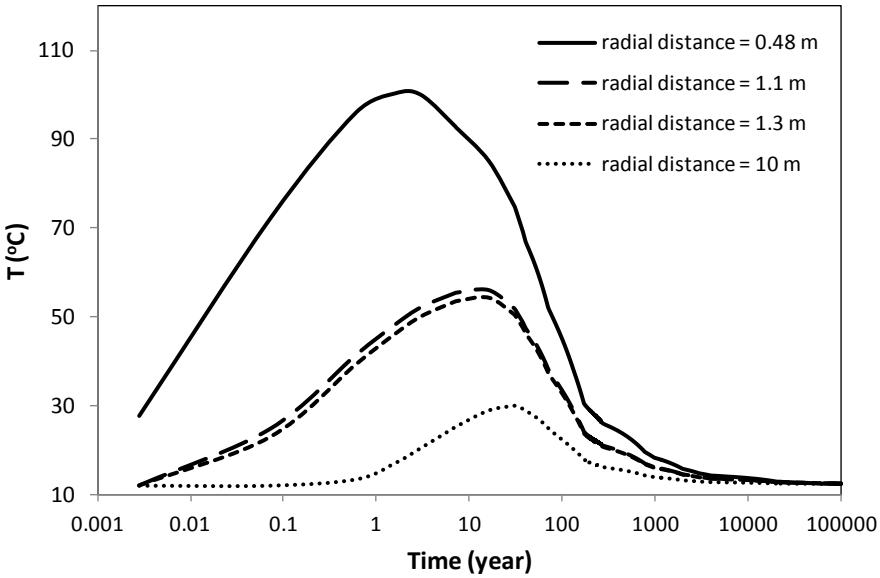

Figure 3-22. Temporal evolution of temperature at several locations (canister surface has a radial distance of 0.45 m).

The stress evolution in bentonite is caused mostly by saturation. As shown in Figures 3-23 and 3-24, after the bentonite become fully saturated, bentonite is under compression, with a stress somewhat stabilized around 8-10 MPa.

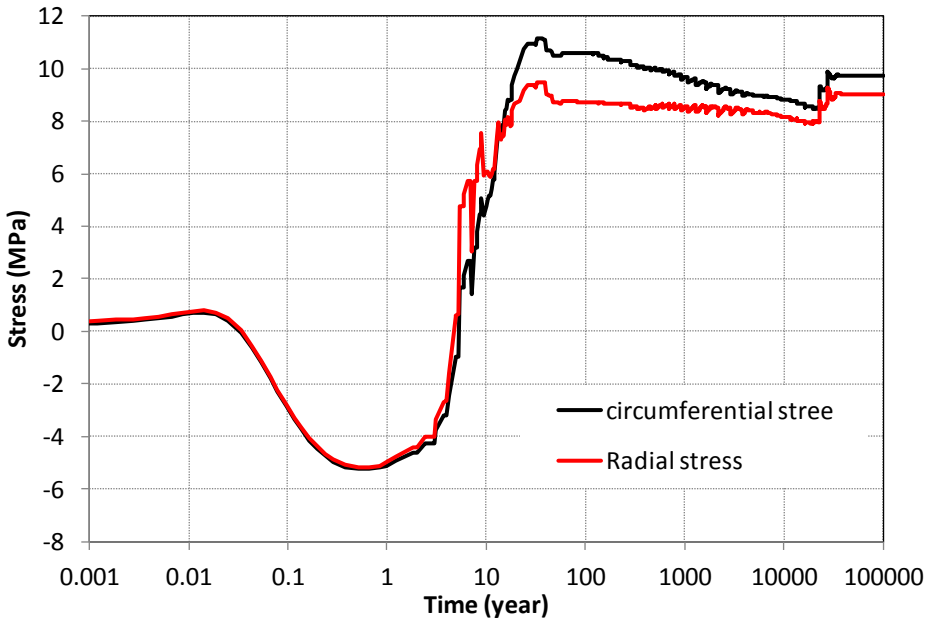

Figure 3-23. Temporal evolution of stress at radial distance of 0.5 m (canister surface has a radial distance of 0.45 m).

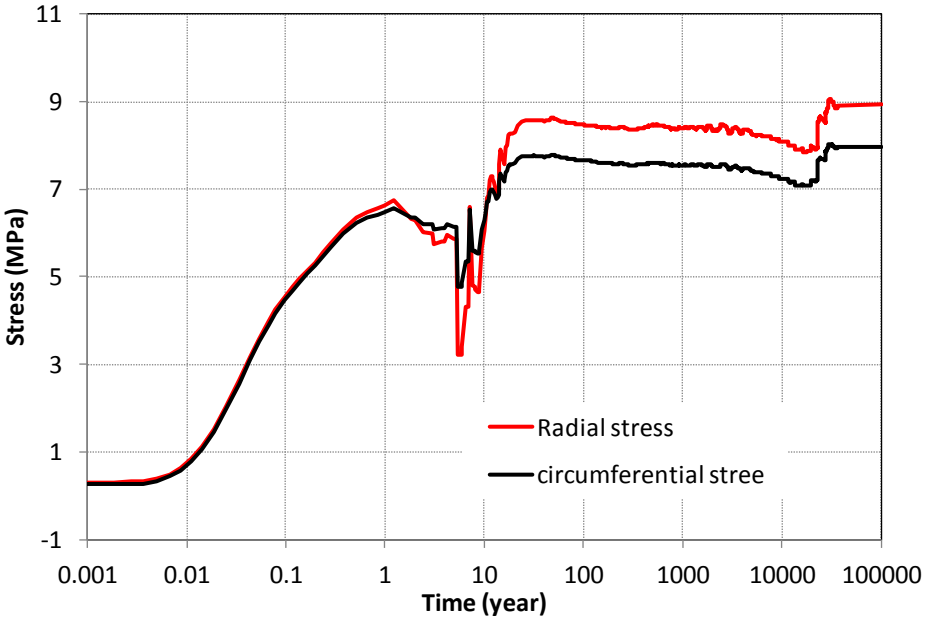

Figure 3-24. Temporal evolution of stress at radial distance of 1.1 m (canister surface has a radial distance of 0.45 m, and bentonite-granite locates at radial distance of 1.14 m).

FEBEX *in situ* test was initially designed to demonstrate the feasibility of Spanish disposal concept that uses granite as host rock. The groundwater in granite at the test site is very dilute, concentrations of major anions and cations are 3-5 orders of magnitude lower than that in pore water of bentonite. As the granite water infiltrates into bentonite, it is expected that ion concentrations in the pore water of bentonite decreases. The concentration change of chloride (a conservative species) clearly illustrate such process. Chloride concentration data collected in the FEBEX *in situ* test and THMC model showed that during the test period, chloride concentration was significantly diluted (see section 4.4.3). When simulation runs longer, as shown in Figure 3-25, chloride concentration further decreases, although chloride concentration in the area very close to the canister remains around 1 mol/L after 100,000 years.

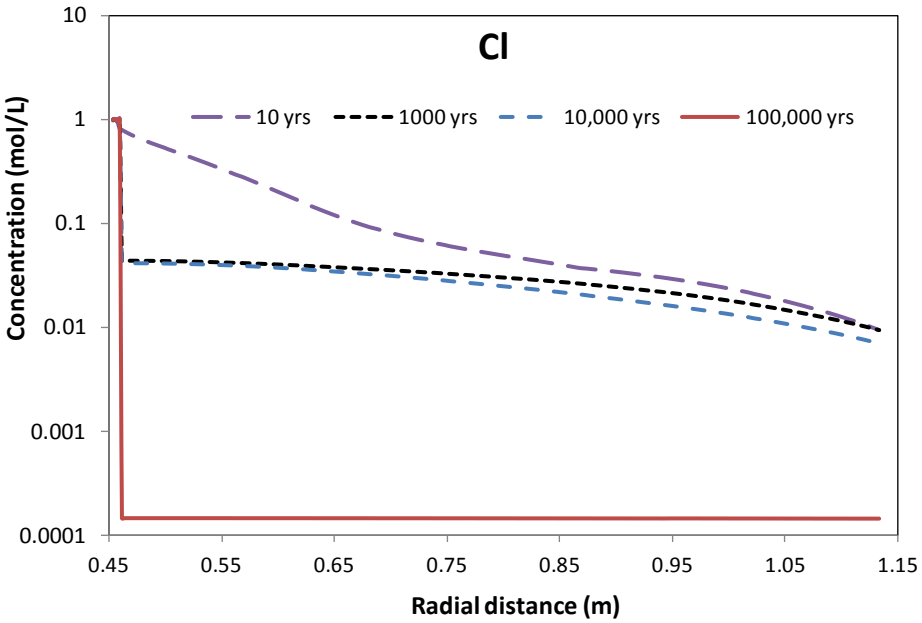

Figure 3-25. Spatial distribution of chloride concentration from the canister (radial distance = 0.45 m) to the granite at several times.

The dilution that controls the chloride concentration also plays out similarly for other reactive species, leading to lower and lower concentration when time proceeds, as illustrated by the concentration profile of sodium at several times (Figure 3-26). By the end of 100,000 years, the concentration of sodium in the pore water of bentonite is very similar to that in the granite.

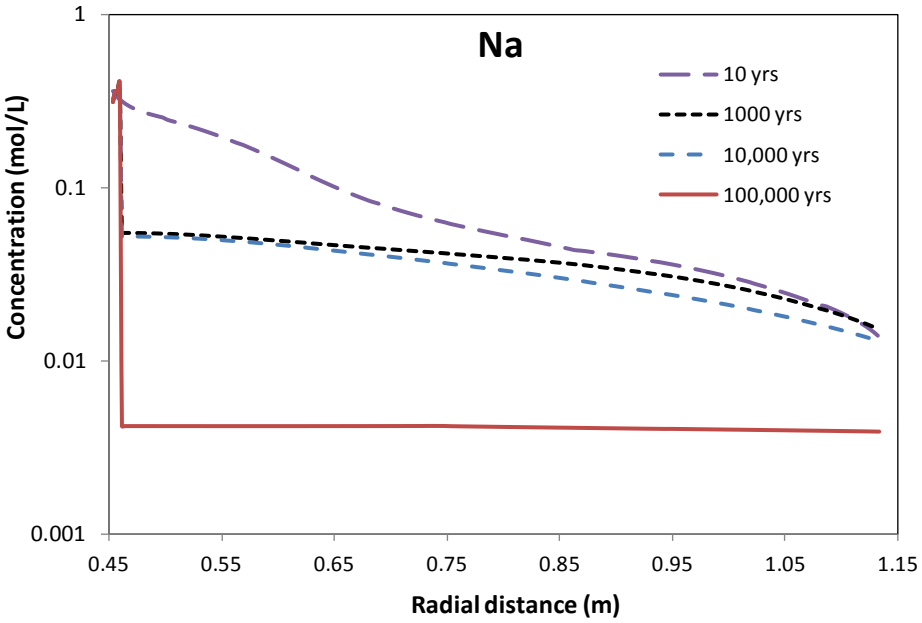

Figure 3-26. Spatial distribution of sodium concentration from the canister (radial distance = 0.45 m) to the granite at several times.

Previous modeling work (e.g., Zheng et al., 2011) and laboratory study (e.g., Zheng et al., 2010) showed that pH in the bentonite barrier is buffered by surface protonation reactions and will stay at a level close to the initial pH. This is consistent observation from data and model for months (Zheng et al., 2010), model for 5 years (Zheng et al., 2011). Chemical data from the FEBEX "*in situ*," the longest full-scale field test that have ever been conducted, and the THMC model that interprets the data, also confirm such observation. As the model runs longer, model results show that surface protonation does buffer pH, and for actually quite long time up to 1000 – 10,000 years, as shown in Figure 3-27. However, the pH buffer capability eventually was deplete and pH starts to rise as granite water has high pH and the evolution of the minerals phase favors high pH.

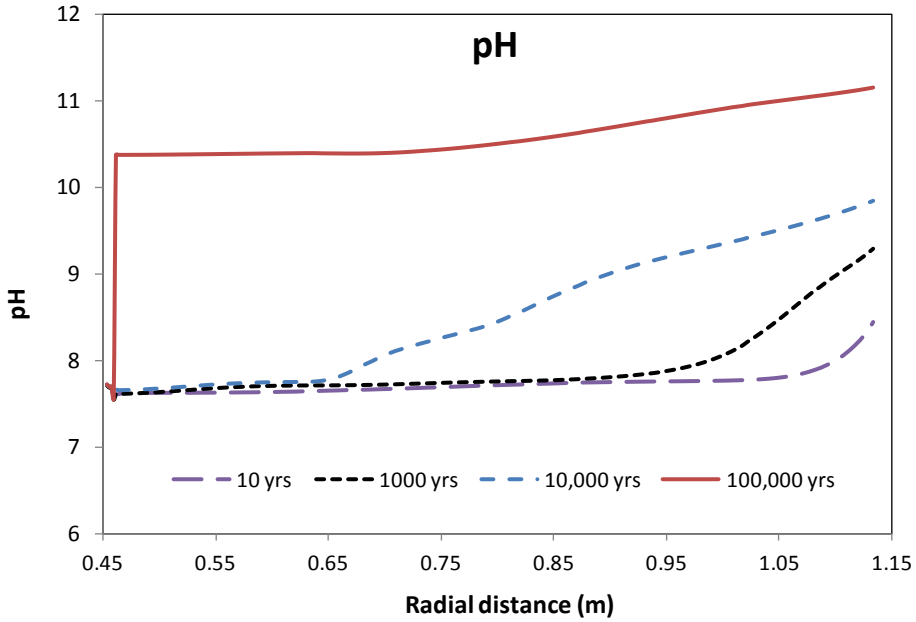

Figure 3-27. Spatial distribution of sodium concentration from the canister (radial distance = 0.45 m) to the granite at several times

In current model, the dissolution of smectite is simulated as the reaction 3.6, which clearly shows that the continuously decrease of concentrations of sodium, magnesium, silicates and aluminum and the increase in pH (Figure 3-27) will drive the reactions toward the right hand side, i.e., the dissolution of smectite. As a result, we see progressive dissolution of smectite in bentonite (Figure 3-28). By the end of 100,000 years, smectite, initially presented with a volume fraction of 0.546, is close to be depleted in the most area.

$$\text{Na-smectite} + 0.68H^{+} \Leftrightarrow 0.66H_2O + 0.33Mg^{+2} + 0.33Na^{+} + 0.5SiO_2(aq) + 1.67AlO_2^{-} \quad 3.6$$

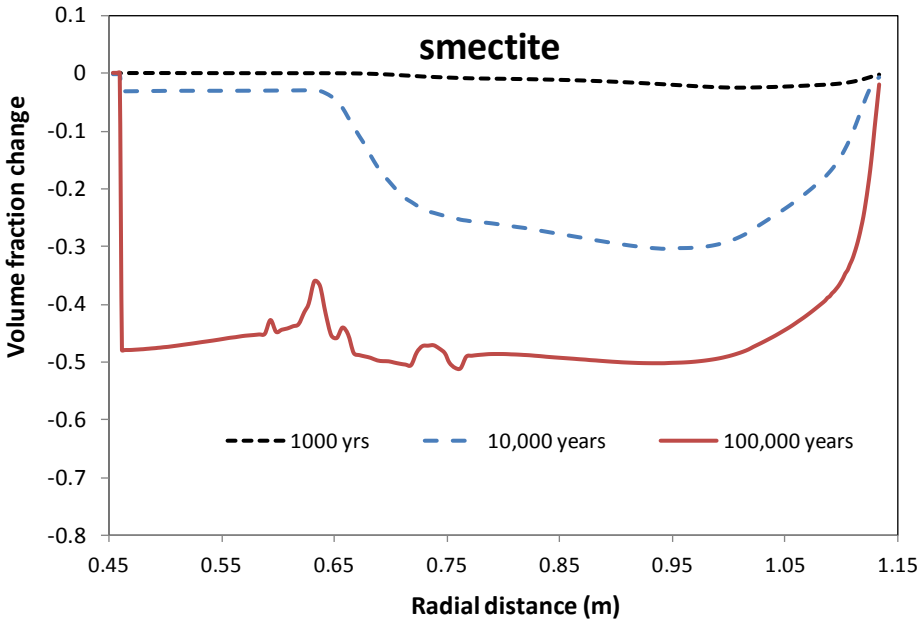

Figure 3-28. Spatial distribution of smectite volume fraction from the canister (radial distance = 0.45 m) to the granite at several times.

The changes in aqueous concentration initiate the dissolution of smectite, i.e., make the chemical condition favors the dissolution of smectite, but it is the precipitation of other silicate-aluminum minerals that drive the continuation of smectite dissolution, otherwise the dissolution of smectite will stop at some point when the concentration of related ions built up. Current model shows the precipitation of illite (Figure 3-29), quartz (Figure 3-30) and K-feldspar (Figure 3-31).

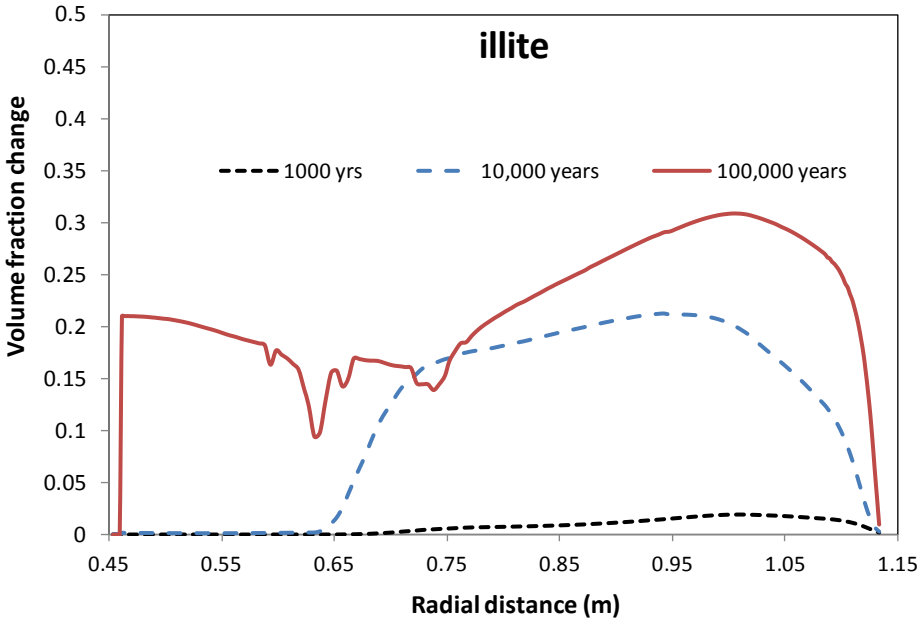

Figure 3-29. Spatial distribution of illite volume fraction from the canister (radial distance = 0.45 m) to the granite at several times.

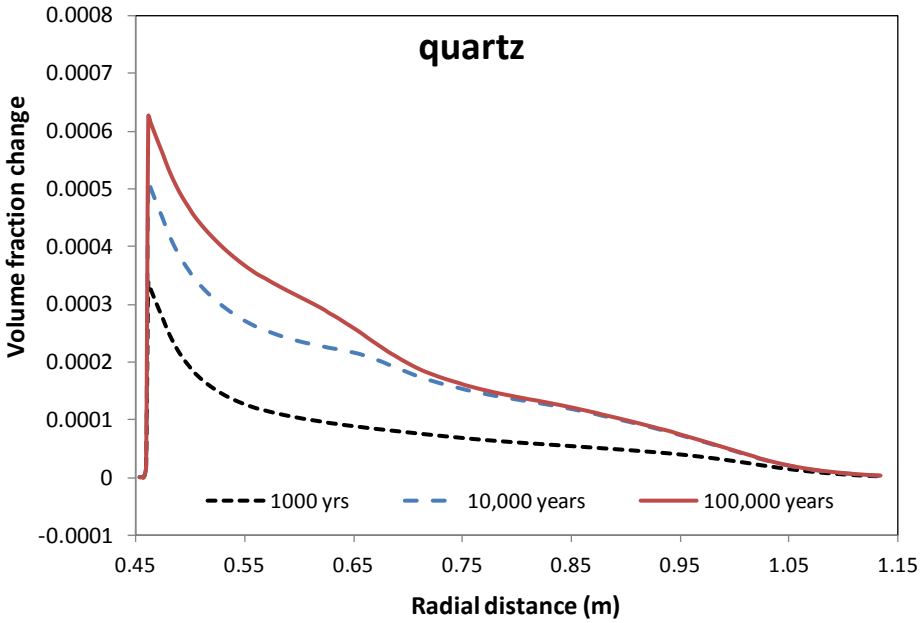

Figure 3-30. Spatial distribution of quartz volume fraction from the canister (radial distance = 0.45 m) to the granite at several times.

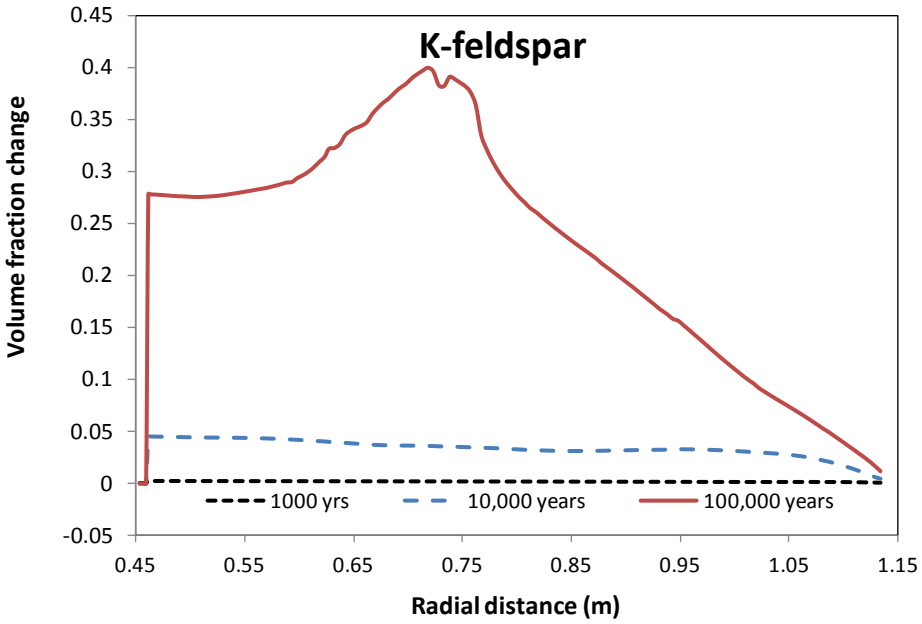

Figure 3-31. Spatial distribution of K-feldspar volume fraction from the canister (radial distance = 0.45 m) to the granite at several times.

The prediction based on the model for FEBEX *in situ* test is very different from the previous generic models (Figure 3-6) in the following aspects. First, the dissolution of smectite in model based on *in situ* test is orders of magnitude higher than the previous model (brief description of the model is in Section 3.2). Second, K-feldspar precipitates in the model based on *in situ* test whereas it dissolves in previous

model. The dissolution/precipitation of K-feldspar is an important issue because previous models show that the dissolution of K-feldspar is source of potassium for illitization and significantly affect the dissolution of smectite and precipitation of illite.

Why the prediction based on FEBEX *in situ* test is so different from previous model in terms of illitization? The reason is the host rock. Host rock in the model for FEBEX *in situ* test is granite at Grimsel, Switzerland and that in previous generic model is Opalinus Clay. Table 3-6 shows the difference of ion concentration in the pore water of Opalinus Clay and granite— ion concentrations in the pore water of Opalinus Clay is orders of magnitude higher than that in granite, and they are actually higher than ion concentration in the pore water of FEBEX bentonite. The infiltration of much dilute granite water into bentonite decrease the concentration of most ions and subsequently triggers dissolution of most minerals including smectite. The dissolution of smectite then leads to precipitation of silicate-aluminum minerals including illite, K-feldspar and quartz. Then the question is where potassium comes from to support the precipitation of illite and K-feldspar? Model results show that the exchangeable sites actually provides potassium for illite and K-feldspar precipitation, as shown in Figure 3-15 that the exchangeable potassium is almost the exhausted after 100,000 years; the concentration of exchangeable potassium is down to about 0.01 meq/100 g which is a very small value of exchangeable cations. On the contrary, in previous models in which the host rock is Opalinus clay, because of high ion concentration in the host rock, pore water in bentonite is not diluted and therefore minerals dissolution cannot be driven by dilution. What really drives the dissolution of smectite is actually the precipitation of illite, i.e., illite precipitation in bentonite due to influx of potassium from host rock initiates dissolution of smectite, and then the dissolution of K-feldspar make the dissolution of smectite continue, but only to a rather small amount. As shown in Figure 3-3 in the low T case (100 °C) smectite dissolve only a volume fraction of 0.0005. In summary, because the model for FEBEX *in situ* test is in granite host rock, the reaction paths of illitization is quite different from previous model in which the host rock is Opalinus Clay and subsequently much more dissolution of smectite has been observed.

Table 3-6. Pore-water composition (mol/kg water, except pH) of FEBEX bentonite (Fernández et al., 2001), Opalinus Clay (Fernández et al., 2007) and granite (Zheng et al., 2011).

	FEBEX Bentonite	Opalinus Clay	Granite
pH	7.72	7.40	8.35
Cl	1.60E-01	3.32E-01	1.31E-05
SO_4^{-2}	3.20E-02	1.86E-02	7.86E-05
HCO_3^-	4.1E-04	5.18E-03	3.97E-04
Ca^{+2}	2.2E-02	2.26E-02	1.81E-04
Mg^{+2}	2.3E-02	2.09E-02	1.32E-06
Na^+	1.3E-01	2.76E-01	3.76E-04
K^+	1.7E-03	2.16E-03	7.80E-06
Fe^{+2}	2.06E-08	3.46E-06	2.06E-08
SiO_2(aq)	1.1E-04	1.10E-04	6.07E-04
AlO_2^-	1.91E-09	3.89E-08	3.89E-08
O_2(aq)	2.57e-4	1.2E-51	-

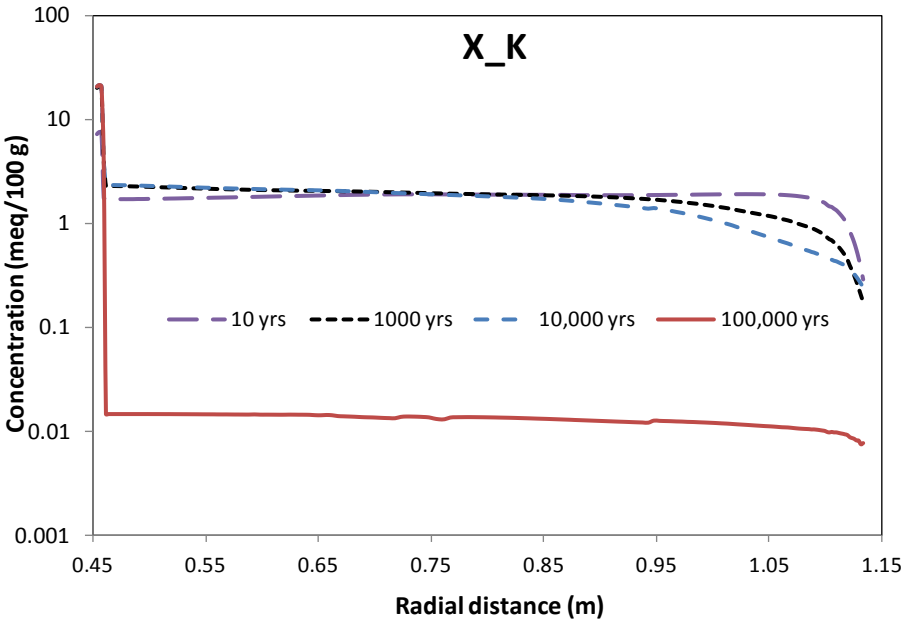

Figure 3-32. Spatial distribution of exchangeable potassium (X_K) from the canister (radial distance = 0.45 m) to the granite at several times.

3.5 Conclusions

3.5.1 Summary of Current Modeling Work

In FY16, THMC models utilize dual structure Barcelona Expansive Clay Model (BExM) (Sánchez et al., 2005) to link mechanical process with chemistry, allowing us to simultaneously incorporate the effects of exchangeable cations, ionic strength of pore water and abundance of swelling clay on the swelling stress of bentonite. In FY17, we re-calibrated the parameters of BExM Model for FEBEX bentonite, and used it on a generic repository to consider the interaction between EBS bentonite and the NS clay formation. The following observations have been concluded from the model results:

- Three chemical changes including the change in the volume fraction of smectite, change in exchangeable cations and ionic strength contribute distinctively to the stress evolution in bentonite. In current model, dissolution of smectite leads to decrease in the volume fraction of smectite which decrease the stress. Because the enrichment of exchangeable sodium in the interlayer, the change in exchangeable cations cause the increase in stress. The infiltration of more concentrated water from clay formation to EBS bentonite leads to the increase in osmotic suction and subsequently lowers the stress. The combination of these three effects determines whether chemical change enhances or suppresses the stress. The chemical changes as a whole reduce both total stress and effective/net stress in the bentonite buffer in the "high T" cases. The difference between the result computed with C-M coupling ("THMC") and the result without C-M coupling ("THM") ranges from 0.6 MPa to 1 MPa in bentonite.
- In comparison with the THMC that used extended linear swelling model (Zheng et al., 2015b), THMC model using BExM showed less chemical effect on stress. The first reason is that exchangeable cations, which could not be taken into account by extended linear swelling model, is now considered in BExM. For FEBEX bentonite, change in exchangeable cations has positive

effect on the stress, which cancel out the negative effect due to the change of ionic strength (via osmotic suction) and consequently the chemical change overall has less effect on stress in THMC model using BExM than that in the THMC model that used extended linear swelling model. The second reason is that the mechanical-chemical coupling via BExM, the dissolution of smectite was factored in directly via the volume fraction of smectite by modifying the bulk modulus for micro-structure, but in BExM, bulk modulus is a function of stress and change significantly in the model, the bulk modulus changes by smectite dissolution was overshadowed by the stress change.

While the generic THMC models shed light on various aspects of chemical alteration of bentonite and its impact of mechanical properties of bentonite, predictions based model that has been calibrated against THMC data will provide more tangible results and further deepen our understanding the long-term alteration of bentonite. The THMC model that has been calibrated for the FEBEX *in situ* was extended to 100,000 years with a modified boundary condition for the canister. Model results show significant dissolution of smectite and precipitation of illite, quartz and K-feldspar, which are very different from the results in the generic THMC models. The main reason is that the water in granite host rock in the model for FEBEX *in situ* test has much lower ion concentrations than the water in clay formation host rock in the generic model, which completely changes the reaction path and leads much more dissolution of smectite in bentonite in the model for FEBEX *in situ* test. The predictions by the model for FEBEX *in situ* test indicate that interaction between EBS bentonite and host rock is critical for the alteration in EBS bentonite.

3.5.2 Future Work

The current coupled THMC model greatly improves our understanding of the coupled processes contributing to chemical and mechanical alteration in EBS bentonites and NS argillite formations and answers questions regarding the thermal limit of EBS bentonite in clay repository. However, more questions remain to be answered regarding the THMC alteration of bentonites and clay formations under high temperature. Further refinement of current models and improvements for the TOUREACT-FLAC3D simulator are needed in the future. The following activities are proposed:

- The calibration on parameters of BExM for specific material is needed for better prediction of the material behavior during in-situ experiments.
- The model needs to be simplified to improve its numerical robustness and to apply easily on different materials.

In FY17 up to now, the THMC model for the FEBEX *in situ* test was extended for 100,000 years to predict the bentonite alteration in granite host rock. The boundary condition for the canister was modified to make a case that the temperature at the canister surface peaks at 100 °C. In order to evaluate the impact of higher temperature on bentonite, in the remaining months of FY17 and FY18, high temperature case in which the temperature at the canister surface reaches 200 °C will be created to evaluate bentonite alteration in granite host rock under high temperature.

4. UNDERSTANDING THE THMC EVOLUTION OF BENTONITE IN FEBEX-DP – COUPLED THMC MODELING AND EXAMINATION OF THE STRUCTURE OF BENTONITE

4.1 Introduction

The clay and crystalline radioactive water repository typically involves a multi-barrier system. In addition to the natural barrier system (NBS), i.e., the host rock and its surrounding subsurface environment, it also has an engineered barrier system (EBS). The EBS represents the fabricated, engineered materials placed within a repository, including the waste form, waste canisters, buffer materials, backfill, and seals.

The most common buffer material for EBS is compacted bentonite, which features low permeability and high retardation of radionuclide transport. The safety functions of EBS bentonite include limiting transport in the near field; damping the shear movement of the host rock; preventing the sinking of canisters (if emplaced in the center of the tunnel), limiting pressure on the canister and rock, and reducing microbial activity. To assess whether EBS bentonite can maintain these favorable features when undergoing heating from the waste package and hydration from the host rock, we need a thorough understanding of the thermal, hydrological, mechanical, and chemical evolution of bentonite under disposal conditions. While numerous laboratory experiments, field tests, and numerical models have been conducted to improve the understanding of each individual process or coupled THC/THM processes, there is a lack of studies on coupled THMC processes due to the challenges of conducting experiments and developing models that can cover all the THMC processes. Recently in the UFD program, coupled THMC models have been developed for a generic disposal system in clayey host rock with EBS bentonite (Liu et al., 2013; Zheng et al., 2014; Zheng et al., 2015b). However, model validation was difficult for lack of THMC data from long-term, large-scale experiments. The FEBEX (Full-scale Engineered Barrier EXperiment) *in situ* test (ENRESA, 2000), which has been operated for 18 years, provides a unique opportunity of validating coupled THMC models.

In the FEBEX *in situ* test, two heaters surrounded by bentonite blocks about 0.7 m thick were emplaced in a tunnel excavated in granite. The heaters were switched on in 1997. In 2002, heater 1 was dismantled; in 2015, the second heater was dismantled in the FEBEX-DP project, which is comprised of extensive THMC and biological characterization of bentonite, and development of numerical models. LBNL/DOE joined the FEBEX-DP project in FY15. The ultimate goal is to use THMC data from FEBEX-DP to validate THMC models and therefore enhance our understanding of coupled THMC process. From 2015 to 2017, extensive THMC characterization of bentonite samples collected during the dismantling of the second were carried by partners of FEBEX-DP. In this chapter, we present coupled THMC models that interpret the THM data and were tested against the chemical data in bentonite. The model showed reliable predictability of evolution of conservative chemical species, but further refinement of the chemical model is needed to understand the behavior of reactive species. In addition, synchrotron X-ray microtomography measurements of the bentonite samples were carried out to examine the microstructure of bentonite that underwent 18 years of *in situ* heating and hydration.

4.2 A Brief Description of FEBEX Experiments

FEBEX (**F**ull-scale **E**ngineered **B**arrier **Ex**periment in crystalline host rock) is a research and demonstration project that was initiated by ENRESA (Spain). Its objective was to demonstrate the feasibility of constructing an engineered barrier system and to study the behavior of components in the near-field for a high-level radioactive waste (HLW) repository in crystalline rock. Specifically, the project aimed to demonstrate the feasibility of fabricating and assembling the EBS and developing methodologies and models for the evaluation of the thermo-hydro-mechanical (THM) and thermo-hydro-chemical (THC) behavior of the near-field (ENRESA, 2000). These objectives were to be attained through the

combination of *in situ* and mock-up tests, numerous small-scale laboratory tests, and THC/THM modeling. The project was initially scheduled for a period of 7 years, from 1994 to 2001, but was extended several times as the experiments continued. Figure 4-1 shows the history of FEBEX projects, with different project names representing different operational stages.

Figure 4-1. The operational stages of FEBEX *in situ* test (Vomvoris, personal communication).

The centerpiece of the FEBEX experiments is, of course, the *in situ* test conducted at the Grimsel underground laboratory, Switzerland. The test consists of five basic units: the drift, the heating system, the bentonite barrier, the instrumentation, and the monitoring and control system (Figure 4-2). The drift is 70.4 m long and 2.28 m in diameter. The test area, which was sealed with a concrete plug, is located at the last 17.4 m of the drift where heaters, bentonite and instrumentation were installed. The main elements of the heating system are two heaters (#1 and #2), 1 m apart, which simulate full-sized canisters. Heaters were placed inside a cylindrical steel liner. Each heater is made of carbon steel, measures 4.54 m in length and 0.9 m in diameter, and has a wall thickness of 0.1 m. Heaters were operated at a constant power output of 1200 W/heater during the first 20 days and 2000 W/heater for the following 33 days. Afterwards, the heaters were switched to a constant-temperature control mode to maintain a maximum temperature of 100 ºC at the steel liner/bentonite interface.

The bentonite barrier is made of blocks of highly compacted bentonite, situated in vertical sections normal to the axis of the tunnel. There were gaps between blocks, but the volume of gaps has not been reliably estimated. Although the dismantling of bentonite barrier revealed that all gaps were sealed, these gaps might affect the initial hydration of bentonite, but such an effect is difficult for models to take into account. The average values of the initial dry density and the water content of compacted bentonite blocks are 1.7 g/cm^3 and 14.4%, respectively.

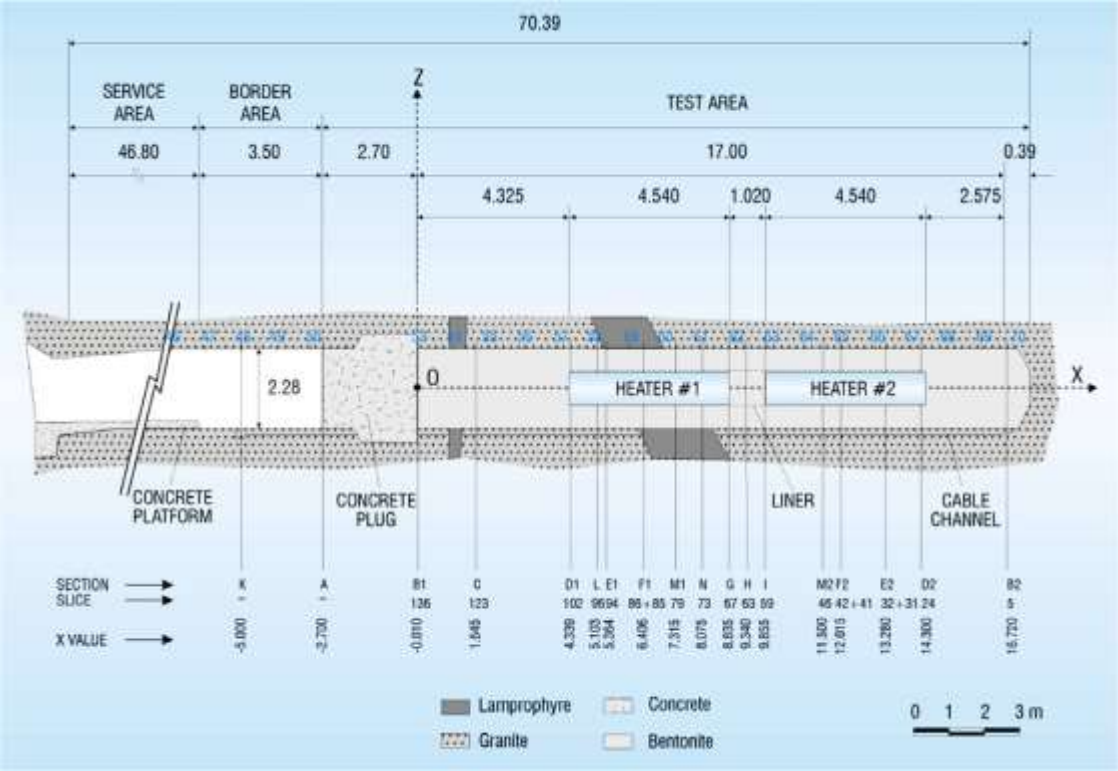

Figure 4-2. The initial configuration of the FEBEX *in situ* test at the Grimsel underground laboratory (Switzerland) (ENRESA, 2000).

The *in situ* test began on February 27, 1997. Heater #1 was switched off in February 2002 and dismantled from May to September in 2002. The buffer and all components were removed up to a distance of 2 meters from heater #2 to minimize disturbance of the non-dismantled area. A dummy steel cylinder with a length of 1 m was inserted in the void left by heater #1 in the center of the buffer. The description of the partial dismantling operation is given by Bárcena et al. (2003). A comprehensive post-mortem bentonite sampling and analysis program was performed on the solid and liquid phases to check the physical and chemical changes induced by the combined effect of heating and hydration and to test THM and THC model predictions (ENRESA, 2006a; b). The layout of the sampling sections for THC and THM measurements after the dismantling of heater #1 is given in Figure 4-3.

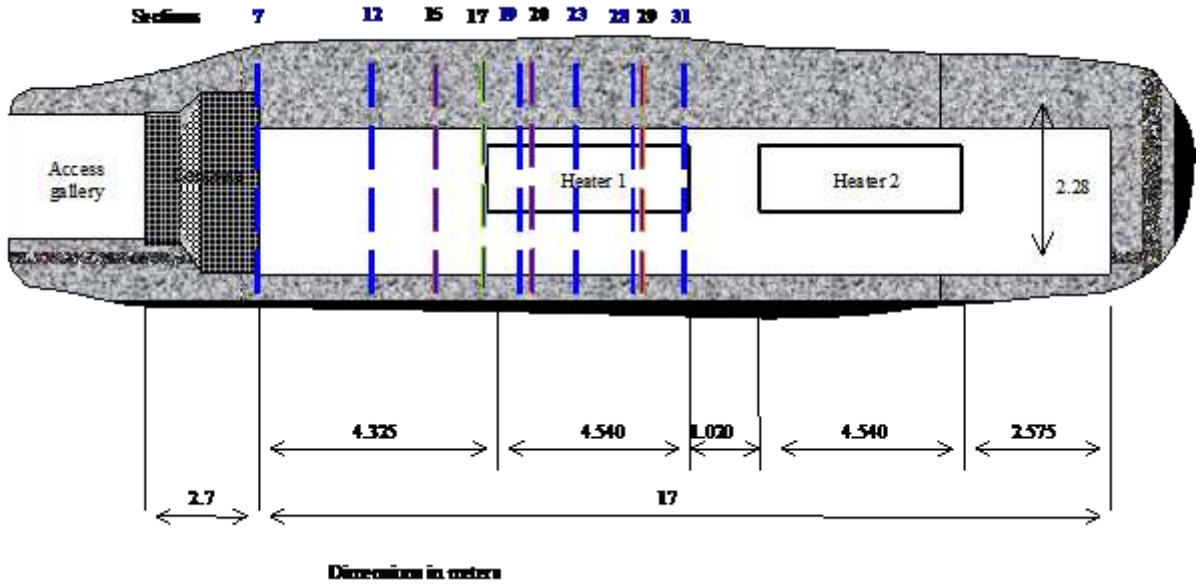

Figure 4-3. Layout of the sampling sections during the dismantling of heater 1 in 2002. In blue color are the common sections for THC and THM analyses (Fernández and Rivas, 2003)

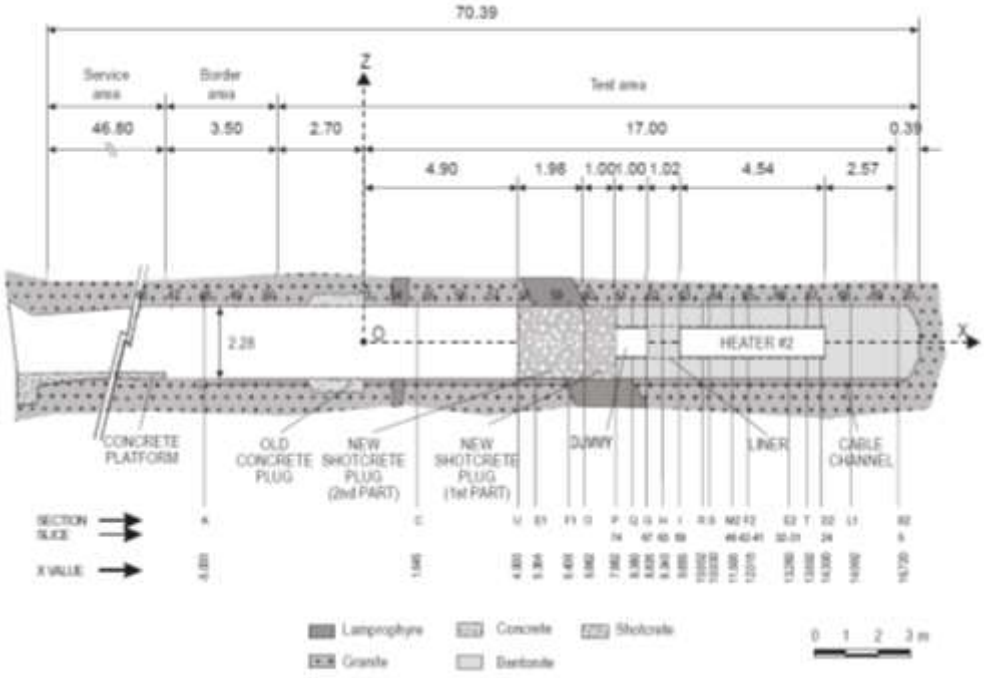

Figure 4-4. *In situ* test configuration following dismantling of heater 1 (Huertas et al., 2005)

After the dismantling of heater #1, the tunnel was plugged with shotcrete (Figure 4-4) and heater #2 was kept working under normal conditions to maintain a constant 100 ^{o}C at the steel liner/bentonite interface. In 2014, considering that changes in the state of bentonite buffer were very slow and it was unlikely for

bentonite to fully reach saturation in the project lifetime, the decision was made to turn off and dismantle heater #2. The objective of the second dismantling operation, carried out throughout 2015, was to dismantle all the remaining parts of the *in situ* test, including heater #2. This operation included carrying out a complete sampling of the bentonite, rock, relevant interfaces, sensors, metallic components and tracers to allow the analysis of the barriers' condition after ~18 years of heating and natural hydration. On April 24, 2015, heater #2 was switched off. After a short cool-off period, dismantling was carried out from the shotcrete towards the bentonite section by sections (see Figure 4-5) and samples were taken for THMC and microbiological characterization. Details about the dismantling of heater #2 are given in Garcia-Sineriz et al. (2016). THM characterization revealed that the bentonite away from the heater is fully saturated, but the bentonite at the vicinity of heater #2 has not been fully saturated yet.

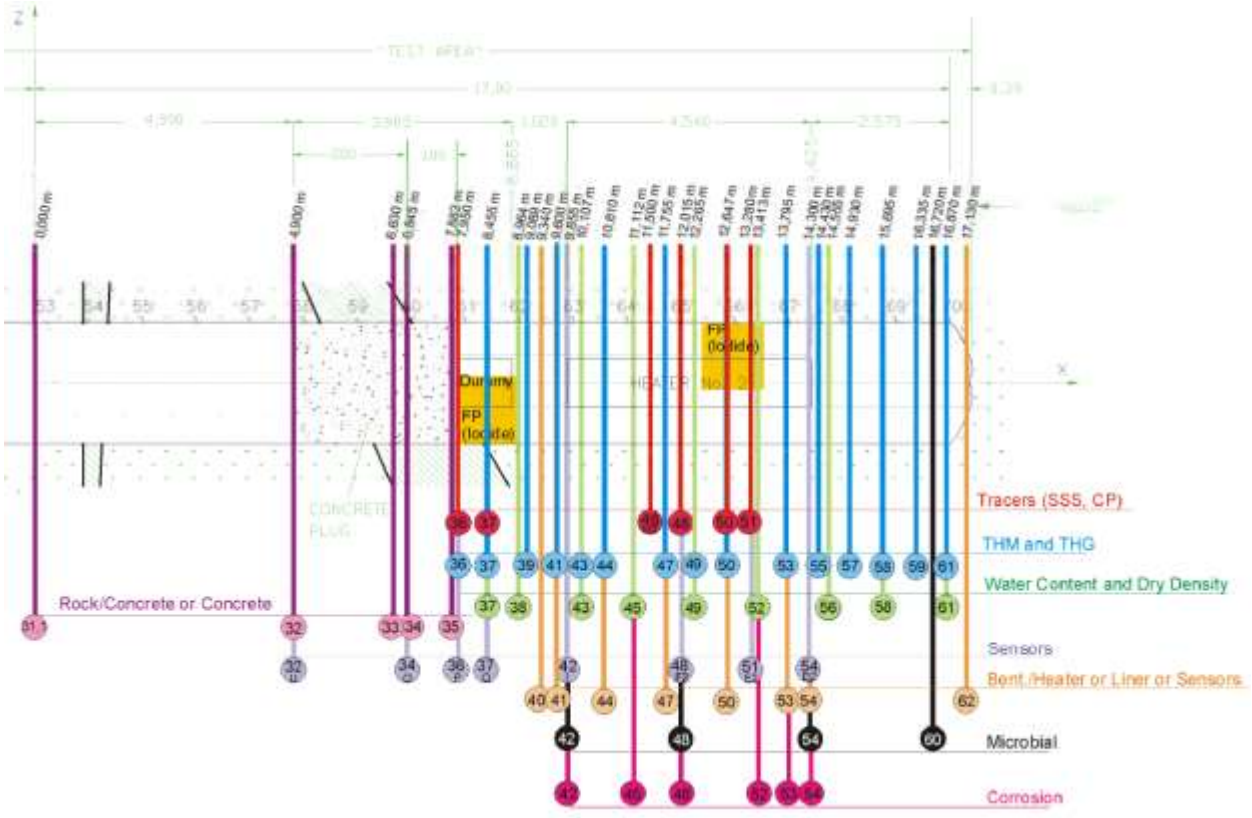

Figure 4-5. Section layout during the dismantling operation of heater #2 (Detzner and Kober, 2015)

The long-term FEBEX *in situ* test with comprehensive THMC data provides a unique opportunity to validate coupled THMC models and strengthen our understanding of coupled processes in bentonite. In addition, experiments at different scales with the same type of bentonite are also very useful to evaluate the key parameters obtained at different scales and study the scaling effect of modeling THMC processes. Up to now, several THM/THC models have been developed to interpret the FEBEX experiments, including the THM model for the mock-up test (Sánchez et al., 2005; 2012a) and *in situ* test (Sánchez et al., 2012b), and THC models for the small scale heating and hydration experiment (Zheng et al., 2010), mock-up test (Zheng and Samper, 2008), and *in situ* tests (Samper et al., 2008a; Zheng et al., 2011; Zheng et al., 2015b).

4.3 Model Development

In FY16, the THMC model was developed and validated against THM data and chemical data at 5.3 years when heater #1 was dismantled in 2002. In FY17, the THMC was further revised such that the model can match all THM data and the concentration profile of chloride at 5.3 years, then the predictions for the concentration profiles at 18.3 years were compared with chemical data obtained from the dismantling of heater #2 in 2015. The THMC model reliably predicts the evolution of conservative chemical species whereas the chemical model needs to be fine-tuned to match the concentration of reactive species. In this section, we briefly present the model setup: more details about the model development can be found in Zheng et al. (2016).

4.3.1 Simulator

The numerical simulations are conducted with TOUGHREACT-FLAC3D, which sequentially couples the multiphase fluid flow and reactive transport simulator, TOUGHREACT (Xu et al., 2011), with the finite-difference geomechanical code FLAC3D (Itasca, 2009). The coupling of TOUGHREACT and FLAC was initially developed by Zheng et al. (2012) to provide the necessary numerical framework for modeling fully coupled THMC processes. It was equipped with a linear elastic swelling model (Zheng et al., 2012; Rutqvist et al., 2013) to account for swelling as a result of changes in saturation and pore-water composition and the abundance of swelling clay (Liu et al., 2013; Zheng et al., 2014). A recent addition to the code is the capability of simulating Non-Darcian flow (Zheng et al. 2015b) and thermal osmosis.

4.3.2 Modeling Setup

Because the hydration of bentonite is fairly symmetrical, we use an axi-symmetrical mesh (Figure 4-6) to save computation time so that we can focus on the key coupling processes. However, such a model can only be used to interpret and predict the THMC behavior in the "hot sections", i.e., sections of bentonite block surrounding the heater including sections 41-54 (or more typically section 49) in Figure 4-5. 3-D models that have both "hot" and "cold" sections (such as sections 55-62 in Figure 4-5) could be developed in the future.

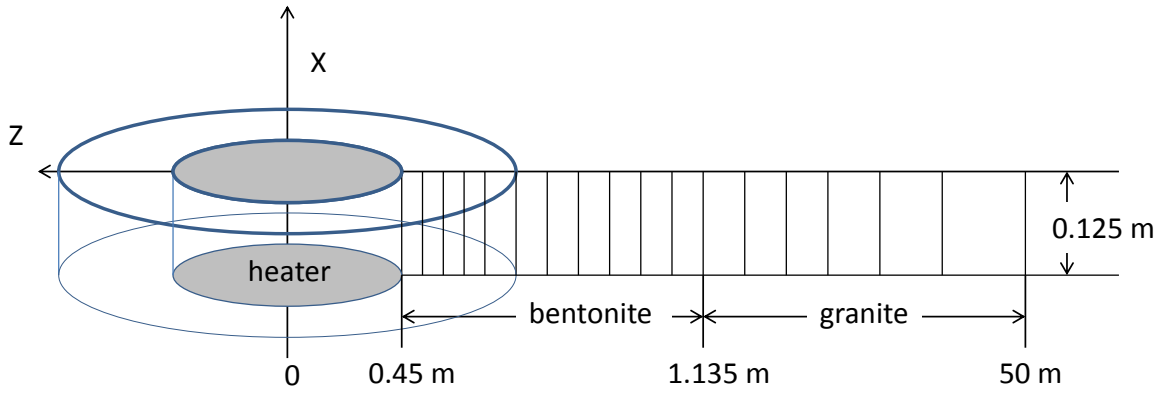

Figure 4-6. Mesh used for the model, not to the scale.

The model considers two material zones for the bentonite and granite. The first two nodes (1 and 2) are located on the external wall of the heater (r = 0.45-0.46 m). Bentonite is located within 0.45 m < r < 1.135 m. The remaining domain up to 50 m is used to simulate the granite. The simulation time starts on February 27, 1997 and ends on July 1, 2015, a total of 6,698 days (18.3 years).

The initial temperature is uniform and equal to 12 ºC. A constant temperature of 100 ºC is prescribed at the heater/bentonite interface (r = 0.45 m) while temperature is assumed to remain constant at its initial value of 12 ºC at the external boundary (r = 50 m) because the thermal perturbation induced by the heaters does not extend to this boundary.

The bentonite has initially a gravimetric water content of 14%, which corresponds to a saturation degree of 55% and a suction of 1.11×10^5 kPa. The boundary conditions for flow include: 1) no flow at r = 0.45 m and 2) a prescribed liquid pressure of 7 bars at r = 50 m.

4.3.3 The TH Model

The model considers non-isothermal two-phase (air and water) flow, with each individual phase fluxes given by a multiphase version of Darcy's Law. For the vapor flow in the air phase, in addition to Darcy flow, mass transport can also occur by diffusion and dispersion according to Fick's law. Thermal behavior is relatively well understood because it is less affected by coupled processes in comparison with hydrological and chemical processes and the relevant parameters can be reliably measured. In current model, both conductive (Fourier's law) and convective heat flux are considered in the model and thermal conductivity is the key parameter.

Because over the span of water saturation that FEBEX bentonite went through (from an initial degree of water saturation 55-59% to 100%), the thermal conductivity/water saturation relationship can sufficiently be represented by a linear relationship; we use a linear relationship implemented in TOUGH2 (Pruess et al., 1999):

$$K_{th} = K_{wet} + S_l(K_{wet} - K_{dry}) \tag{4.1}$$

where K_{wet} is the thermal conductivity under fully saturated conditions, K_{dry} is the thermal conductivity under dry conditions, and S_l is the liquid saturation degree. K_{wet} and K_{dry} are given in Table 4-1.

The key parameters affecting the hydration of bentonite are the permeability of granite, the relative permeability and retention curves of bentonite, the vapor diffusion coefficient and permeability of bentonite. In Zheng et al. (2015b), the most plausible values for these parameters were discussed and illustrated with sensitivity analyses.

Granite is a fractured medium and should ideally be represented by fractures and matrix. Just as previous models for *in situ* tests (Samper et al., 2008a; Sánchez et al., 2012b), the current model also assumes granite is a homogeneous porous medium, which requires us to use an equivalent permeability. Based on the total water flow from tunnel wall at the entire length of test zone (17.4 m, see Figure 4-2) (ENRESA, 2000), the permeability of fractured granite is around 5×10^{-18} to 8×10^{-18} m^2. ENRESA (2000) also reports that the most frequent permeability is 1×10^{-18} but deems it is more representative of rock matrix. Zheng et al. (2011) used 8×10^{-18} m^2, Kuhlman and Gaus (2014) estimated a permeability of 6.8×10^{-19} m^2, and Sánchez et al. (2012b) used a surprisingly small value, 8.18×10^{-21} m^2. Based on the published values, it seems that a permeability value between 7×10^{-19} to 8×10^{-18} m^2 is plausible. Based on the evaluation in Zheng et al. (2015b), a permeability of 2×10^{-18} m^2 is used (Table 4-1).

The capillary pressure (retention curve) is calculated by van Genuchten function as:

$$P_{cap} = -\frac{1}{\alpha}\left(\left[S^*\right]^{-1/m} - 1\right)^{1-m} \tag{4.2}$$

where P_{cap} is the capillary pressure (Pa), $S^* = (S_l - S_{lr})/(1 - S_{lr})$ and S_l is the water saturation, S_{lr} is the residual water saturation. S_{lr} is 0.1 for bentonite and 0.01 for granite. The values of α and m are given in

Table 4-1. The retention curve was fairly well studied for FEBEX bentonite. For example, ENRESA (2000) presented the retention curve for both the drying and wetting path and van Genuchten function (van Genuchten, 1980) were derived with an *m* ranging from 0.3 to 0.6. Kuhlman and Gaus (2014) estimated an *m* of 0.3 and Zheng et al. (2011) and Sánchez et al. (2012b) use an *m* of 0.18, which is slightly lower.

Table 4-1. Thermal and hydrodynamic parameters.

Parameter	Granite	Bentonite
Grain density [kg/m^3]	2700	2780
Porosity ϕ	0.01	0.41
Saturated permeability [m^2]	2.0×10^{-18}	2.15×10^{-21}
Relative permeability, k_{rl}	$k_{rl} = S$	$k_{rl} = S^3$
Van Genuchten $1/\alpha$ [1/Pa]	4.76×10^{-4}	1.1×10^{-8}
Van Genuchten *m*	0.7	0.45
Compressibility, β [1/Pa]	3.2×10^{-9}	5.0×10^{-8}
Thermal expansion coeff. [1/^{o}C]	1.0×10^{-5}	1.5×10^{-4}
Dry specific heat [J/kg-^{o}C]	793	1091
Thermal conductivity [W/m-^{o}C] dry/wet	3.2/3.3	0.47/1.15
Effective vapor diffusion coefficient (m^2/s)	1.03×10^{-4}	1.03×10^{-4}

Note: in the relative permeability function, *S* is water saturation

The effective permeability of bentonite has been under scrutiny by modelers (e.g., Zheng et al., 2011) due to its critical role in determining the hydration of bentonite. It is the product of intrinsic permeability (k) (or saturated permeability, absolute permeability) and relative permeability (k_r). Relative permeability using $k_r=S_l^3$ (where S_l is water saturation degree) has been consistently used by different models (Zheng et al., 2011; Sánchez et al., 2012b; Kuhlman and Gaus, 2014) and we use the same function here. The plausible saturated permeability for FEBEX bentonite in the initial state could range from 1×10^{-21} to 9×10^{-21} m^2 based on various sources (Zheng et al., 2011; Sánchez et al., 2012b; Kuhlman and Gaus, 2014; Chen et al., 2009) and we use 2.15×10^{-21} m^2 in the model. However, as demonstrated by Zheng et al. (2015b), a constant intrinsic permeability for bentonite could not explain the relative humidity data over the entire thickness of the bentonite barrier. The stress-dependence of permeability for low-permeability sedimentary rock is fairly well known and has been studied extensively (e.g., Ghabezloo et al., 2009; Kwon et al., 2001). Many empirical relationships were put forward to describe the permeability changes with effective stress. One of them is the exponential law (David et al., 1994), which is used in the previous model (Zheng et al., 2016):

$$k = k_0 \exp[-\gamma(\sigma - \sigma_0)] \quad 4.3$$

where k is the permeability at the effective stress σ, k_0 is the permeability at initial stress σ_0 and is equal to 2.15E-21 m^2; γ is the stress sensitivity coefficient and equal to 1E-7 Pa^{-1} in the current model based on the calibration against THM data. However, a THMC model using equation 4.3 provided a sufficient fit the THM data (Zheng et al., 2016), but failed to match the chloride concentration profile obtained after the dismantling of heater #1. Eventually, in this report we used an empirical relationship obtained by fitting the permeability-dry density data (ENRESA, 2000) as in equation 4.4:

$$\log k = -2.96\rho_d - 8.57 \quad (4.4)$$

where ρ_d is dry density.

Then a scaling factor was added to equation 4.4, as shown in equation 4.5, such that initial permeability is 2.15×10^{-21} m^2:

$$\log k = (-2.96\rho_d - 8.57)/\alpha \quad (4.5)$$

In addition to revising the constitutive relationship that describes the evolution of saturated permeability, in the THMC developed in FY17, we added another coupled process: thermal osmosis. According to coupled transport phenomena, thermal, hydraulic and chemical gradients all have effects on the heat, liquid and solute fluxes. The direct and coupled phenomena for different transport processes can be described by the Onsager matrix (Table 4-2).

Table 4-2. Direct and coupled flux and phenomena (Horseman et al., 1996; Mitchell, 1993; Soler, 2001)

Flux	Gradient			
	Hydraulic	Temperature	Chemical	Electrical
liquid	Hydraulic flow Darcy's law	Thermo-osmosis	Chemical osmosis	Electro-osmosis
Heat	Convective heat flow	Thermal conduction Fourier's law	Dufour effect	Peltier effect
Solute	Hyperfiltration	Thermal diffusion or Soret effect	Diffusion Fick's law	Electro-phoresis
Electrical current	Rouss effect	Thompson effect	Diffusion and membrane potentials	Electric current Ohm's law

Thermal osmosis is a coupled process that can produce a fluid flux. Zhou et al. (1999) showed that additional coupled flow terms due to a temperature gradient had significant effects on the distribution of capillary pressure and saturation degree in a THM model of a thick cylinder-heating test. The flux of fluid caused by thermal osmosis v_{to} can be written as (Dirksen, 1969):

$$v_{to} = -k_T \nabla T \quad (4.6)$$

where T is temperature and k_T is the thermo-osmotic permeability ($m^2/K/s$). Liquid flux caused by thermal osmosis term can be added to Darcian terms (Ghassemi and Diek, 2002; Zhou et al., 1999). In current model, k_T of 1.2E-12 $m^2/K/s$ is used.

4.3.4 Mechanical Model

In Zheng et al. (2016), we had tested two mechanical models for bentonite: a linear swelling model and dual structure Barcelona expansive clay model (BExM), and found out that both models led to similar fit to measured THM data. Given that BExM is more computationally expensive, in the model presented in this report, we only used the linear swelling model, which is briefly given as follows.

The linear swelling models have been used in the generic model evaluation of bentonite barrier in Zheng et al. (2015a; b). The advantage of this method is its simplicity and easy calibration of key parameters, but the disadvantage is that it does not describe correctly the transient state of swelling. For nonisothermal behavior of unsaturated soils, we may partition the total incremental strain into elastic (ε^e), plastic (ε^p), suction (ε^s), thermal strains (ε^T) and chemical strains (ε^c) (Zheng et al., 2015b):

$$d\varepsilon = d\varepsilon^e + d\varepsilon^p + d\varepsilon^s + d\varepsilon^T + d\varepsilon^c \quad 4.7$$

where the suction strain represents the strain associated with changes in suction and chemical strain represents the strains associated with change in chemical conditions, including changes in ion concentration and abundance of swelling clays.

A linear elastic swelling model essentially defines the suction stress as a function of water saturation:

$$d\varepsilon^s = \beta_{sw} dS_l \quad 4.8$$

where S_l is the water saturation and β_{sw} is a moisture swelling coefficient.

Under mechanically constrained conditions and considering the linear relationship between swelling stress and suction strain, $d\sigma_s = 3Kd\varepsilon^s$, we have a swelling stress that is linearly proportional to the saturation:

$$d\sigma_s = 3K\beta_{sw} dS_l \quad 4.9$$

where K is the bulk modulus. Equation (4.9) is what was used for EBS bentonite in Rutqvist et al. (2011). In this report, β_{sw} is 0.238, calibrated based using the swelling pressure of 5 MPa for FEBEX bentonite under full saturation. The swelling pressure for FEBEX bentonite ranges from 4.5 MPa (Castellanos et al., 2008) to 7 MPa (ENRESA, 2000).

The porosity change in bentonite is given by the following state-surface expression (Lloret and Alonso, 1995):

$$e = A + B\ln\sigma' + C\ln(\psi + p^a) + D\ln\sigma'\ln(\psi + p^a) \quad 4.10$$

where e is the void ratio, which is equal to the volume of voids divided by the volume of the solids; p^a is the atmospheric pressure (Pa), σ' is the mean effective stress (Pa); ψ is the suction (Pa), and A, B, C and

D are empirical constants which for the FEBEX compacted bentonite are equal to A = 0.91, B = - 0.0552, C = - 0.0606413 and D = 0.00479977.

4.3.5 Chemical Model

The establishment of the chemical model requires first the knowledge of initial chemical conditions in bentonite and granite, i.e., the initial mineralogical and pore water compositions. ENRESA (2000) and Fernández et al. (2004) conducted extensive mineralogical characterization. Ramírez et al. (2002) also reported the mineralogical composition of FEBEX bentonite, which is slightly different from that reported by ENRESA (2000). In this report, we take the average of mass fraction reported in ENRESA (2000), Fernández et al. (2004) and Ramírez et al. (2002) and transformed the mass fraction to volume fraction (ratio of the volume for a mineral to the total volume of medium) using a porosity of 0.41 (see Table 4-3). Note the minerals that have zero volume fractions are the secondary minerals that could be formed. Detailed mineralogical composition of granite has not been found in current literature search, probably because the chemical conditions in granite are not supposed to be actively changed by repository conditions. Previous THC models for the *in situ* test (Samper et al., 2008a; Zheng et al., 2011) only include quartz in the mineral assemblage in granite. Siitari-Kauppi et al. (2007) reported that Grimsel granite is composed of quartz, K-feldspar, plagioclase and a small amount of "dark material". In the current model, we consider quartz, K-feldspar, plagioclase in granite with their volume fractions listed in Table 4-3.

Table 4-3. Mineral volume fraction (dimensionless, ratio of the volume for a mineral to the total volume of medium) FEBEX bentonite (ENRESA, 2000; Fernández et al., 2004; Ramírez et al., 2002) and granite (Zheng et al., 2011).

Mineral	FEBEX Bentonite	Granite
Calcite	0.00472	0
Smectite	0.546	0.
Chlorite	0.0024	0
Quartz	0.012	0.37
K-Feldspar	0.0059	0.35
Plagioclase	0	0.27
Dolomite	0.0	0
Illite	0.0	0
Kaolinite	0.0	0
Siderite	0.0	0
Ankerite	0.0	0

FEBEX bentonite blocks have an initial gravimetric water content of 13.5–14% (ENRESA 2000). As described in Bradbury and Baeyens (2003), obtaining the pore-water chemistry of compacted bentonite with such a low water content is difficult. Because the concentration of ions for the initial state of compacted bentonite cannot be measured directly, indirect measurement methods must be used. Squeezing and aqueous extract are the most commonly used methods. Squeezing is a straightforward method — pore-water is squeezed out and concentrations are measured. However, pore water cannot be extracted by squeezing from clay samples with gravimetric water contents less than 20% (Fernández et al. 2001, 2004), which means that squeezing cannot be done for FEBEX bentonite blocks. In an aqueous extract test, a crushed sample is placed in contact with water at a low solid/liquid ratio (ranging from 1:16 to 1:1). After establishing equilibrium, the solid phase is separated and the liquid phase is analyzed

(Fernández et al., 2001). Geochemical modeling was needed to retrieve the aqueous ion concentrations at low water content (Zheng et al., 2008). Therefore, any uncertainties associated with the geochemical models affect the evaluation of initial aqueous concentration levels at low water content (the water content at the initial state). The model presented in this report uses the pore water composition (see Table 4-4) inferred by Fernández et al. (2001) from aqueous extract data. The pore water composition for granite (Table 4-4) is taken from Zheng et al. (2011).

Table 4-4. Pore-water composition (mol/kg water except for pH) of FEBEX bentonite (Fernández et al., 2001) and granite (Zheng et al., 2011).

	EBS Bentonite: FEBEX	**Granite**
pH	7.72	8.35
Cl	1.60E-01	1.31E-05
SO_4^{-2}	3.20E-02	7.86E-05
HCO_3^-	4.1E-04	3.97E-04
Ca^{+2}	2.2E-02	1.81E-04
Mg^{+2}	2.3E-02	1.32E-06
Na^+	1.3E-01	3.76E-04
K^+	1.7E-03	7.80E-06
Fe^{+2}	2.06E-08	2.06E-08
SiO_2(aq)	1.1E-04	6.07E-04
AlO_2^-	1.91E-09	3.89E-08

In the chemical model, we consider aqueous complexation, cation exchange, surface complexation and mineral dissolution/precipitation. Aqueous complexes and their disassociation constants for reactions that are written in terms of the primary species in Table 4-4 are listed in Table 4-5. These thermodynamic data were taken from Data0.dat.YMPv4.0, an EQ3/6 (Wolery, 1993) database qualified by the U.S. Department of Energy for the Yucca Mountain project. Surface protonation reactions are given in Table 4-6 and cation exchange reactions are given in Table 4-7.

Table 4-5. Aqueous complexes and their dissociation constants

Species	Log K (25°C)	Species	Log K (25°C)
OH^-	13.99	$MgHCO_3^+$	-1.03
Al^{+3}	-22.88	$CO_2(aq)$	-6.34
$HAlO_2(aq)$	-6.45	CO_3^{-2}	10.33
$NaAlO_2(aq)$	0.75	$CaCO_3(aq)$	7.01
$AlOH^{+2}$	-17.87	KCl(aq)	1.50
$Al(OH)_2^+$	-12.78	$MgCl^+$	0.14
$Al(OH)_3(aq)$	-6.72	$MgSO_4(aq)$	-2.38
$CaCl^+$	0.70	$NaSO_4^-$	-0.81
$CaCl_2(aq)$	0.65	KSO_4^-	-0.88
$CaSO_4(aq)$	-2.10	$NaHSiO_3(aq)$	8.30
NaCl(aq)	0.78	$CaOH^+$	12.85
$FeCl^+$	0.17	NaOH(aq)	14.15
$FeHCO_3^+$	-2.04	$NaCO_3^-$	9.82
$FeCO_3(aq)$	4.88	$NaHCO_3(aq)$	-0.17
$FeCl_4^{-2}$	1.94	$CaHCO_3^+$	-1.04

Table 4-6. Surface protonation reactions on montmorillonite (Bradbury and Baeyens, 2005)

Surface complexation	Log K
$mon\_sOH_2^+ = mon\ \_sOH + H^+$	-4.5
$mon\_sO^- + H^+ = mon\ \_sOH$	7.9
$mon\_w1OH_2^+ = mon\_w1OH + H^+$	-4.5
$mon\_w1O^- + H^+ = mon\_w1OH$	7.9
$mon\_w2OH_2^+ = mon\_w2OH + H^+$	-6
$mon\_w2O^- + H^+ = mon\_w2OH$	10.5

Table 4-7. Cation exchange reactions on montmorillonite and illite (Bradbury and Baeyens, 2005)

Cation exchange reaction	$K_{Na/M}$
$Na^+ + mon\text{-}H = mon\ \text{-}Na + H^+$	1
$Na^+ + mon\ \text{-}K = mon\ \text{-}Na + K^+$	0.0775
$Na^+ + 0.5\ mon\ \text{-}Ca = mon\ \text{-}Na + 0.5Ca^{+2}$	0.302
$Na^+ + 0.5\ mon\ \text{-}Mg = mon\ \text{-}Na + 0.5Mg^{+2}$	0.302

Table 4-8. Equilibrium constants for mineral precipitation/dissolution at 25 °C

Primary Mineral	log(*K*)	Secondary Mineral	log(*K*)
Calcite	1.85	Siderite	1.543
Smectite-Na	-34.62	Dolomite	2.524
Quartz	-3.75	Ankerite	-1.035
K-feldspar	-22.91	Illite	-47.33
Albite	-20.133	Chlorite	4.298
Anorthite	-19.19	Kaolinite	-39.9

The equilibrium constants for precipitation/dissolution of primary minerals (minerals that are present initially) and secondary minerals are listed in Table 4-8. Note that plagioclase is a solid solution with albite and anorthite as its end members. In the current model, we assume plagioclase contains 10% anorthite and 90% albite so that there is a quasi-equilibrium between pore water and plagioclase.

Mineral dissolution/precipitation is kinetically controlled. The kinetic law for mineral dissolution/precipitation is given in Xu et al. (2011). The kinetic rates and surface areas for the minerals considered in the model were taken mostly from Xu et al. (2006) (Table 4-9). However, the illitization rate (the rate of illite precipitation and smectite dissolution) was calibrated (Liu et al., 2013) based on the measured illite percentage in an illite/smectite (I/S) mixed layer from Kinnekulle bentonite, Sweden (Pusch and Madsen, 1995).

Table 4-9. Kinetic properties for minerals considered in the model (Xu et al., 2006).

Mineral	A (cm^2/g)	Parameters for Kinetic Rate Law							
		Neutral Mechanism		Acid Mechanism			Base Mechanism		
		k_{25} (mol/m^2-s)	E_a (kJ/mol)	k_{25} (mol/m^2-s)	E_a (kJ/mol)	$n(H^+)$	k_{25} (mol/m^2-s)	E_a (kJ/mol)	$n(H^+)$
Quartz	9.8	1.023×10^{-14}	87.7						
K-feldspar	9.8	3.89×10^{-13}	38	8.71×10^{-11}	51.7	0.5	6.31×10^{-12}	94.1	-0.823
Kaolinite	151.6	6.91×10^{-14}	22.2	4.89×10^{-12}	65.9	0.777	8.91×10^{-18}	17.9	-0.472
Illite	1.18×10^{4} (1)	1.66×10^{-13}	105 (2)						
Chlorite	9.8	3.02×10^{-13}	88	7.76×10^{-12}	88	0.5			
Calcite	3.5	1.63×10^{-7}	23.5						
Dolomite	12.9	2.52×10^{-12}	62.76	2.34×10^{-7}	43.54	1			
Ankerite	9.8	1.26×10^{-9}	62.76	6.46×10^{-4}	36.1	0.5			
Smectite - Na	1.18×10^{4} (1)	1.66×10^{-13}	105 (2)						

(1) Calibrated based on the field illitization data (Liu et al., 2013)
(2) From Pusch and Madsen (1995)

4.4 Model Results

The ultimate goal of using coupled THMC model to interpret the data collected in the FEBEX *in situ* test is to understand the THMC evolution of bentonite under simulated repository conditions so that we can use most plausible processes and parameters to describe the behavior of bentonite. Once the coupled THMC model that can simultaneously match the measured temperature, relative humidity, water content, stress, aqueous concentrations, and minerals phase change, we can further use it to predict the long term (e.g., 100,000 years as required by most performance assessment) under different conditions, such as under higher temperature as was done by Zheng et al. (2015a).

Although the THMC models developed in FY16 (Zheng et al., 2016) successfully matched the THM data, they failed to desirably match the measured concentration profile of conservative species (chloride) at 5.3 years and subsequently the concentration profile of reactive species. In FY17, we first revised the THM model such that the THMC model can match THM data and concentration profile of conservative species (chloride) at 5.3 years (dismantling of heater #1), then the THMC model was tested against the chemical data obtained at 18.3 years (the dismantling of heater #2).

4.4.1 Revising the THM Model

In the FEBEX *in situ* test, some data were collected real time by the sensors installed in the bentonite block such as temperature, relative humidity and stress; and some of them had to be measured in the laboratory using the bentonite sample that were taken after dismantling of test sections, including water content, dry density, concentration of ions in pore water and mineralogical composition. Table 4-10 list some key dates of the FEBEX *in situ* test to facilitate the discussion of the model results. The dismantling of heater #1 in 2002 and heater #2 in 2015 provides two snapshots of measured water content, dry density, and concentrations of ions in pore water and mineralogical composition, which are very valuable for understanding the temporal evolution of these key data, as shown later in the report.

Table 4-10. Timeline of FEBEX *in situ* test.

Event	Date	Time (day)	Time (year)
Commencement of heating	2/27/1997	0	0.0
Shutdown of Heat #1	2/2/2002	1827	5.0
Sampling after heat #1 was dismantled	5/2/2002	1930	5.3
Shutdown of heat #2	4/24/2015	6630	18.2
Sampling after heat #2 was dismantled	7/3/2015	6700	18.3

The FY16 THMC model (Zheng et al., 2016) provided a decent match of measured temporal evolution of temperature, relative humidity and stress at several radial distances and measured spatial distribution of water content and dry density at 5.3 and 18.3 years, as shown in Figures 4-7 to 4-16. Considering that the transport of conservative chemical species (e.g., chloride) is largely controlled by water movement, one would expect that the FY16 THMC model should be able to match the concentration profile of chloride. However, as shown in Figure 4-17, the FY16 THMC model overestimates significantly the measured chloride concentration in bentonite near the granite and underestimates the measured chloride concentration near the heater. Therefore, in FY17, two changes were introduced to the THMC model. First, a coupling process, thermal osmosis (see Section 4.3.3 for details) were added to the model, with a calibrated thermal osmotic permeability. Second, the permeability changes as a result of swelling was revised — instead of relating permeability to stress (see equation 4.3), permeability is related to dry density (which is a function of porosity) based on the measured permeability at different dry density (ENRESA, 2000) as in equation 4.5. Both the FY16 model and FY17 model match the measured

temperature very well (Figures 4-7 and 4-9), and the FY17 model provides slightly better matches for the relative humidity data (Figures 4-10 to 4-12) and stress data (Figure 4-15 and 4-16). In terms of water content data, as shown in Figure 4-13, the FY17 model and FY16 model are very similar at 5.3 years and their difference at 18.3 years are within the uncertainties of the data; regarding the dry density data, the FY16 and FY17 model are similar: both of them match adequately the data at 18.3 years. However, the FY17 THMC model outperforms significantly the FY16 THMC model in matching the measured chloride concentration profile at 5.3 years (Figure 4-17). After we tested the FY17 THMC model with THM data and chloride concentration measured at 5.3 years, we tested the model with chemical data collected at 18.3 years, as elaborated in the next sections.

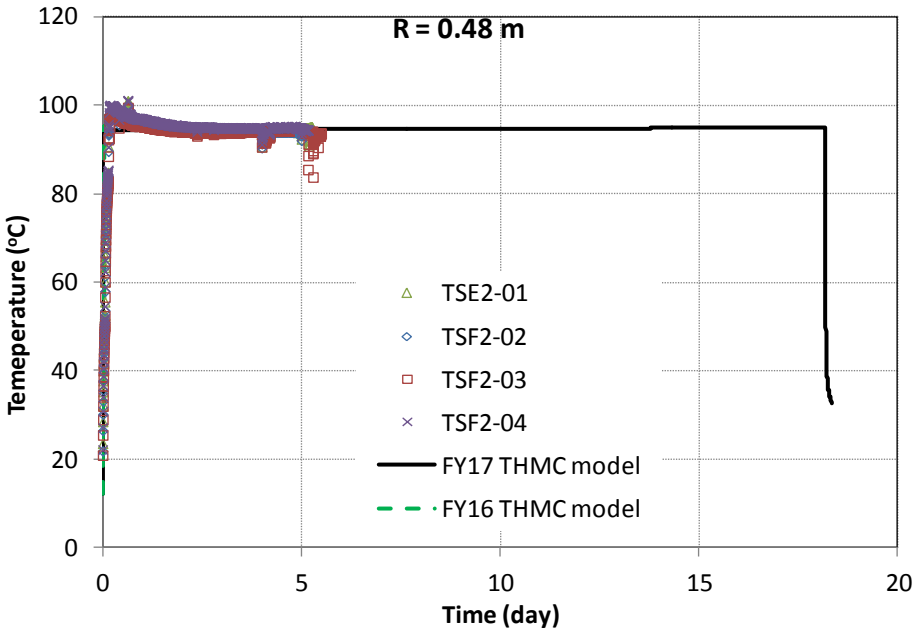

Figure 4-7. Measured temperature by sensors located at a radial distance of 0.48 m in sections E2 and F2 (see Figure 4-2 for their locations) and model results from the FY16 THMC model and FY17 THMC model.

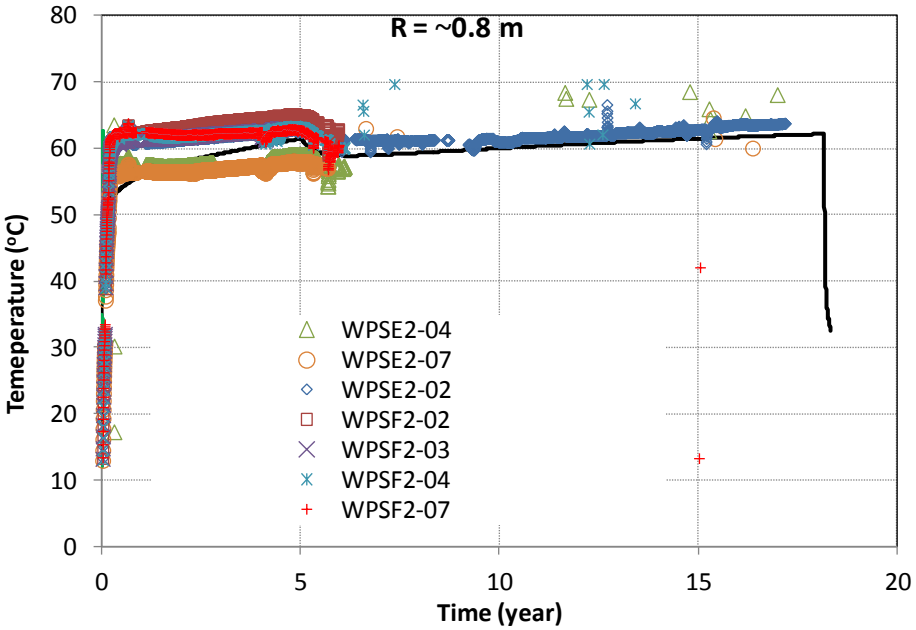

Figure 4-8. Measured temperature by sensors located at a radial distance of 0.8 m in sections E2 and F2 (see Figure 4-2 for their locations) and model results from the FY16 THMC model and FY17 THMC model.

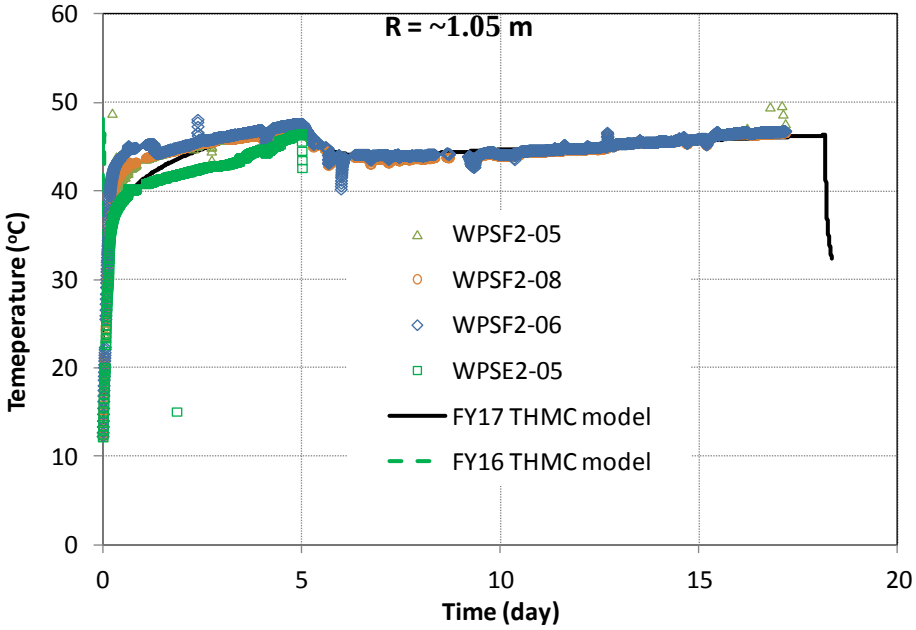

Figure 4-9. Measured temperature by sensors located at a radial distance of 1.05 m in sections E2 and F2 (see Figure 4-2 for their locations) and model results from the FY16 THMC model and FY17 THMC model.

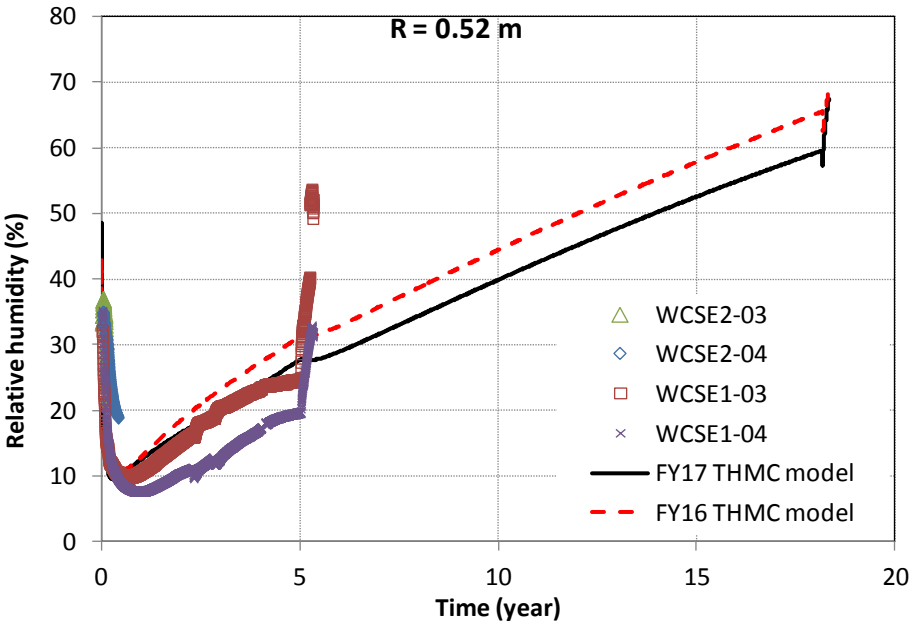

Figure 4-10. Measured relative humidity by sensors located at a radial distance of 0.52 m in sections E2 and E1 (see Figure 4-2 for their locations) and model results from the FY16 THMC model and FY17 THMC model.

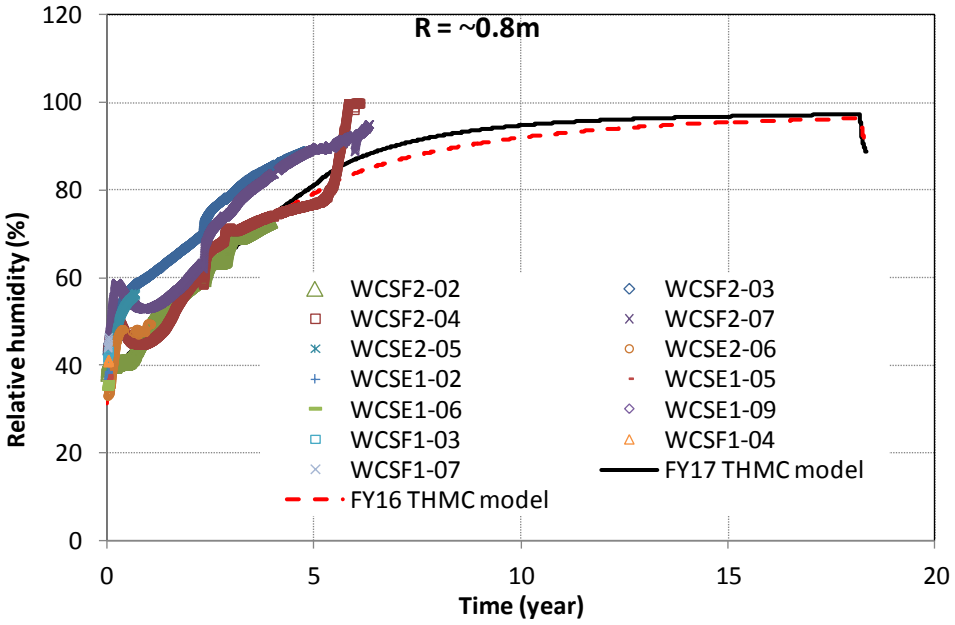

Figure 4-11. Measured relative humidity by sensors located at a radial distance of ~0.8 m in sections E1, E2, F1 and F2 (see Figure 4-2 for their locations)and model results from the FY16 THMC model and FY17 THMC model.

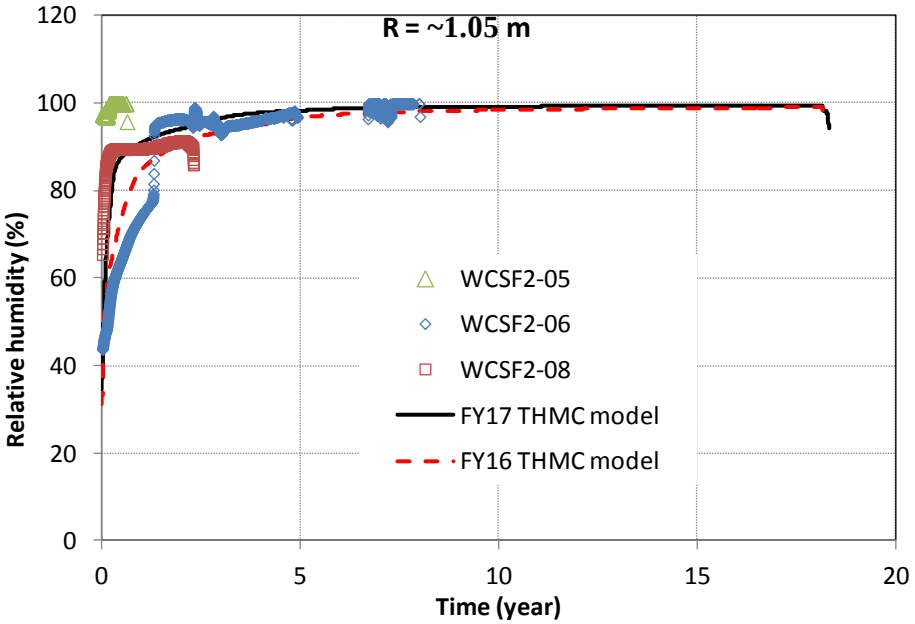

Figure 4-12. Measured relative humidity by sensors located at radial distance of ~1.05 m in section F2 (see Figure 4-2 for their locations) and model results from the FY16 THMC model and FY17 THMC model.

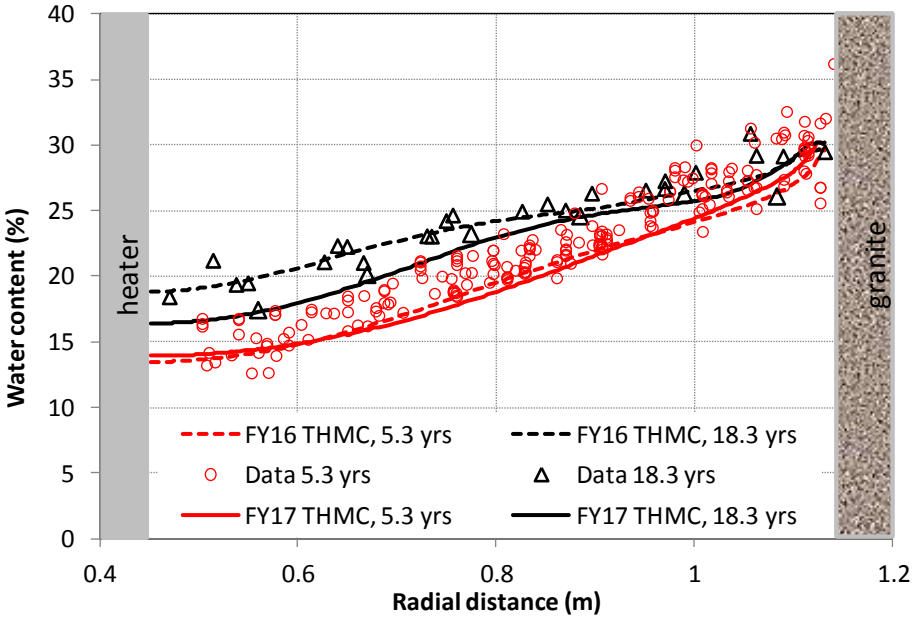

Figure 4-13. Measured water content at 5.3 and 18.3 years, and model results from the FY16 THMC model and FY17 THMC model.

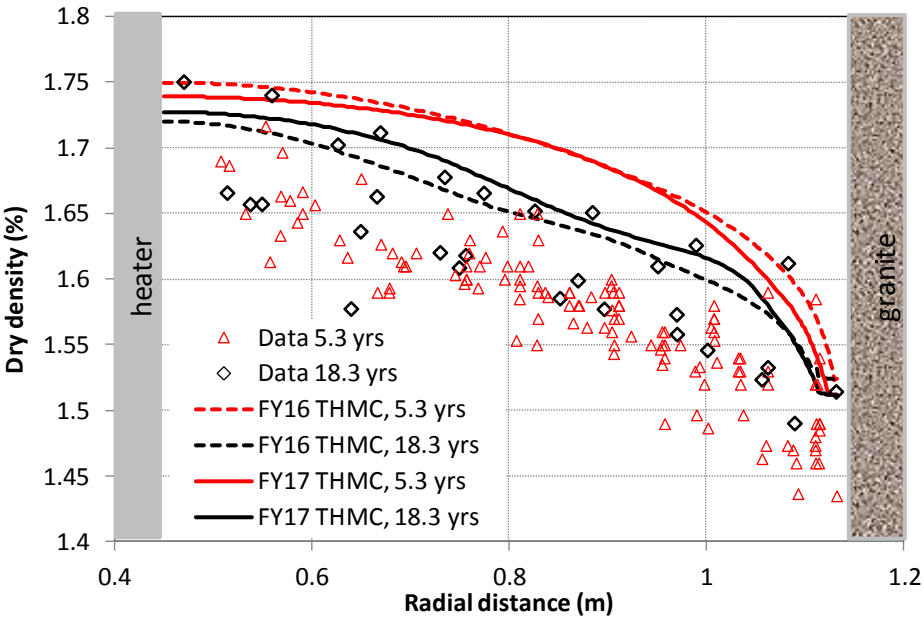

Figure 4-14. Measured dry density at 5.3 and 18.3 years, and model results from the FY16 THMC model and FY17 THMC model.

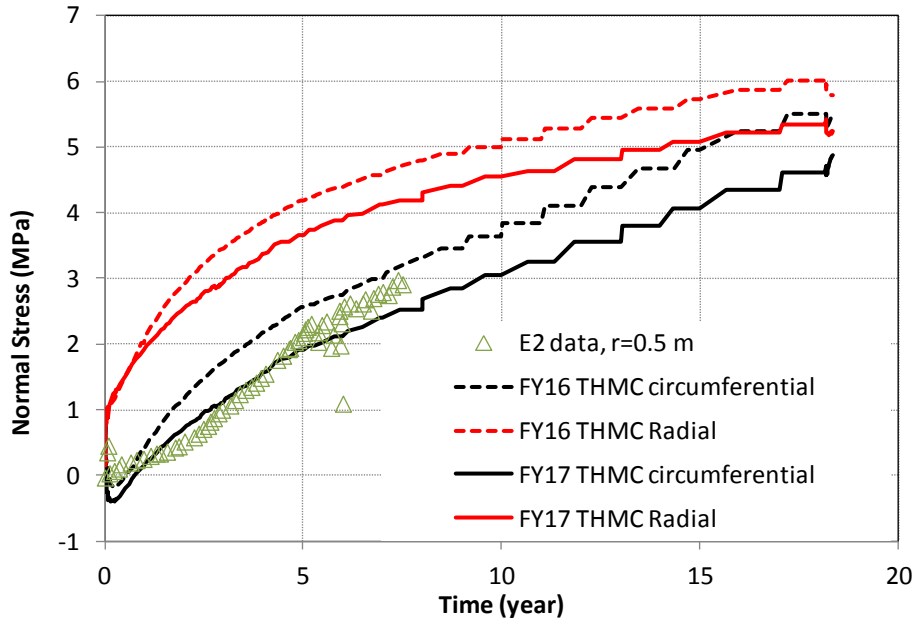

Figure 4-15. Measured stress by sensors located at a radial distance of ~0.5 m in section E2 (see Figure 4-2 for their locations) and model results from the FY16 THMC model and FY17 THMC model.

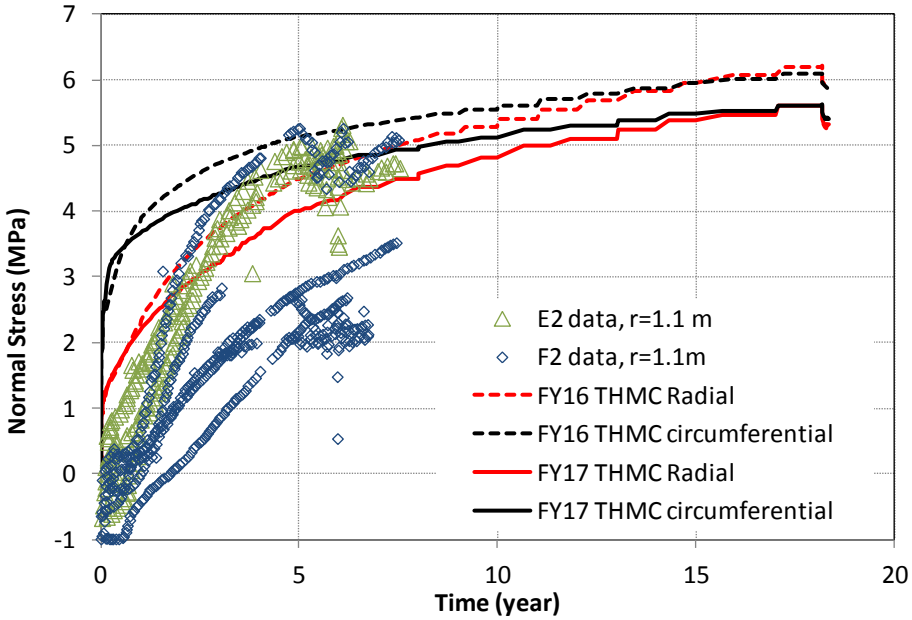

Figure 4-16. Measured stress by sensors located at radial distance of ~1.1 m in sections E2 and F2 (see Figure 4-2 for their locations), and model results from the FY16 THMC model and FY17 THMC model.

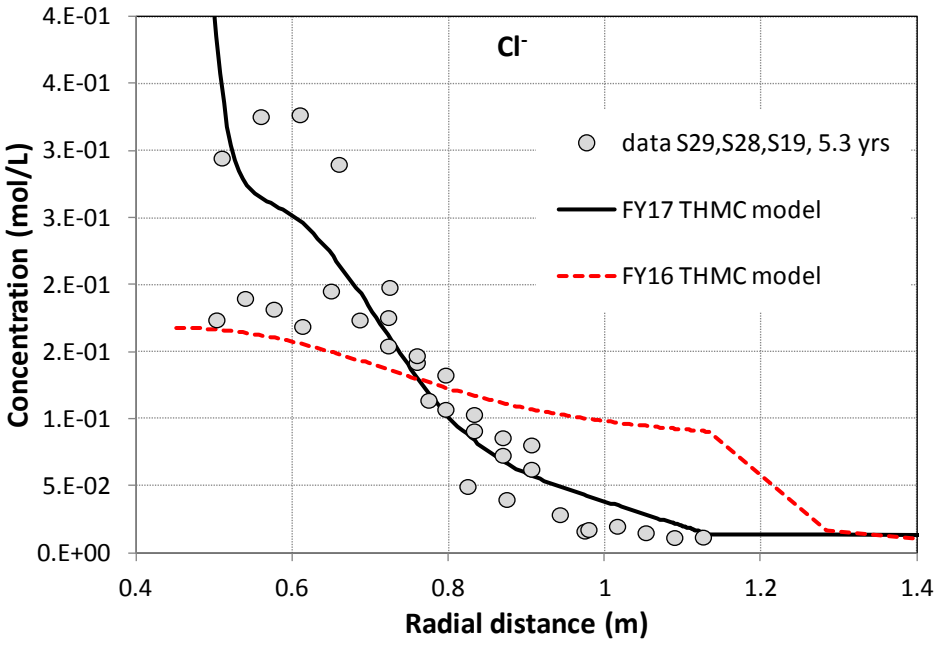

Figure 4-17. Measured chloride concentration at 5.3 years (after dismantling of heater #1) and model results from the FY16 THMC model and FY17 THMC model.

4.4.2 Calibrating Chemical Data

The chemical results from THMC model are primarily tested against data of ion concentrations in pore water. However, such comparison is not straightforward, because pore water concentrations were not measured directly and subsequently calibration is required. The bentonite samples collected after the final dismantling were preserved and pore water concentration were measured by two methods: squeezing and aqueous extract tests (AET).

The squeezing process involves the expulsion of interstitial fluid from the saturated argillaceous material being compressed (Entwisle and Reeder, 1993). In squeezing experiments, the volume of water extracted depends on the water content of the rock sample, the rock properties (e.g., dry density, the relative contents of easily-squeezed clays and of stiffer materials like quartz and calcite), and the experimental conditions, such as, the pressure applied, the duration time of squeezing and size of the squeezing cell (Fernández and Rivas, 2003). Fernández et al. (2017) conducted squeezing test for three samples at section 36, three at section 47 and five at section 59 (see Figure 4-5 for the locations of sections). Because our model only represents the "hot" sections (sections at the around the middle of heater), we will only use the data from section 47, which is shown in Table 4-11. Sample BB-47-7 was taken from out rings of bentonite, with a radial distance from the tunnel axis of 1.02 m, sample BB-47-8 is from the middle ring with a radial distance of 0.79 m and sample BB-47-9 is from the inner rings (near the heater) with radial distance of 0.56 m.

Table 4-11. Chemical composition of the pore water collected from the BB-47-7, BB-47-8 and BB-47-9 bentonite blocks at different pressures (Fernández et al., 2017).

Sample			BB-47-7	BB-47-8	BB-47-8	BB-47-9	BB-47-9
Pressure		MPa	20	30	40	70	85
Extracted water		g	11.2	1.5	4.0	0.58	2.58
Sensoric Parameter Lab							
Color / Turbidity			No	No	No	No	No
Physical-Chemical Parameter Lab							
pH value (20 °C) Lab. (Glove box / lab)	pH		7.9	7.8	7.6	6.8	7.8
Redox potential	Eh (SHE)	mV	n.d.	n.d.	n.d.	n.d.	n.d.
Spec. electr. conductivity (25 °C) Lab.	Cond.	µS/cm					
Alkalinity (pH 4.3) Lab.	Alk.4.3	mmol/L	4.63	2.58	2.53	<5	2.59
Main Ions							
Sodium	Na^+	mg/L	710	2300	1500	4161	3210
Potassium	K^+	mg/L	9.2	24	13	23	23
Calcium	Ca^{2+}	mg/L	32	380	210	1700	2000
Magnesium	Mg^{2+}	mg/L	20	260	150	1400	1000
Chloride	Cl^-	mg/L	481	1600	976	12000	10700
Sulfate	SO_4^{2-}	mg/L	779	4300	2900	2300	1400
Nitrate	NO_3^-	mg/L	1.9	15	8.3	124	114
Nitrite	NO_2^-	mg/L	<d.l.	<d.l.	<d.l.	<0.2	<2
Phosfate	PO_4^{3-}	mg/L	<1	<1	<1	<0.1	<2
Bromide	Br^-	mg/L	1.1	2.5	0.74	12.7	11.9
Fluoride	F^-	mg/L	<d.l.	<d.l.	<d.l.	<1	<2
Thiosulfate	$S_2O_3^{2-}$	mg/L	<0.5	<1	<1	<0.5	20
Trace Compounds							
Aluminium	Al	mg/L	<0.1	<0.3	<0.3	<2.9	<0.3
Silicon	Si	mg/L	23	22	24	15	14
Iron	Fe (II/III)	mg/L	<0.1	<0.3	<0.3	<2.9	<0.3
Strontium	Sr	mg/L	0.59	6.7	4.0	29	30
Copper	Cu	mg/L	0.15	1.4	0.3	<2.9	0.5
Boron	B	mg/L	1.5	1.8	1.3	<2.9	1.4
Manganese	Mn	mg/L	0.15	0.70	0.3	5.6	4.6
Nickel	Ni	mg/L	0.09	0.41	<0.3	<2.9	0.6
Lead	Pb	mg/L	0.18	<0.3	<0.3	<2.9	<0.3
Zinc	Zn	mg/L	0.08	0.59	<0.3	<2.9	<0.3
Organic Parameter							
Total organic carbon	TOC	mg/L	38	--	83	n.d.	n.d.
Acetate	CH_3-COO	mg/L	<0.1	86	45	142	141
Formiate	HCOO	mg/L	0.36	25	12	1.3	13
Oxalate	$(COO)_2^{2-}$	mg/L	--	--	--	17.7	23

AET is a method to quantify the total content of soluble salts of a clay sample. An *1:R* AET consists on adding to a mass M_s of powdered clay sample a mass of distilled water equal to R times M_s. Clay sample and water are stirred during a period of time of usually 2 days during which equilibration of water and clay sample is allowed. Chemical analyses are performed on supernatant solution after phase separation by centrifugation (Sacchi et al., 2001). In addition to dilution, several chemical reactions take place during porewater extraction from clay samples, which change the concentrations of dissolved species in a complex nonlinear manner. This makes it difficult to derive the chemical composition of the original (before aqueous extraction) clay porewater from aqueous extract data (Bradbury and Baeyens, 2003; Sacchi et al. 2001). The inference of dissolved concentration for reactive species requires geochemical modeling based on mineralogical data (Bradbury and Baeyens, 2003; Zheng et al., 2008).

For the sample collected at the final dismantling of FEBEX *in situ* test, Fernández et al. (2017) conducted 1:4 AET for 154 samples, and among them, 36 are for section 47, a "hot" section. The procedure of AET is shown in Figure 4-18. Clearly the concentrations of ions (C_{aq} in Figure 4-18) measured in AET do not represent the pore water concentration. In addition to dilution, chemical reactions also occur, which requires geochemical modeling to re-build the concentration of ions in the original pore water (concentrations (C_{pore}) that corresponds to a sample with original water content θ_i). We therefore develop

a geochemical model to reverse the procedure of AET. In this model, a water+bentonite system with known water content (θ_f) and concentration (C_{aq}) undergoes an "evaporation" and eventually reaches the water content of θ_i (the water content of bentonite sample before conducting AET) and C_{pore} was obtained and will be compared with model results from THMC models.

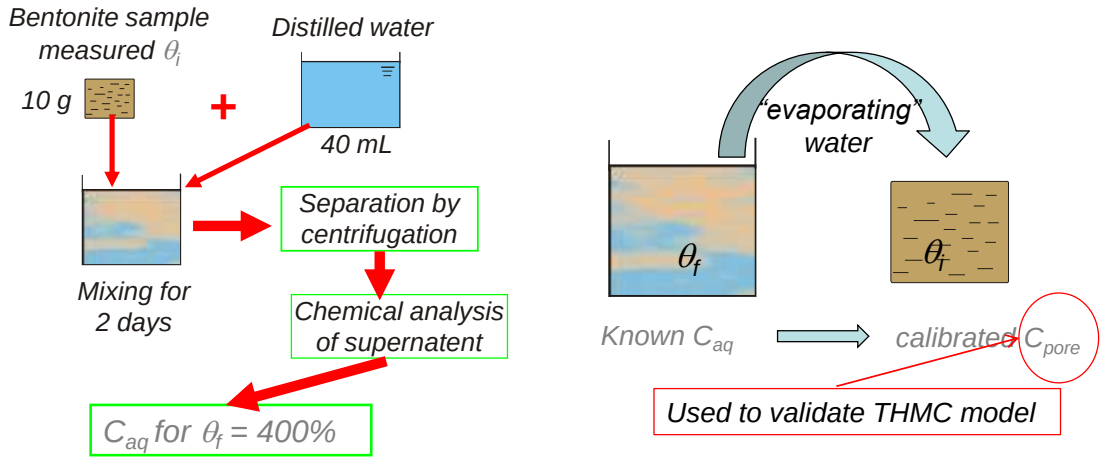

Figure 4-18. The aqueous extract test (AET) procedure (left) used for measuring pore water concentration for samples collected at the final dismantling of FEBEX *in situ* test, and the geochemical model (left) that reverses the AET procedure to calibrate the ion concentration for the original pore water.

The chemical model used to calibrate C_{pore} from C_{aq} is the same as that in the coupled THMC model (Section 4.3.5) except calcite is assumed to be in equilibrium due to the large liquid to solid ratio. The original FEBEX bentonite contains trace amount of calcite. Over the course of heating and hydration, given the high solubility of calcite, we would expect that the pore water is in equilibrium with calcite before AET. Figure 4-19 depicts the saturation index (SI) for calcite after the AET, which shows most samples are close to equilibrium with calcite, with an average SI of 0.04. Therefore, in the model, it is assumed that there is small amount of calcite that can dissolve quickly and the water is maintained at equilibrium with respect to calcite.

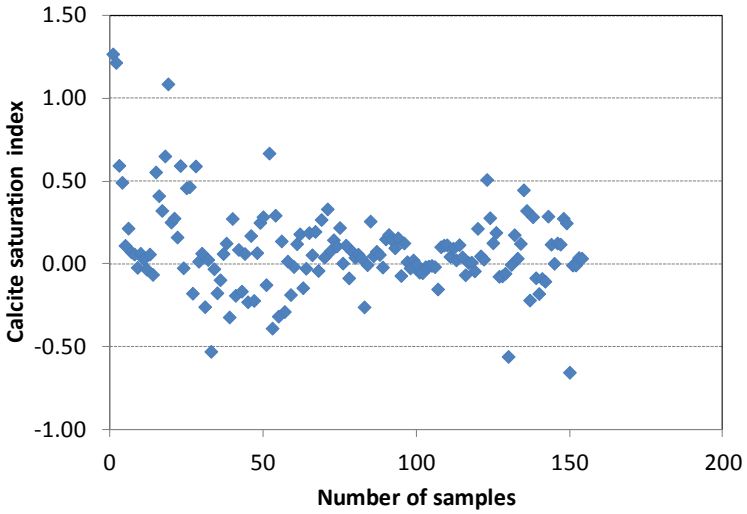

Figure 4-19. Calcite Saturation index calculated based on the concentration of bicarbonate, Ca^{+2}, pH obtained by AET for all the samples.

4.4.3 Testing the Prediction of Ion Concentrations

The THMC model presented in Section 4.4.1 was calibrated based on the chloride concentration data at 5.3 years. In this section, we compare the predicted ion concentrations with the ion concentrations in pore water measured by squeezing and calibrated from AET concentration, to see how the model performs in terms of predicting the concentration evolution in the bentonite barrier. Figure 4-20 show the comparison of calibrated chloride concentration data and model results. The THMC model nicely fit the data near the heater, indicating that the chloride concentration could be fairly high at the canister-bentonite interface. If such trend persists for an extended time period until the canister is fully corroded, high chloride concentration might significantly affect the degradation of waste. As granite water (which has much lower chloride concentration than bentonite pore water) infiltrates into the bentonite, it dilutes the bentonite pore water significantly as shown by the very low chloride concentration near the granite (radial distance between 0.8 and 1.1 m). Meanwhile, bentonite pore water was pushed further near the heater and evaporation causes an increase in chloride concentration, as manifested by the high chloride concentration near the heater.

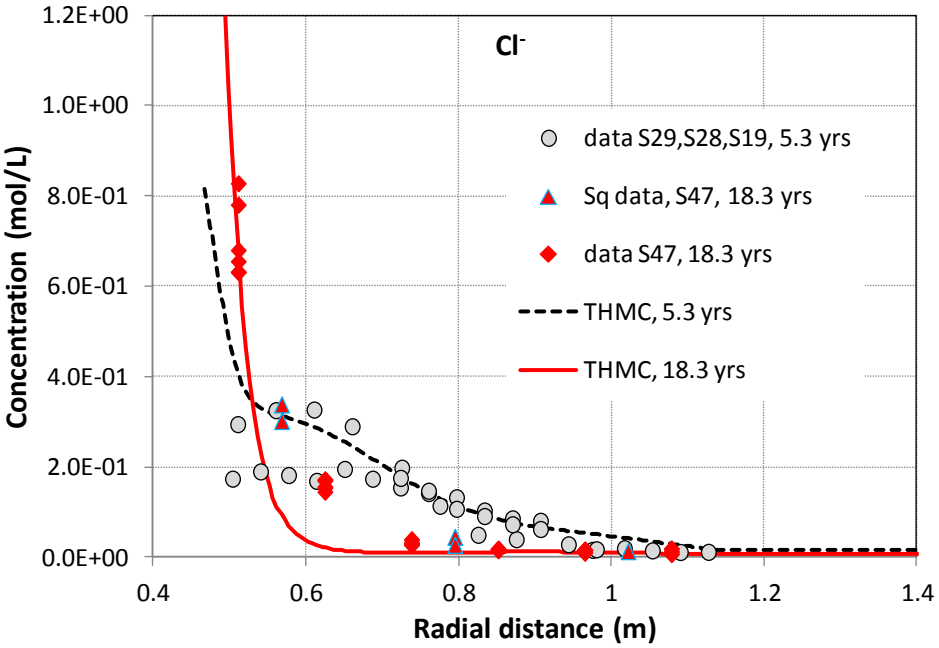

Figure 4-20. Calibrated chloride concentration data at 5.3 years from aqueous extract test for sections 29, 28, and 19 (Zheng et al., 2011), calibrated chloride concentration data at 18.3 years from aqueous extract test for section 47 ("data S47, 18.3 yrs"), chloride concentration data from squeezing test for section 47 ("Sq data, S47, 18.3 yrs") and model results from the THMC model.

Measured sulfate data (Figure 4-21) show a spatial profile that is nothing like that of chloride, indicating chemical reactions dominate the spatial and temporal evolution of sulfate. In current model, the reactions that have been shown to affect significantly sulfate concentration are gypsum dissolution (Figure 4-22) in most parts of the bentonite barrier and gypsum precipitation in a small area near the heater. The original FEBEX bentonite contains small amount of gypsum, because of the high solubility of gypsum, gypsum dissolves as soon as granite water arrives, which raise the concentration of sulfate. Later as more granite water infiltrates into bentonite, dilution leads decrease in sulfate concentration and apparently bentonite in the area near the granite undergoes more dilution and has lower concentration. The simulated concentration profiles at 5.3 and 18.3 years are basically a reflection of these processes. Apparently, the model results cannot match the measured data, especially the data at 18.3 years. As we are synthesizing the measured pore water concentration, gas, biological and mineralogical data, a better match between the sulfate data and model results is expected after current chemical model is refined. The possible reactions that could affect sulfate concentration are pyrite oxidation at the early stage of the *in situ* test and sulfate reduction when the bentonite become more reducing at the latter stage of the test.

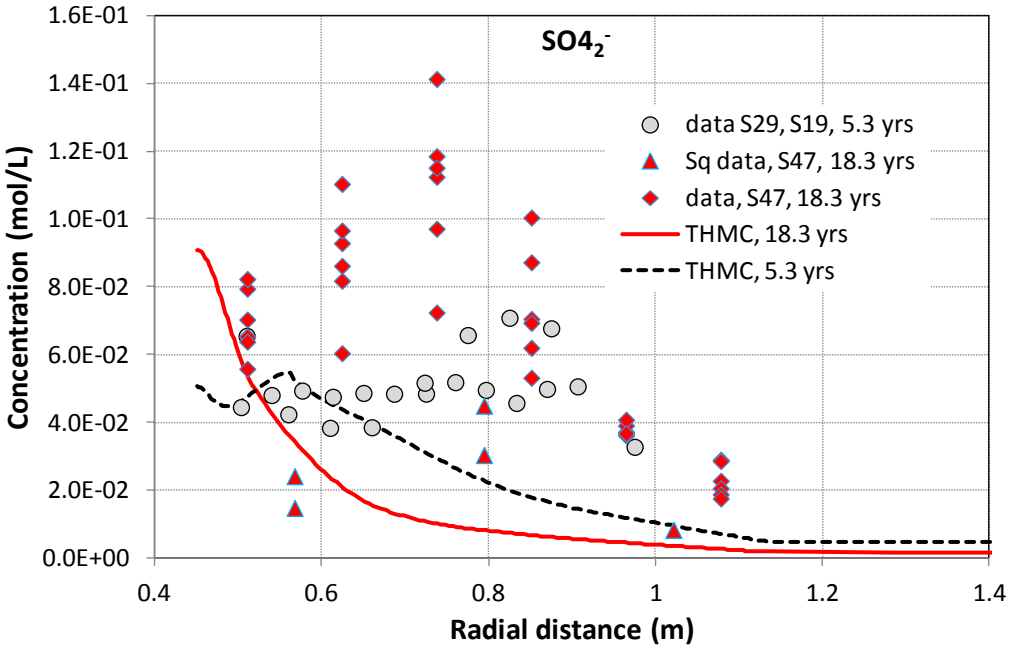

Figure 4-21. Calibrated sulfate concentration data at 5.3 years from aqueous extract test for sections 29, 28, and 19 (Zheng et al., 2011), calibrated chloride concentration data at 18.3 years from aqueous extract test for section 47 ("data S47, 18.3 yrs"), sulfate concentration data from squeezing test for section 47 ("Sq data, S47, 18.3 yrs") and model results from the THMC model.

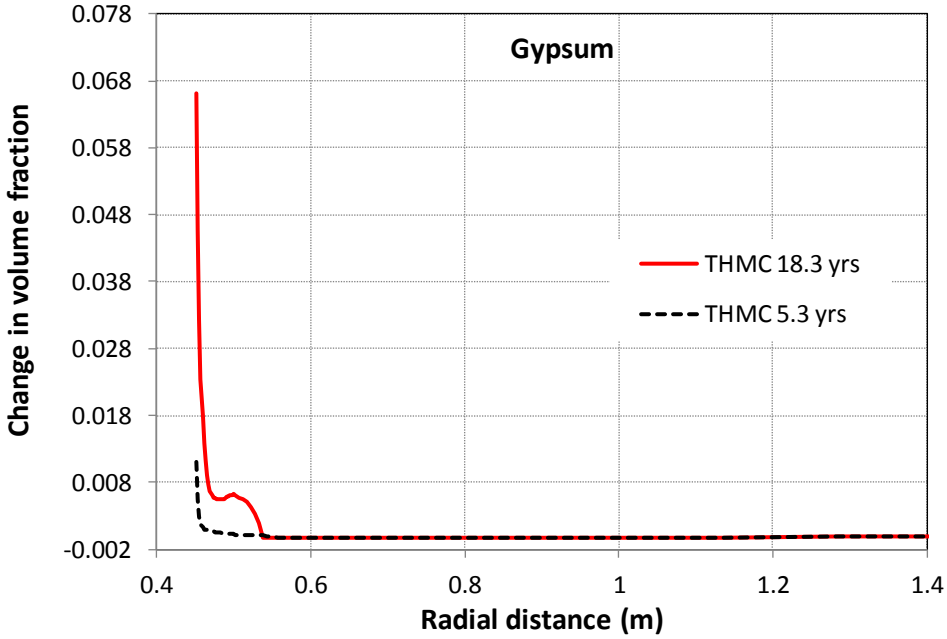

Figure 4-22. Model results of gypsum volume fraction change at 5.3 and 18.3 years. Negative value means dissolution and positive value means precipitation.

It was discovered in previous modeling (e.g., Zheng et al., 2011; Zheng et al., 2015a) that pH is buffered by surface protonation and maintained at the initial level. As shown in Figure 4-23, from 5.3 years to 18.3 years, pH does not change significantly. The spatial profile of pH is also fairly flat, except that in the area near granite the pH is slightly higher due to infiltration of granite water, which has higher pH. The current model confirms that surface protonation buffers pH. Because many other reactions affect pH, it remains to be seen whether the surface protonation will continue dominating pH when the chemical model is refined by adding redox reactions, pyrite dissolution/precipitation and gas evolution.

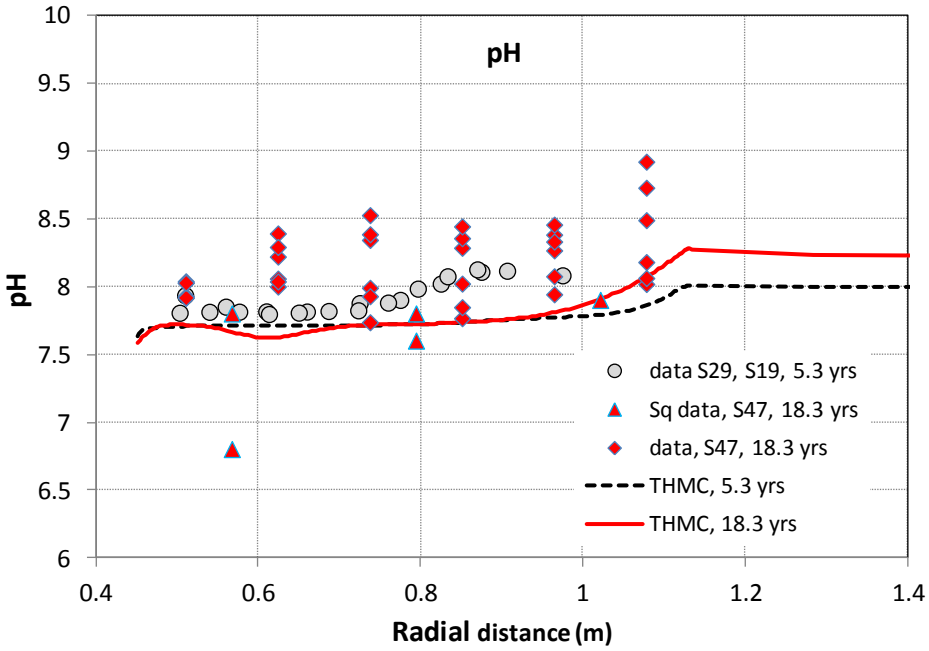

Figure 4-23. Calibrated pH data at 5.3 years from aqueous extract test for sections 29, 28, and 19 (Zheng et al., 2011), pH data at 18.3 years from aqueous extract test for section 47 ("data S47, 18.3 yrs"), pH data from squeezing test for section 47 ("Sq data, S47, 18.3 yrs") and model results from the THMC model.

Bicarbonate concentration data have been very difficult to match by modeling because of the uncertainties in both the CO_2 gas evolution in the bentonite barrier in the *in situ* test, and the calibration of bicarbonate concentration data from aqueous extract. To correctly account for the CO_2 gas evolution, we need consider both the inorganic reactions (e.g., gas dissolution and mineral precipitation) and organic reactions, i.e., bacteria-mediated reaction. Unless we have all the reactions in place, it will be very difficult to match bicarbonate data.

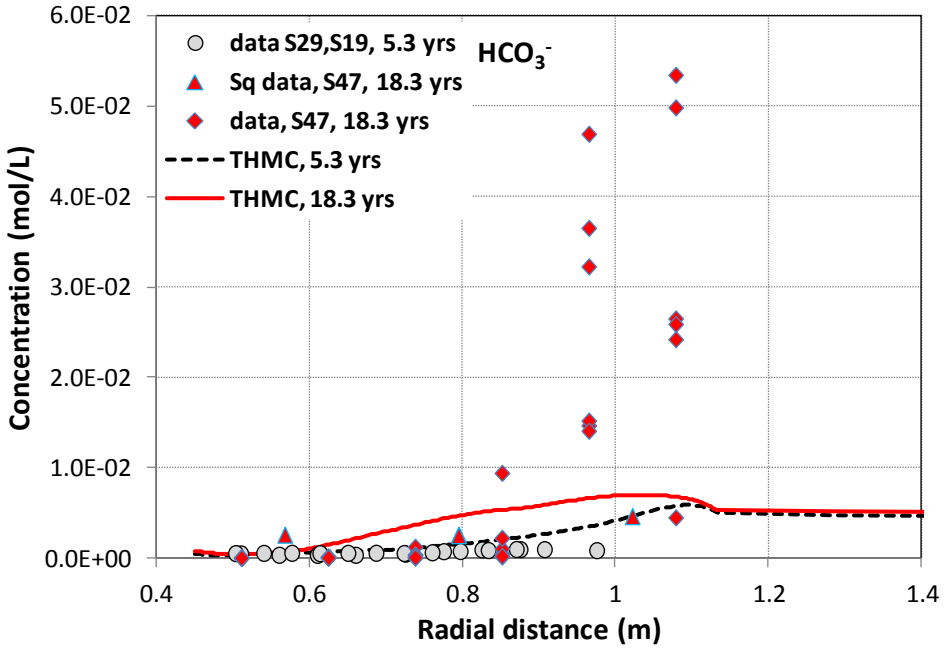

Figure 4-24. Calibrated bicarbonate concentration data at 5.3 years from aqueous extract test for sections 29, 28, and 19 (Zheng et al., 2011), calibrated bicarbonate concentration data at 18.3 years from aqueous extract test for section 47 ("data S47, 18.3 yrs"), bicarbonate concentration data from squeezing test for section 47 ("Sq data, S47, 18.3 yrs") and model results from the THMC model.

Sodium concentration in the bentonite barrier goes through similar transport processes that control chloride concentration profiles in bentonite, which leads to higher sodium concentrations near the heater and lower concentrations near the granite. However, chemical reactions, especially cation exchange, mitigate the concentration change such that the concentration of sodium is not as low as that of chloride near the granite and not as high as that of chloride near the heater. Higher sodium concentration in pore water near the heater drives more sodium to go to the exchangeable sites and therefore exchangeable sodium concentrations increase near the heater, as shown by the model results in Figure 4-25. However, measured exchangeable sodium concentrations at 18.3 years show the opposite: a decreasing trend near the heater. One plausible reason is related to the measuring procedure of exchangeable cations — as minerals precipitate near the heater, for the same amount of solid, the relative mass fraction of clay minerals is smaller comparing with bentonite samples collected far away from the heater, which make the exchangeable cations per unit mass of solid lower.

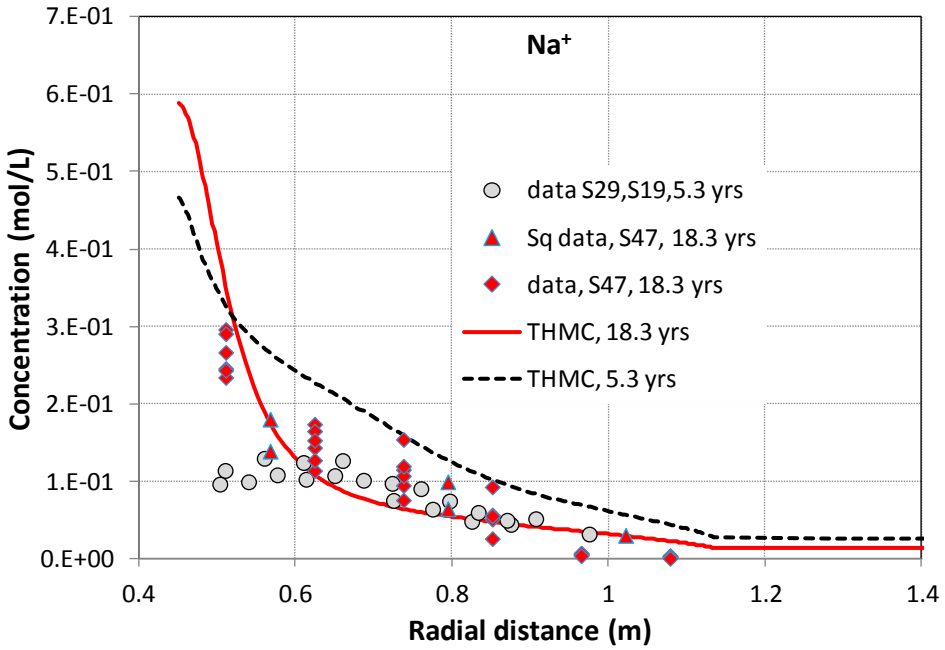

Figure 4-25. Calibrated sodium concentration data at 5.3 years from aqueous extract test for sections 29, 28, and 19 (Zheng et al., 2011), calibrated sodium concentration data at 18.3 years from aqueous extract test for section 47 ("data S47, 18.3 yrs"), sodium concentration data from squeezing test for section 47 ("Sq data, S47, 18.3 yrs") and model results from the THMC model.

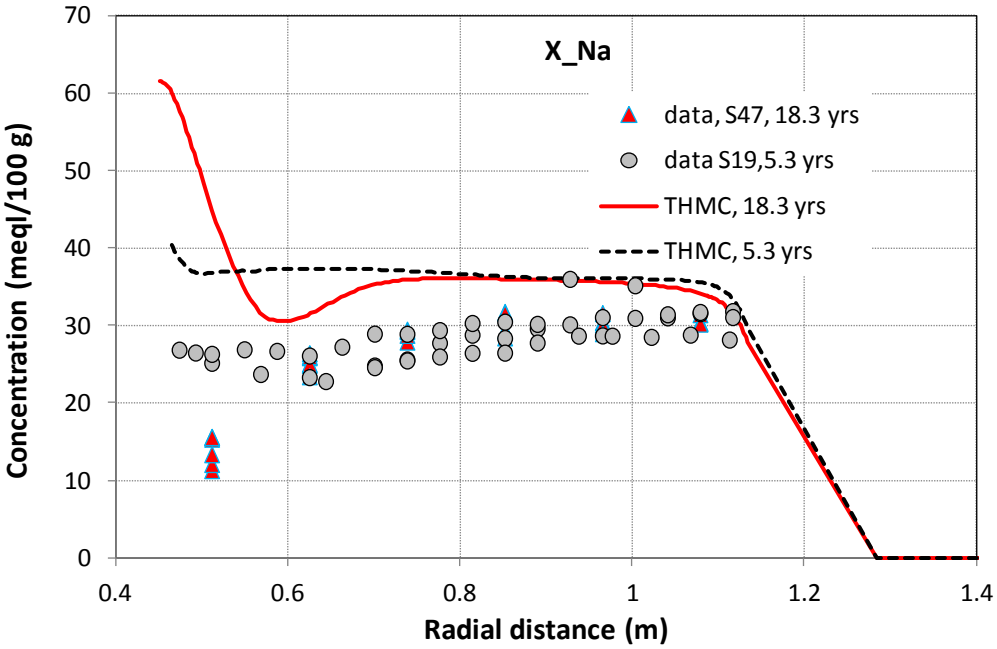

Figure 4-26. Exchangeable sodium (X_Na) concentration data at 5.3 years for section 19 ("data S19, 5.3 yrs"), and at 18.3 years for section 47 ("data S47, 18.3 yrs"), and model results from the THMC model.

A reliable prediction of the evolution of potassium concentration is important because potassium is critical for illitization, which is one of the major concerns of the bentonite barrier. The FEBEX *in situ* test, the longest field test, provides a great opportunity to learn about the evolution of potassium concentration. Current THMC model reproduce reasonably the concentration data at 5.3 years and 18.3 years (Figure 4-27). Modeling work shows that, in addition to the transport processes, cation exchange (Figure 4-28) is the most important reaction that regulates the temporal and spatial distribution of potassium. Models show that by the end of test (18.3 years), illite precipitates in the area from the middle of bentonite barrier to the bentonite-granite interface, and dissolves around the area near the heater (Figure 4-29). Lower aluminum concentration (Figure 4-30) near the heater is the reason that illite dissolves (based on modeling results), which in turn raises the concentration of potassium near the heater. Note that aluminum concentration is too low to be detected and therefore has not been reported.

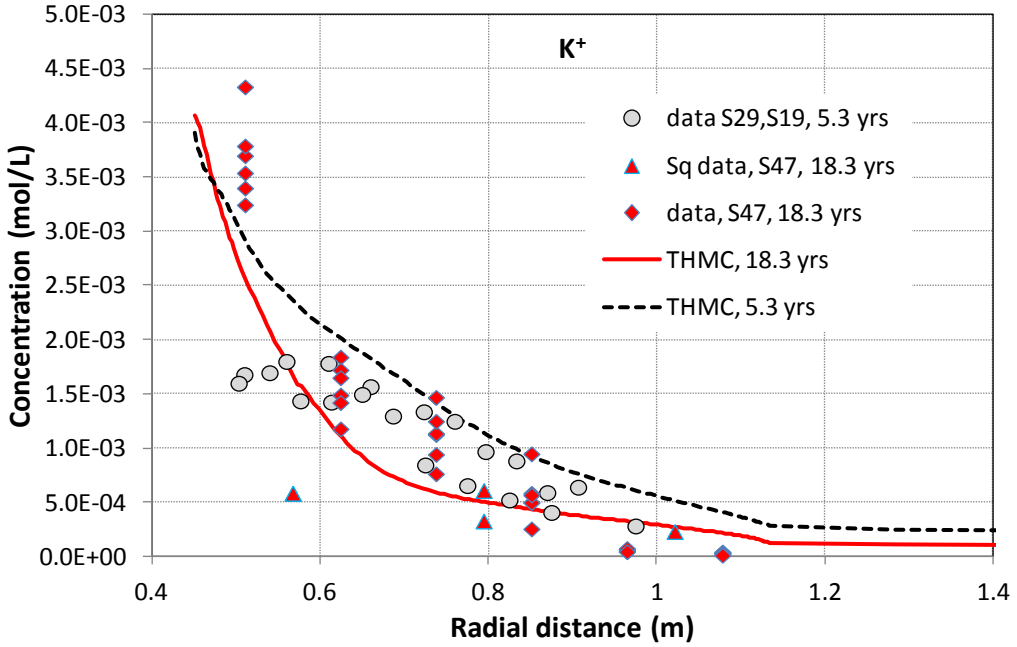

Figure 4-27. Calibrated potassium concentration data at 5.3 years from aqueous extract test for sections 29, 28, and 19 (Zheng et al., 2011), calibrated potassium concentration data at 18.3 years from aqueous extract test for section 47 ("data S47, 18.3 yrs"), potassium concentration data from squeezing test for section 47 ("Sq data, S47, 18.3 yrs") and model results from the THMC model.

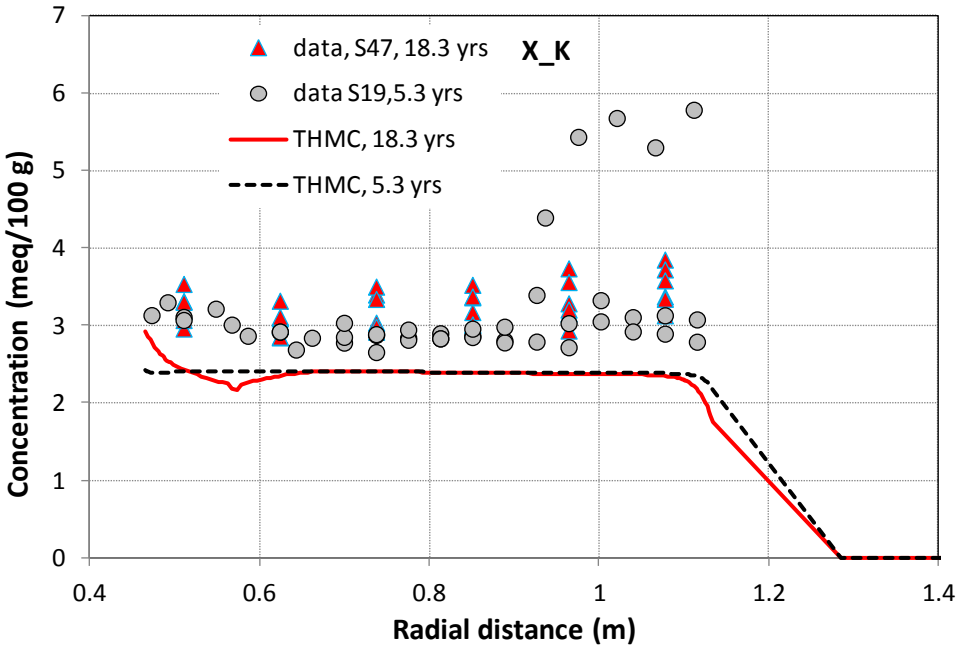

Figure 4-28. Exchangeable potassium (X_K) concentration data at 5.3 years for section 19 ("data S19, 5.3 yrs"), and at 18.3 years for section 47 ("data S47, 18.3 yrs"), and model results from the THMC model.

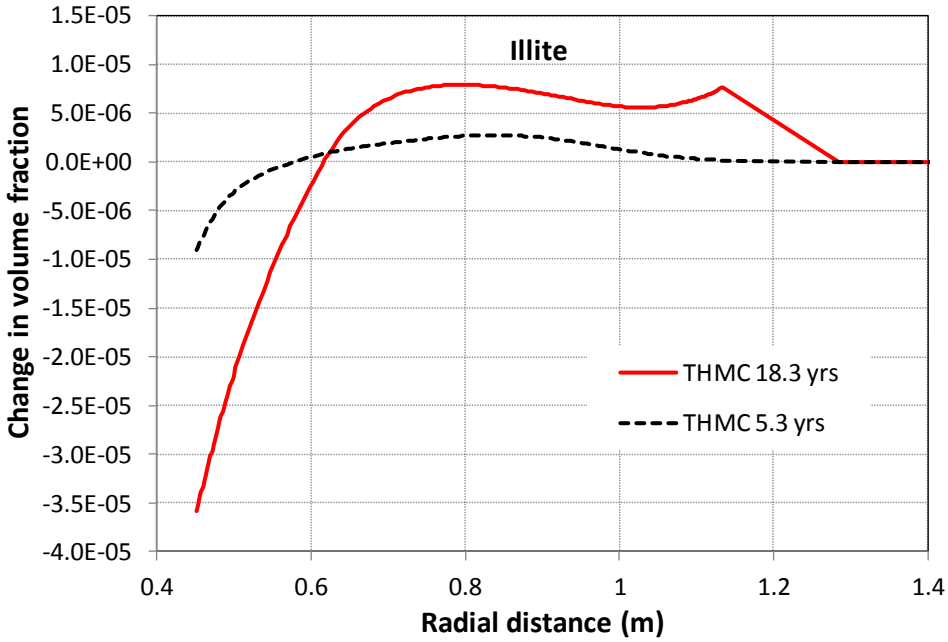

Figure 4-29. Model results of illite volume fraction change at 5.3 and 18.3 years. Negative value means dissolution and positive value means precipitation.

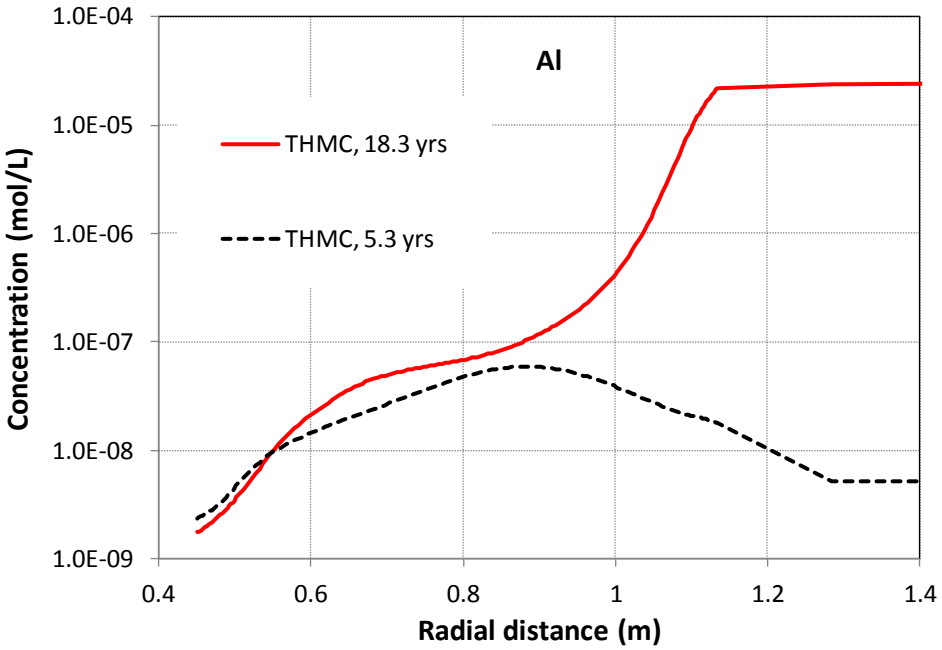

Figure 4-30. Model results of aluminum at 5.3 and 18.3 years.

The relevance of calcium evolution in the bentonite to the performance of the bentonite barrier lies in its interference of pH through dissolution/precipitation of carbonate minerals such as calcite, dolomite, and its impact on redox conditions via gypsum dissolution and sulfate reduction. The current model matches well the calcium data at 5.3 years but falls short of matching calcium data at 18.3 years (Figure 4-31). The reason could be either that initially there is more gypsum present in the bentonite, or calcite dissolves more than the current model predicts (see Figure 4-33 for the volume fraction change of calcite). Exchangeable calcium data are quite scattered at 5.3 and 18.3 years; a communication with a FEBEX-DP partner who measured Cation Exchange Capacity (CEC) and exchangeable cations indicates that exchangeable cations data are less reliable to be used to constrain the chemical model because of the measuring procedure of exchangeable cations.

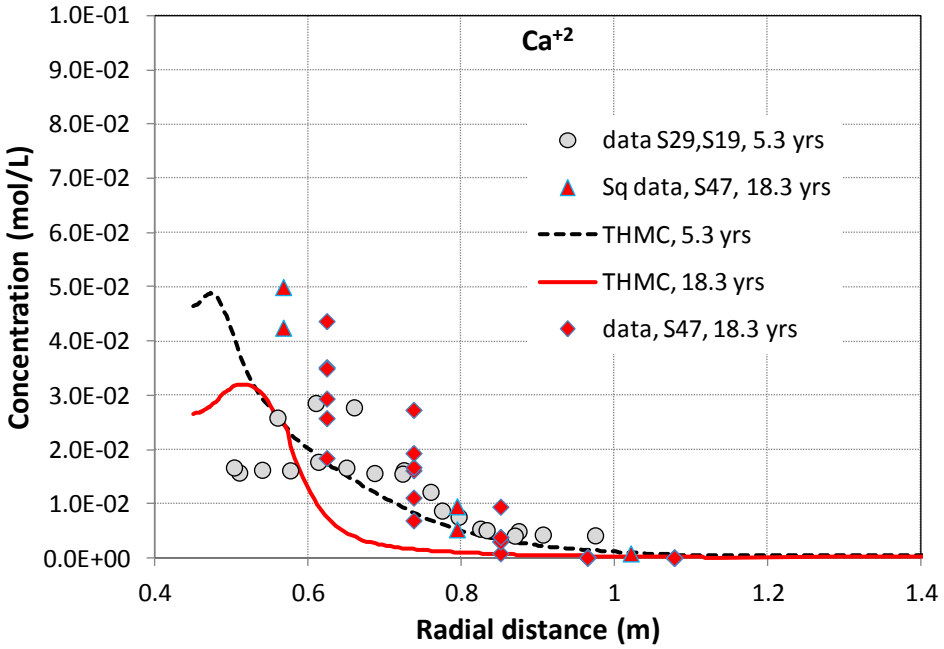

Figure 4-31. Calibrated calcium concentration data at 5.3 years from aqueous extract test for sections 29, 28, and 19 (Zheng et al., 2011), calibrated calcium concentration data at 18.3 years from aqueous extract test for section 47 ("data S47, 18.3 yrs"), calcium concentration data from squeezing test for section 47 ("Sq data, S47, 18.3 yrs") and model results from the THMC model.

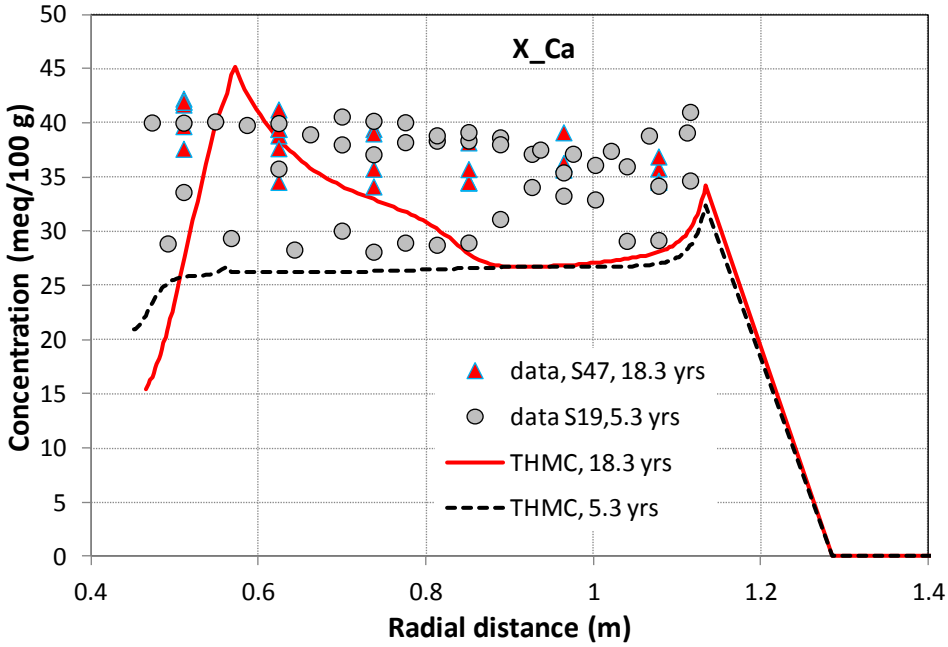

Figure 4-32. Exchangeable calcium (X_Ca) concentration data at 5.3 years for section 19 ("data S19, 5.3 yrs"), and at 18.3 years for section 47 ("data S47, 18.3 yrs"), and model results from the THMC model.

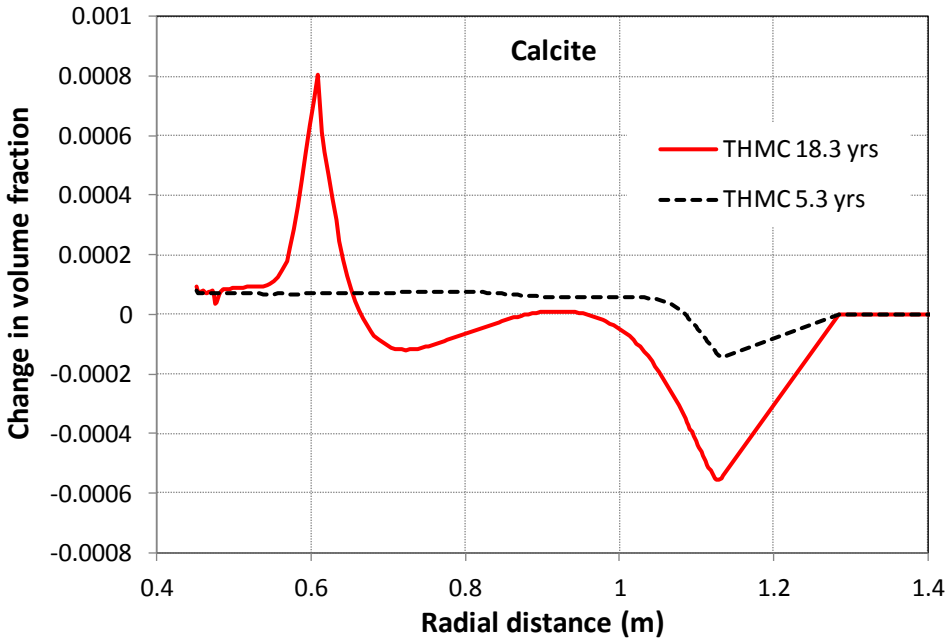

Figure 4-33. Model results of calcite volume fraction change at 5.3 and 18.3 years. Negative value means dissolution and positive value means precipitation.

The current THMC model matches decently the magnesium data at 5.3 years, but underestimates data at 18.3 years (Figure 4-34), and as a result, the model underestimates the exchangeable magnesium data as well (Figure 4-35). Further refinement of the current chemical model is needed to better understand the evolution of magnesium.

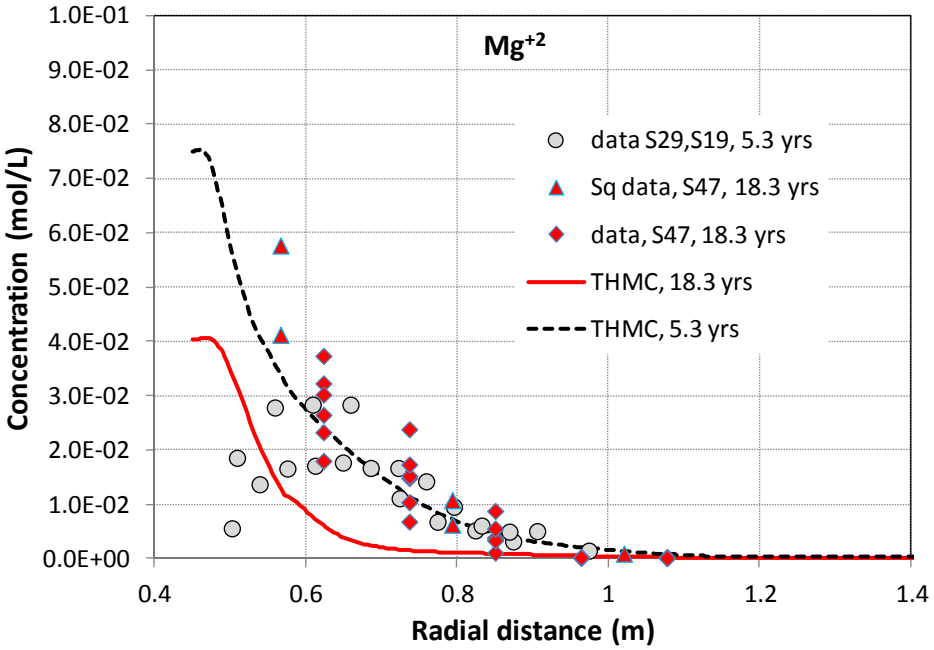

Figure 4-34. Calibrated magnesium concentration data at 5.3 years from aqueous extract test for sections 29, 28, and 19 (Zheng et al., 2011), calibrated chloride concentration data at 18.3 years from aqueous extract test for section 47 ("data S47, 18.3 yrs"), chloride concentration data from squeezing test for section 47 ("Sq data, S47, 18.3 yrs") and model results from the THMC model.

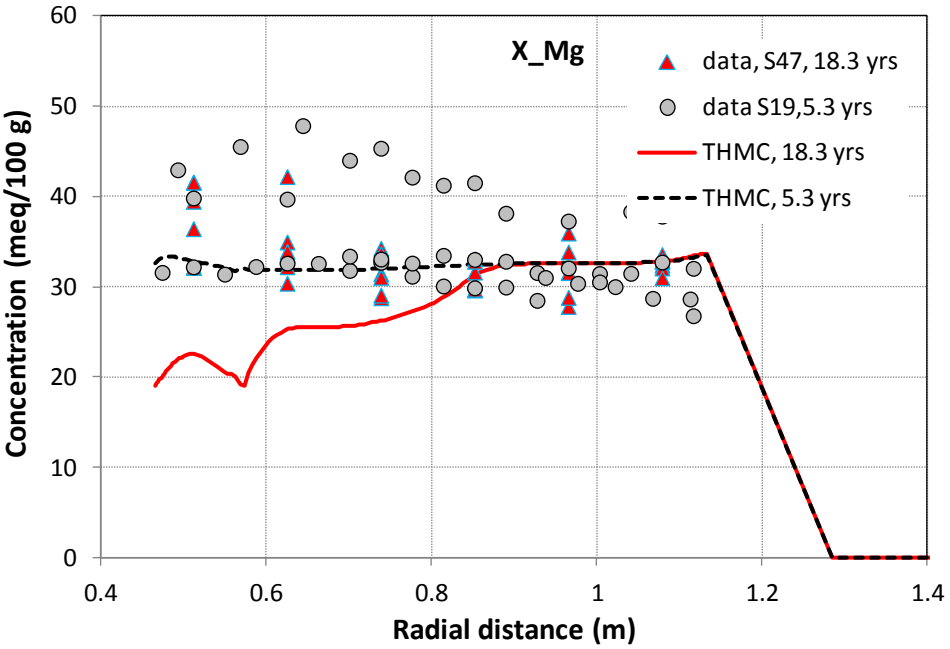

Figure 4-35. Exchangeable magnesium (X_Mg) concentration data at 5.3 years for section 19 ("data S19, 5.3 yrs"), and at 18.3 years for section 47 ("data S47, 18.3 yrs"), and model results from the THMC model.

In summary, the THMC model that was calibrated based on THM data and chloride concentration at 5.3 years predicts nicely the chloride concentration at 18.3 years. It also matches decently the concentration data of sodium, potassium and pH. However, the model falls short of explaining the concentration of sulfate, bicarbonate, calcium and magnesium. The chemical part of the THMC model is far from being complete and accurate enough to explain the evolution of all chemical components. The concentration of a reactive species is one chain of a complex reaction network that is encountered in the FEBEX *in situ* test. Unless all the pieces of the reaction network are assembled together, it is not possible to match all the chemical data sufficiently. After more chemical data, including gas phase (CO_2, O_2, CH_4 and H_2), bentonite-canister interaction, biological and mineralogical change in bentonite, and ion concentrations and mineralogical characterization of granite, are available in the near future, a synthesis of all these data will be carried out to establish a reaction network that can explain all the chemical data, which will lay a strong foundation to predict the long term chemical evolution in the bentonite barrier.

4.5 Examination of the Structure of Bentonite Using Synchrotron X-Ray MicroCT Experiments

4.5.1 Introduction

In a radioactive waste repository with bentonite-backfilled engineered barrier systems, the bentonite barrier undergoes simultaneously heating and hydration. The hydration leads to swelling, which helps the bentonite to seal gaps and pre-existing micro-fractures. On the other hand, the heating could lead to desiccation of bentonite and create micro-fractures due to the material shrinkage. How these two competitive processes play out in the long run, or in extreme situations, is important for estimating the permeability change in bentonite and therefore assessing the sealing performance of the bentonite barrier. Theoretical and empirical relationships for permeability change have been tested in the models for the FEBEX *in situ* test. Although the comparison between model and THMC data has been very helpful in calibrating the "right" relationships (or key parameters for the relationships), uncertainties in other processes and interaction of coupled processes might result in non-unique sets of parameters that could lead to equal or similar reasonable fit between model and data. Checking the microstructure of the bentonite buffer will serve as additional evidence to delineate the right permeability change functions and increase the predictability of models.

Bentonite samples were taken from the FEBEX *in situ* test after the dismantling of heater #2. In this section, we describe a series of synchrotron X-ray microCT (SXR-μCT) experiments to examine the microstructure of bentonite and find its role in its sealing properties. In the report for FY16, we focused on characterization of the fracture network in a quantitative fashion and looked for heterogeneity in different parts of the sealing barrier, while in this FY17 report we have focused more in the modeling part, targeting the impact of the evolution of the microstructure due to drying and hydration on the calculated hydraulic properties of the FEBEX bentonite.

4.5.2 The Technique

SXR-μCT has so far proven to be a very valuable tool for studying the fracture network of these samples. While some sample conservation and preparation issues might be present, the basically non-destructive aspect of the technique puts SXR-μCT at an advantage to other imaging methods such as scanning electron microscopy (SEM). In electron microscopy, the sample is usually kept in vacuum, under an electron beam, and in such conditions some dehydration occur. But also measurements in environmental SEM's would still require a non-trivial sample preparation: the sample would need to be cut to create a flat surface for the analysis, and the surface would be of course the part of the sample most subject to artifacts due to cutting. The very surface itself is also the part of the sample more prone to dehydration, given its immediate contact with the atmosphere. In addition to that, there is of course the issue of having to deal with 2D data. For all these reasons, we used SXR-μCT to look at the interior of the sample,

undisturbed as much as possible, in a non-destructive fashion. The collected data can be used for 3D visualization of the samples via software rendering, where operations such as virtual cuts are possible to investigate the interior of the sample, but the data can be used to characterize the microstructure of the sample in a quantitative fashion, using a variety of morphometric parameters (see e.g., Zandomeneghi et al., 2010). A quantitative characterization is especially important when looking at differences within a series of samples.

The experiments were carried out at the 8.3.2. beamline at the Advanced Light Source (ALS) at LBNL (MacDowell et al., 2012). The experiment consists of placing the sample on a rotating stage, and taking radiographs over 180 degrees of rotation, at regular angular intervals. Software based on the concept of the filtered-back projection will provide as a result, starting from the radiographs, a virtual volume of the sample in the form of a stack of horizontal "slices" (e.g., Kak and Slaney, 1988).

In these experiments the samples were measured with monochromatic X-rays (34 keV), 650 ms of exposure time, collecting 2049 projections, with a continuous tomography and "local area" (sample larger than the field of view) setup. The advantage of using a sample larger than the field of view in this specific context is important: the outer part of the sample is not actually measured, but that part of the sample is the one theoretically more subject to issues due to the sample preparation, so instead of performing a conventional tomographic measurement and then extensively cropping the dataset, we decided to use this strategy to be able to acquire a larger usable dataset with each measurement. The resulting voxel size of these measurements was 3.22 μm and the usable datasets were cylinders of 1820 vx (= 5.86 mm) diameter and 500 vx (= 1.61 mm) height.

In addition to the static experiments, an *in-situ* experiment involving the heating of the sample to monitor the development of cracks had been also carried out. The sample was heated up to ~180 °C for 8 minutes, sealed (but vented) in an unconfined pressure state. This was carried out in order to both mimic a worst-case scenario (sudden heating), but also, and mostly, to check the mechanisms of crack nucleation and propagation under heating conditions typical of this material. This dataset was also used as the starting point for the rehydration modeling part, aimed at simulating a recovery of the damaged system by hydration and subsequent swelling of the clay matrix, presented in detail in this report.

4.5.3 Sample Selection and Preparation

The samples were protected in vacuum-sealed bags that were delivered to LBNL from the source, until sampling for SXR-μCT took place. The sample was prepared by carefully cutting a ~1.5 cm piece from each of the bulk bentonite samples, making sure that the sample was not coming from the outer surface of the blocks. Just after cutting the sample, the fragments were immediately sealed in plastic wrap and aluminum foil to minimize as much as possible the loss of moisture, which would likely develop new cracks. Maximum care was taken to expose the samples to air for any significant amount of time, since drying processes – and therefore cracking – in small samples can occur quickly, and not to generate new cracks in general. For the *in-situ* heating experiment, no plastic wrap was used, but only aluminum foil.

The stability of the material over time was also further confirmed by the lack of appreciable motion artifacts in the collected datasets. This kind of artifact is very common in samples rich in highly hydrated clays or organic material measured in air, but it was not observed in our datasets, highlighting the high stability of the samples.

The sample used for heating and rehydration simulation was a FEBEX bentonite from the BD 59 (sample #3), i.e., from a block on the outer rim (closer to the wall of the tunnel) of a section without heater (see FY16 review for further details).

4.5.4 Dehydration-Induced Fracturing: SXR-µCT *In Situ* Heating

The most likely fracturing mechanism in these samples is due to the shrinkage caused by the loss of water. In the FEBEX *in situ* test, the bentonite near the heater underwent (see section 4.4.1.1) a fairly long time period (about 3000 days) of desaturation—relative humidity decreased from the initial 40% to 8% after 500 days and took about 2500 days to recover to the initial values, and then gradually got hydrated and reached an relative humidity about 80-90% by the end of test (about 6700 days). Questions raised include whether fractures are developed during the desaturation period and whether those fractures vanished after the moisture content in bentonite increases. The desaturation of bentonite near the heater in FEBEX *in situ* test or in a typical repository condition occurs in a confined condition and is accompanied by the rise of stress. Although it is extremely difficult to monitor the development of fractures under the same conditions, in this report, we have performed an *in situ* SXR-µCT measurement of a sample from BD-59-3 subjected to heating at a relatively high temperature under unconfined conditions, hopefully to shed light on the fracturing mechanism while we are fully aware the difference between the laboratory and field conditions. The sample, sealed in aluminum foil, was mounted onto the rotating stage of the SXR-µCT beamline and a baseline scan was done. After the baseline scan, the sample was heated with a hot air blower to ~ 180 °C for 8 minutes. After the heating, a final measurement of the sample was done again. The visual results are presented in Figure 4-36.

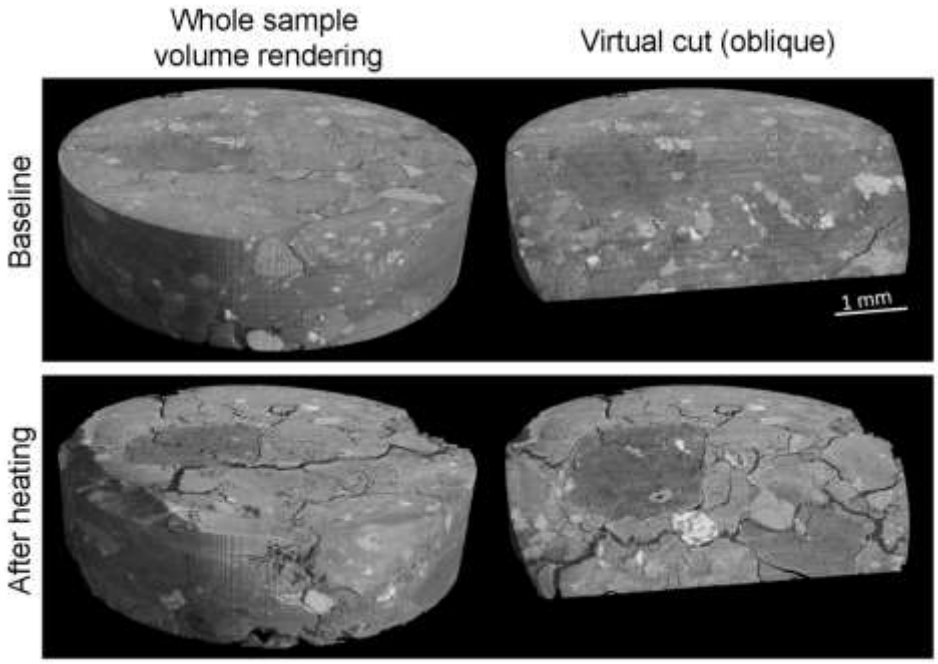

Figure 4-36. Sample from BD-59-3 before and after heating. A virtual cut of the sample is also shown to better appreciate the interior of the sample.

The results displayed in Figure 4-36 clearly show a dramatic increase in the number and size of the fractures. Different fracturing mechanisms can be observed here as well, with fractures connecting different aggregate particles, running along their interfaces, but through them as well. In addition to that, an extensive network of small fractures also develops in the clay-rich parts of the sample.

Although we have observed rapid development of fractures after heating we need to emphasize that such a case would be very unlikely in a real use case scenario, where a constant supply of moisture should be

provided by the host rock, so that the migration of moisture would be limited by the surrounding material; and the confining stress of the bentonite barrier would make the development of fractures more difficult. Nevertheless, such an experiment does give insight into the development of fractures in bentonite, i.e., fractures would be created along the interfaces of clay aggregates and through the aggregates as well.

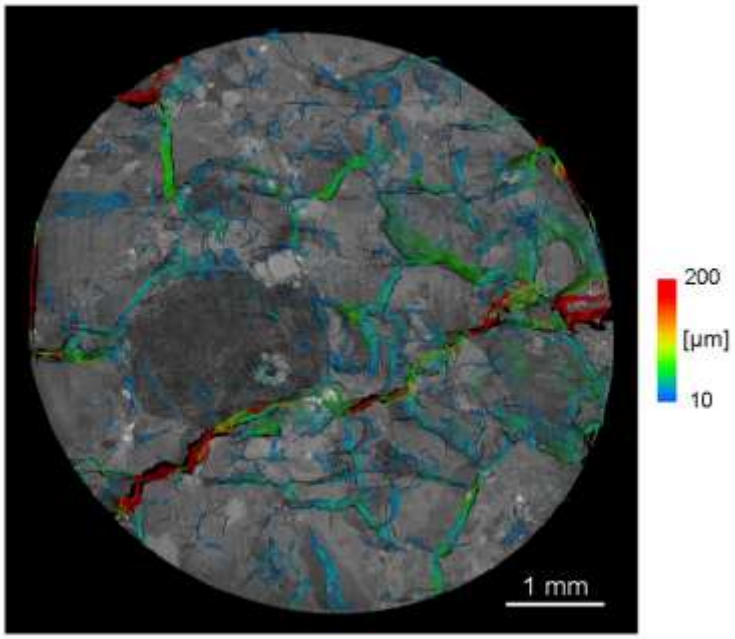

Figure 4-37. Thin horizontal slice of the sample BD-59-3 after heating. A thicker volume of the LT labeled medial axes of the fractures has been superimposed to highlight the topological features of the fracture network.

The development of the fracture network after heating is rather dramatic. As shown in Figure 4-37, samples after heating have much larger aperture values (the scale in this figure is linear) and a more pervasive fracture network was developed than what was observed in the sample before heating. Major fractures running across the whole sample are present, with a very large number of small fractures (see the blue values), which create a very dense network of connected fractures.

4.5.5 Permeability Simulation and Modeled Re-Hydration and its Impact in the Hydraulic Properties

The micro-fracture network observed from the tomographic measurements opens the question about its influence on the sample sealing properties. The topology of the fracture network is likely to have a large impact on its hydraulic properties such as permeability. Factors such as the distribution of fracture apertures is an important parameter, but given the nature of the material the main constraint is likely to be the connectivity of the fractures. The extremely low permeable matrix would lead the permeability values in case of an unconnected network (i.e., the transition of the fluid from fracture to fracture through the matrix); while in a well-connected network, the morphology of the fractures would control the permeability. Permeability measured in conventional size cores is indeed extremely small, as expected from a clay-based sealant, suggesting an unconnected network, at the core scale.

For the permeability simulations, we used the workflow presented in Figure 4-38. First, a cubic volume (1.72 mm, at a resolution of 6.44 µm per vx) was cropped from the full datasets. On this volume, the first

analysis was to operate a connected component analysis, i.e., we aimed at identifying the fracture network connected to inlet (top face of the cubic sample) and outlet (bottom). The connected fracture network is highlighted in blue, while the unconnected fractures are rendered in yellow. The connected fracture network is the feature controlling the flow properties in this simulation. As per the full-scale datasets, the aperture values of the connected fracture network can be calculated (bottom left). A step further was taken with using a Stokes solver (as in Zuo et al., 2016) to calculate the flow properties of the system. Only the flow in fractures is taken into account, as the clay matrix is considered impermeable. A flow velocity map along the flow direction is plotted in Figure 4-38, bottom-right.

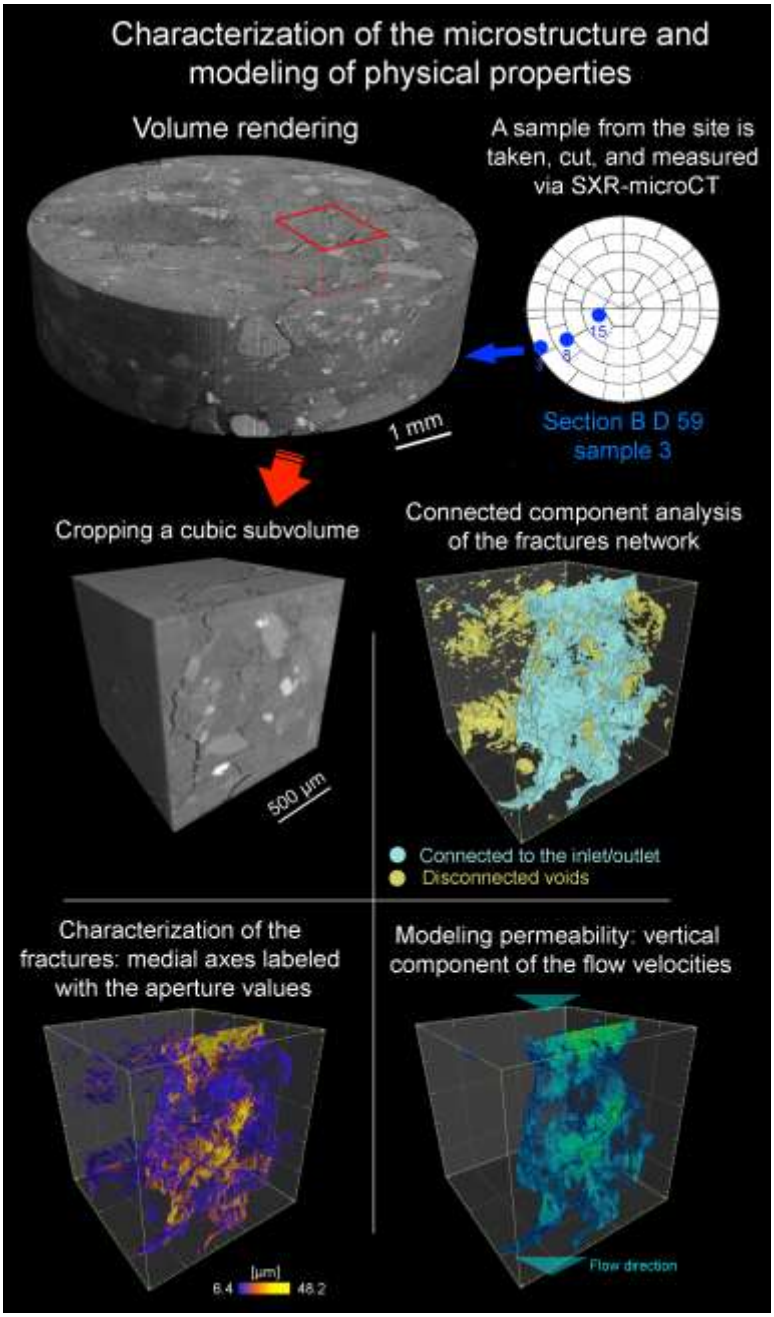

Figure 4-38. Workflow for the permeability simulation analysis.

The first step was the comparison of the heated vs. the unheated sample, in terms of network topology and flow properties. In Table 4-12 we summarize the results for the sample as-is and after heating:

Table 4-12. Basic parameters of the fracture network before and after heating. As for "voids," we mean only the voids (micro-fractures, pores, etc.) with a size larger than the resolution of the imaging measurement.

	As-is	Heated
Total voids [%]	1.97	10.64
Connected voids [% of total]	69.04	87.22
Unconnected voids [% of total]	30.96	12.78

From these results, we can observe the large increase in the amount of voids after the heating process, due to dehydration of the matrix and consequent shrinkage and fracturing. The increase in the connected fraction of voids also highlights an increase in connectivity and in size of the cracks, dramatically increasing the potential permeability of the system.

A visual summary of the evolution of the porosity and connectivity is presented in Figure 4-39, where the sample before and after heating is shown, with the connected void network in light blue and the unconnected voids in yellow:

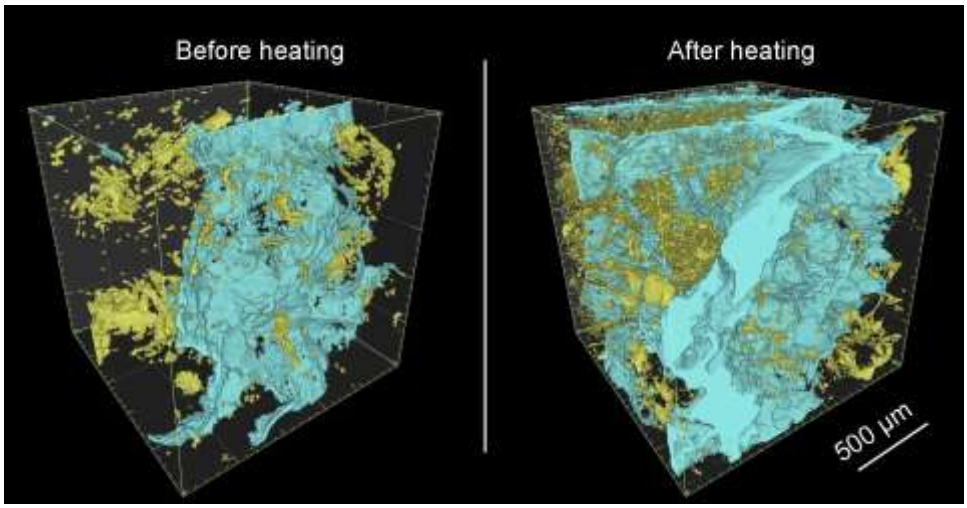

Figure 4-39. Evolution of the pore/fracture network and its connectivity (the voids connected to the inlet/outlet have been highlighted in light blue).

From the observations of Figure 4-39, we can appreciate the dramatic increase in the void fraction. In the sample as-is the only flow system is a single vertical (micro-)fracture connecting inlet (top) and outlet (bottom), while the reminder of the cracks and porosity are isolated. After heating, the preexisting fracture becomes much larger in aperture, and other new fractures connected to the initial one develop. The total amount of unconnected fractures increases as well.

After this experiment, we decided to proceed towards answering two questions: 1) How does this behavior affect the permeability of the system, 2) How would the permeability of the system change if the sample were re-hydrated? The answer to the first question would provide some insights about how a

catastrophic drying of the sample would affect the permeability of the system. The answer to the second question would highlight the importance of the hydration level of the system in keeping the fracture network as small and as unconnected as possible. For the first question, we run a Stokes flow solver on the volume to calculate the permeability of the different volumes, as cited above. To answer the second question, we run a virtual hydration experiment, on both the before and after heating volumes. This virtual hydration experiment consisted in considering the matrix continuously, uniformly, swelling: the typical mechanism for each step is that if a voxel is in contact with a "void" (i.e., the clay matrix is in contact with water, we are simulating full hydration) the material will swell, swelling simulated by adding a single voxel on the surface (i.e., a "dilate" algorithm with a single voxel structuring element). This is a purely geometrical and static model, where time is not considered. It is not necessary to consider the time factor when the target is only to observe (and characterize) the modification of the voids network upon ideal swelling conditions.

For the sample before heating, the sample taken as-is from the FEBEX site, a single cycle of swelling disconnects the inlet from the outlet, setting the permeability of the model to zero, i.e., the hydraulic properties of the sample are controlled by the matrix (considered ideally impermeable, in the Stokes model). The sample after heating needed seven swelling cycles before setting the permeability of the fracture network to zero. This means that we can easily neutralize the single vertical fracture of Figure 4-39 (left) by swelling the matrix by 6.44 μm only. That small amount is enough to completely disconnect the inlet from the outlet. On the other hand, the sample after heating needs a much larger amount of swelling. This is mostly due to the presence of a large -single- fracture, requiring multiple steps of swelling to get it closed, whereas the many small fractures of the network will disconnect very quickly, after one or two swelling cycles. Hence, the importance of considering also the fracture size distribution, in addition to the connectivity, plus of course their total amount. In Figure 4-40, the sequence of the evolution of the connected void network geometry of the heated sample is shown: the thin fractures are sealed rather quickly, while the main vertical large fracture controls the bulk of the permeability of the system. At the end of the swelling sequence an isolated fraction of the main fracture connected only to the inlet remains.

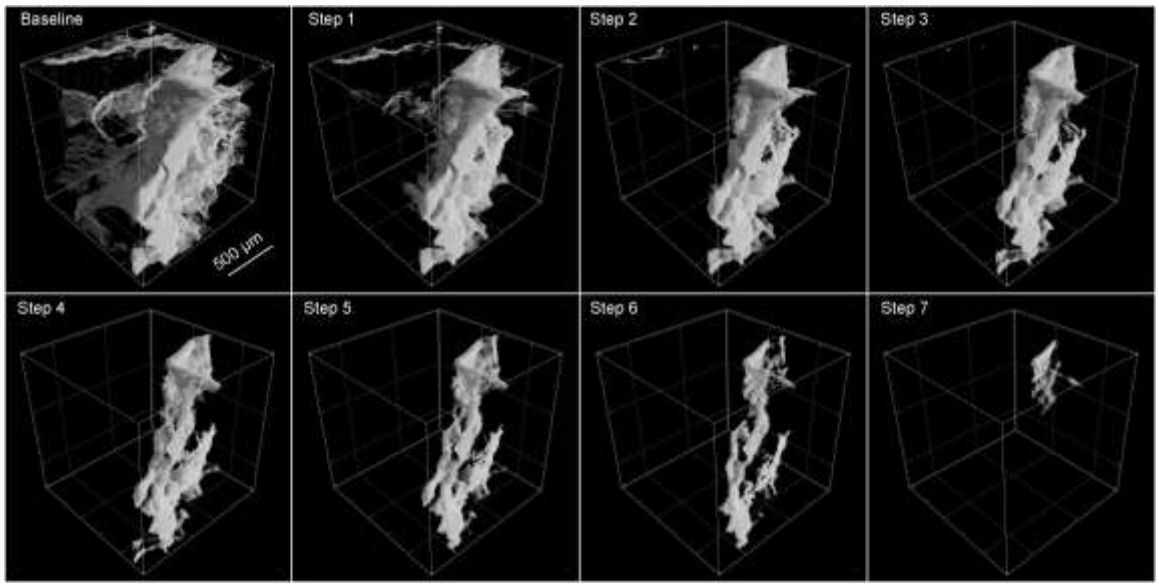

Figure 4-40. Evolution of the connected void/fracture network of the heated sample in the swelling simulation during the different cycles.

The numerical results of the analysis of the hydraulic properties of the fracture network in the different scenarios (as-is, after heating, and during swelling) are summarized in Table 4-13 and the plot in Fig. 4-41:

Table 4-13. Evolution of the connected voids and permeability of the sample before (blue) and after heating (orange), and during the simulated swelling for both.

Step #	Total voids [%]	Inlet - outlet connected voids [%]	Permeability [d]
Baseline	1.97	1.36	0.32
1	0.48	0	0
Baseline	10.64	9.28	28.86
1	6.17	5.97	17.81
2	4.44	4.35	10.75
3	3.37	3.33	6.28
4	2.51	2.49	3.57
5	1.80	1.79	1.96
6	1.22	1.17	1.03
7	0.78	0	0

The plot of the permeability simulations for the void network and the porosity analysis are presented in Figure 4-40. The most evident result is the striking difference of the sample before and after heating. The permeability parameter differs by two orders of magnitude before and after heating the sample. The simulated swelling highlights how quickly the unheated sample can close the pathway for flowing in the fractures, and while the minor fractures in the sample after heating close quickly, the bulk of the flow, happening in the largest fractures (the difference of connected and unconnected porosity decreases to almost zero just after the 3rd cycle), still controls the permeability of the void network, even though the decrease of permeability follows an exponential trend.

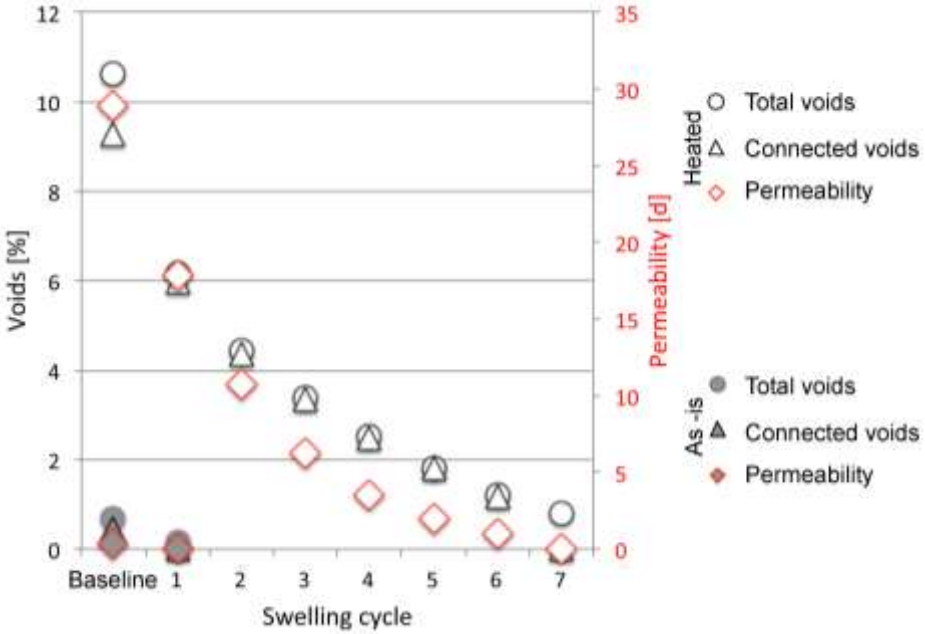

Figure 4-41. Plot showing the permeability (red) and void evolution of the network for both the "as-is" sample (solid marks) and after heating (empty marks) in the swelling simulation during the different cycles.

4.5.6 Conclusions

SXR-µCT has so far proven to be a very valuable tool for studying the fracture network of these samples. While some sample conservation and preparation issues might be present, the basically non-destructive network of the technique puts SXR-µCT at an advantage with respect to other imaging methods such as scanning electron microscopy (SEM). In the FY16 report (Zheng et al., 2016), we addressed the issue of resolution, field of view, and representativeness issues. We have found what seems to be an ideal balance between resolution vs. volume of sample analyzed, and we have tested multiple duplicates for each sample from different radial distances in the two sections. The variability among duplicates from the same part of the bentonite samples is significant, mostly linked to the heterogeneity of the material; nevertheless some weak correlation has been found. This correlation highlights a difference in the ratio of large vs. small aperture fractures dependent on the distance from the heater, and is correlated with a different moisture content. Apparently the samples in the drier zones develop more small fractures. While a truly statistically meaningful validation of this result is still needed, this correlation is clearly present in our sample survey.

Heating completely modifies the microstructure of the material, generating a pervasive network of fractures, featured by very large aperture and a thick network of small ones especially in the clay-rich parts of the sample. This emphasizes the importance of keeping this material well hydrated to ensure a good sealing effect. The sub-micron resolution dataset shows a more detailed fracture network in one sample. This measurement seems to highlight that most of the fractures are visible already with the lower resolution measurements, but adds some information on specific features such as the connectivity of the fracture network and some more microporosity. This means that the resolution/FOV used in the bulk of the analysis are good enough to take into account the role of fractures (but not the role of nanopores, where also the higher resolution test would not be enough to resolve them).

The simulations of the permeability of the system further confirm these conclusions and add new insights as well. First, the fracture connectivity is very important. However, it seems to be scale-dependent: different sub-volumes provide different connectivity, with some sub-volumes showing no link from inlet to outlet in the original (before heating) samples. The connectivity seems to be extremely variable at this scale, and it is not to be considered representative of the bulk material at larger scales. This is further confirmed by the permeability measurements showing values comparable to those of compressed clays without preferential flow paths connecting inlet and outlet such as a crack network. This holds true no more when looking at the sample at the mm scale, as per our experiments. Again, a larger FOV would require a decrease in resolution and therefore a loss of a significant part of the fracture network, so at present no 3D imaging technique could provide an adequate FOV with the required resolution. Compromises and coupling with other complementary techniques is at present the best path to follow. Once the analyzed sub-volume has a fracture network-connecting inlet and outlet the permeability becomes very high. The untreated sample displays a permeability of 320 mD, all due to the flow in the main fracture, which is a value that is orders of magnitude higher from the physical measurements on the large core plugs. This is due to the different connectivity at the different scales. The effect of heating on permeability is dramatic: the drying generates new fractures and enlarges the preexisting ones, plus the unconfined condition put no real restraints to the expansion of the sample — a similar scenario at the site is extremely unlikely to happen, only in case of total loss of moisture supply, close to the heater where the shrinkage and fracturing could happen in a partially confined fashion for a thin layer. Nevertheless, the behavior of the material in such a catastrophic scenario and its potential recovery due to re-hydration can help to better understand the general behavior of this material. This led us to heat the sample *in situ* during the experiment and to simulate the swelling of the sample during re-hydration via a simulated model approach. The simulated swelling is purely geometrical, but interesting insights can be obtained. For the untreated sample, only a single cycle of swelling (each cycle the sample swells of 6.44 μm at the water-clay interface) brings the permeability to zero, i.e., the permeability is controlled by the matrix properties, no more by the fracture network, as observed in the core plug permeability measurements. Only a minor amount of swelling is able to close the cracks in the samples as collected from the sites. With a fracture network that is much more pervasive, connected and with larger aperture values, the situation in the heated sample is completely different. The starting permeability is two orders of magnitude higher compared to its unheated state. More cycles of swelling are necessary to bring the permeability to "zero", even if the first cycles are extremely effective in closing most of the fractures, leaving only the main one still open and connected for flowing. This highlights how potentially recoverable is a completely fractured sample with only a small amount of swelling due to hydration. This analysis highlights again the importance of keeping this material in a hydrated state as much as possible, but it also gives hints about its potential ease of recovery in the case of partial drying followed by re-hydration: only a moderate amount of swelling is necessary to completely modify the hydraulic properties of the fracture network.

At this stage, the results suggest that SXR-μCT is an ideal tool for checking the properties of bentonite for a nuclear waste repository, the ability to monitor their modifications depending on their position/hydration level, and provide some quantitative parameters to directly compare different samples. This could be an excellent opportunity to test different sealing materials before deploying them. As an example, to check different clay vs. aggregate ratios, different type of clays, the use of surfactants / antiflocculants / interlayer exchangeable molecules, etc. to obtain clay aggregates with different mechanical properties and/or response to the dehydration, or even completely different sealing materials. The ability of *in situ* heating also provides the unique opportunity to see directly the modification of the sample during the loss of moisture.

Besides the visualization and quantitative characterization of the sealing materials, SXR-μCT is also able to provide 3D volume datasets which can be used in a digital rock physics context. If the volume(s) obtained are meaningful, in terms of resolution vs. field of view, for measuring a given property, some

software able to calculate those properties (such as permeability, invasion of non-wetting fluids, diffusion, etc.) from the datasets are available or under development. This ability of calculating some physical properties of the samples following the SXR-μCT measurement would complete the path that started from the scientific question and would end with a predictive tool available to the scientific community.

4.6 Summary and Future Work

4.6.1 Coupled THMC Modeling of FEBEX *In Situ* Test

The FEBEX *in situ* test that lasted more than 18 years is extremely valuable for validating the coupled THMC model and deepening our understanding of the evolution of the bentonite barrier over the course of heating and hydration. In the FEBEX-DP project, heater #2 was dismantled and extensive THMC characterization was conducted. The ultimate goal is to use THMC data from FEBEX-DP to validate THMC models and therefore enhance our understanding of coupled THMC processes in bentonite.

Since FY15, the model for the FEBEX *in situ* test evolved from TH model to THMC model. Significant efforts were dedicated to understand the lower-than-expected relative humidity data near the heater, hypotheses that have been tested include Non-Darcian flow, swelling via Barcelona Expansive Clay model or linear swelling model, various constitutive relationships for saturated permeability in bentonite as functions of either stress or dry density. After extensive calibration, THMC models developed in FY16 (Zheng et al., 2016) matched reasonably the measured temporal evolution of temperature, relative humidity and stress at several compliance points in the bentonite barrier and the measured spatial distribution of water content and dry density at 5.3 years when the heater #1 was dismantled and at 18.3 years when the heater #2 was dismantled. However, they failed to explain the spatial profile of chloride concentration at 5.3 years. In FY17, the THMC model was further revised by adding thermal osmosis and using a revised permeability-dry density relationship. After the model reproduced reasonable THM data and spatial profile of chloride concentration at 5.3 years, the model predictions of the concentration profile were tested against the calibrated ion concentration in the pore water for the samples collected during the dismantling of heater #2. The major findings from current modeling work are as follows:

- Chemical data are actually important for calibrating THM model. The model that was tested with more types of data is more reliable.
- The key coupling processes that are required to match THM data and concentration of conservative species (e.g., chloride) include vapor diffusion, porosity change due to swelling, permeability change as a function of dry density (or porosity), and thermal osmosis.
- The THMC model predicted nicely the chloride concentration profile at 18.3 years. Model results show that high chloride concentration (up to 1.2 mol/L) is expected near the heater, which might be important for waste form degradation.
- The THMC model also predicted decently the concentration data of sodium, potassium and pH. However, the model fell short of matching the concentration of sulfate, bicarbonate, calcium and magnesium. Chemical species that are involved in more chemical reaction are more challenging to predict.

In the remaining months of FY17 and FY18, as more chemical data, besides ion concentrations are available, the chemical model will be further improved based on the synthesis of all chemical data, to answer important questions relevant to performance assessment. Specifically the chemical model will be improved in the following aspects:

- The evolution of redox conditions in the bentonite barrier needs to be added to the model. A thorough understanding of the evolution of redox conditions, especially near the canister, is

critical for studying canister corrosion and waste form degradation. A synthesis of measured gas concentrations, biological data and redox sensitive minerals and aqueous species will be conducted and an updated chemical model will integrate all these reactions.

- Bentonite-canister interaction, e.g., the corrosion of canister and interaction of corrosion products with bentonite will be improved, and model will be tested against measured mineralogical phase change in bentonite and canister.

4.6.2 Quantitative Characterization of the Fracture Network in the FEBEX Samples

Although the comparison between model and THMC data has been very helpful in calibrating the "right" relationships (or key parameters for the relationships), uncertainties in other processes and interaction of coupled processes might result in non-unique sets of parameters that could lead to equal or similar reasonable fit between model and data. Checking the microstructure of the bentonite buffer will serve as additional evidence to delineate the right permeability change functions and increase the predictability of models. Bentonite samples were taken from the FEBEX *in situ* test after the dismantling of heater #2. In FY16, we have conducted a series of synchrotron X-ray microCT (SXR-μCT) examination of the microstructure of bentonite samples. The major accomplishments are as follows:

- A total of five samples from different locations were examined with three duplicates for each sample. Fracture networks for each sample were identified and quantified. We found that the variability among duplicates from the same location in bentonite barrier is significant, mostly linked to the heterogeneity of the material. Nevertheless, some weak correlation has been found: the ratio of large to small aperture fractures is larger from samples with higher water content (they are also close to the bentonite/granite interface). In other words, samples closer to the bentonite/granite interface tend to have a larger amount of large fractures, whereas samples close to the heater or to the center of the section tends to have larger amount of small fractures. While a truly statistically meaningful validation of this result is still needed, this correlation is clearly present in our sample survey. It is noteworthy that a larger amount of measurements would be experimentally impractical to carry out, and the quantitative analyses of five different samples with 3 duplicates for each sample that were accomplished in this report is already something not commonly found in the SXR-μCT literature.
- SXR-μCT imaging was also conducted for a sample at the "as is" state (the state that we received from the FEBEX *in situ* test) and a heated state under unconfined conditions. Comparison between the fracture network before and after heating showed heating completely modified the microstructure of the material, generating a pervasive network of fractures, both very large in size with an expansive network of small ones especially in the clay aggregates of the sample, but whether this is due to the heating itself or moisture loss over the course of heating needs further study. While we are fully aware that the sample was heated under different conditions than what would be expected in the field, such an exercise seems to emphasize the importance of keeping bentonite well hydrated to ensure a good sealing effect.
- During the experiment, we also addressed some important technical issues: (1) we have found *the best resolution vs. field of view compromise, and representativeness issues as well*. We have tried to maximize the analyzed volume while avoiding losing important details due to too low resolution. (2) *We have successfully developed a protocol/software for the analysis of the fracture network, focusing on the aperture value distributions.*

At this stage, the results suggest that SXR-µCT is an ideal tool for checking the microstructure of clay-based backfill for a nuclear waste repository, and providing some quantitative parameters to directly compare different samples. This opens new opportunities to advance the research in the bentonite barrier such as:

- *Testing the behavior of different candidate sealing materials before deploying them.*

This includes advanced characterization (multi-technique, when needed) and *in situ* experiments. As an example, analyses could be conducted to check different clay vs. aggregate ratios, different type of clays, the use of surfactants / antiflocculants / interlayer exchangeable molecules / etc. to obtain clay aggregates with different mechanical properties and/or response to dehydration, or even completely different sealing materials. The ability of *in situ* heating also provides the unique opportunity to see directly the modification of the sample during the loss of moisture. XR-µCT can also be coupled with other XR scattering-based techniques when a precise correlation with the hydration state of the clay structure (wide-angle X-ray powder diffraction) or the size of the clay tactoids (small-angle X-ray scattering) needs to be directly correlated with the development of desiccation cracks (e.g., Suuronen et al. 2014).

- *Using the measured datasets to build predictive tools.*

Besides the visualization and quantitative characterization of the sealing materials, SXR-µCT is also able to provide 3D volume datasets which can be used in a digital rock physics context: if the volume(s) obtained are meaningful, in terms of resolution vs. field of view, for measuring a given property, specific software able to calculate those properties (such as permeability, invasion of non-wetting fluids, diffusion, etc.) from the datasets are available or under development. This ability of calculating some physical properties of the samples following the SXR-µCT measurement would complete the path that started from the scientific question and would result with a predictive tool available to the scientific community.

This page is intentionally left blank.

5. SCOPING CALCULATION IN SUPPORT OF HOTBENT, AN EXPERIMENT THAT STUDIES THE EFFECTS OF HIGH TEMPERATURES ON CLAY BUFFERS/NEARFIELD

5.1 Introduction

Several international disposal programs have recently initiated investigating if clay-based barriers can withstand temperatures higher than the 100 °C threshold for bentonite performance usually assumed in advanced repository designs. For example, the UFD campaign has investigated the feasibility of direct geological disposal of large spent nuclear fuel canisters currently in dry storage (Hardin et al., 2014), which would benefit from much higher emplacement temperatures. The performance of bentonite barriers in the <100 °C temperature range is underpinned by a broad knowledge base built on laboratory and large-scale in-situ experiments. Bentonite parameter characterization above 100 °C is sparser (especially for pelletized materials); although up to about 150 °C, no significant changes in safety-relevant properties are indicated. At temperatures above 150 °C, it is possible that a potentially detrimental temperature-driven physicochemical response of materials (cementation, illitization) may occur, the characteristics of which are highly dependent on, and coupled with, the complex moisture transport processes induced by strong thermal gradients. The impact of such complex processes on the performance of a repository cannot be realistically reproduced and properly (non-conservatively) assessed at the smaller laboratory scale. Such an assessment needs to be conducted by large in-situ experiments in underground research laboratories (URLs), where the most relevant features of future emplacement conditions can be adequately reproduced.

Potential options for a targeted high-temperature experiment (150 °C to 200 °C) in a fractured rock environment are currently being considered under the leadership of NAGRA with several international partners, including DOE (Vomvoris et al., 2015). In FY16, NAGRA proposed the so-called HotBENT experiment, a full-scale high-temperature heater test using the well-characterized FEBEX drift at the Grimsel Test Site. The benefit of such a large-scale test, accompanied by a systematic laboratory program and modeling effort, is that the temperature effects can be evaluated under realistic conditions of strong thermal, hydraulic and density gradients, which cannot be reproduced in the laboratory. This will lead to improved mechanistic models for the prediction of temperature-induced processes, including chemical alteration and mechanical changes, which can then be used for performance assessment (PA) analysis of high-temperature scenarios. The key question is whether higher repository temperatures would trigger mechanisms that compromise the various barrier functions assigned to the engineered components and host rock. If the barrier function is (partially) compromised, PA analysis can evaluate whether reduced performance of a sub-barrier (or parts thereof) would still give adequate performance.

In FY16, NAGRA held two planning meetings to discuss the interest of potential partners in the project and to develop a plan/design for the HotBENT project. Potential partners of the HotBENT project proposed a modular design with several test modules (Figure 5-1) that would differ mainly in terms of the type of bentonite and canister, temperature range, design with/without concrete liner, etc. Meanwhile, a small-scale “Hot Mock-up” test was proposed by SURAO, the Czech waste management agency (Kober, 2016), which would greatly complement the full-scale HotBENT experiment. In FY17, the design of experiment should be finalized, and, if enough international partners join the project, the heater test is expected to start in 2018. LBNL has very actively participated in the project since the very beginning and have conducted scoping calculations in FY17 to facilitate the final design of the experiment. Potential HotBENT partners include NAGRA, GRS, SURAO, NUMO, RWM, and SKB. DOE’s participation in this new collaboration effort could be very beneficial; substantial cost savings would be achieved in the design of a repository if HotBENT demonstrates that the maximum temperature of bentonite backfill can be raised without drastic performance implications.

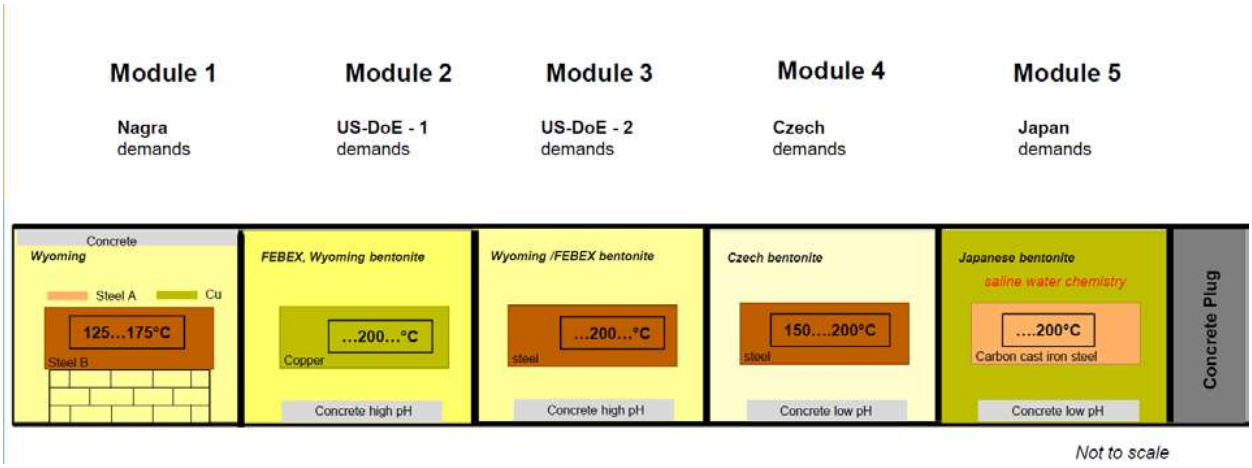

Figure 5-1. Design modules for HotBENT from partners of the project (Kober, 2016).

In this section, we describe the scoping calculations we have done to support the design of HotBENT, which include 2-D TH models to evaluate the impact of heater length on the temperature distribution, and 1-D axi-symmetrical coupled THMC models to illustrate the expected THMC response in the hot cross sections that cut through the middle of heater.

5.2 Simulator

The numerical simulations are conducted with TOUGHREACT-FLAC3D, which sequentially couples the multiphase fluid flow and reactive transport simulator, TOUGHREACT (Xu et al., 2011), with the finite-difference geomechanical code FLAC3D (Itasca, 2009). The coupling of TOUGHREACT and FLAC was initially developed in Zheng et al. (2012) to provide the necessary numerical framework for modeling fully coupled THMC processes.

5.3 2-D Axi-Symmetrical TH Model

5.3.1 Model Setup

Typically in the heating test, areas (such as areas in between section AA' and BB') that cross-cut the middle of heater have a relatively uniform distribution of temperature along the axis of the tunnel (X direction) whereas the areas that surround both ends of heater exhibit obvious changes in temperature along the X direction. Having enough length along the X direction in bentonite with uniform distribution of temperature is important for the success of the experiment because multiple sections that undergo similar temperature conditions are needed for sampling. However, longer heater results in higher cost. Therefore, the heater should have a length that is able to produce enough large area with uniform distribution of temperature along the axis, but not too long to waste money. In this report, we tested two designs: Design A has a 4.5-meter long heater (Figure 5-2) and Design B has a 3-meter long heater (Figure 5-3). Parameters used for the model are listed in Table 5-1.

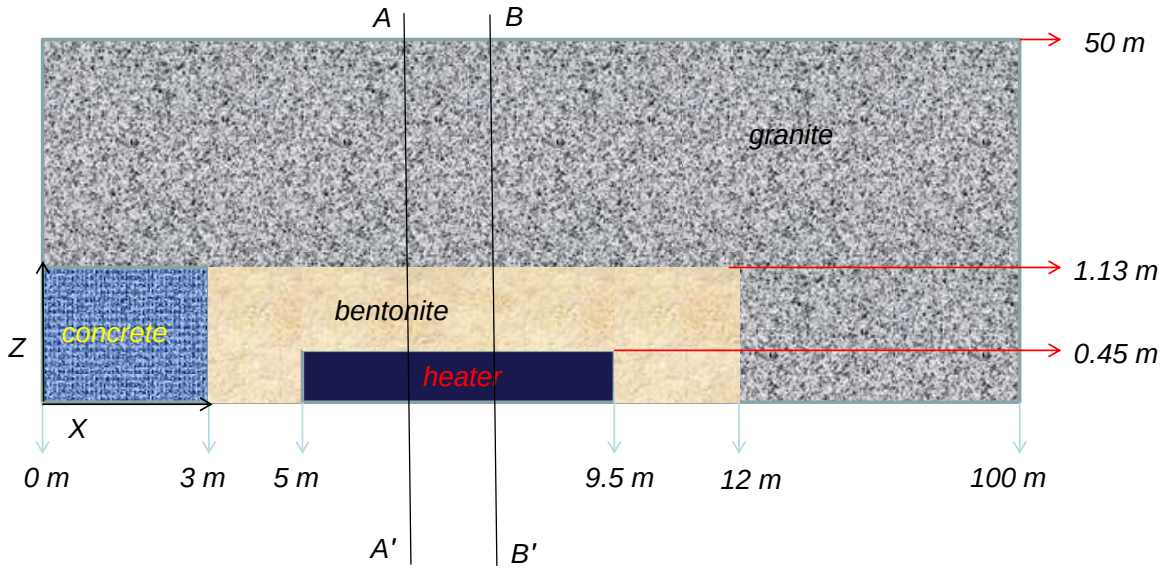

Figure 5-2. Design A for HotBENT with a 4.5-meter long heater.

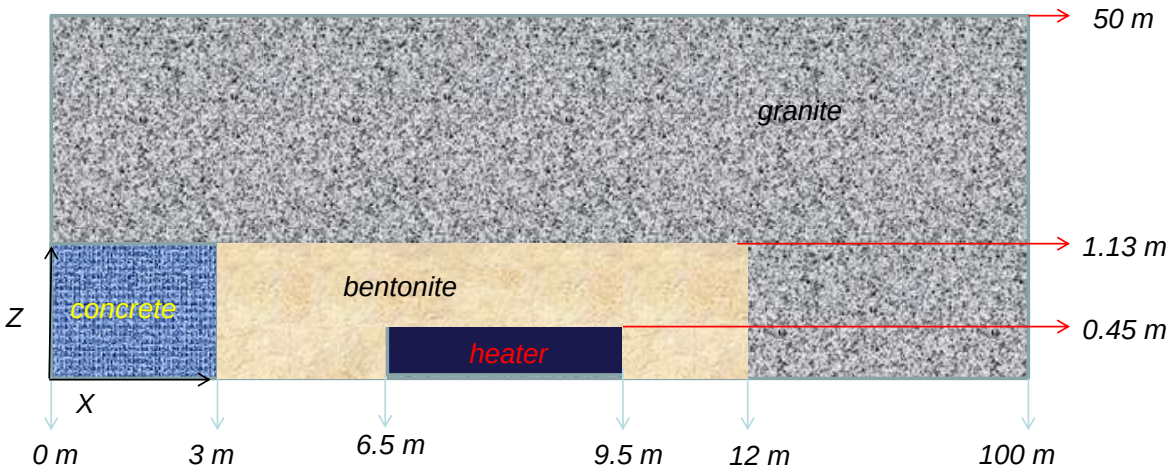

Figure 5-3. Design B for HotBENT with a 3-meter long heater.

Table 5-1. Thermal and hydrodynamic parameters (Zheng et al., 2016; Houseworth et al., 2013).

Parameter	Granite	Bentonite	Concrete
Grain density [kg/m^3]	2700	2780	2780
Porosity ϕ	0.01	0.41	0.15
Saturated permeability [m^2]	2.0×10^{-18}	2.15×10^{-21}	3.5×10^{-21}
Relative permeability, k_{rl}	$k_{rl} = S$	$k_{rl} = S^3$	$k_{rl} = S^3$
Van Genuchten $1/\alpha$ [1/Pa]	4.76×10^{-4}	1.1×10^{-8}	9.1×10^{-8}
Van Genuchten m	0.7	0.45	0.29
Compressibility, β [1/Pa]	3.2×10^{-9}	5.0×10^{-8}	5.0×10^{-9}
Thermal expansion coeff. [1/^{o}C]	1.0×10^{-5}	1.5×10^{-4}	1.0×10^{-4}
Dry specific heat [J/kg-^{o}C]	793	1091	800
Thermal conductivity [W/m-^{o}C] dry/wet	3.2/3.3	0.47/1.15	1.06/1.7
Effective vapor diffusion coefficient (m^2/s)	1.03×10^{-4}	1.03×10^{-4}	1.03×10^{-4}

5.3.2 Model Results

Because the 2-D model is primarily used to answer the question whether a shorter heater can produce enough length of relatively uniformed distribution of temperature in the bentonite along the axis of the tunnel, here we focus on the model results of temperature. Figure 5-4 shows the spatial distribution of temperature after 5 years (the planned experiment duration of the HotBENT). As shown in Figures 5-2 and 5-3, the heater has a radius of 0.45 m and bentonite barrier is about 0.7 m thick. The area beyond Z=1.13 m is granite. Regarding design A, about 1 m into the granite, the spatial distribution of temperature along the X direction shows a peak in the middle of the heater (X=7.25m) and gradually decreases towards both ends of the heater, and the peak in the middle of heater is very obvious. However, the spatial distribution of temperature along the X direction inside the bentonite (Z<1.13m) is flat and does not show a clear drop until the very end of the heater. Similar observations can be seen for design B. The temperature inside the bentonite does not change much along the X direction for ± 1.2 m from the middle of the heater, although the heater is shorter than design A. Model results suggest that shorter heater can be used and there will be enough (at least 2 m in X direction) area that has similar temperature distribution that will allow sampling for different purposes.

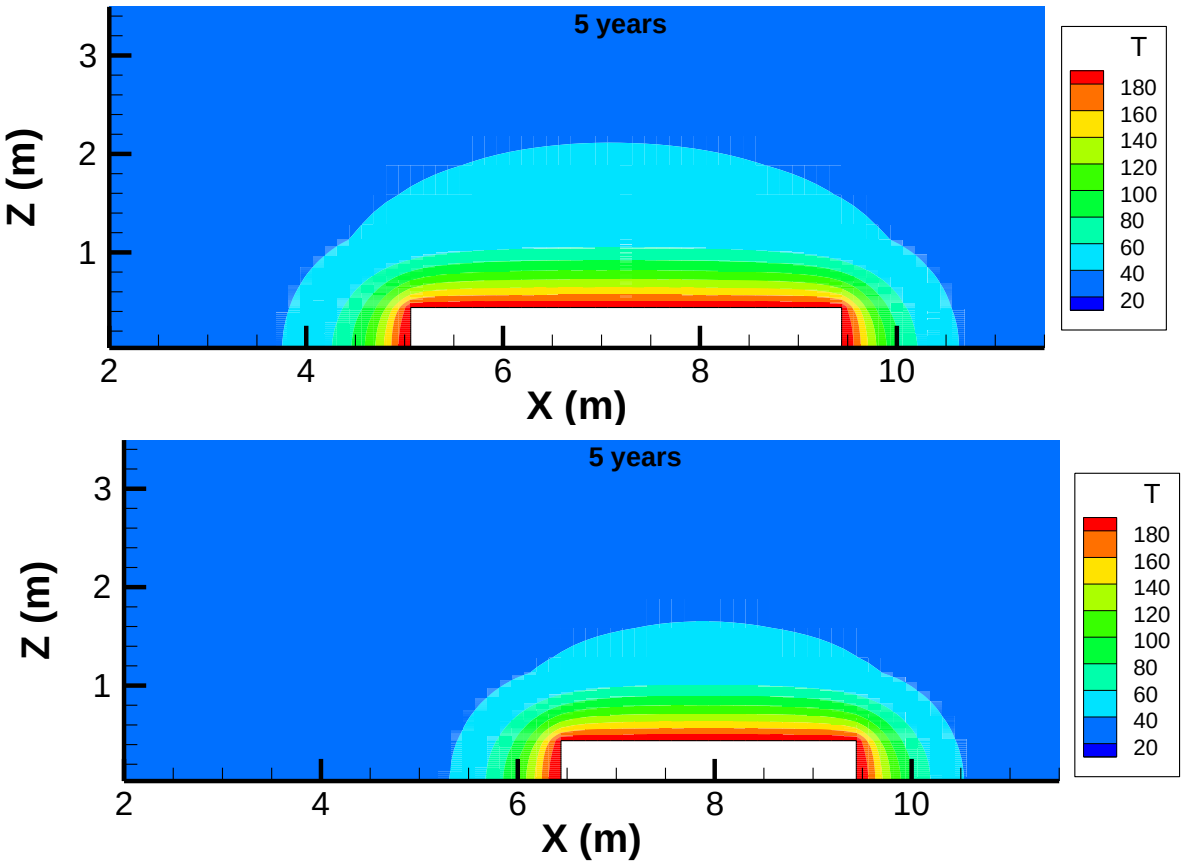

Figure 5-4. Spatial distribution of temperature after 5 years for Design A (upper) and B (lower).

5.4 1-D Axi-Symmetrical Model

5.4.1 Modeling Setup

The HotBENT experiment will be conducted in the same granite tunnel where the FEBEX *in situ* test was conducted, and the experiment setup will be similar to the FEBEX *in situ* test except that the temperature at the heater surface will be 200 °C. We therefore used exactly the same 1-D axi-symmetrical model for FEBEX *in situ* test to conduct scoping calculations for HotBENT. Regarding the model setup, including mesh, initial conditions, parameters, please refer to Section 4.3. The only modification from the model for the FEBEX *in situ* test is the boundary condition for the heater; instead of fixing it at 100 °C, the heater has a constant temperature of 200 °C.

5.4.2 Model Results

With a heater maintained at 200 °C in HotBENT, the temperatures in bentonite and granite are much higher when compared with the FEBEX *in situ* test, as shown in Figures 5-5 to 5-8 at several radial distances in bentonite and granite. Just like the FEBEX *in situ* test, which ran for 18.3 years, the model for HotBENT reported here was also run for 18.3 years including a 70-day cooling period during which the heater is switched off. Model results show that the temperature in bentonite near granite reaches about 90 °C and drops to 57 °C after the 70-day cooling period, suggesting that a longer cooling period might be needed for HotBENT at the end of experiment before dismantling can be carried out.

As expected, the granite will undergo heating and the heat pulse can penetrate as deep as 10 m into granite (radial distance of 11 m). Nevertheless, the temperature is expected to be lower than 100 °C so that boiling in granite should not be a concern.

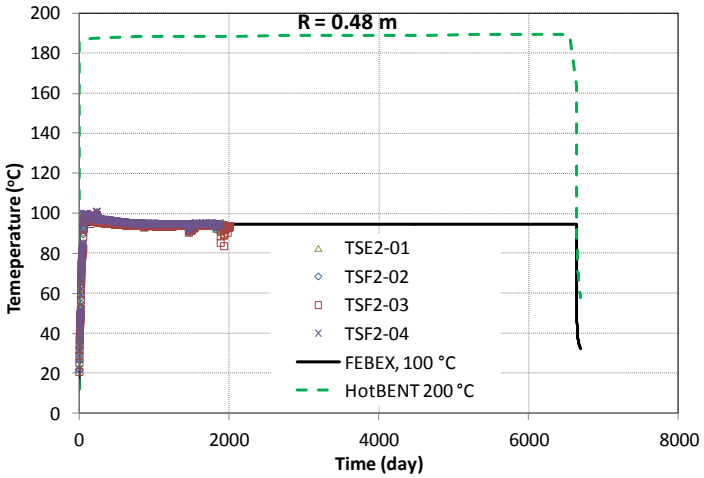

Figure 5-5. Measured and simulated temperature at a radial distance of 0.48 m in the FEBEX *in situ* test and simulated temperature in HotBENT.

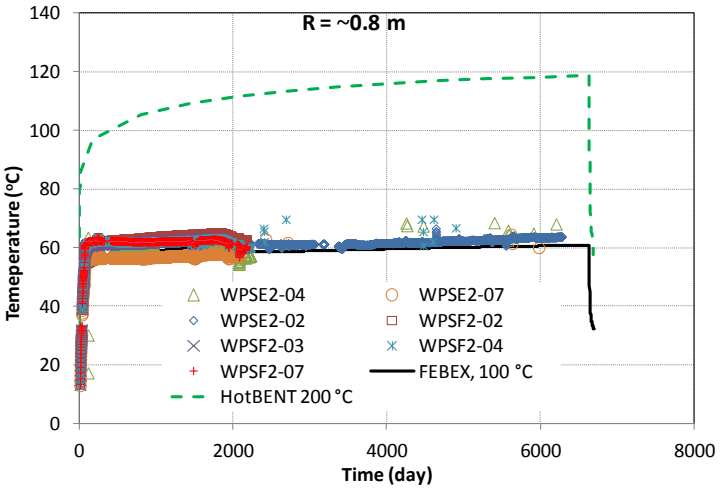

Figure 5-6. Measured and simulated temperature at a radial distance of 0.8 m in the FEBEX *in situ* test and simulated temperature in HotBENT.

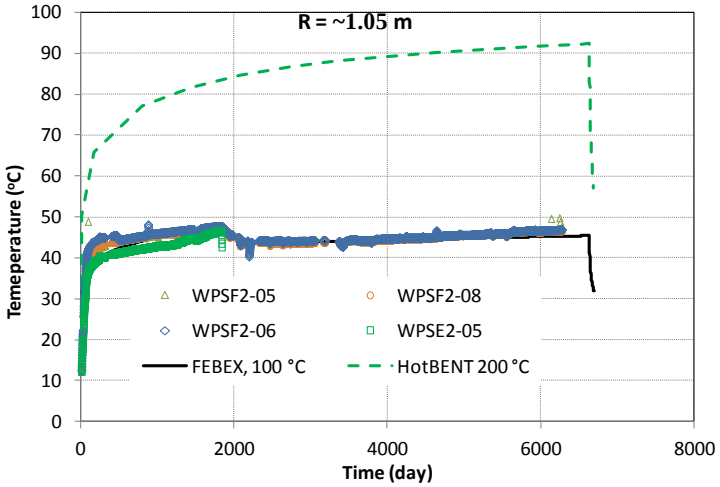

Figure 5-7. Measured and simulated temperature at a radial distance of 1.05 m in the FEBEX *in situ* test and simulated temperature in HotBENT.

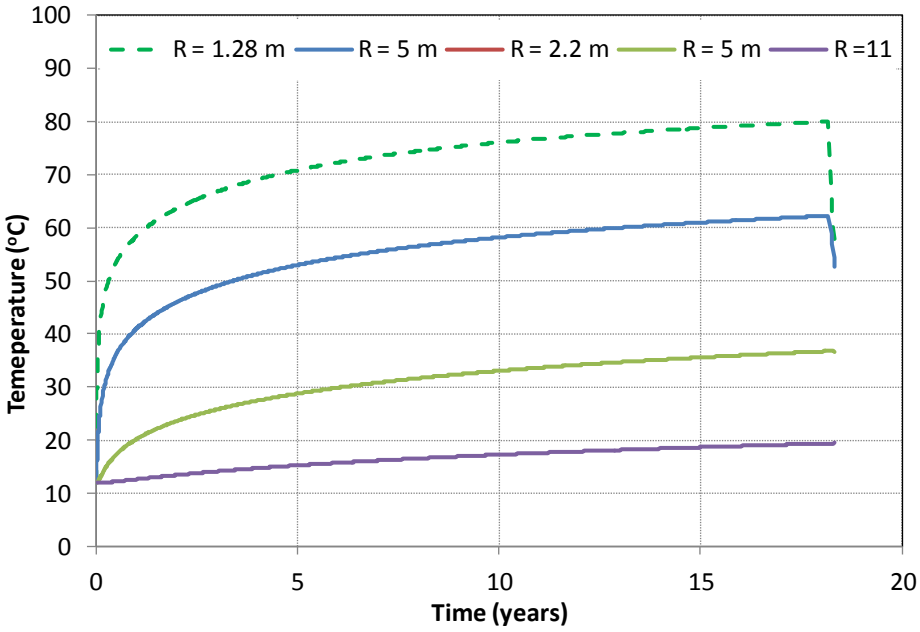

Figure 5-8. Simulated temperature in HotBENT at several radial distances in granite.

Relative humidity, water content and dry density are three types of hydrological data that are available for the FEBEX *in situ* test, so in this section we presented model results of relative humidity, water content and dry density for HotBENT to illustrate the expected hydrological behavior in HotBENT. Relative humidity in bentonite near the heater in HotBENT is expected to be much lower than that in the FEBEX *in situ* test (Figure 5-9): it drops to around 5% after a very short time period and recovers to about 20% slowly before entering into the cooling period, where it eventually rises up to 70% after the cooling period. The low relative humidity near the heater raises the concern of the quality of the relative humidity sensor. Sensors with the capacity of detecting much lower relative humidity are needed. Relative

humidity at the middle of bentonite barrier in HotBENT is also expected to be about 10% lower than that observed in the FEBEX *in situ* test (Figure 5-10), whereas the relative humidity near the granite in HotBENT is quite similar to that in the FEBEX *in situ* test: reaching 100% quickly (Figure 5-11).

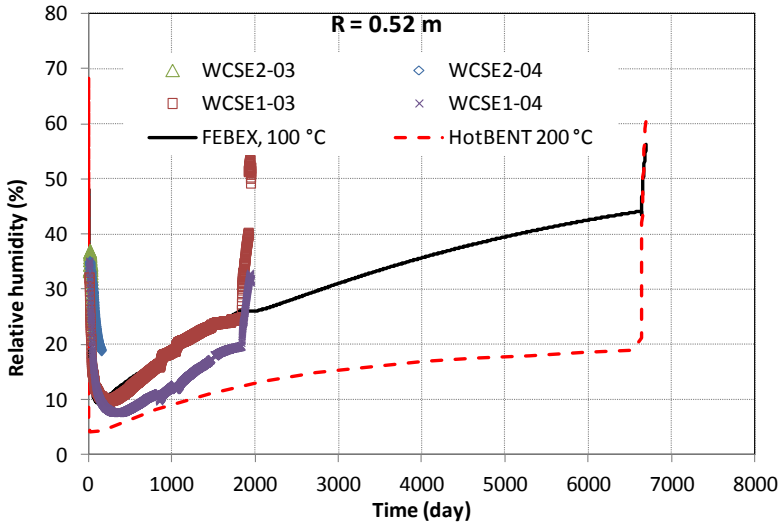

Figure 5-9. Measured and simulated relative humidity at a radial distance of 0.52 m for the FEBEX *in situ* test and simulated results for HotBENT.

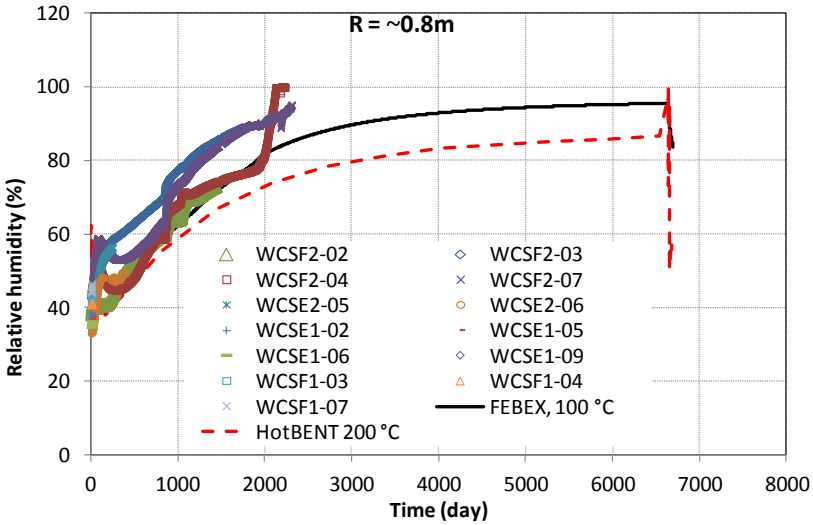

Figure 5-10. Measured and simulated relative humidity at radial distance of 0.8 m for the FEBEX *in situ* test and simulated results for HotBENT.

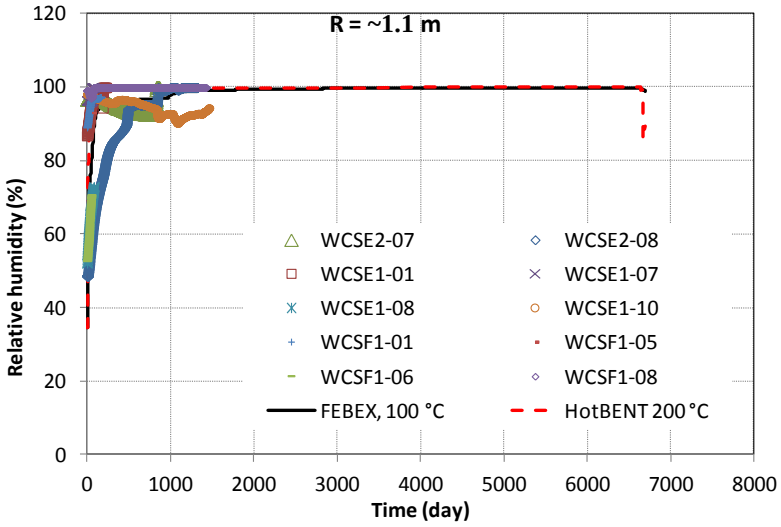

Figure 5-11. Measured and simulated relative humidity at a radial distance of 1.1 m for the FEBEX *in situ* test and simulated results for HotBENT.

One simulation was also stopped at 5.3 years with a cooling period from 5 to 5.3 years and another simulation was stopped at 10.3 years with a cooling period from 10 to 10.3 years, to check the water content profile assuming that the HotBENT test will be operated either for 5.3 years or for 10.3 years. Modeling results of these two simulations are shown in Figure 5-12, together with the data and model results for the FEBEX *in situ* test at 5.3 years. Because of swelling, a water content larger than 25% usually indicates full saturation. For HotBENT, except the area near granite (about 0.04 m away from granite), which is close to full saturation, most areas are still unsaturated even after 10 years.

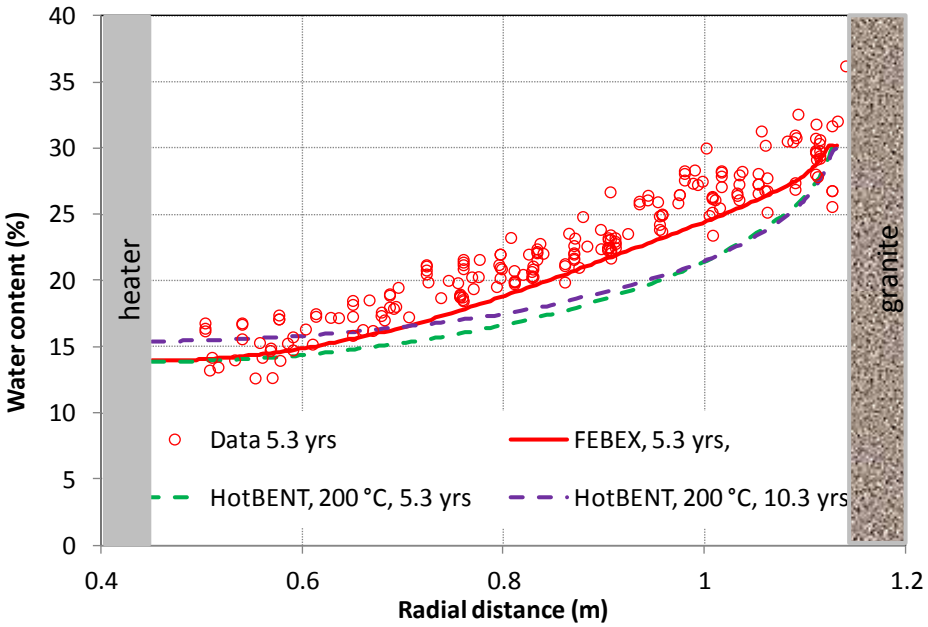

Figure 5-12. Measured and simulated water content data at 5.3 years for the FEBEX *in situ* test and simulated results for the HotBENT after 5.3 and 10.3 years.

In the FEBEX *in situ* test, while some properties were monitored by the sensors installed in the bentonite barrier, such as temperature, relative humidity, pore pressure and stress, other properties, especially those related to chemical alteration, have to be measured after dismantling the test. However, before the dismantling, a cooling period is required so that the temperature conditions in the tunnel are suitable for operation. Such a cooling period leads to significant redistribution of moisture, which compromise the usefulness of the measured water content data and complicates the model interpretation. In HotBENT, we found out that such an effect is aggravated. First, in both simulations (5.3 years and 10.3 years), after 70 days of cooling, the temperature is still about 45-50 °C (Figure 5-13), which is still too high for field operations, indicating that a longer cooling time is needed. Second, the water content during the cooling period undergoes significant changes (Figure 5-14) — water content is predicted to rise as much as 10% near the heater and drop as much as 10% near the granite.

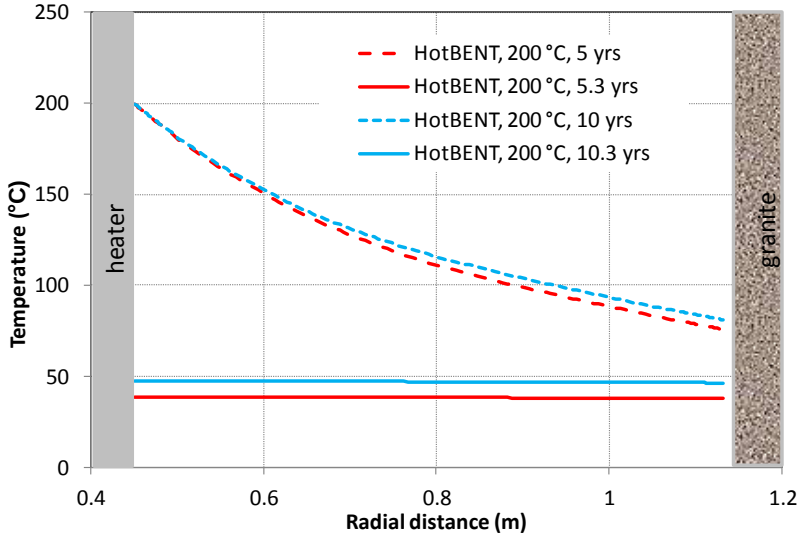

Figure 5-13. Simulated temperature for HotBENT after 5.3 years with 70 days of cooling period and 10.3 years with 70 days of cooling period.

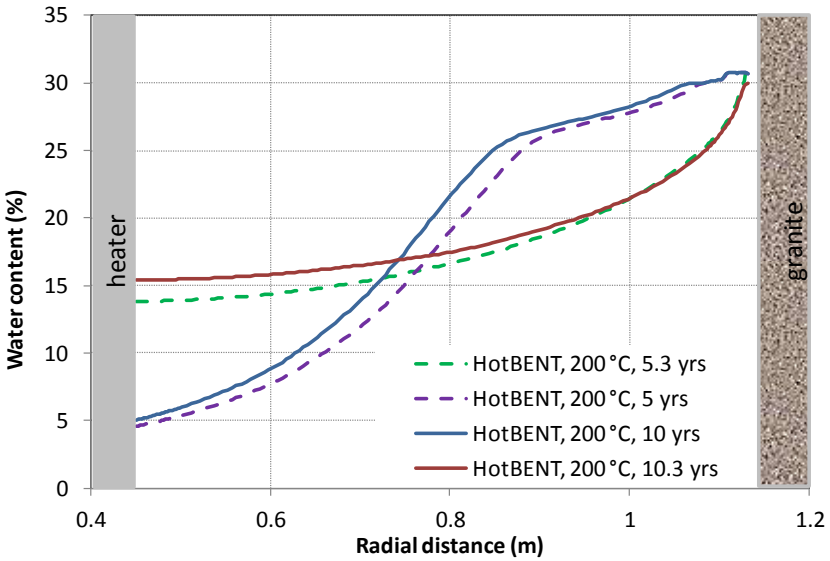

Figure 5-14. Simulated water content for HotBENT after 5.3 years with 70 days of cooling period and 10.3 years with 70 days of cooling period.

Sensors for measuring stress were also emplaced in the bentonite block in the FEBEX *in situ* test, and data at two radial distances, 0.5 m (very near the heater) and 1.1 m (right at the bentonite/granite interface), were used to validate the model for the FEBEX *in situ* test. Here we also check the stress data at these two locations predicted by the mode for HotBENT. Figures 5-15 and 5-16 show the measured stress and model results for the FEBEX *in situ* test and predicted by the model for HotBENT. In HotBENT, because of lower water content throughout most of bentonite barrier and lower pore water pressure compared with that in the FEBEX *in situ* test, the stress is lower than that in FEBEX *in situ* test despite the higher temperature conditions for HotBENT.

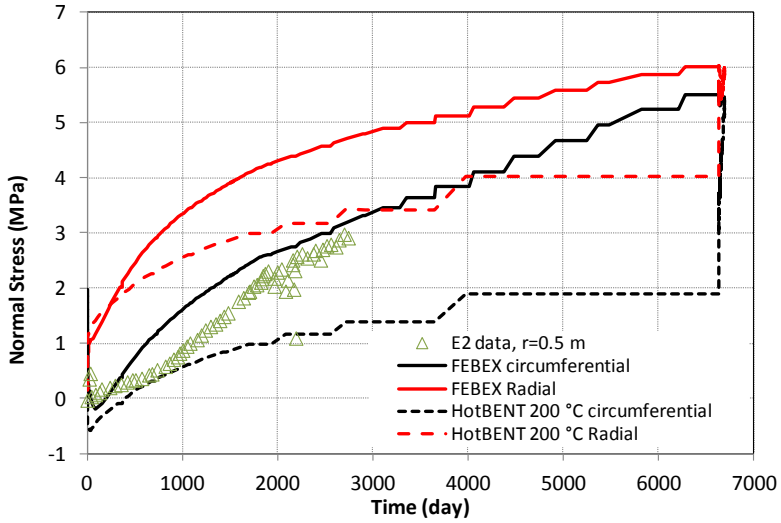

Figure 5-15. Measured and simulated stress at a radial distance of ~0.5 m for the FEBEX *in situ* test and model results for HotBENT.

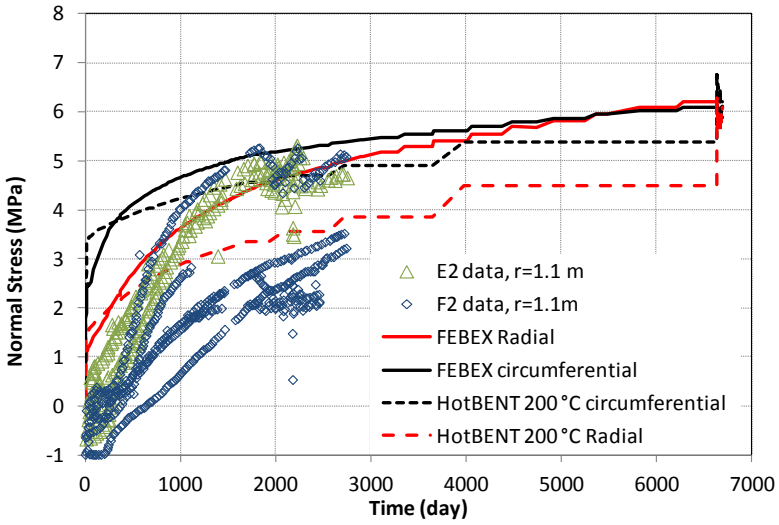

Figure 5-16. Measured and simulated stress at a radial distance of 1.1 m for the FEBEX *in situ* test and model results for HotBENT.

After the partial dismantling of the FEEBX *in situ* test in 2002 (5.3 years after heating started), samples were collected and pore water concentrations were measured. A model for the FEEBX *in situ* test matches reasonably the chloride concentration profiles (see Section 4.3), and the model shows that the concentration of chloride near the heater is quite a bit higher due to evaporation. For HotBENT, it is expected that chloride concentrations will be even higher in the area near the heater (Figure 5-17).

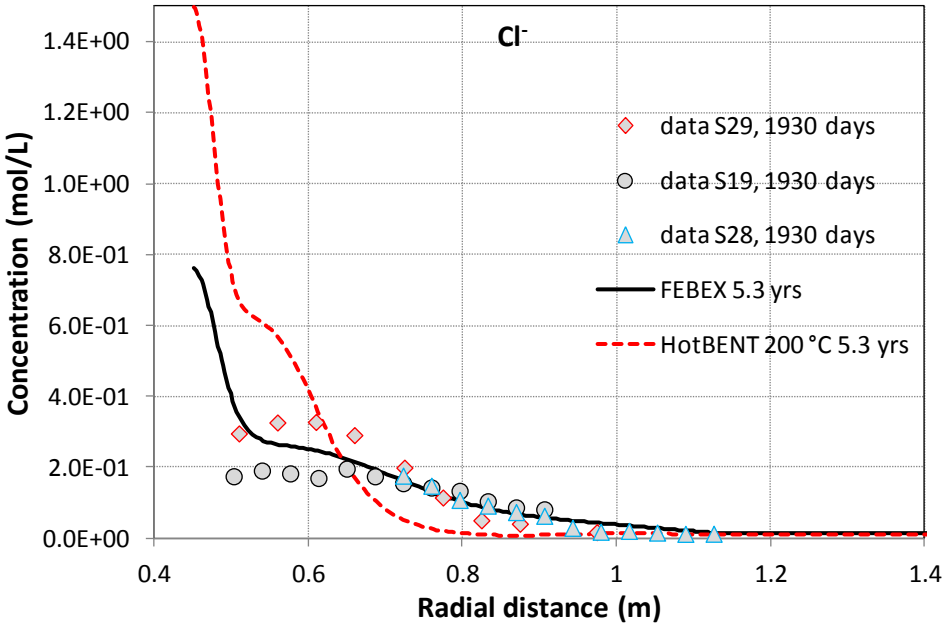

Figure 5-17. The measured concentration profile of chloride at 5.3 years (Zheng et al., 2011) and model results for the FEEBX *in situ* test, and simulated for HotBENT at 5.3 years.

5.4.3 Sensitivity Analyses to Heater Temperature

Over the course of planning for HotBENT, one of the concerns is that a heater temperature of 200 °C might be too high. Therefore, a simulation that runs for 10.3 years with a 70-day cooling period and a fixed heater temperature at 175 °C was conducted. Figure 5-18 shows the temperature profiles before cooling (10 years) and after cooling (10.3 years). By the end of the heating period, a 25 °C difference in temperature near the heater only results in a difference of about 7 °C near the granite. Figure 5-19 shows the difference of water content in these two cases. It appears that a heater temperature of 175 °C does not significantly increase the water content in comparison with the case with the heater at 200 °C. The relative humidity in the bentonite usually undergoes an initial sharp drop after the heating starts and then gradually increases as water infiltrates from the host rock. Using a heater temperature of 175 °C seems to lead to a similar magnitude of initial drop of relative humidity compared to a heater at 200 °C (Figures 5-20 and 5-21); but as the end of the heating period is approached (10 years), a heater temperature of 175 °C leads a relative humidity that is about 7-8% higher than that obtained using a heater at 200 °C for areas near the heater (Figure 5-20) and in the middle of bentonite barrier (Figure 5-21).

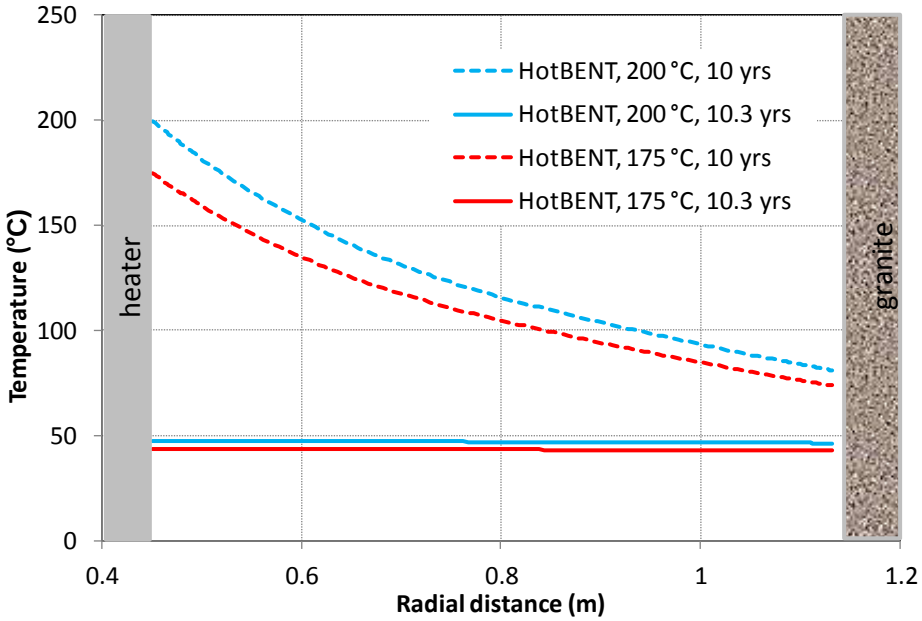

Figure 5-18. The predicted temperature profile after 10 and 10.3 years for 2 simulations with heater temperatures of 200 °C and 175 °C, respectively.

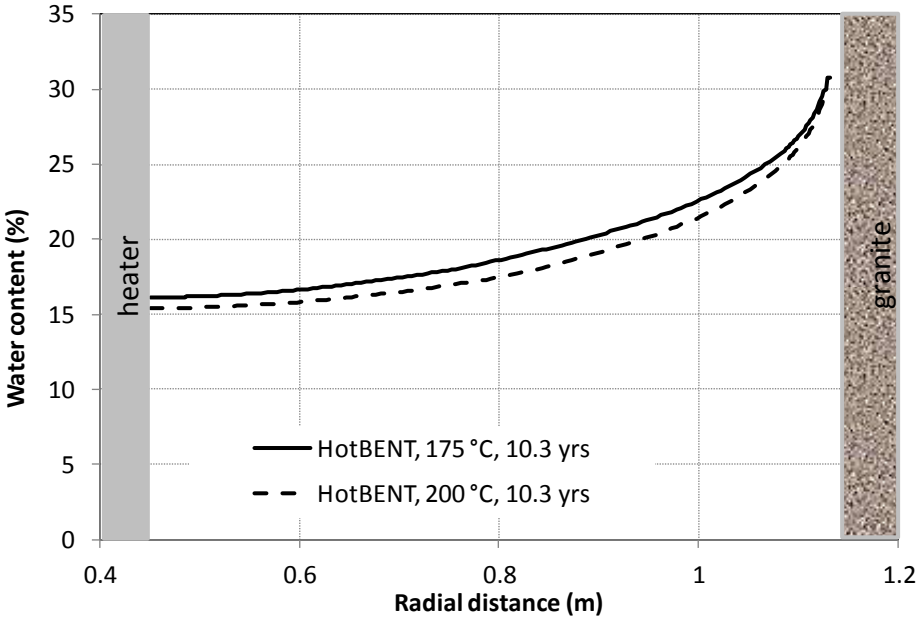

Figure 5-19. The predicted water content profile after 10 and 10.3 years for 2 simulations with heater temperatures of 200 °C and 175 °C, respectively.

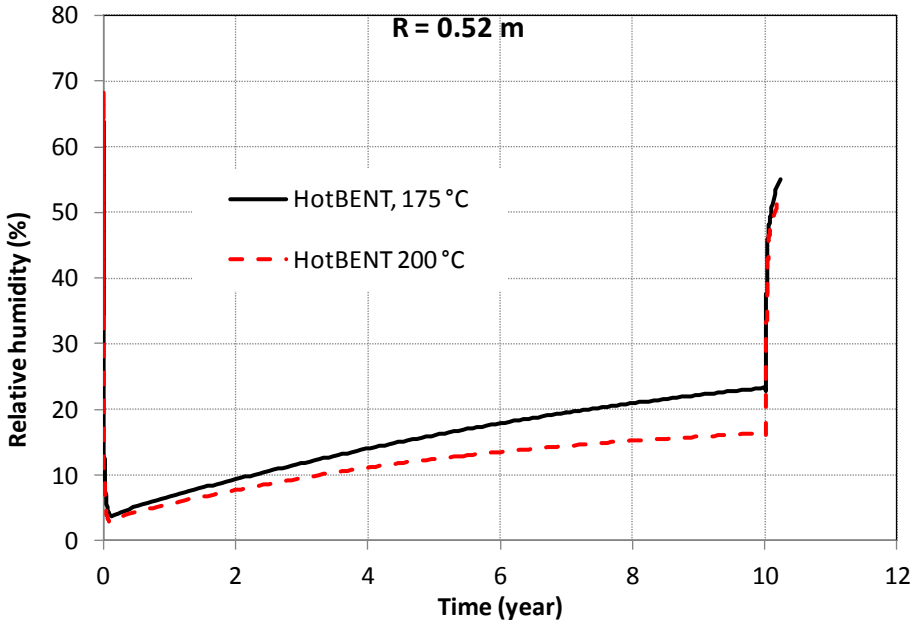

Figure 5-20. The predicted relative humidity at a radial distance of 0.52 m for two simulations with heater temperatures of 200 °C and 175 °C, respectively.

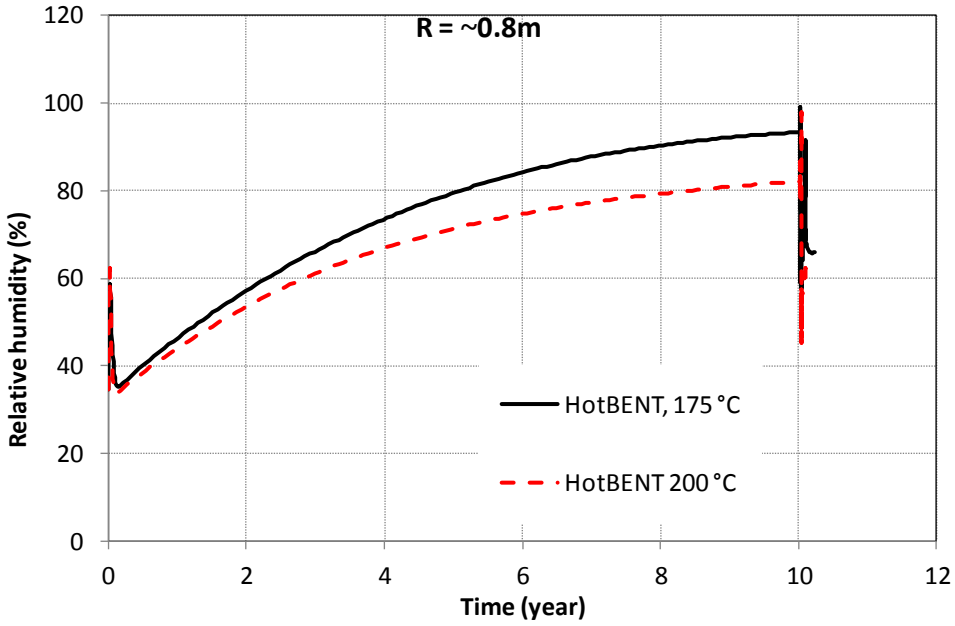

Figure 5-21. The predicted relative humidity at a radial distance of 0.8 m for two simulations with heater temperatures of 200 °C and 175 °C, respectively.

5.4.4 Model Result for Artificial Hydration

Model results in section 5.4.2 show that bentonite will stay dry for most portions of the bentonite barrier for a long time. If the test is planned for 10 years or even up to 18 years, a large part of the bentonite barrier will still remain quite dry, which may lead very little geochemical change in bentonite, which would be undesirable for learning about the chemical changes in bentonite barrier under high temperature conditions. In a typical repository condition, the high temperature pulse might last longer than the time that the bentonite becomes full saturated so that there is a period that bentonite is in a hot and wet condition. In order to learn what happens to the bentonite barrier for a period of hot and wet conditions, we are trying to make HotBENT wetter than models in previous sections showed. One way of doing it is "artificial" hydration, i.e., injecting water at a faster rate than "natural" hydration from granite. In this section, we present two simulations with "artificial" hydration.

5.4.4.1 Artificial Hydration from the Middle of the Bentonite Barrier

One way of artificially hydrating bentonite barrier is to inject water via pipes installed in the middle rings of the bentonite barrier, as shown in Figure 5-22. Artificial hydration through the middle of the bentonite barrier is quite efficient. Model results of relative humidity at various radial distance (Figures 5-23 and 5-24) of 0.52 m show that after about one year, the bentonite barrier is close to full saturation everywhere. Figure 5-25 shows the water content distribution at several times, which shows a rapid increase in water content in the middle of the bentonite barrier.

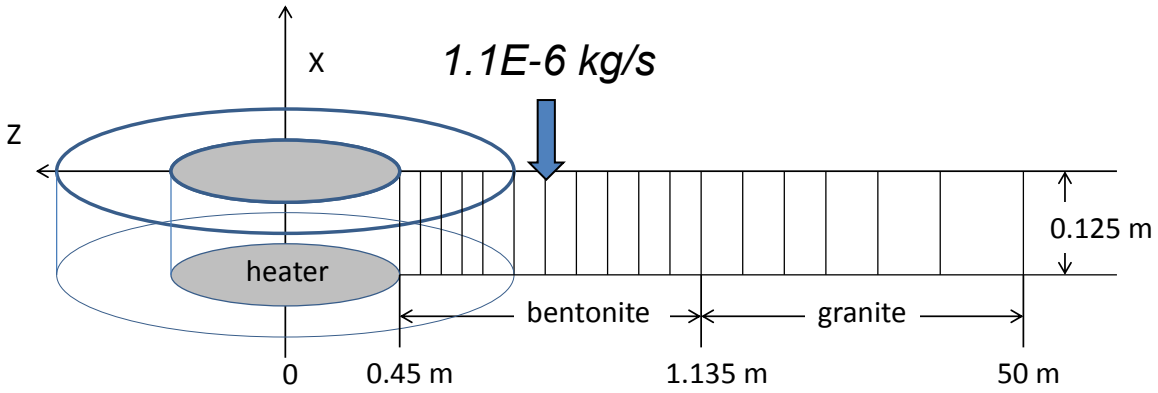

Figure 5-22. A model simulating the injection of water uniformly at the middle of the bentonite barrier.

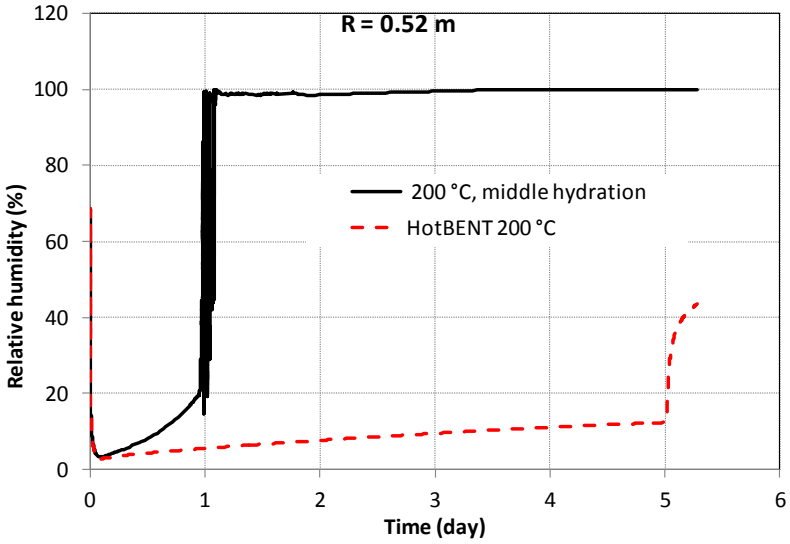

Figure 5-23. Model results of relative humidity at a radial distance of 0.52 m in the case with natural hydration only (HotBENT 200 °C) and a case with artificial hydration through the middle of the bentonite barrier (200 °C, middle hydration).

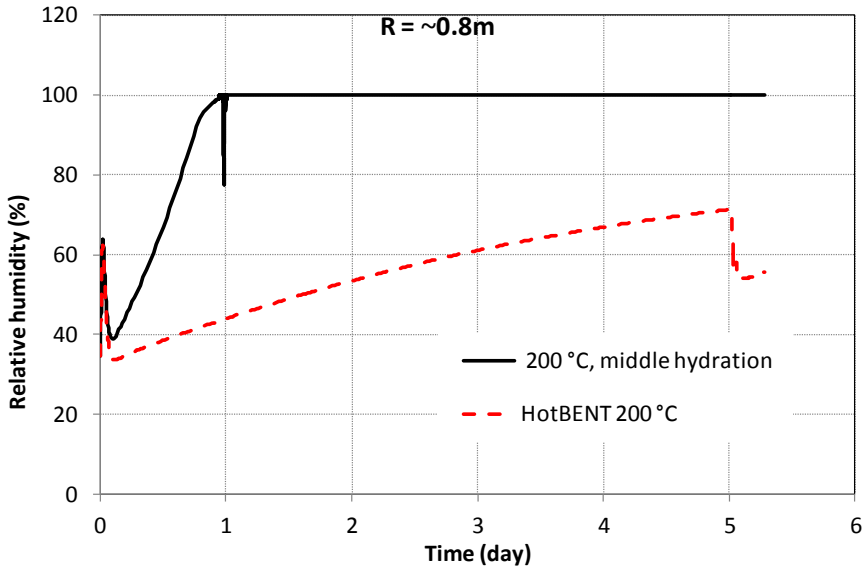

Figure 5-24. Model results of relative humidity at a radial distance of 0.8 m in the case with natural hydration only (HotBENT 200 °C) and a case with artificial hydration through the middle of the bentonite barrier (200 °C, middle hydration).

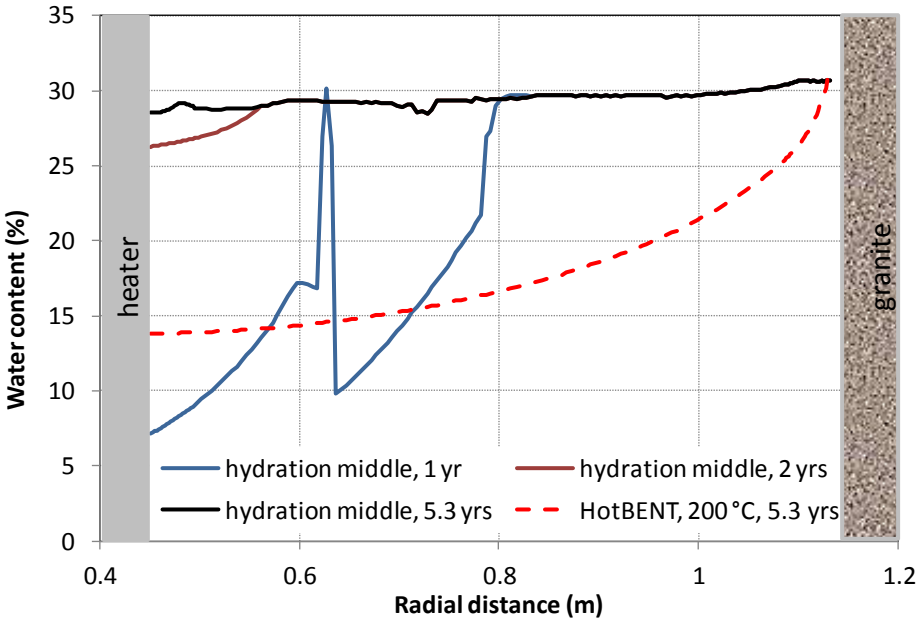

Figure 5-25. Model results of water content at 1, 2 and 5.3 years in a case with artificial hydration through the middle of the bentonite barrier and a case with natural hydration only.

5.4.4.2 Artificial Hydration from the Bentonite-Granite Interface

Artificial hydration through the middle of the bentonite barrier leads to quite atypical water content spatial distributions, which will complicate significantly the interpretation of the test results of hydraulic and chemical evolution at the early stage. Artificially hydrating bentonite via injecting water at the bentonite-granite interface will make the hydration of bentonite have a pattern similar to natural hydration but at a higher rate. Therefore, a simulation with water uniformly injected at the bentonite-granite interface was conducted (Figure 5-26). However, simulation results of relative humidity, as exemplified by the temporal evolution at two radial distances (Figures 5-27 and 5-28), and spatial distribution water content at several times show that artificial hydration is not very effective — injecting water through bentonite-granite interface leads to higher water content in the bentonite barrier, but it is far from fully saturating the whole bentonite barrier. The reason is that granite has higher permeability, so water injected at the bentonite-granite interface preferably goes into granite rather than the bentonite.

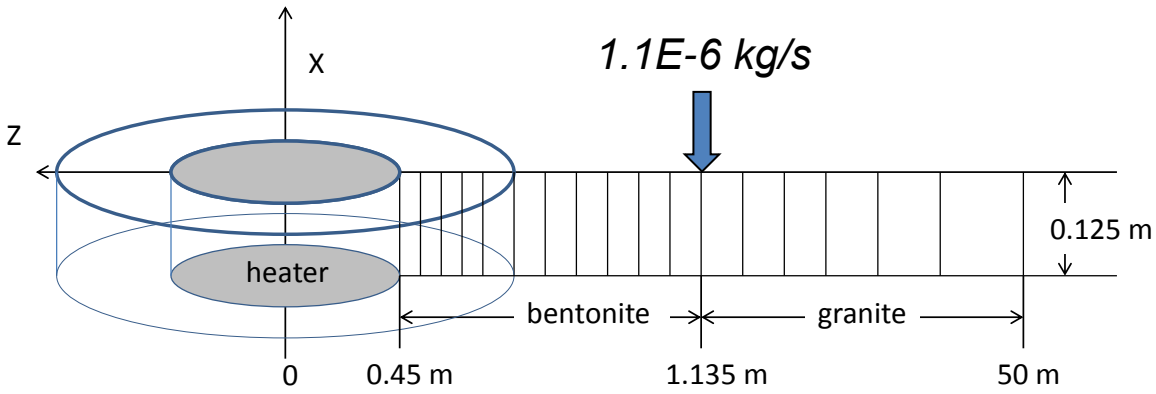

Figure 5-26. A model simulating the injection of water uniformly at the bentonite-granite interface.

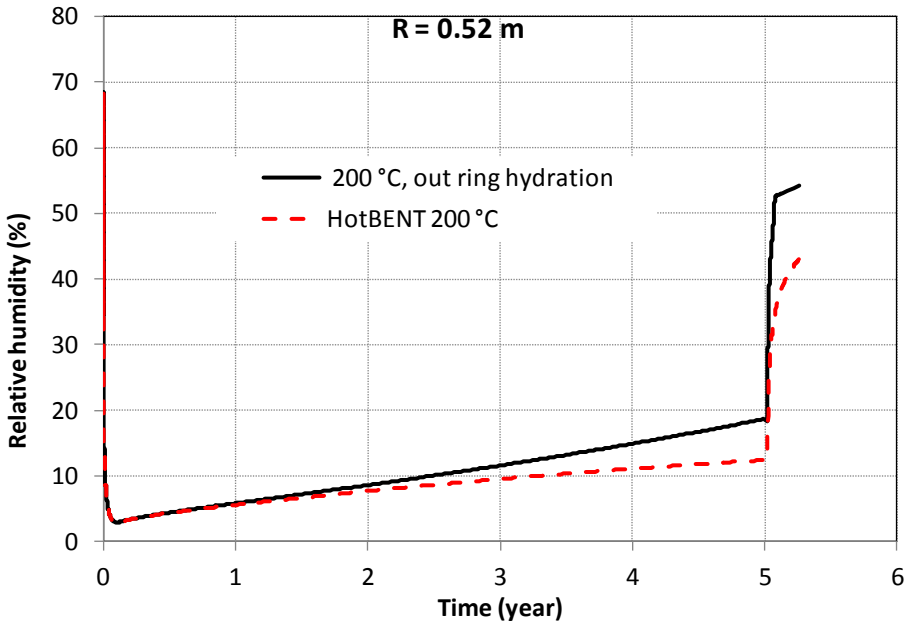

Figure 5-27. Model results of relative humidity at a radial distance of 0.52 m in the case with natural hydration only (HotBENT 200 °C) and a case with artificial hydration of the bentonite-granite interface (200 °C, outer ring hydration).

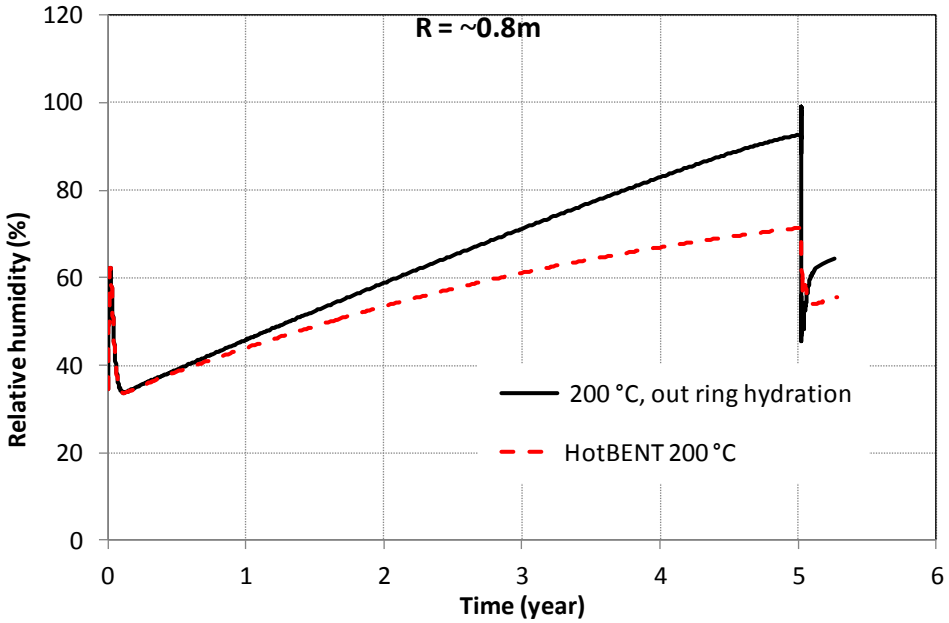

Figure 5-28. Model results of relative humidity at a radial distance of 0.8 m in the case with natural hydration only (HotBENT 200 °C) and a case with artificial hydration of the bentonite-granite interface (200 °C, outer ring hydration).

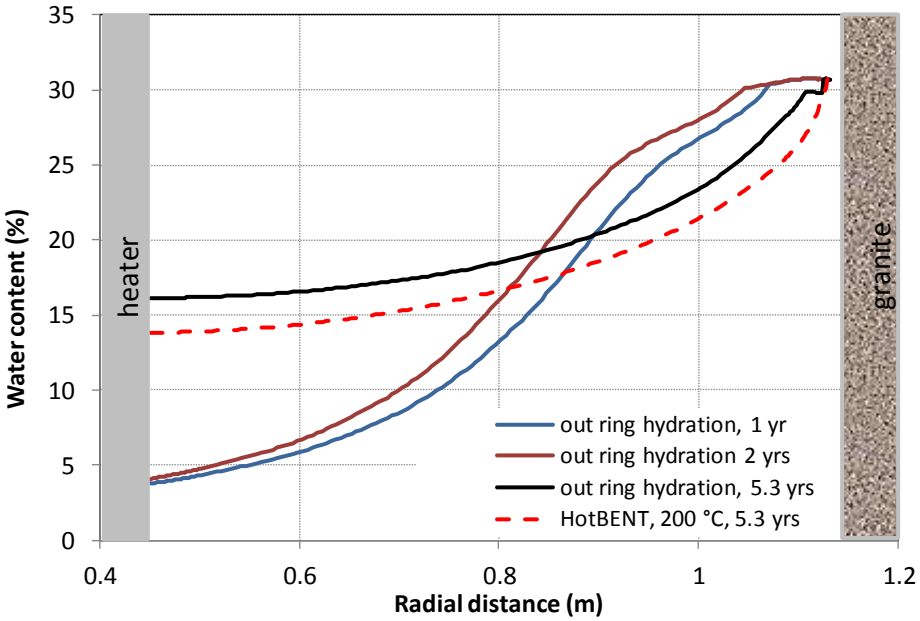

Figure 5-29. Model results of water content at 1, 2 and 5.3 years in a case with artificial hydration through the bentonite-granite interface and a case with natural hydration only.

5.5 Summary and Future Work

Raising the maximum allowed temperature for clay-based barriers has clear benefit for crystalline and argillite repository such as decreasing the footprint of the repository. However, higher temperatures can lead to complex processes that affect the performance of a repository that cannot be realistically reproduced and properly (non-conservatively) assessed at the smaller laboratory scale. Such an assessment needs to be conducted by large in-situ experiments in underground research laboratories (URLs), where the most relevant features of future emplacement conditions can be adequately reproduced. Therefore, HotBENT, a high-temperature experiment (200 °C) in a fractured rock environment are currently being considered under the leadership of NAGRA with several international partners, including DOE (Vomvoris et al., 2015). In FY17, the design of the experiment should be finalized, and, if enough international partners join the project, the heater test is expected to start in 2018. LBNL has very actively participated in the project since the very beginning. In this report, we present scoping calculations to facilitate the final design of the experiment. The accomplishments include 2-D TH models to evaluate the impact of heater length on the temperature distribution, and 1-D axi-symmetrical coupled THMC models to illustrate the expected THMC response in the hot sections. The major findings from these simulations include:

- In comparison with the 4.5 m long heater used in the FEBEX *in situ* test, model results suggest that a 3 m long heater of for HotBENT will be enough to have sufficient area that has a similar temperature distribution to satisfy the multi-purpose sampling requirements.
- HotBENT with a heater of 200 °C will lead to a temperature around 90 °C in granite, thus boiling in granite is therefore probably not a concern.

- Most part of bentonite barrier for HotBENT with a heater of 200 °C will stay dry for a very long time — an 18-year long simulation shows that bentonite is far from being fully saturated.
- Despite the higher temperature in HotBENT, the stress is actually lower than that in the FEBEX *in situ* test (where the heater temperature was 100 °C).
- In HotBENT, very high concentrations of chloride (up to 3 mol/L) are expected.
- A HotBENT with a heater of 175 °C does not significantly differ from the case with a heater of 200 °C in terms of hydrological behavior.
- Artificial hydration from the middle of bentonite barrier is effective in saturating the bentonite barrier, but it complicates the spatial water content distribution.
- Artificial hydration from the bentonite-granite interface is ineffective because water mostly flows into the higher permeability granite.

In the remaining months and FY18, we will continue to use a coupled THMC model to facilitate the final design of HotBENT; specifically we have the following tasks planned:

- More sensitivity analyses to design key variables will be conducted
- In HotBENT, the heater will be emplaced on a pedestal and the bentonite barrier will be filled in with bentonite pellets. Therefore the hot sections will be represented by two 1-D THMC models: one for the pellet bentonite and another for the pedestal area
- The modeling work will focus on predicting the evolution of chemical variables (salinity, mineral phase, etc.), mechanical variables (stress, swelling pressure, etc.), hydro-mechanical (HM) coupling (porosity-stress, permeability-porosity and possibly MC coupling (swelling stress-salinity, swelling stress-smectite, etc.).

This page is intentionally left blank.

6. MODELING OF GAS MIGRATION IN CLAY USING TOUGH-FLAC AND TOUGH_RBSN (DECOVALEX-2019)

In this section, we present LBNL's activities for modeling gas migration in clay related to Task A of the international DECOVALEX-2019 project. This is an international collaborative activity in which DOE and LBNL gain access to unique laboratory and field data of gas migration that are studied with numerical modeling to better understand the processes, to improve numerical models and to eventually be applied in the performance assessment of nuclear waste disposal in clay host rocks and bentonite backfill. The Task A of DECOVALEX-2019 is coordinated by the British Geological Survey (BGS), that is also sharing their extensive data set on coupled THM responses during gas migration in bentonite and clay stone.

6.1 Gas migration in clay

Gas migration in clay-based buffer materials has been the subject of a number of international research programmes in the field of nuclear waste disposal, including both laboratory scale and *in situ* experiment (e.g., Horseman et al., 1990; 2004; Harrington et al., 2012; Cuss et al., 2014). Substantial insight has been gained in the phenomenology of gas transport processes in bentonite and clay stone under different THM conditions. A number of model approaches have been proposed for the interpretation of the experimental results and for the analysis of gas release scenarios from geological repositories in the context of long-term safety assessment. The predictive capability of the gas transport models is yet limited, indicating that basic mechanisms of gas transport in bentonite are not understood in sufficient detail to provide the ground for robust conceptual and quantitative models.

The processes governing the movement of repository gases through bentonite and argillaceous host rocks can be split into two components, (i) molecular diffusion (governed by Fick's Law) and (ii) bulk advection (Harrington, 2016). In repository concepts such as the Swedish KBS-3, corrosion of metallic materials under anoxic conditions will lead to the formation of hydrogen. Radioactive decay of the waste and the radiolysis of water are additional source terms. If the rate of gas production exceeds the rate of gas diffusion within the pores of the barrier or host rock, a discrete gas phase will form. Under these conditions, gas will continue to accumulate until its pressure becomes sufficiently large for it to enter the surrounding material.

Four primary phenomenological models describing gas flow can be defined (Figure 6-1): (1) gas movement by diffusion and/or solution within interstitial fluids along prevailing hydraulic gradients; (2) gas flow in the original porosity of the fabric, commonly referred to as viscocapillary (or two-phase) flow; (3) gas flow along localized dilatant pathways, which may or may not interact with the continuum stress field; and (4) gas fracturing of the rock similar to that performed during hydrocarbon stimulation exercises (Harrington, 2016).

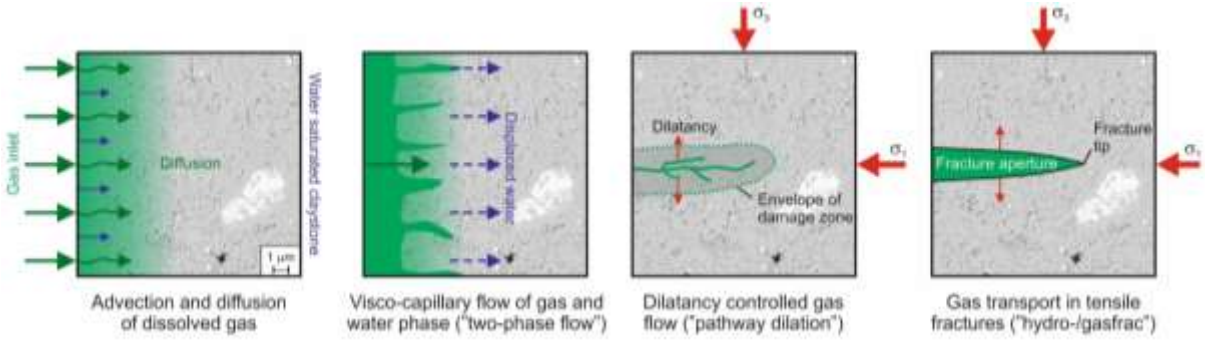

Figure 6-1. Conceptual models of gas flow (Harrington, 2016).

Studies on gas migration in clays (Horseman et al., 1999; 2004; Harrington and Horseman, 1999) indicate that classic concepts of porous medium two-phase flow are inappropriate and continuum approaches to modelling gas flow may be questionable, depending on the scale of the processes and resolution of the numerical model. However, the detail of the dilatant mechanisms controlling gas entry, flow and pathway sealing are unclear. As such, development of new and novel numerical representations for the quantitative treatment of gas in clay-based repository systems is therefore required (Harrington, 2016).

6.2 DECOVALEX-2019 Task A and International Modeling Teams

The purpose of Task A in DECOVALEX-2019 is to better understand the processes governing the adjective movement of gas in low permeability clay barrier materials (Harrington, 2016). Special attention is given to the mechanisms controlling factors such as gas entry and flow, as well as pathway stability and sealing, which will affect barrier performance. In Task A of DECOVALEX-2019, the participant international modeling teams will develop new numerical representations for the quantitative prediction of gas fluxes. The models will be tested against a series of controlled laboratory tests, in a staged manner, building in complexity (both in terms of the experimental and modelling approaches). It is anticipated that the development of these models will provide a valuable tool to assess the impact of gas flow on barrier and host materials, providing information which could be used to support future repository design.

Data from a series of flow tests performed on initially saturated samples will be made available to project participants. These long-term tests, performed under carefully controlled laboratory conditions, provide detailed datasets with which to examine gas migration behavior under steady state conditions. As such, a number of test geometries have been used, ranging in complexity from relatively simple one-dimensional flow tests on bentonite, to triaxial tests performed on natural samples of Callovo-Oxfordian claystone. To gain insights into the adjective movement of gas through these materials, laboratory data will be used to guide and benchmark numerical model development in an iterative process, increasing in model complexity from one test stage to the next (Harrington, 2016).

The initial plan of the task includes four distinct stages (Harrington, 2016):

- Stage 0 (code development):
    - Initial aim is to understand and reflect on the apparent stochastic behavior of all experimental data to be considered. References and publications will be made available and the teams will be asked to develop one or more modelling approaches.

- Stage 1: 1D gas flow through saturated bentonite under controlled laboratory conditions
    - Data will be provided from a 1D-gas flow test, performed on saturated bentonite subjected to a constant volume boundary condition.
- Stage 2: 3D spherical gas flow under controlled laboratory conditions
    - A: spherical flow through saturated bentonite, under a constant volume boundary condition.
    - B (optional): a second dataset under the same experimental boundary conditions is also offered, against which the models can be tested.
- Stage 3: Application of previous models to a natural clay-based system
    - A: triaxial test performed on a sample Callovo-Oxfordian claystone (Cox). This dataset comprises a number of stages including initial hydration, hydraulic testing and gas injection.
    - B (optional): gas flow through hydrated bentonite pellets under constant volume conditions. If appropriate, data from a long-term test performed by the Commission for Atomic Energy and Alternative Energies (CEA) will be made available for Teams participating in this task.

The following international organizations and modeling teams are involved in DECOVALEX-2019, Task A (gas migration in clay):

- UK: British Geological Survey (BGS-Task Leader)
- UK: Quintessa
- Germany: Bundesanstalt für Geowissenschaften und Rohstoffe (BGR)
- Germany: Helmholtz-Centre for Environmental Research (UFZ)
- USA: Sandia National Laboratory
- USA: Lawrence Berkeley National Laboratory
- France: Institut de Radioprotection et de Sûreté Nucléaire (IRSN)
- Korea: Korea Atomic Energy Research Institute (KAERI)
- Canada: Canadian Nuclear Safety Commission (CNSC)
- Spain: Universitat Politècnica de Catalunya (UPC)
- Taiwan: Taiwan Power Company (Taipower)

Currently, the modeling teams are working on Stage 1, which is the modeling of 1D gas flow through a saturated sample of MX-80 bentonite. The experimental data is provided to the DEOCOVALEX-2019 modeling teams by the task coordinators from BGS, who is also conducting the gas-migration experiments. The experiment is conducted on a cylindrical bentonite sample, 120 mm in height and 60 mm in diameter. The sample is placed in a pressure vessel that allows for monitoring of the evolution of pressure and stress at different locations along the sample, as well as inflow and outflow rates through filters (Figure 6-2).

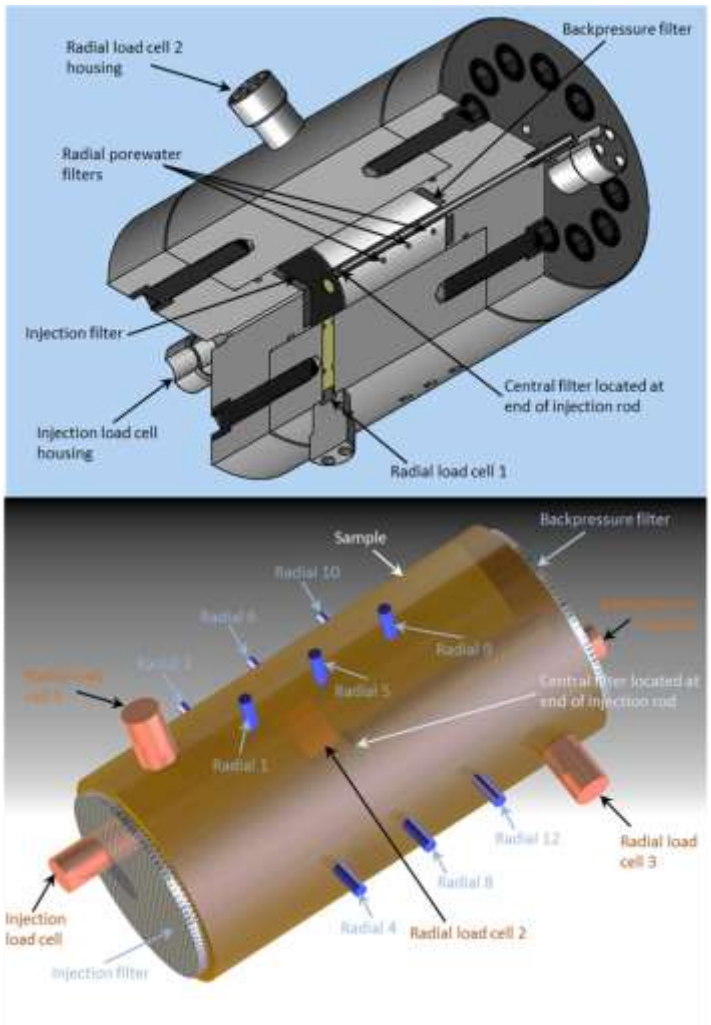

Figure 6-2. Above: Cut-away diagram of the pressure vessel showing the apparatus components and instrumentation. Below: image of the sample showing the relative positions of the load cells and pore pressure filters (Harrington, 2016).

Part of the experimental results related to pressure and outflow is shown in Figure 6-3. In the experiment, the bentonite sample was hydrated prior to gas testing through all radial and backpressure filters. The water was infiltrated and equilibrated at a pressure of 1 MPa. The hydration resulted in swelling and development of swelling stress within the sample (not shown here). Once total stress began to plateau, helium gas was introduced in to the injection filter at an initial pressure of 3 MPa (blue line Figure 6-3a and b). This was left to equilibrate with the water in the pump for 7 days. Thereafter, gas was injected into the injection chamber resulting in a gradual increase of injection gas pressure (blue line in Figure 6-3a and b), while keeping the back pressure constant at 1 MPa (yellow line in Figure 6-3a). When the injection pressure reached about 10 MPa, an abrupt increase in pressure was observed at monitoring points along the sample (green, red, purple lines in Figure 6-3a). At the same time, there is a sudden temporal increase of gas outflow (green line in Figure 6-3b). The injection is also shutdown and the injection pressure then goes down slowly along with pressure measured at other points along the sample.

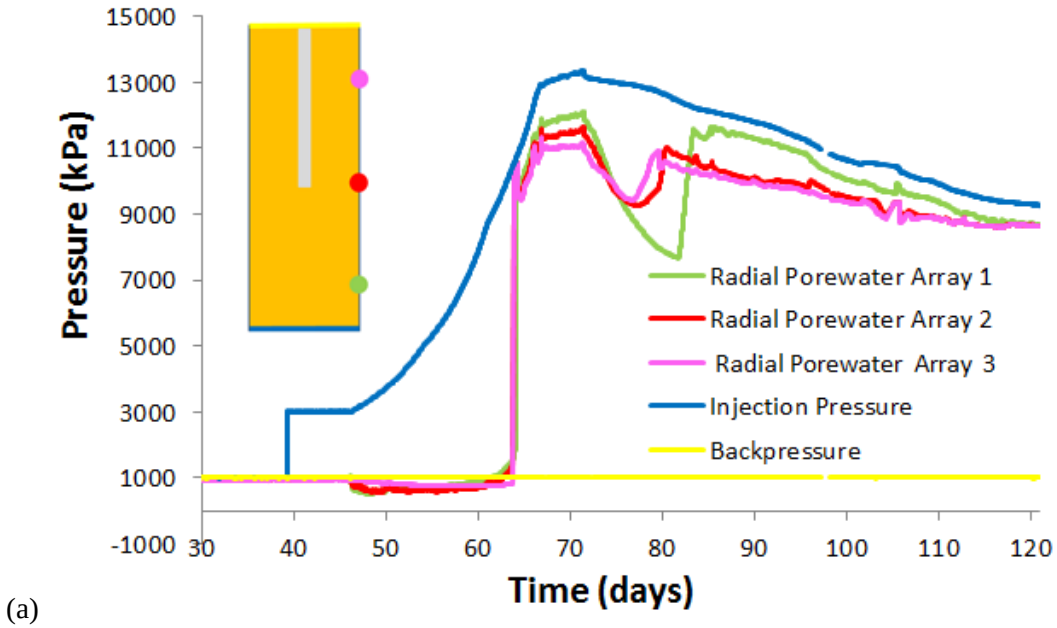

(a)

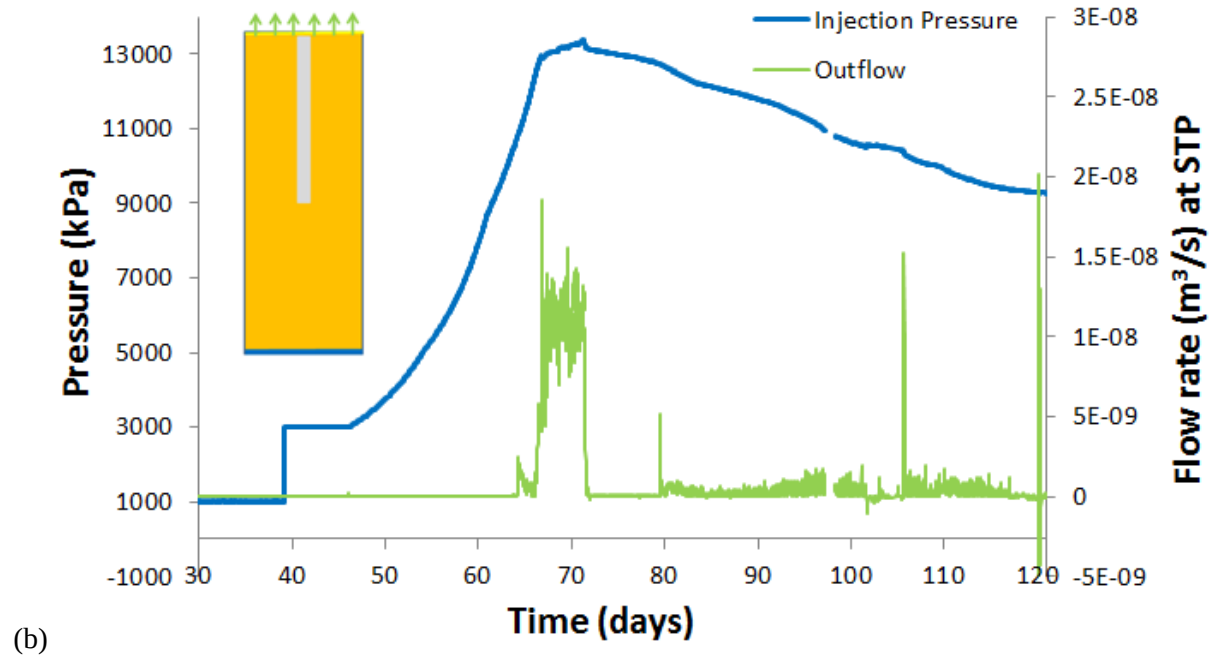

(b)

Figure 6-3. (a) Observed pressure evolution and (b) outflow rate (Modified from Harrington, 2016).

6.3 LBNL Modeling Approaches and Results

LBNL will explore two different approaches for modeling gas migration associated with DECOVALEX-2019; Task A (Figure 6-4):

1) Continuum modeling approach using TOUGH-FLAC simulator (Rutqvist, 2011)

2) Discrete fracture modeling approach using TOUGH-RBSN simulator (Kim et al., 2017)

The two approaches are complementary. The continuum approach will be based on current development and applications of TOUGH-FLAC on bentonite and clay host rocks for the modeling of long-term THM performance of nuclear waste repositories in clay host rocks. The TOUGH2 code and other continuum models have been used in the past to model gas migration in clay considering heterogeneous clay properties with pressure dependent permeability, but without considering geomechanical coupling (e.g., Senger and Marschall, 2008; Senger et al., 2014). In this study, such a continuum approach will be extended to include full geomechanics coupling within the framework of TOUGH-FLAC. The discrete fracture modeling approach will be based on current development of the TOUGH-RBSN simulator, in which the opening of grain boundaries for dilatant gas migration is modeled explicitly using a fracture mechanics approach. The TOUGH-RBSN has previously been applied for modeling fluid driven hydraulic fracturing and complex fracturing in clay host rocks (Kim et al., 2017). The TOUGH-RBSN should be suitable for modeling development of complex flow paths associated with dilatant gas migration in clays.

In the following two subsections, the approach and initial modeling results related to modeling of DECOVALEX-2019, Task A, Step 1are presented. This involves modeling of 1D gas migration through a 120 mm long sample of water saturated MX-80 bentonite.

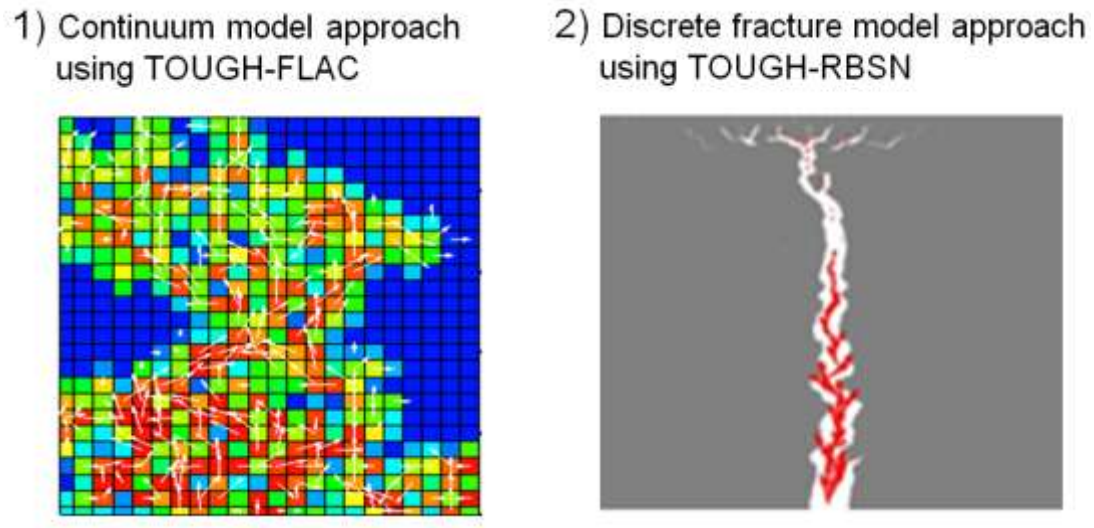

Figure 6-4. Schematic of modeling approach employed by LBNL for modeling gas migration through clay associated with DECOVALEX-2019 Task A. To the left, the continuum approach using TOUGH-FLAC is illustrated involving heterogeneous properties with the possibility of the formation of dilatant flow paths through pressure or stain dependent permeability in individual cells. The actual color figure to the left is from TOUGH2 modeling in Senger and Marschall (2008), in which the white arrows shows gas flow velocity and colors is gas saturation. To the right, the discrete fracture modeling approach using TOUGH-RBSN, involving complex fracturing to simulate the formation of dilatant flow paths. The red shows the fluid flow vectors and white shows the opening of fracture path.

6.3.1 TOUGH-FLAC modeling of gas migration experiments

As a first step in the continuum approach modeling, a sensitivity study was conducted using TOUGH2 (Pruess et al., 2012) to investigate the possibilities of modeling the abrupt gas flow responses shown in the experimental results shown in Figure 6-3. For this sensitivity study, an axisymmetric model was created as shown in Figure 6-5. In the base case modeling, the permeability and porosity was set to 3.4×10^{-21} m^2 and 44% respectively according to specifications given by the task lead. For the water retention curve, van Genuchten (1980) model was used with the capillary scaling parameter P_0 = 18 MPa and the shape parameter, λ = 0.45. The relative permeability of Corey (1954) was used for liquid and gas relative permeability. These parameters for water retention curve and relative permeability was selected based on previous work by Senger and Marschall (2008) on TOUGH2 modeling gas migration through MX-80 samples. In addition, following Senger and Marschall (2008), the residual saturation in the relative permeability function was set to S_{lr} = 0.9, assuming that 90% of the water is immobile over the duration of this gas migration experiment.

Two approached were tested for creating the abrupt changes in gas migration observed in the experiments: (1) a gas-entry pressure below which no gas could enter the sample and (2) a pressure-dependent permeability-simulating opening of a fracture-like flow path.

The gas entry pressure was simulated using residual gas saturation below which gas mobility is zero (Senger and Marschall, 2008). An effective gas-entry pressure, P_{ge} was defined by the capillary pressure at a given residual gas saturation. S_{gr} (Figure 6-6a). In this approach, the residual gas saturation is an input parameter for the relative permeability meaning that relative permeability and gas mobility will be zero when the gas saturation is less than S_{gr}. As seen from Figure 6-6a, to increase the gas saturation above this S_{gr} value, the capillary pressure $P_c = P_g - P_l$ should be higher than P_{ge}.

A pressure dependent permeability function was developed and tested, in which the permeability increases substantially when pressure reaches close to 10 MPa (Figure 6-6b). The particular form and equations for describing the pressure dependent permeability is summarized in Figure 6-7. We consider that a flow path opens in a fracture-like behavior and the aperture-vs-stress relationship corresponds to Bandis et al. (1983) model (Figure 6-7a). The input parameters for the stress-aperture function where calibrated by matching pressure and gas outflow responses observed in the experiments. σ_n would represent the total stress normal to the fracture; it is here set to 10 MPa so that substantial increase in permeability would occur at an injection pressure of about 10 MPa. Another parameter is the b_{h0}, which is the maximum aperture. It is here set to 3 μm. Thus, an opening of the flow path of only a few microns is simulated. Figure 6-7b shows how the equivalent permeability of the continuum elements is calculated based on the initial matrix permeability with superimposed fracture permeability.

In the following of this subsection some of the key simulation results of the sensitivity study are presented. The goal of this sensitivity study is to explore the possible mechanisms that could explain the abrupt gas migration behavior observed in the experiments.

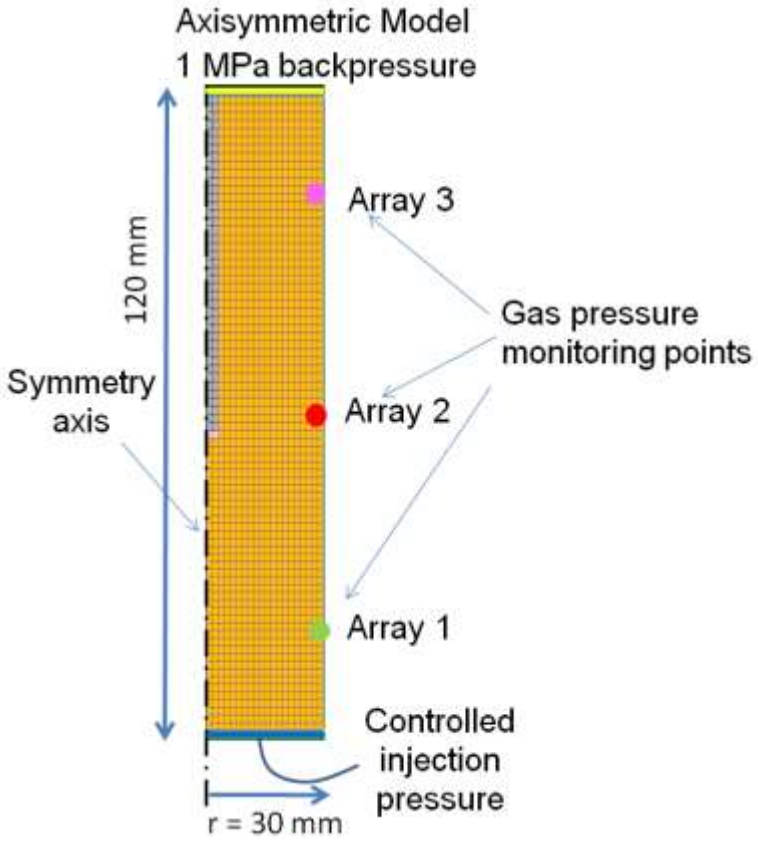

Figure 6-5. Axisymmetric model used for TOUGH2 sensitivity study of the gas migration experiment associated with DECOVALEX 2019, Task A.

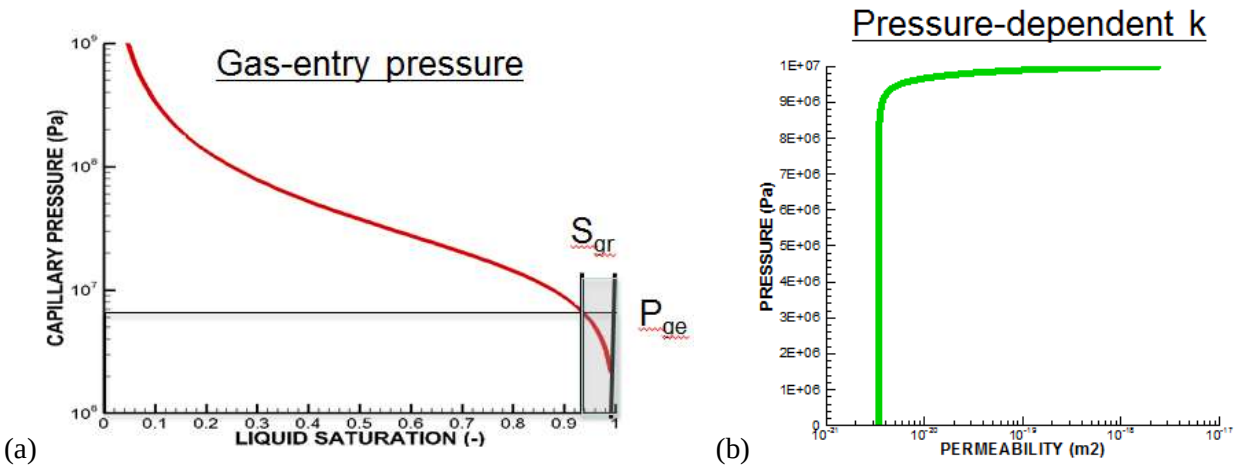

Figure 6-6. (a) van Genuchten (1980) capillary pressure curve used in the modeling for MX-80 bentonite and the concept of equivalent air-entry pressure, P_{ge}, using residual gas saturation, S_{gr}. (b) pressure-dependent permeability (see also Figure 6-7).

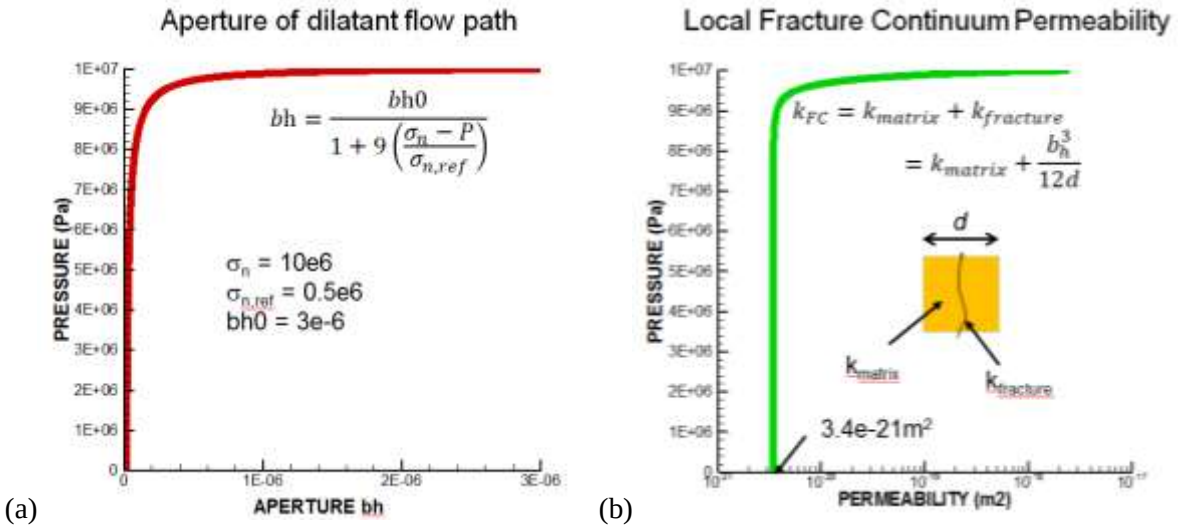

Figure 6-7. (a) Aperture-versus-pressure based on Bandis et al. (1983) model for normal-stress-versus-aperture relations, and (b) local fracture continuum permeability based on superposition of matrix and fracture permeability.

A base-case modeling was conducted with constant permeability of 3.4×10^{-21} m^2 and $S_{gr} = 0$, implying a low gas entry pressure and that gas can migrate into the bentonite at low injection pressure. The results in Figure 6-8 show that the pressure evolution and outflow display different characteristics from that of the experimental results in Figure 6-3. Specifically, the modeling results in Figure 6-8a does not show as abrupt pressure increase along the sample as in the experimental results in Figure 6-3a. Moreover, the outflow in the modeling is continuous and the maximum flow rate is much smaller than in the experiment. This indicates that some other mechanism is required to be able to model the abrupt behavior observed in the experimental data.

A simulation using the concept of an equivalent gas-entry pressure is presented in Figure 6-9. In this case, the residual gas saturation, S_{gr} was set to 0.03, which corresponds to an effective gas-entry pressure P_{ge} = 5 MPa. In the case, abrupt gas flow and pressure changes along the sample occurs when the injection pressure reaches about 6 MPa. Note that the initial liquid pressure in the sample is 1 MPa and therefore gas pressure should exceed $P_g = P_{ae} + P_l = 5 + 1 = 6$ MPa for gas entry. The simulation results in Figure 6-9b shows very similar behavior related to outflow from the sample, with an abrupt outburst during 5 days. In the simulation, this outburst occurred a little earlier than the observed because it was not possible to increase the S_{gr} sufficiently due to numerical issues. However, the simulated pressure evolution at monitoring points along the sample does not agree well with the observed pressure evolution in the experiment (compare Figure 6-9a with Figure 6-3a). The simulation capture the abrupt increase, but the maximum pressure along the sample is much smaller than the observed. This indicates that the gas permeability in the simulation is too low.

The final key simulation results presented is the use of pressure dependent permeability for simulating dilatant gas migration (Figure 6-10). In this case, the simulation is conducted with the pressure dependent permeability function shown in Figure 6-7b. In this case, the simulation can capture an abrupt increase in gas outflow when the injection pressure reaches about 10 MPa. After reaching the critical injection pressure of 10 MPa, the pressure at monitoring points away from the injection point reaches the same

magnitude as the injection pressure (Figure 6-10a). At the same time, the gas flow rate increases to about same maximum flow rate as that observed (compare Figure 6-10b and Figure 6-3b). However, in the simulation, the high gas flow rate continues for much longer time, whereas in the experiments, the gas flow shuts down much earlier.

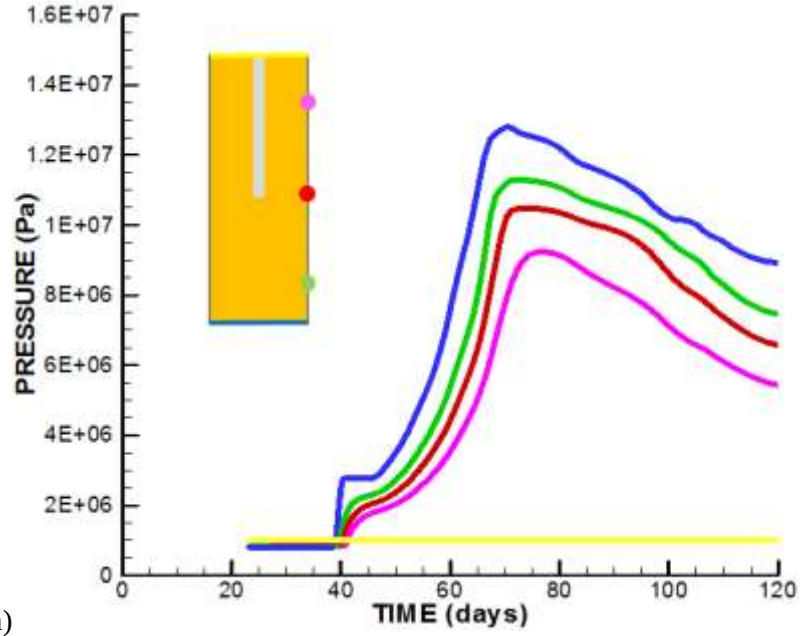

(a)

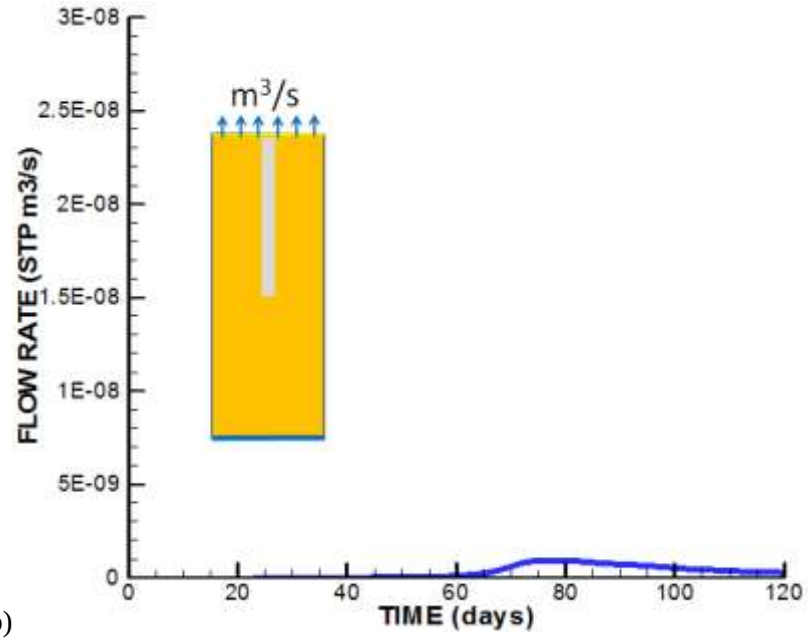

(b)

Figure 6-8. Base-case simulation results involving two-phase flow but without considering air-entry pressure or pressure-dependent permeability. Modeled evolution of (a) pressure, and (b) flow rate at standard temperature and pressure (STP).

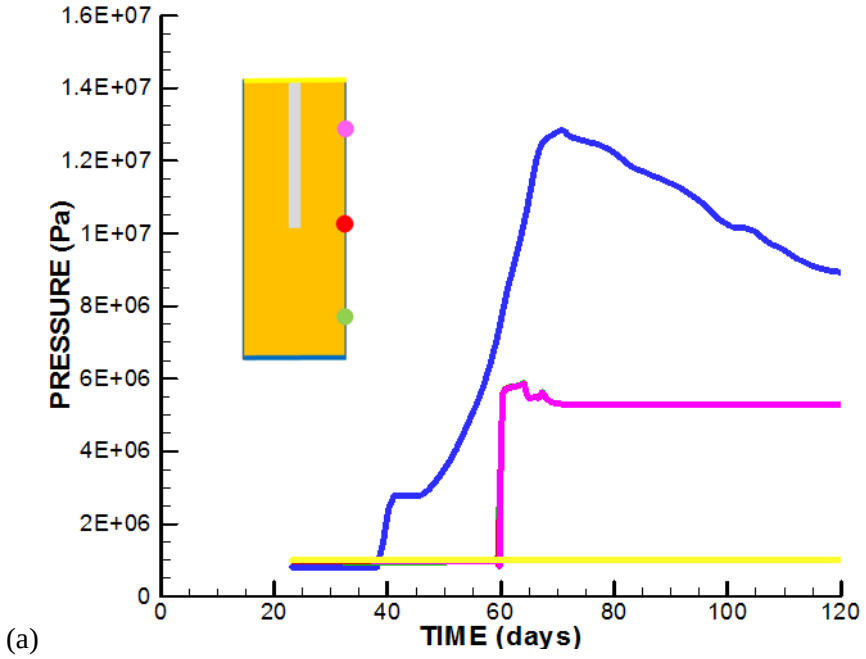

(a)

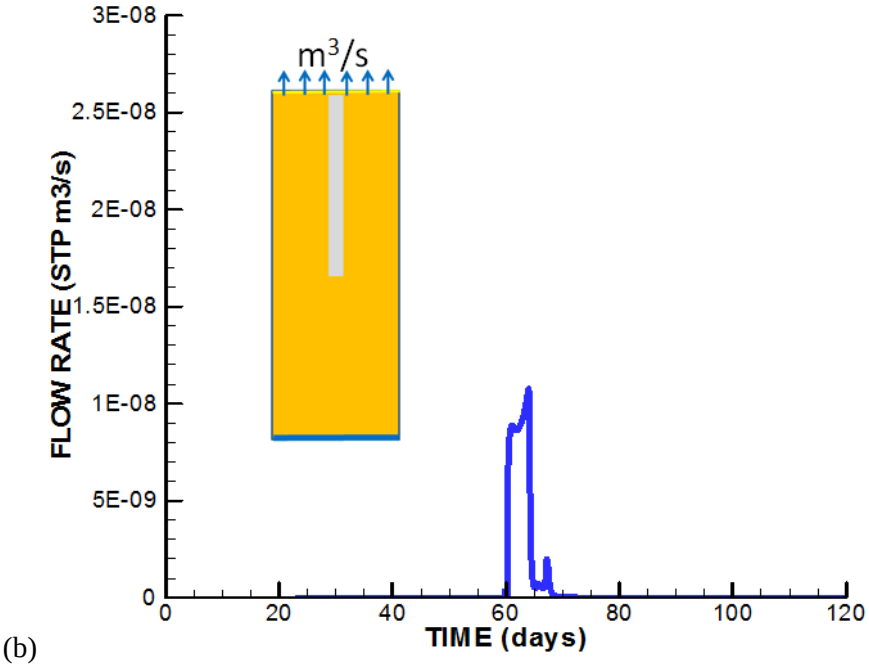

(b)

Figure 6-9. Simulation using the concept of equivalent air-entry pressure as described in Figure 6-6a, with an equivalent air entry pressure of approximately 5 MPa. Modeled evolution of (a) pressure, and (b) flow rate.

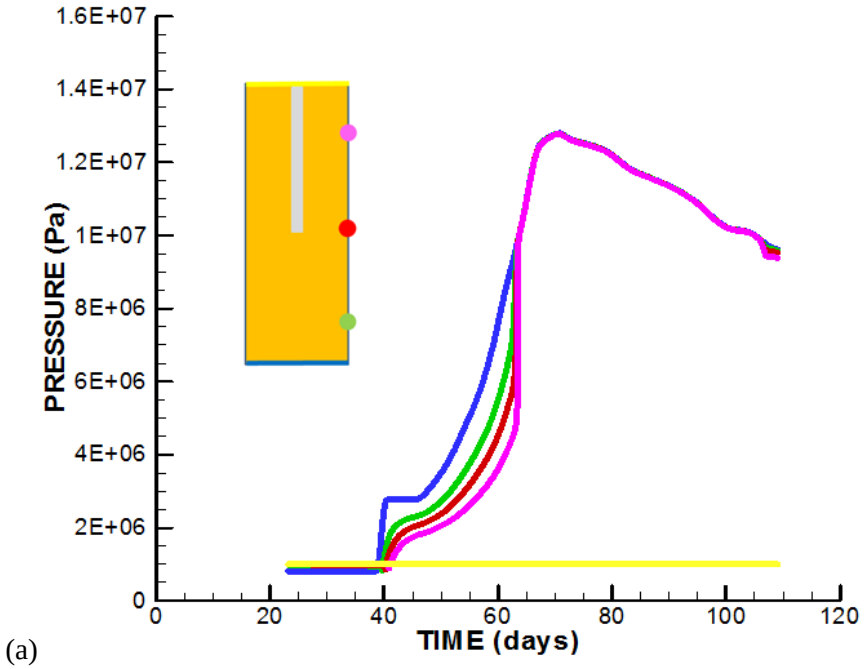

(a)

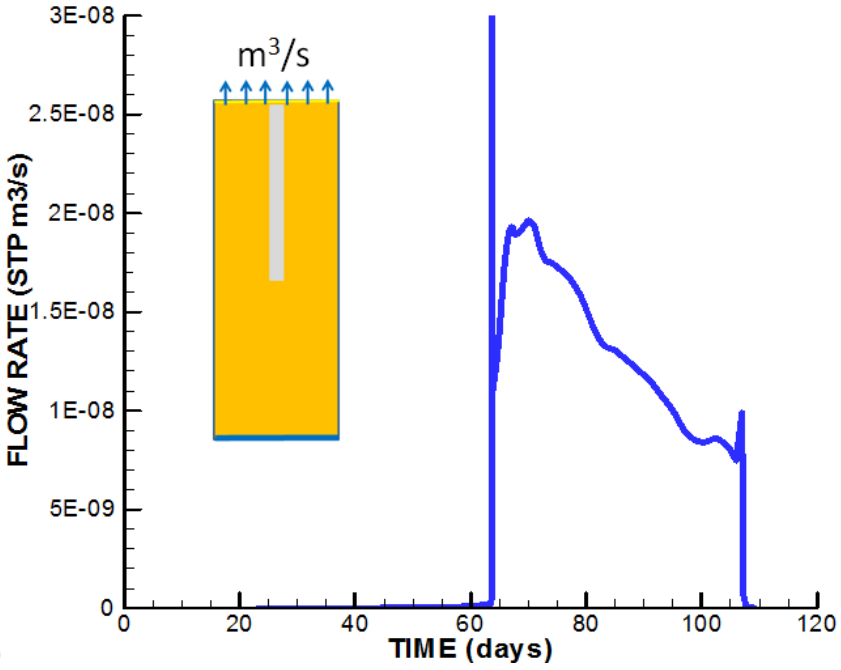

(b)

Figure 6-10. Simulation using pressure-dependent permeability as described in Figure 6-7, with a critical pressure of 10 MPa. Modeled evolution of (a) pressure, and (b) flow rate at standard temperature and pressure (STP).

In summary, the initial continuum modeling of gas migration shows that such modeling approach indeed can capture some of the phenomena observed in the laboratory experiments. Using the concept of gas-entry pressure and pressure-dependent permeability, the abrupt increase in gas flow rate could be simulated. An exact match of the observed data was not attempted in these initial simulations, but may be obtained by a combination of the two concepts of gas-entry pressure and pressure-dependent permeability. However, next step in the continuum modeling will be to employ the full hydromechanical coupling, using TOUGH-FLAC. This will involve modeling of the initial hydration and development of swelling pressure, followed by gas injection and permeability dependent on stress and strain. This will also involve the use of heterogeneous material properties for potential creation of localized dilation-induced flow paths.

6.3.2 TOUGH-RBSN modeling of gas migration experiments

As a complementary modeling approach to TOUGH-FLAC, the TOUGH-RBSN simulator has been used to demonstrate gas migration in the MX-80 bentonite. The most distinguishing feature of TOUGH-RBSN from TOUGH-FLAC and other continuum-based approaches is that it is capable of discrete representation of fracture formations during coupled THM processes. In the linkage between the TOUGH2 and RBSN codes, the hydrological and mechanical calculations are sequentially coupled to each other. The general coupling procedure is similar to that applied for the TOUGH-FLAC simulator (Rutqvist et al., 2002; Rutqvist, 2011), but the TOUGH-RBSN coupling modules have been substantially modified to account for the fluid flow through discrete fractures (Asahina et al., 2014; Kim et al., 2017).

The computational domain for both the TOUGH2 and RBSN calculations is tessellated using a Voronoi diagram (Okabe et al., 2000). The discretization process is carried out in three steps: 1) nodal point insertion, 2) Delaunay tessellation, and 3) Voronoi discretization. The dual Delaunay-Voronoi discretization is not only an effective method for partitioning a spatial domain, but also an essential part of the RBSN model formulation, which serves to scale the element coefficients for the system equations (Bolander and Saito, 1998; Berton and Bolander, 2006). Moreover, sharing the same grid geometry for the TOUGH2 and RBSN models enables a tight coupling without any spatial interpolation of primary variables.

The discrete fracture network (DFN) approach is facilitated in the Voronoi discretization via a fully automated modeling procedure. Voronoi cells generally represent the matrix component in a geomaterial constitution, and pre-existing or newly generated fractures are placed on the Voronoi cell boundaries. Pre-existing fractures and such discontinuities can be explicitly modeled within the Voronoi grid, for which the fracture geometry (e.g., orientation, length, curvature) are supplied from observational mapping data, computer-generated statistical reproductions, or mechanical simulation results. Kim et al. (2017) presented the modeling procedure for the DFN approach within TOUGH-RBSN in more detail.

The fracture process of a local rigid-body-spring element is realized by degrading the springs. A fracture event entails a reduction of spring stiffnesses and a release of the associated elemental forces. For the degraded spring set, the local stiffness matrix is

$$\mathbf{D}' = (1 - \omega)\mathbf{D} \tag{6.1}$$

where ω is a scalar damage index with a range from 0 (undamaged) to 1 (completely damaged). For brittle fracturing, which is applied to the cases presented in this report, ω is directly switched from 0 to 1 once a fracture event occurs (i.e., the stress state of the element exceeds the given material strength). To determine the criticality of the stress state, a stress ratio is calculated for each lattice element:

$$R_f = \sigma_e / \hat{\sigma} \tag{6.2}$$

where σ_e is the element stress state and $\hat{\sigma}$ is the critical stress defined by fracture criteria. Herein, the tensorial stress state of an element is considered to evaluate the stress criticality, which involves the calculation of nodal stress tensor.

The stress tensor at a Voronoi cell node is calculated from the equilibrium conditions of the spring forces. Sets of the spring forces are applied at the boundaries surrounding a Voronoi cell (Figure 6-11a), and nodal force components F_{nn}, F_{ns}, and F_{nt} can be calculated for an arbitrary section passing through the Voronoi cell node with its corresponding local *n*-*s*-*t* coordinates, which satisfy the equilibrium condition with all the forces acting on the remaining cell boundaries (Figure 6-11b). Moment contributions to equilibrium are not considered here. By dividing these force components by the cut-face area, the corresponding stress components σ_n, σ_s, and σ_t can be obtained. By repeating this process for three mutually perpendicular sections, the full stress tensor is obtained (Figure 6-11c). From the stress tensors at two neighboring nodes, the stress tensor of the inter-element is calculated according to

$$\bar{\boldsymbol{\sigma}} = (\boldsymbol{\sigma}_i + \boldsymbol{\sigma}_j)/2 \tag{6.3}$$

where $\boldsymbol{\sigma}_i$ and $\boldsymbol{\sigma}_j$ are the stress tensors at the neighboring nodes *i* and *j*, respectively. The maximum principal tensile stress of $\bar{\boldsymbol{\sigma}}$ serves as σ_e in equation (6.2). In this way, fracture under multiaxial stress conditions can be simulated.

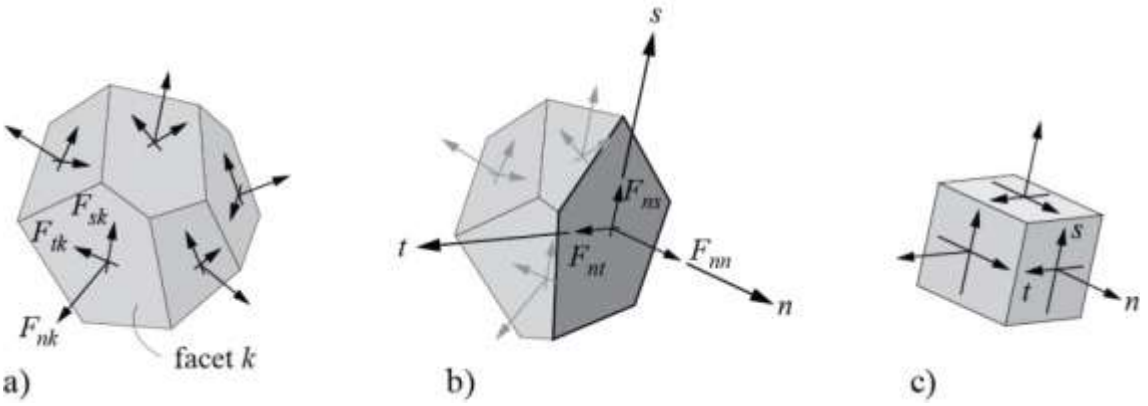

Figure 6-11. Stress tensor at a Voronoi cell node: a) components of spring force local coordinates; b) a set of nodal forces satisfying the equilibrium; and c) complete stress tensor at Voronoi cell node (Adapted from Yip et al., 2005).

For the simulations of 1D gas migration, a 120×60 mm rectangular domain is discretized as shown in Figure 6-12. Padding elements are added on the domain boundaries to facilitate a uniform mechanical confinement (fixed displacement boundary conditions). The initial confining stress values are given from the measurements of load cells in the experimental program (see Figure 6-2), which reads 9 MPa in the axial direction and 6 MPa in the lateral direction. Gas injection is controlled by injection pressure at the left boundary, and the constant backpressure of 1 MPa is kept at the right boundary during the simulations.

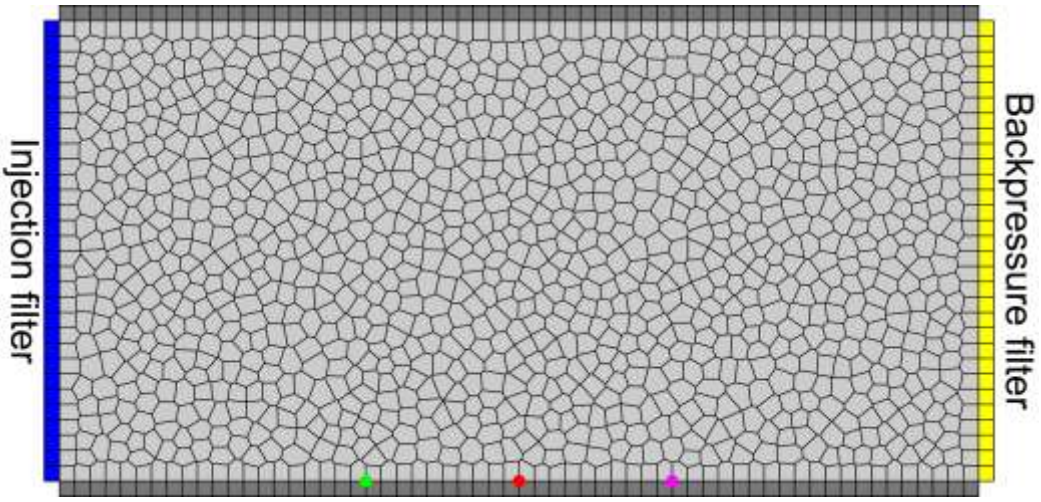

Figure 6-12. 2D rectangular grid for gas migration in the MX-80 sample. Colored marks indicate the measuring points of pressure evolutions during simulations.

The permeability and porosity of the sample are set to be 3.4×10^{-24} m^2 and 44%, respectively. The modeling permeability is three orders of magnitude smaller than the suggested value, but the initial gas entry before fracturing can be avoided with the low permeability. A fractured element increases its permeability following the cubic law with the fracture aperture, and sustains a residual permeability of 8.3×10^{-16} m^2 when the fracture is closed. van Genuchten-Mualem model (Mualem, 1976; van Genuchten, 1980) is adopted for relative permeabilities of liquid and gas phases, in which the relevant parameters are set as follows: the shape parameter $\lambda = 0.45$; the residual liquid saturation $S_{lr} = 0.9$; the limit saturation for complete liquid mobility (i.e., $k_{rl}=1$) $S_{ls} = 1.0$; and the residual gas saturation $S_{gr} = 0.01$. Figure 6-13 presents the two-phase relative permeability curves over liquid saturation.

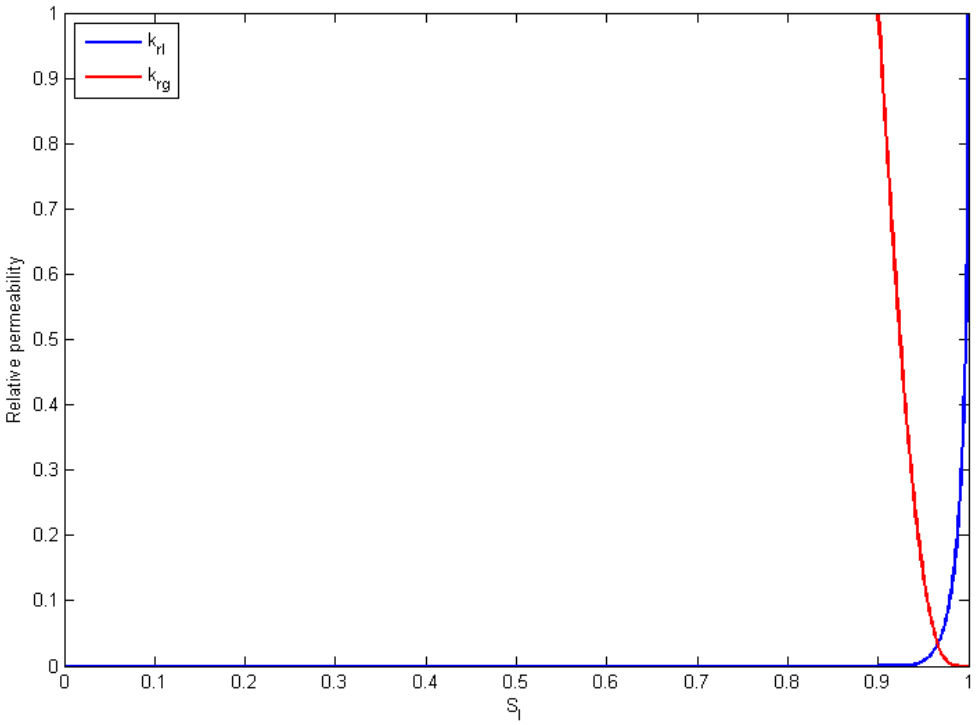

Figure 6-13. Relative permeability curves for two-phase flow using van Genuchten-Mualem model.

The sample was reported to be fully saturated in the experiments. However, with setting of the extremely low gas saturation, the convergence rate became too slow after the fracture initiation, so the simulation was nearly stalled with a very small time increment. This numerical issue will be further examined during the rest of FY2017. For the present, the initial gas saturation is set 0.1.

The MX-80 bentonite sample has high compliance and low strength relative to other geological materials. The mechanical properties are set as follows: Young's modulus E = 300 MPa; tensile strength f_t = 0.1 MPa; cohesive strength c = 0.1 MPa and internal friction angle β = 18° for Mohr-Coulomb failure criterion. Due to the fully confined boundary condition with the initial compressive stress condition, the fracture surfaces are more likely to be in contact, and thus the mechanical resistance may be somewhat recovered at the closed fractures. In this report, a sensitivity study has been conducted to investigate the possible dissimilarity in fracture propagation and the corresponding gas flow paths. Three cases are simulated with different degrees of recovery of the mechanical resistance: when the fracture is closed, Young's modulus of the fractured element is completely recovered ($\omega = 0$), 50% recovered ($\omega = 0.5$), and 10% recovered ($\omega = 0.1$), respectively.

Figure 6-14 arranges the snap shots of fracture patterns and pressure distributions around gas breakthrough with the full recovery of Young's modulus for closed fractures. Fractures initiate and propagate uniformly across the section up to about 10 mm from the injection boundary. Then, inclined fractures form gradually in next 4 days as if the sample is subject to a triaxial compression loading. At 68.7 days, a sudden breakthrough occurs by connecting the inclined fractures and reaching the backpressure boundary. However, the resulting fractures are not uniformly distributed across the section. The points for the pressure measurement (at the bottom boundary) are isolated from the connected fracture cluster, so the pressure evolutions are not changed during the simulation (Figure 6-15).

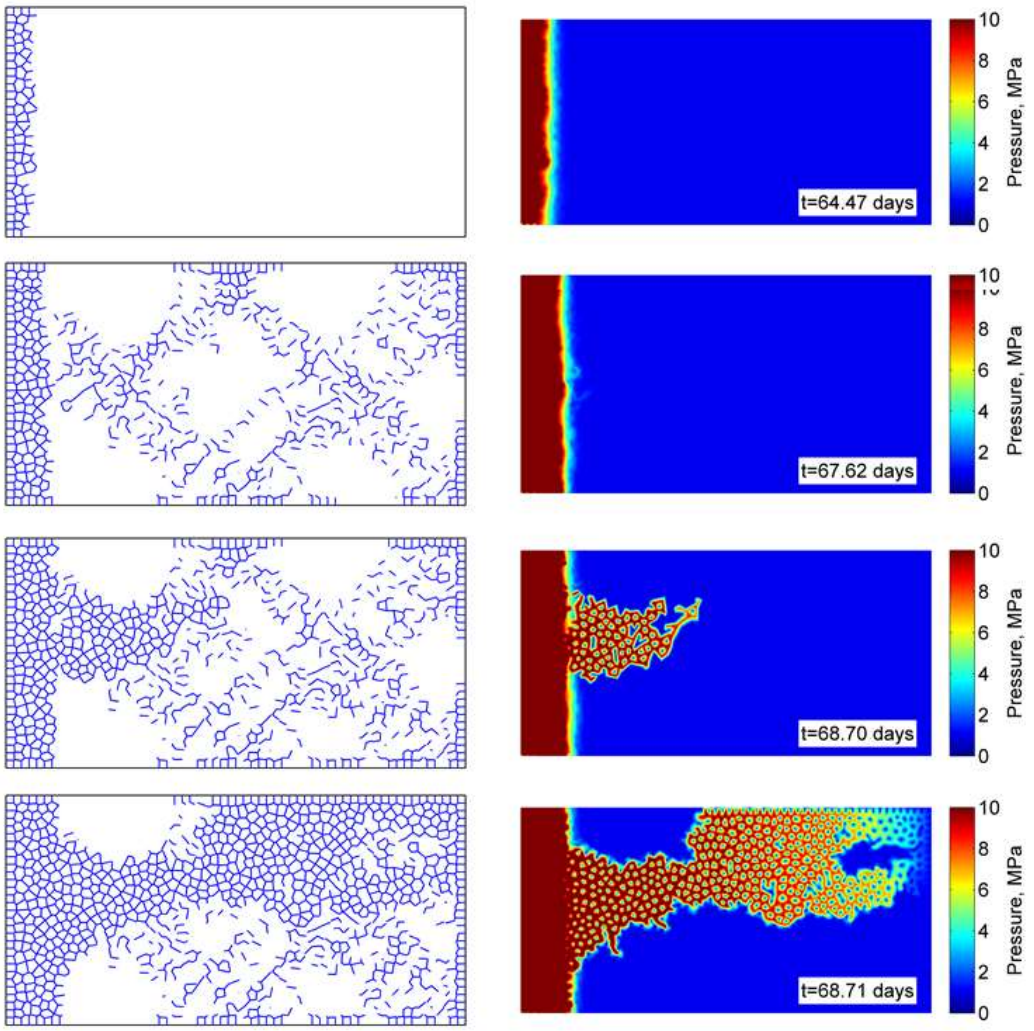

Figure 6-14. Fracture patterns and pressure distributions in the case of full recovery of Young's modulus for closed fractures.

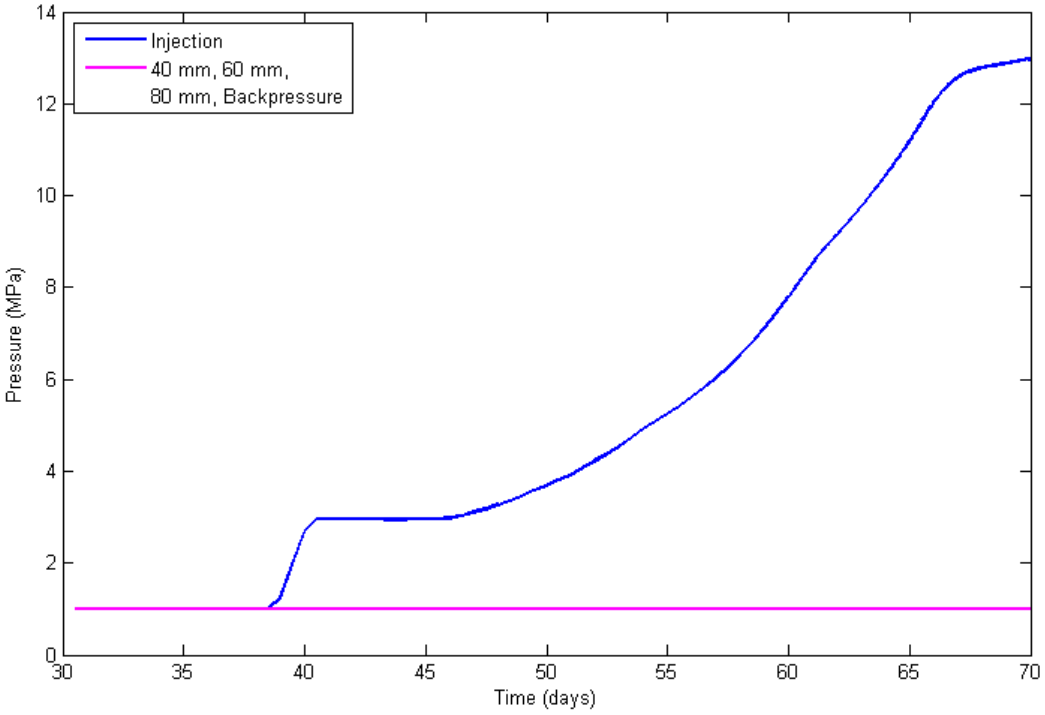

Figure 6-15. Pressure evolutions in the case of full recovery of Young's modulus for closed fractures.

In the next case, 50% of mechanical resistance is recovered for closed fractures. The fracture patterns and pressure distributions are presented in Figure 6-16. In the beginning of the fracture propagation, fractures are distributed uniformly across the section, which is similar to the first snap shot in Figure 6-14. However, unlike the previous case, the second stage of fracture propagation forms a uniform sectional pattern. Interestingly, a strip of intact zone exists between the first stage and the second stage of fracture propagation. Once the two stages are bridged with fractures at the upper left part of the domain, an accelerated flow is realized in the second stage of fractures. There is another gap between the second stage and third stage of fracture propagation, which acts like a flow barrier. Figure 6-17 presents abrupt pressure increases in the domain when the breakthrough occurs. Finally, the steady-state flow demonstrates the pressure evolutions grading with the distance from the injection boundary.

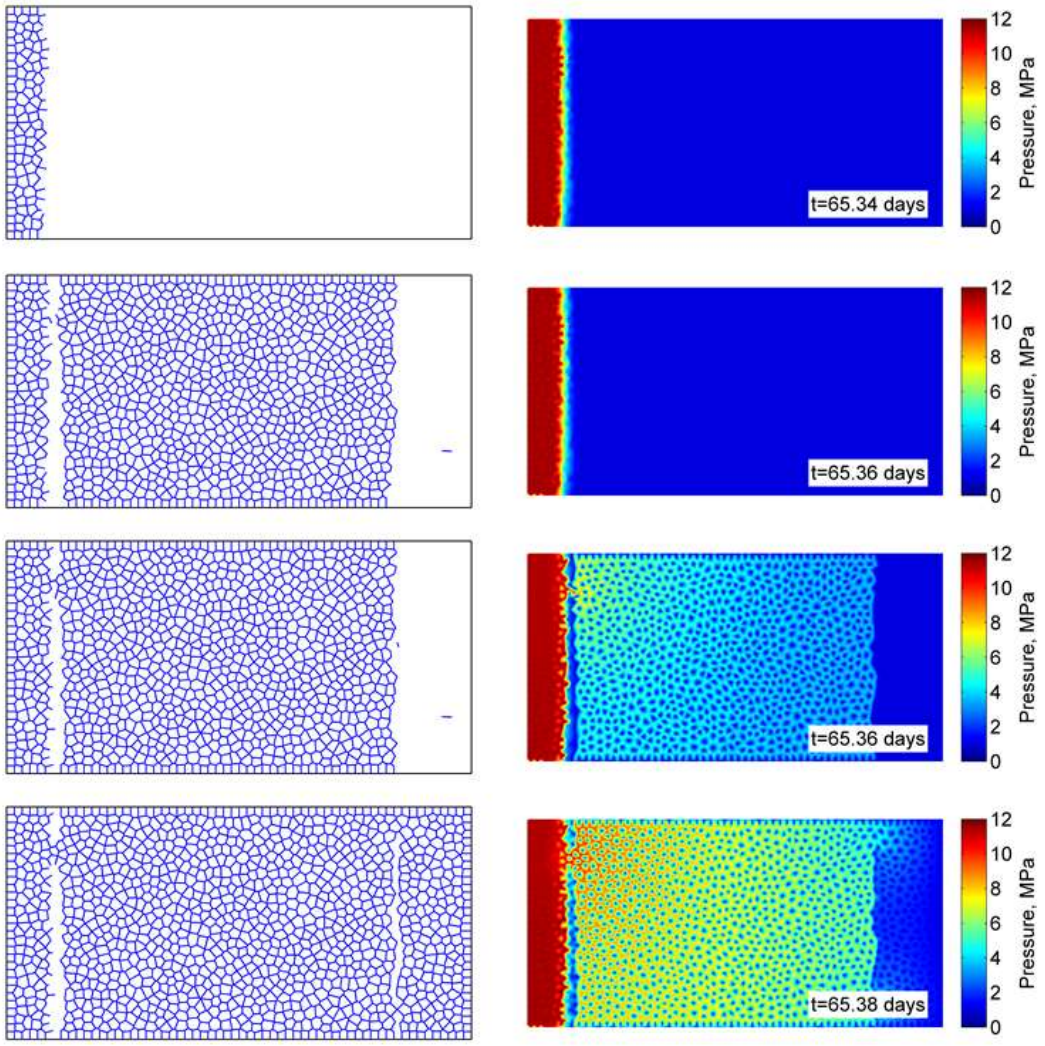

Figure 6-16. Fracture patterns and pressure distributions in the case of 50% recovery of Young's modulus for closed fractures.

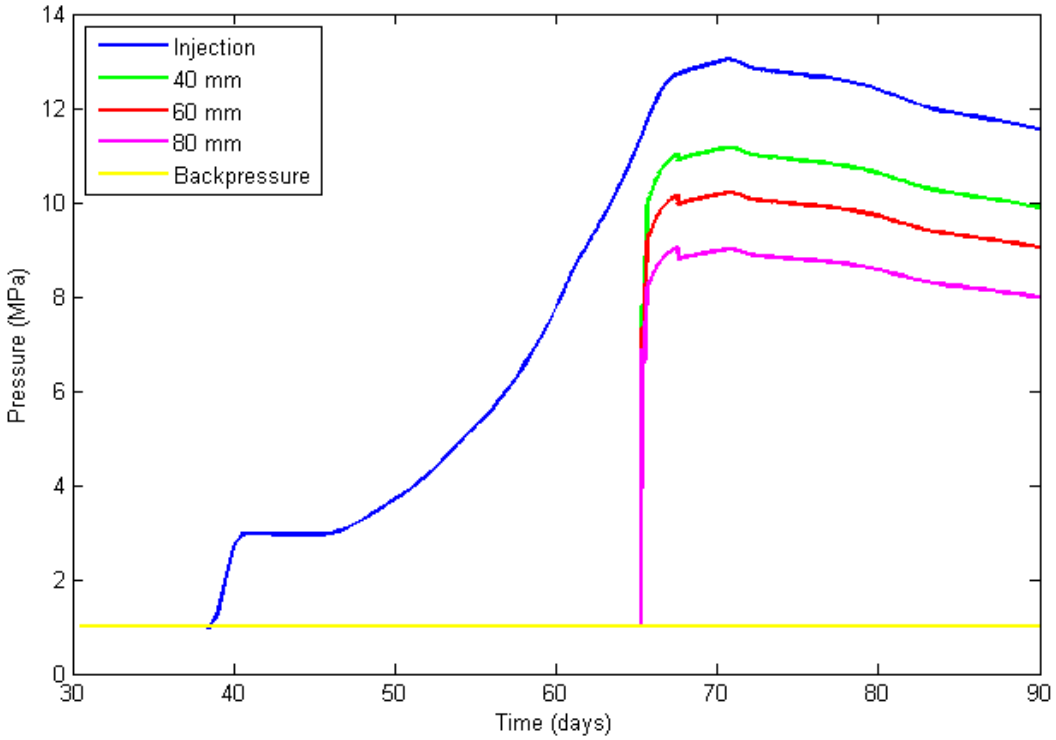

Figure 6-17. Pressure evolutions in the case of 50% recovery of Young's modulus for closed fractures.

As shown in Figure 6-18, 10% recovery of Young's modulus for closed fractures leads to more uniform fracture propagation and, thus gas migration is close to 1D flow through the fractures. Fractures initiate from the injection boundary, and almost all rigid-body-spring elements are fractured throughout the domain. However, the last layer of elements is not fractured so the fracture network is not connected to the backpressure boundary, so the pressure measurement of the fracture network is uniform in the steady-state flow. Figure 6-19 indicates that the three measuring points exhibit abrupt pressure increases at the same time, and the pressure measurements track exactly the injection pressure in the steady-state flow.

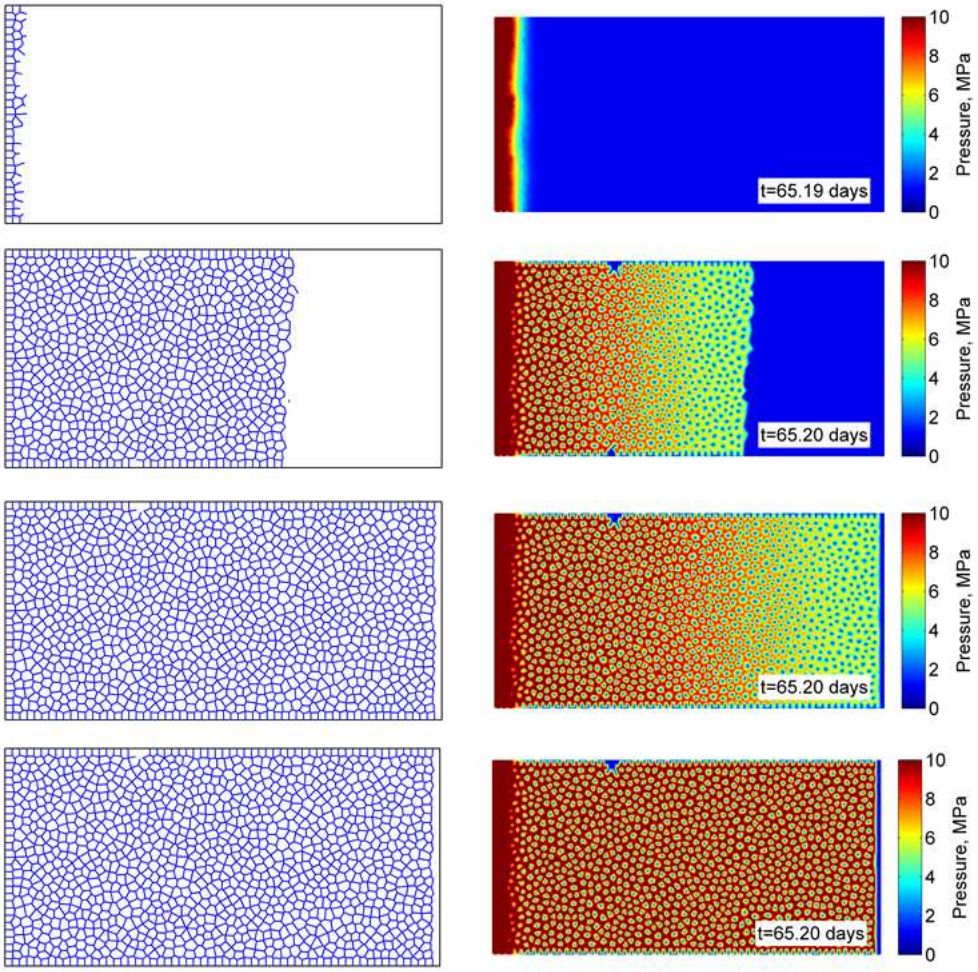

Figure 6-18. Fracture patterns and pressure distributions in the case of 10% recovery of Young's modulus for closed fractures.

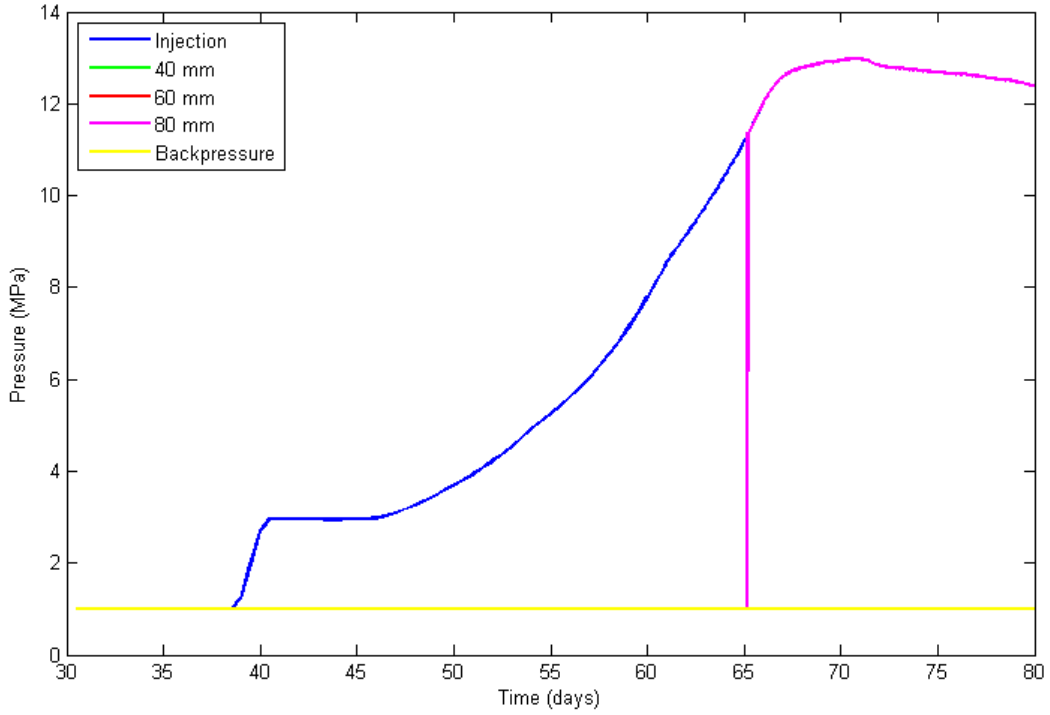

Figure 6-19. Pressure evolutions in the case of 10% recovery of Young's modulus for closed fractures.

In summary, the gas migration in the discrete fractures can be demonstrated using the TOUGH-RBSN simulator. As an initial step of the modeling task, the simulation results are not exactly matched with the experimental data, but some key features such as abrupt pressure increase due to fracturing in the domain can be captured from the coupled hydro-mechanical simulation results. In the next step, the simulation results are expected to be more plausible by tuning the modeling parameters. The numerical issues of the slow convergence rate and the stalling problem (with very small time increments) also will be addressed.

6.3.3 Summary and Status of Gas Migration Modeling

The initial simulations of gas migration using TOUGH-FLAC and TOUGH-RBSN, shows that both approaches can be used to capture some of the key responses of dilatancy controlled gas flow. During the rest of FY2017, we plan to expand the continuum modeling using full hydromechanical coupling in TOUGH-FLAC, involving stress and strain dependent permeability to simulate the creation of dilatant flow path through an embedded fracture approach. To more effectively model gas-driven discrete fracture propagation, TOUGH-RBSN simulation will continue to resolve some of the numerical issues. For FY2018, we propose to continue to participate in the DECOVALEX-2019 Task A, with access to additional laboratory data, for better understanding of the processes of dilatancy controlled gas migration and to develop the models.

7. SUMMARY

(1) TOUGH-FLAC and Modeling of Heater experiments at Mont Terri and Bure URLs (Section 2)

DOE and LBNL greatly benefit from participating in these international activities for developing expertise and testing advanced models for coupled THM processes to be used for predicting long-term THM evolution of a multibarrier nuclear waste repository system, involving backfilled emplacement tunnels in argillite host formations. FY2017 work has been focused on modeling of the FE experiment at Mont Terri in Opalinus clay and the TED experiment at Bure URL in Cox clay stone. Participating in these two international activities provides experience and model validation for two different clay stone host rocks and for two different repository design concept; the emplacement in horizontal tunnels (Swiss concept) and emplacement in micro-tunnels, extended from the walls of larger tunnels (French concept).

For the rest of remainder of FY2017 we plan to improve the interpretative modeling of the FE experiment related to the relative humidity evolution in the bentonite blocks. We will also review the current evolution of the stress in the buffer, to determine if swelling stress is starting to develop and can be used for model validation. Related to the modeling of the heater experiments at Bure, the modeling of the TED experiment will be improved by considering excavation effects on absolute pressure. Moreover, we will initiate modeling of the larger scale ALC experiment as a part of the upscaling task within the DECOVALEX-2019 project

The FY2018 work on the Mont Terri FE experiment will be focused on modeling of the mechanical evolution of the buffer and host rock, including the application of the BExM model at a large scale. It will be a great opportunity to apply and test the BExM at the larger scale on the FE experiment, in particular because one the other international modeling teams is the University of Catalonia group in Barcelona, Spain that is the origin of the BExM model and they will apply BExM for the modeling of the Mont Terri FE experiment, but using a different numerical simulator. At the same time we will continue to validate and gain experiences in the use of the BExM. We will also expand the analysis with more comparison of the host rock behavior, including the excavation disturbed zone.

The FY2018 work on the heater experiments at Bure will be focused on the modeling of the large-scale ALC experiment. This will first involve a predictive analysis of the coupled THM behavior, using the model and THM parameters that were calibrated against the smaller scale TED experiment. This will involve comparison to the modeling results of other international modeling teams within the DECOVALEX-2019 project.

(2) Investigation of the impacts of high temperature limits with THMC modeling (Section 3)

In FY16, THMC models utilize dual structure Barcelona Expansive Clay Model (BExM) (Sánchez et al., 2005) to link mechanical process with chemistry, allowing us to simultaneously incorporate the effects of exchangeable cations, ionic strength of pore water and abundance of swelling clay on the swelling stress of bentonite. In FY17, we re-calibrated the parameters of BExM Model for FEBEX bentonite, and used it on a generic repository to consider the interaction between EBS bentonite and the NS argillite formation. The following observations have been concluded from the model results:

- Three chemical changes including the change in the volume fraction of smectite, change in exchangeable cations and ionic strength contribute distinctively to the stress evolution in bentonite. In current model, decrease in the volume fraction of smectite leads to a decrease in stress; Because the enrichment of exchangeable sodium in the interlayer, the change in exchangeable cations cause the increase in stress; The infiltration of more concentrated water from clay formation to EBS bentonite leads to the increase in osmotic suction and subsequently lowers the stress. The combination of these three effects determines whether chemical change enhances or suppresses the stress. The chemical changes as a whole reduce both total stress and

effective/net stress in the bentonite buffer in the "high T" cases. The difference between the result computed with MC coupling ("THMC") and the result without MC coupling ("THM") ranges from 0.6 MPa to 1 MPa in bentonite.

- In comparison with the THMC that used extended linear swelling model (Zheng et al., 2015), THMC model using BExM showed less pronounced chemical effect on stress. The first reason is that exchangeable cations which was not able to be taken into account by extended linear swelling model, is now considered in BExM. For FEBEX bentonite, change in exchangeable cations has positive effect on the stress, which cancel out the negative effect due to the change of ionic strength (via osmotic suction) and consequently the chemical change overall has less effect on stress in THMC model using BExM than that in the THMC model that used extended linear swelling model. The second reason is that the MC coupling via BExM, the dissolution of smectite was factored in directly via the volume fraction of smectite by modifying the bulk modulus for micro-structure, but in BExM, bulk modulus is a function of stress and change significantly in the model, the bulk modulus changes by smectite dissolution was overshadowed by the stress change.

The current coupled THMC model greatly improves our understanding of the coupled processes contributing to chemical and mechanical alteration in EBS bentonites and argillite formations and answers questions regarding the thermal limit of EBS bentonite in clay repository. However, more questions remain to be answered regarding the THMC alteration of bentonites and clay formations under high temperature. Further refinement of current models and improvements for the TOUREACT-FLAC3D simulator are needed in the future. The following activities are proposed for FY18:

- The calibration on parameters of BExM for specific material is needed for better prediction of the material behavior during in-situ experiments.
- The model needs to be simplified to improve its numerical robustness and to apply easily on different materials.

While the generic THMC models shed light on various aspects of chemical alteration of bentonite and its impact of mechanical properties of bentonite, predictions based model that has been calibrated against THMC data will provide more tangible results and further deepen our understanding the long term alteration of bentonite. The THMC model that has been calibrated for the FEBEX *in situ* was extended to 100,000 years with a modified boundary condition for the canister. Model results show significant dissolution of smectite and precipitation of illite, quartz and K-feldspar, which are very different from the results in the generic THMC models. The main reason is that the water in granite host rock in the model for FEBEX *in situ* test has much lower ion concentrations than the water in clay formation host rock in the generic model, which completely changes the reaction path and leads much more dissolution of smectite in bentonite in the model for FEBEX *in situ* test. The predictions by the model for FEBEX *in situ* test indicate that interaction between EBS bentonite and host rock is critical for the alteration in EBS bentonite.

In FY17 up to now, the THMC model for the FEBEX *in situ* test was extended for 100,000 years to predict the bentonite alteration in granite host rock. The boundary condition for the canister was modified to make a case that the temperature at the canister surface peaks at 100 °C. In order to evaluate the impact of higher temperature on bentonite, in the remaining months of FY17 and FY18, high temperature case in which the temperature at the canister surface reaches 200 °C will be created to evaluate bentonite alteration in granite host rock under high temperature.

(3) Understanding the THMC evolution of bentonite in FEBEX-DP— Coupled THMC modeling and examination of the structure of bentonite (Section 4)

Coupled THMC modeling

The FEBEX *in situ* test that lasted more than 18 years is extremely valuable for validating the coupled THMC model and deepening our understanding of the evolution of the bentonite barrier over the course of heating and hydration. In the FEBEX-DP project, heater #2 was dismantled and extensive THMC characterization was conducted. The ultimate goal is to use THMC data from FEBEX-DP to validate THMC models and therefore enhance our understanding of coupled THMC processes in bentonite.

Since FY15, the model for the FEBEX *in situ* test evolved from TH model to THMC model. Significant efforts were dedicated to understand the lower-than-expected relative humidity data near the heater, hypotheses that have been tested include Non-Darcian flow, swelling via Barcelona Expansive Clay model or linear swelling model, various constitutive relationships for saturated permeability in bentonite as functions of either stress or dry density. After extensive calibration, THMC models developed in FY16 (Zheng et al., 2016) matched reasonably the measured temporal evolution of temperature, relative humidity and stress at several compliance points in the bentonite barrier and the measured spatial distribution of water content and dry density at 5.3 years when the heater #1 was dismantled and at 18.3 years when the heater #2 was dismantled. However, they failed to explain the spatial profile of chloride concentration at 5.3 years. In FY17, the THMC model was further revised by adding thermal osmosis and using a revised permeability-dry density relationship. After the model reproduced reasonablly THM data and spatial profile of chloride concentration at 5.3 years, the model predictions of the concentration profile were tested against the calibrated ion concentration in the pore water for the samples collected during the dismantling of heater #2. The major findings from current modeling work are as follows:

- Chemical data are actually important for calibrating THM model. The model that was tested with more types of data is more reliable.
- The key coupling processes that are required to match THM data and concentration of conservative species (e.g., chloride) include vapor diffusion, porosity change due to swelling, permeability change as a function of dry density (or porosity), and thermal osmosis.
- The THMC model predicted nicely the chloride concentration profile at 18.3 years. Model results show that high chloride concentration (up to 1.2 mol/L) is expected near the heater, which might be important for waste form degradation.
- The THMC model also predicted decently the concentration data of sodium, potassium and pH. However, the model fell short of matching the concentration of sulfate, bicarbonate, calcium and magnesium. Chemical species that are involved in more chemical reactions are more challenging to predict.

In the remaining months of FY17 and FY18, as more chemical data beside ion concentrations are available, the chemical model will be further improved based on the synthesis of all chemical data, to answer important questions relevant to performance assessment. Specifically the chemical model will be improved in the following aspects:

- The evolution of redox conditions in the bentonite barrier needs to be added to the model. A thorough understanding of the evolution of redox conditions, especially near the canister, is critical for studying canister corrosion and waste form degradation. A synthesis of measured gas concentrations, biological data and redox sensitive minerals and aqueous species will be conducted and an updated chemical model will integrate all these reactions.
- Bentonite-canister interaction, e.g., the corrosion of canister and interaction of corrosion products with bentonite will be improved, and model will be tested against measured mineralogical phase change in bentonite and canister.

Quantitative characterization of the fracture network in the FEBEX samples

Although the comparison between model and THMC data has been very helpful in calibrating the "right" relationships (or key parameters for the relationships), uncertainties in other processes and interaction of coupled processes might result in non-unique sets of parameters that could lead to equal or similar reasonable fit between model and data. Checking the microstructure of the bentonite buffer will serve as additional evidence to delineate the right permeability change functions and increase the predictability of models. Bentonite samples were taken from the FEBEX *in situ* test after the dismantling of heater #2. In FY16 and FY17, we have conducted a series of synchrotron X-ray microCT (SXR-μCT) examination of the microstructure of bentonite samples. The major accomplishments are as follows:

- A total of 5 samples from different locations were examined with three duplicates for each sample. Fracture networks for each sample were identified and quantified. We found that the variability among duplicates from the same location in bentonite barrier is significant, mostly linked to the heterogeneity of the material. Nevertheless some weak correlation has been found: the ratio of large to small aperture fractures is larger from samples with higher water content (they are also close to the bentonite/granite interface). In other words, samples closer to the bentonite/granite interface tend to have a larger amount of large fractures, whereas samples close to the heater or to the center of the section tends to have larger amount of small fractures. While a truly statistically meaningful validation of this result is still needed, this correlation is clearly present in our sample survey. It is noteworthy that a larger amount of measurements would be experimentally impractical to carry out, and the quantitative analyses of 5 different samples with 3 duplicates for each sample that were accomplished in this report is already something not commonly found in the SXR-μCT literature.
- SXR-μCT imaging was also conducted for a sample at the "as is" state (the state that we received from the FEBEX *in situ* test) and a heated state under unconfined conditions. Comparison between the fracture network before and after heating showed heating completely modified the microstructure of the material, generating a pervasive network of fractures, both very large in size with a expansive network of small ones especially in the clay aggregates of the sample, but whether this is due to the heating itself or moisture loss over the course of heating needs further study. While we are fully aware that the sample was heated under different conditions than what would be expected in the field, such an exercise seems to emphasize the importance of keeping bentonite well hydrated to ensure a good sealing effect.
- During the experiment, we also addressed some important technical issues: (1) we have found *the best resolution vs. field of view compromise, and representativeness issues as well*. We have tried to maximize the analyzed volume while avoiding losing important details due to too low resolution. (2) *We have successfully developed a protocol/software for the analysis of the fracture network, focusing on the aperture value distributions.*

At this stage, the results suggest that SXR-μCT is an ideal tool for checking the micro-structure of clay-based backfill for a nuclear waste repository, and providing some quantitative parameters to directly compare different samples. This opens new opportunities to advance the research in the bentonite barrier such as:

- *Testing the behavior of different candidate sealing materials before deploying them.*

  This includes advanced characterization (multi-technique, when needed) and *in situ* experiments. As an example, analyses could be conducted to check different clay vs. aggregate ratios, different type of clays, the use of surfactants / antiflocculants / interlayer exchangeable molecules / etc. to obtain clay aggregates with different mechanical properties and/or response to dehydration, or even completely different sealing materials. The ability of *in situ* heating also provides the unique

opportunity to see directly the modification of the sample during the loss of moisture. XR-µCT can also be coupled with other XR scattering-based techniques when a precise correlation with the hydration state of the clay structure (wide-angle X-ray powder diffraction) or the size of the clay tactoids (small-angle X-ray scattering) needs to be directly correlated with the development of desiccation cracks (e.g., Suuronen et al. 2014).

- - *Using the measured datasets to build predictive tools.*

  Besides the visualization and quantitative characterization of the sealing materials, SXR-µCT is also able to provide 3D volume datasets which can be used in a digital rock physics context: if the volume(s) obtained are meaningful, in terms of resolution vs. field of view, for measuring a given property, specific software able to calculate those properties (such as permeability, invasion of non-wetting fluids, diffusion, etc.) from the datasets are available or under development. This ability of calculating some physical properties of the samples following the SXR-µCT measurement would complete the path that started from the scientific question and would result with a predictive tool available to the scientific community.

(4) Scoping calculation in support of HotBENT, an experiment that study the effects of high temperatures on clay buffers/nearfield (section 5)

Raising the maximum allowed temperature for clay-based EBS has clear benefit for crystalline and argillite repository such as decreasing the footprint of the repository. However, higher temperatures can lead to complex processes that affect the performance of a repository that cannot be realistically reproduced and properly (non-conservatively) assessed at the smaller laboratory scale. Such an assessment needs to be conducted by large in-situ experiments in underground research laboratories (URLs), where the most relevant features of future emplacement conditions can be adequately reproduced. Therefore, HotBENT, a high-temperature experiment (200 °C) in a fractured rock environment are currently being considered under the leadership of NAGRA with several international partners, including DOE (Vomvoris et al., 2015). In FY17, the design of the experiment should be finalized, and, if enough international partners join the project, the heater test is expected to start in 2018. LBNL has very actively participated in the project since the very beginning. In this report, we present scoping calculations to facilitate the final design of the experiment. The accomplishments include 2-D TH models to evaluate the impact of heater length on the temperature distribution, and 1-D axi-symmetrical coupled THMC models to illustrate the expected THMC response in the hot sections. The major findings from these simulations include:

- In comparison with the 4.5 m long heater used in the FEBEX *in situ* test, model results suggest that a 3 m long heater of for HotBENT will be enough to have sufficient area that has a similar temperature distribution to satisfy the multi-purpose sampling requirements.
- HotBENT with a heater of 200 °C will lead to a temperature around 90 °C in granite, thus boiling in granite is therefore probably not a concern.
- Most part of bentonite barrier for HotBENT with a heater of 200 °C will stay dry for a very long time — a 18 year long simulation shows that bentonite is far from being fully saturated.
- Despite the higher temperature in HotBENT, the stress is actually lower than that in the FEBEX *in situ* test (where the heater temperature was 100 °C).
- In HotBENT, very high concentrations of chloride (up to 3 mol/L) are expected.
- A HotBENT with a heater of 175 °C does not significantly differ from the case with a heater of 200 °C in terms of hydrological behavior.

- Artificial hydration from the middle of bentonite barrier is effective in saturating the bentonite barrier, but it complicates the spatial water content distribution.
- Artificial hydration from the bentonite-granite interface is ineffective because water mostly flows into the higher permeability granite.

In the remaining months of FY17 and FY18, we will continue to use a coupled THMC model to facilitate the final design of HotBENT, specifically we have the following tasks planned:

- More sensitivity analyses to key design variables will be conducted
- In HotBENT, the heater will be emplaced on a pedestal and the bentonite barrier will be filled in with bentonite pellets. Therefore the hot sections will be represented by two 1-D THMC models: one for the pellet bentonite and another for the pedestal area
- The modeling work will focus on predicting the evolution of chemical variables (salinity, mineral phase, etc.), mechanical variables (stress, swelling pressure, etc.), HM coupling (porosity-stress, permeability-porosity and possibly MC coupling (swelling stress-salinity, swelling stress-smectite, etc.).

(5) Modeling of gas migration in clay using TOUGH-FLAC-flac and TOUGH-RBSN (DECOVALEX-2019) (Section 6)

The initial simulations of gas migration using TOUGH-FLAC and TOUGH-RBSN, shows that both approaches can be used to capture some of the key responses of dilatancy controlled gas flow. During the rest of FY2017, we plan to expand the continuum modeling using full hydromechanical coupling in TOUGH-FLAC, involving stress and strain dependent permeability to simulate the creation of dilatant flow path through an embedded fracture approach. TOUGH-RBSN simulation will continue to resolve some of the numerical issues to be able to more effectively model gas-driven discrete fracture propagation. For FY2018, we propose to continue to participate in the DECOVALEX-2019 Task A, with access to additional laboratory data, for better understanding of the processes of dilatancy controlled gas migration and to develop the models.

8. ACKNOWLEDGEMENTS

This work was supported by the Spent Fuel and Waste Science and Technology Campaign, Office of Nuclear Energy, of the U.S. Department of Energy under Contract Number DE-AC02-05CH11231 with Lawrence Berkeley National Laboratory.

9. References

Abu Al-Rub, R.K., Voyiadjis, G.Z. (2003). On the coupling of anisotropic damage and plasticity models for ductile materials. International Journal of Solids and Structures 40, 2611–2643.

Alonso, E.E., Gens, A., Josa, A. (1990). A constitutive model for partially saturated soils. Geotechnique. 40: 405-430.

Asahina, D., Houseworth, J.E., Birkholzer, J.T., Rutqvist, J., and Bolander, J.E. (2014). Hydro-mechanical model for wetting/drying and fracture development in geomaterials, Computers & Geosciences, 65, 13–23.

Bandis, S.C., Lumsden, A.C., Barton, N.R. (1983). Fundamentals of rock joint deformation. International Journal of Rock Mechanics and Mining Sciences and Geomechanic Abstracts, 20(6):249–68.

Bárcena, I., Fuentes-Cantillana, J.L., García-Siñeriz, J.L. (2003). Dismantling of the Heater 1 at the FEBEX "*in situ*" test. Description of operations. Enresa Technical Report 9/2003.

Berton, S., Bolander, J.E. (2006). Crack band model of fracture in irregular lattices, Computer Methods in Applied Mechanics and Engineering, 195, 7172–7181.

Bolander, J.E., Saito, S. (1998). Fracture analyses using spring networks with random geometry, Eng. Fract. Mech., 61, 569–91.

Booker, J.R., Savvidou, C. (1985). Consolidation around a point heat source. International Journal for Numerical and Analytical Methods in Geomechanics 9, 173–184.

Bossart, P. (2011). Characteristics of the Opalinus Clay at Mont Terri, http://www.mont-terri.ch/internet/mont-terri/en/home/geology/key_characteristics.html

Bradbury, M.H., Baeyens, B. (2003). Porewater chemistry in compacted resaturated MX-80 bentonite. Journal Contaminant Hydrology 61, 329–338.

Bradbury, M.H., Baeyens, B. (2005). Modelling the sorption of Mn(II), Co(II), Ni(II), Zn(II), Cd(II), Eu(III), Am(III), Sn(IV), Th(IV), Np(V) and U(VI) on montmorillonite: Linear free energy relationships and estimates of surface binding constants for some selected heavy metals and actinides. Geochimica et Cosmochimica Acta 69(4): 875-892.

Brandl, H. (2006). Energy foundations and other thermo-active ground structures. Géotechnique 56, 81–122.

Casciello, E., Cosgrove, J.W., Cesarano, M., Romero, E., Queralt, I., Vergés, J. (2011). Illite-smectite patterns in sheared Pleistocene mudstones of the Southern Apennines and their implications regarding the process of illitization: A multiscale analysis. Journal of Structural Geology 33(11): 1699-1711.

Castellanos, E., Villar, M.V, Romero, E., Lloret, A., Gens, A. (2008). Chemical impact on the hydro-mechanical behaviour of high-density FEBEX bentonite. Physics and Chemistry of the Earth, Parts A/B/C 33, Supplement 1(0): S516-S526.

Chaboche, J.-L. (1992). Damage induced anisotropy: On the difficulties associated with the active/passive unilateral condition. International Journal of Damage Mechanics 1, 148–171.

Chen, Y., Zhou, C., Jing, L., (2009). Modeling coupled THM processes of geological porous media with multiphase flow: theory and validation against laboratory and field scale experiments. Computers and Geotechnics 36 (8), 1308–1329.

Corey, A.T. (1954). The Interrelation Between Gas and Oil Relative Permeabilities, Producers Monthly, 38-41, November 1954.

Cuadros, J. (2006). Modeling of smectite illitization in burial diagenesis environments. Geochimica et Cosmochimica Acta 70(16): 4181-4195.

Cuss, R.J., Harrington, J.F., Noy, D.J., Graham, C.C., Sellin, P. (2014). Evidence of localised gas propagation pathways in a field-scale bentonite engineered barrier system; results from three gas injection tests in the Large scale gas injection test (Lasgit). Applied Clay Science, 102, pp.81-92, doi:10.1016/j.clay.2014.10.014Harrington J (2016) Specification for DECOVALEX-2019: Task A: modElliNg Gas INjection ExpERiments (ENGINEER). Ref: BGS-DX-v3.

David, C., Wong, T.-F., Zhu, W., Zhang, J. (1994). Laboratory measurement of compaction-induced permeability change in porous rocks: Implications for the generation and maintenance of pore pressure excess in the crust. Pure Appl. Geophys. 1994;143:425-456.

Detzner, K., Kober, F. (2015). FEBEX-DP drilling and sampling report sections 32-34, Internal report, AN15-714, NAGRA.

Dirksen, D. (1969). Thermo-osmosis through compacted saturated clay membranes. Soil Sci. Soc. Am. Proc., 33(6): 821-826.

ENRESA (2000). Full-scale engineered barriers experiment for a deep geological repository in crystalline host rock FEBEX Project, European Commission: 403.

ENRESA (2006a). FEBEX: Updated final report. ENRESA Tech. Publ. PT 05-0/2006, 589 pp.

ENRESA (2006b). FEBEX: Final THG modelling report. ENRESA Tech. Publ. PT 05-3/2006, 155 pp.

Fernández, A., Cuevas, J., Rivas, P. (2001). Pore water chemistry of the FEBEX bentonite. Mat. Res. Soc. Symp. Proc. 663, 573–588.

Fernández, A., Rivas, P. (2003). Task 141: post-mortem bentonite analysis. geochemical behaviour. CIEMAT/DIAE/54520/05/03, Internal Note 70-IMA-L-0-107 v0.

Fernández, A.M., Baeyens, B., Bradbury, M., Rivas, P. (2004). Analysis of the porewater chemical composition of a Spanish compacted bentonite used in an engineered barrier. Physics and Chemistry of the Earth, Parts A/B/C 29(1): 105-118.

Fernández, A.M., Sánchez-Ledesma, D.M., Melón, A., Robredo, L.M., Rey, J.J., Labajo, M., Clavero, M.A., Carretero, S., González, A.E. (2017). Thermo-hydro-geochemical behaviour of a Spanish bentonite after dismantling of the FEBEX *in situ* test at the Grimsel Test SitePore water chemistry of the FEBEX bentonite. CIEMAT report, CIEMAT/DMA/2G216/03/16.

Fernández, A.M., Turrero, M.J., Sánchez, D.M., Yllera, A., Melón, A.M., Sánchez, M., Peña, J., Garralón, A., Rivas, P., Bossart, P., Hernán, P. (2007). On site measurements of the redox and carbonate system parameters in the low-permeability Opalinus Clay formation at the Mont Terri Rock Laboratory. Physics and Chemistry of the Earth, Parts A/B/C 32(1-7): 181-195.

Garcia-Sineriz, J.L., Abós, H., Martínez, V., De la Rosa, C., Mäder, U., Kober, F. (2016). FEBEX-DP Dismantling of the Heater 2 at the FEBEX "*in situ*" test. Nagra Arbeitsbericht NAB 16-011. p. 92

Garitte B., Gens A. (2012). TH and THM Scoping computations for the definition of an optimal instrumentation layout in the Full-scale Emplacement (FE) experiment NAGRA NIB 10-34, March 2012.

Gens, A. (2010). Soil environment interactions in geotechnical engineering. Géotechnique 60, 3-74.

Gens, A., Alonso, E. (1992). A framework for the behaviour of unsaturated expansive clays. Can. Geotech. J. 29, 1013–1032.

Gens, A., Sánchez, M., Guimaraes, L.D.N., Alonso, E.E., Lloret, A., Olivella, S., Villar, M.V., Huertas, F. (2009). A full-scale *in situ* heating test for high-level nuclear waste disposal: observations, analysis and interpretation. Geotechnique 59, 377–399

Gens, A., Sánchez, M., Sheng, D. (2006). On constitutive modelling of unsaturated soils. Acta Geotechnica. 1, 137-147.

Ghabezloo, S., Sulem, J., Guédon, S., Martineau, F. (2009). Effective stress law for the permeability of a limestone. Int. J. Rock Mech. Min. Sci., 46:297-306.

Ghassemi, A., Diek, A. (2002). Porothermoelasticity for swelling shales. Journal of Petroleum Science and Engineering, 34: 123-125.

Guimarães, L.D.N., Gens, A., Sánchez, M., Olivella, S. (2013). A chemo-mechanical constitutive model accounting for cation exchange in expansive clays. Géotechnique 63, 221–234

Hardin, E., Bryan, C., Ilgen, A., Kalinina, E., Teich-Goldrick, S., Banerjee, K., Clarity, J., Howard, R., Jubin, R., Scaglione, J., Perry, F., Zheng, L., Rutqvist, J., Birkholzer, J.T., Greenberg, H., Carter, J., Severynse, T. (2014). Investigation of Dual-Purpose Canister Direct Disposal Feasibility, Prepared for U.S. Department of Energy Used Fuel Disposition Campaign, FCRD-UFD-2014-000069 REV 1, Sandia Laboratories.

Harrington, J. (2016). Specification for DECOVALEX-2019: Task A: modElliNg Gas INjection ExpERiments (ENGINEER). Ref: BGS-DX-v3

Harrington, J.F., Horseman, S.T. (1999). Gas transport properties of clays and mudrocks. In: Muds And Mudstones: Physical And Fluid Flow Properties (eds A.C.Aplin, A.J. Fleet, and J.H.S. Macquaker). Geological Society of London, Special Publication No. 158, 107-124.

Harrington, J.F., Milodowski, A.E., Graham, C.C., Rushton, J.C., Cuss, R.J. (2012). Evidence for gas-induced pathways in clay using a nanoparticle injection technique. Mineralogical Magazine. December 2012, Vol. 76(8), pp.3327-3336. DOI: 10.1180/minmag.2012.076.8.45.

Hayakawa, K., Murakami, S. (1997). Thermodynamical modeling of elastic-plastic damage and experimental validation of damage potential. International Journal of Damage Mechanics 6, 333–363.

Hicks, T.W., White, M.J., Hooker, P.J. (2009). Role of Bentonite in Determination of Thermal Limits on Geological Disposal Facility Design, Report 0883-1, Version 2, Falson Sciences Ltd., Rutland, UK, Sept. 2009.

Horseman S.T., McEwen, T.J. (1996). Thermal constrains on disposal of heat-emitting waste in argillaceous rocks, Engineering Geology 41, 5-16.

Horseman, S.T., Harrington, J.F., Sellin, P. (1999). Gas migration in clay barriers. Engineering Geology, Vol. 54, 139-149.

Horseman, S.T., Harrington, J.F., Sellin, P. (2004). Water and gas flow in Mx80 bentonite buffer clay. In: Symposium on the Scientific Basis for Nuclear Waste Management XXVII (Kalmar), Materials Research Society, Vol. 807. 715-720.

Houseworth, J., Rutqvist, J., Asahina, D., Chen, F., Vilarrasa, V., Liu, H.-H., Birkholzer, J. (2013). Report on International Collaboration Involving the FE Heater and HG-A Tests at Mont Terri. Prepared for U.S. Department of Energy, Used Fuel Disposition Campaign, FCRD-UFD-2014-000002, Lawrence Berkeley National Laboratory.

Huertas, F.B. de la Cruz, J.L. Fuentes-Cantillana, et al. (2005). Full-Scale Engineered Barriers Experiment for a Deep Geological Repository for High-Level Waste in Crystalline Host Rock – Phase II. EUR 21922.

Itasca (2009). FLAC3D, Fast Lagrangian Analysis of Continua in 3 Dimensions, Version 4.0, Minneapolis, Minnesota, Itasca Consulting Group.

Itasca (2011). FLAC3D V5.0, Fast Lagrangian Analysis of Continua in 3 Dimensions, User's Guide. Itasca Consulting Group, Minneapolis, Minnesota.

Kachanov, L. (1958). Rupture time under creep conditions. Izvestia Akademii Nauk SSSR, Otdelenie tekhnicheskich nauk 8, 26–31.

Kak, A.C., Slaney, M. (1988). Principles of computerized tomographic imaging (pp. 5-47). IEEE press.

Kamei, G., Mitsui, M.S., Futakuchi, K., Hashimoto, S., Sakuramoto, Y. (2005). Kinetics of long-term illitization of montmorillonite—a natural analogue of thermal alteration of bentonite in the radioactive waste disposal system. Journal of Physics and Chemistry of Solids 66(2–4): 612-614.

Kuhlman U., Gaus I. (2014). THM Model validation modelling of selected WP2 experiments: Inverse Modelling of the FEBEX in situ test using iTOUGH2. DELIVERABLE-N°: D3.3-1, NAGRA.

Kim, J., Tchelepi, H.A., Juanes, R. (2011). Stability and convergence of sequential methods for coupled flow and geomechanics: Fixed-stress and fixed-strain splits. Comput. Methods Appl. Mech. Engrg. 200, 1591–1606.

Kim, K., Rutqvist, J., Nakagawa, S., Birkholzer, J. (In Press, 2017). TOUGH-RBSN simulator for hydraulic fracture propagation within fractured media: Model validations against laboratory experiments. Computers & Geosciences.

Kristensson, O., Åkesson, M. (2008). Mechanical modeling of MX-80 – Quick tools for BBM parameter analysis. Phys Chem Earth, Parts A/B/C. 33, Supplement 1: S508-S515.

Kwon, O., Kronenberg, A.K., Gangi, A.F., Johnson, B. (2001). Permeability of Wilcox shale and its effective pressure law. J. Geophys. Res.-Sol. Ea., 106:19339-53.

Lauber, M., Baeyens, B., Bradbury, M.H. (2000). Physico-Chemical Characterisation and Sorption Measurements of Cs, Sr, Ni, Eu, Th, Sn and Se on Opalinus Clay from Mont Terri. PSI Bericht Nr. 00-10 December 2000 ISSN 1019-0643.

Liu, H.H., Houseworth, J., Rutqvist, J., Zheng, L., Asahina, D., Li, L., Vilarrasa, V., Chen, F., Nakagawa, S., Finsterle, S., Doughty, C., Kneafsey, T., Birkholzer, J. (2013). Report on THMC modeling of the near field evolution of a generic clay repository: Model validation and demonstration, Lawrence Berkeley National Laboratory, August, 2013, FCRD-UFD-2013-0000244.

Lloret, A., Alonso, E.E. (1995). State surfaces for partially saturated soils, In proceedings of the International Conference on Soils Mechanics and Foundation Engineering, Balkema, pp. 557-562.´

Lloret, A., Villar, M.V., Sánchez, M., Gens, A., Pintado, X., Alonso, E.E. (2003). Mechanical behaviour of heavily compacted bentonite under high suction changes. Géotechnique 2003; 53(1):27–40.

MacDowell, A.A., Parkinson, D.Y., Haboub, A., Schaible, E., Nasiatka, J.R., Yee, C.A., Jameson, J.R., Ajo-Franklin, J.B., Brodersen, C.R. and McElrone, A.J. (2012). October. X-ray micro-tomography at the Advanced Light Source. In SPIE Optical Engineering+ Applications (pp. 850618-850618). International Society for Optics and Photonics.

Montes-H., G., Fritz, B., Clement, A., Michau, N. (2005). Modelling of geochemical reactions and experimental cation exchange in MX80 bentonite. Journal of Environmental Management 77(1): 35-46.

Mosser-Ruck, R. Cathelineau, M. (2004). Experimental transformation of Na, Ca-smectite under basic conditions at 150 C. Applied Clay Science 26(1): 259-273.

Mualem, Y. (1976). A New Model for Predicting the Hydraulic Conductivity of Unsaturated Porous Media, Water Resour. Res., 12(3), 513–522.

Nutt, M. (2011). Used Fuel Disposition Campaign Disposal Research and Development Roadmap (FCR&D-USED-2011-000065 REV0), U.S. DOE Used Fuel Disposition Campaign.

Ochs, M., Lothenbach, B., Shibata, M., Yui, M. (2004). Thermodynamic modeling and sensitivity analysis of porewater chemistry in compacted bentonite. Physics and Chemistry of the Earth, Parts A/B/C 29(1): 129-136.

Okabe, A., Boots, B., Sugihara, K., Chiu, S.N. (2000). Spatial Tessellations: Concepts and Applications of Voronoi Diagrams, 2nd ed., Wiley, NYC, 696 pages.

Pacovsky, J., Svoboda, J., Zapletal, L. (2005). Saturation development in the bentonite barrier of the mock-up CZ geotechnical experiment. Clay in Natural and Engineered Barriers for Radioactive Waste Confinement—Part 2. Physics and Chemistry of the Earth 32(8–14), 767–779.

Pruess, K., Oldenburg, C., Moridis, G. (1999). The TOUGH2 User's Guide, Version 2.0, Lawrence Berkeley National Laboratory, Berkeley, CA.

Pruess, K., Oldenburg, C.M., Moridis, G. (2012). TOUGH2 User's Guide, Version 2.1, LBNL-43134(revised), Lawrence Berkeley National Laboratory, Berkeley, California.

Pusch, R., Karnland, O. (1996). Physico/chemical stability of smectite clays, Engineering Geology 41: 73-85.

Pusch, R., Kasbohm, J., Thao, H.T.M. (2010). Chemical stability of montmorillonite buffer clay under repository-like conditions—A synthesis of relevant experimental data. Applied Clay Science 47(1–2): 113-119.

Pusch, R., Madsen, F.T. (1995). Aspects on the illitization of the kinnekulle bentonites. Clays and Clay Minerals 43(3): 261-270.

Ramírez, S., Cuevas, J., Vigil, R., Leguey, S. (2002). Hydrothermal alteration of "La Serrata" bentonite (Almeria, Spain) by alkaline solutions. Applied Clay Science 21(5–6): 257-269.

Rutqvist, J. (2011). Status of the TOUGH-FLAC simulator and recent applications related to coupled fluid flow and crustal deformations. Computers & Geosciences, 37, 739–750.

Rutqvist, J., Davis, J., Zheng, L., Vilarrasa, V., Houseworth, J.,Birkholzer, J. (2014a). Investigation of Coupled THMC Processes and Reactive Transport: FY14 Progress. Prepared for U.S. Department of Energy, Used Fuel Disposition, FCRD-UFD-2014-000497, Lawrence Berkeley National Laboratory, LBNL-6720E.

Rutqvist, J., Zheng, L., Chen, F, Liu, H.-H, Birkholzer, J. (2014b). Modeling of Coupled Thermo-Hydro-Mechanical Processes with Links to Geochemistry Associated with Bentonite-Backfilled Repository Tunnels in Clay Formations. Rock Mechanics and Rock Engineering, 47, 167–186.

Rutqvist, J., Ijiri, Y., Yamamoto, H. (2011). Implementation of the Barcelona Basic Model into TOUGH–FLAC for simulations of the geomechanical behavior of unsaturated soils. Computers & Geosciences 37(6): 751-762.

Rutqvist, J., Wu, Y.-S., Tsang, C.-F., Bodvarsson, G. (2002). A modeling approach for analysis of coupled multiphase fluid flow, heat transfer and deformation in fractured porous rock, International Journal of Rock Mechanics & Mining Sciences, 39, 429–442.

Rutqvist, J., Zheng, L., Chen, F., Liu, H.-H., Birkholzer, J. (2013). Modeling of Coupled Thermo-Hydro-Mechanical Processes with Links to Geochemistry Associated with Bentonite-Backfilled Repository Tunnels in Clay Formations. Rock Mechanics and Rock Engineering: 1-20.

Sacchi, E., Michelot, J.L., Pitsch, H., Lalieux, P., Aranyossy, J.F. (2001). Extraction of water and solution from argillaceous rock for geochemical characterisation: methods, processes, and current understanding. Hydrogeology Journal 9, 17–33.

Samper, J., Zheng, L., Montenegro, L., Fernández, A.M., Rivas, P. (2008a). Coupled thermo-hydro-chemical models of compacted bentonite after FEBEX "*in situ*" test. Applied Geochemistry 23(5): 1186-1201.

Sánchez, M., Gens, A., do Nascimento Guimarães, L., & Olivella, S. (2005). A double structure generalized plasticity model for expansive materials. Int. J. Numer. Anal. Meth. Geomech., 29, 751–787.

Sánchez, M., Gens, A., Guimarães, L. (2012a). Thermal–hydraulic–mechanical (THM) behaviour of a large-scale "*in situ*" heating experiment during cooling and dismantling. Canadian Geotechnical Journal 49(10): 1169-1195.

Sánchez, M., Gens, A., Olivella, S. (2012b). THM analysis of a large-scale heating test incorporating material fabric changes. International Journal for Numerical and Analytical Methods in Geomechanics 36(4): 391-421.

Senger, R., Marschall, P. (2008). Task Force on EBS / Gas Transport in Buffer Material, Nagra Arbeitsbericht NAB 08-24.

Senger, R., Romero, E., Ferrari, A., Marschall, P. (2014). Characterization of gas flow through low-permeability claystone: laboratory experiments and two-phase flow analyses. Norris, S., Bruno, J., Cathelineau, M., Delage, P., Fairhurst, C., Gaucher, E. C., Ho¨hn, E. H., Kalinichev, A., Lalieux, P. & Sellin, P. (eds) Clays in Natural and Engineered Barriers for Radioactive Wast Confinement. Geological Society, London, Special Publications, 400, http://dx.doi.org/10.1144/SP400.15

Shao, J., Zhou, H., Chau, K. (2005). Coupling between anisotropic damage and permeability variation in brittle rocks. International Journal for Numerical and Analytical Methods in Geomechanics 29, 1231–1247.

Siitari-Kauppi, M., Leskinen, A., Kelokaski, M., Togneri, L. Alonso, U., Missana, T., García - Gutiérrez, M. (2007). Physical Matrix Characterisation: Studies of Crystalline Rocks and Consolidated Clays by PMMA Method and Electron Microscopy as Support of Diffusion Analyses. CIEMAT Technical Report, 1127, December 2007.

Simo, J., Hughes, T. (1998). Computational inelasticity, Interdisciplinary applied mathematics. Springer-Verlag, New York.

Simo, J., Ortiz, M. (1985). A unified approach to finite deformation elastoplastic analysis based on the use of hyperelastic constitutive equations. Computer Methods in Applied Mechanics and Engineering 49, 221–245.

Sonnenthal, E. Chapter 5 in: Birkholzer, J., Rutqvist, J., Sonnenthal, E., Barr, D. (2008). Long-Term Permeability/Porosity Changes in the EDZ and Near Field due to THM and THC Processes in Volcanic and Crystalline-Bentonite Systems, DECOVALEX-THMC Project Task D Final Report.

Suuronen, J.P., Matusewicz, M., Olin, M., Serimaa, R. (2014). X-ray studies on the nano-and microscale anisotropy in compacted clays: Comparison of bentonite and purified calcium montmorillonite. Applied Clay Science, 101, pp.401-408.

Tsang, C.-F., Bernier, F., Davies, C. (2005). Geohydromechanical processes in the excavation damaged zone in crystalline rock, rock salt, and indurated and plastic clays-in the context of radioactive waste disposal. International Journal of Rock Mechanics & Mining Sciences 42, 109–125.

Van Genuchten, M.T. (1980). A closed-form equation for predicting the hydraulic conductivity of unsaturated soils. Soil science society of America journal 44(5): 892-898.

Vilarrasa V., Rutqvist J., Blanco-Martin L., Birkholzer J. (2016). Use of a dual structure constitutive model for predicting the long-term behavior of an expansive clay buffer in a nuclear waste repository. ASCE's International Journal of Geomechanics, 16, article number D4015005.

Vomvoris, S., Birkholzer, J.T., Zheng, L., Gays, I., Blechschmidt, I. (2015). THMC behavior of clay-based barriers under high temperature – from laboratory to URL scale, Proceedings, International High-Level Radioactive Waste Management Conference, Charleston, NC, USA, April 12-16, 2015.

Wang, Y. (2011). Research & Development (R&D). Plan for Used Fuel Disposition Campaign (UFDC). Natural System Evaluation and Tool Development, U.S. DOE Used Fuel Disposition Campaign.

Wersin, P., Johnson, L.H., McKinley, I.G. (2007). Performance of the bentonite barrier at temperature beyond 100oC: A critical review, Physics and Chemistry of the Earth 32: 780-788.

Wolery, T.J. (1993). EQ3/6, A software package for geochemical modelling of aqueous systems,Version 7.2. Lawrence Livermore National Laboratory, USA.

Xu, H. (2014). Theoretical and numerical modeling of anisotropic damage in rock for energy geomechanics, PhD thesis, Georgia Institute of Technology, Atlanta, GA.

Xu, H., Arson, C. (2014). Anisotropic damage models for geomaterials: Theoretical and numerical challenges. International Journal of Computational Methods, Special Issue on Computational Geomechanics 11.

Xu, H., Prévost, J.-H. (2016). Integration of a continuum damage model for shale with the cutting plane algorithm. International Journal for Analytical and Numerical Methods in Geomechanics. doi:10.1002/nag.2563

Xu, T., Sonnenthal, E., Spycher, N., Pruess, K. (2006). TOUGHREACT: A Simulation Program for Non-isothermal Multiphase Reactive Geochemical Transport in Variably Saturated Geologic Media. Computers and Geosciences 32: 145-165.

Xu, T., Spycher, N., Sonnenthal, E., Zhang, G., Zheng, L., Pruess, K. (2011). TOUGHREACT Version 2.0: A simulator for subsurface reactive transport under non-isothermal multiphase flow conditions. Computers & Geosciences 37(6): 763-774.

Yip, M., Mohle, J., Bolander, J. (2005). Automated modeling of three-dimensional structural components using irregular lattices, Computer-Aided Civil and Infrastructure Engineering, 20, 393–407.

Zandomeneghi, D., Voltolini, M., Mancini, L., Brun, F., Dreossi, D., Polacci, M. (2010). Quantitative analysis of X-ray microtomography images of geomaterials: Application to volcanic rocks. Geosphere, 6(6), pp.793-804.

Zheng, L., Rutqvist, J., Steefel, C., Kim, K., Chen, F., Vilarrasa, V., Nakagawa, S., Houseworth, J., Birkholzer J. (2014). Investigation of Coupled Processes and Impact of High Temperature Limits in

Argillite Rock. Prepared for U.S. Department of Energy, Used Fuel Disposition, FCRD-UFD-2014-000493, Lawrence Berkeley National Laboratory, LBNL-6719E.

Zheng, L., Kim, K., Xu, H., Rutqvist, J. (2016). DR Argillite Disposal R&D at LBNL. FCRD-UFD-2016-000437, LBNL-1006013, Lawrence Berkeley National Laboratory.

Zheng, L., Li, L., Rutqvist, J., Liu, H., Birkholzer, J.T. (2012). Modeling Radionuclide Transport in Clays. Lawrence Berkeley National Laboratory. FCRD-URD-2012-000128

Zheng, L., Rutqvist, J., Birkholzer, J.T., Liu, H.-H. (2015a). On the impact of temperatures up to 200 °C in clay repositories with bentonite engineer barrier systems: A study with coupled thermal, hydrological, chemical, and mechanical modeling. Engineering Geology 197: 278-295.

Zheng, L., Rutqvist, J. Kim, K., Houseworth, J. (2015b), Investigation of Coupled Processes and Impact of High Temperature Limits in Argillite Rock. FCRD-UFD-2015-000362, LBNL-187644.

Zheng, L., Samper, J. (2008). A coupled THMC model of FEBEX mock-up test. Physics and Chemistry of the Earth, Parts A/B/C 33, Supplement 1: S486-S498.

Zheng, L., Samper, J., Montenegro, L. (2008). Inverse hydrochemical models of aqueous extracts tests. Physics and Chemistry of the Earth, Parts A/B/C 33(14–16): 1009-1018.

Zheng, L., Samper, J., Montenegro, L. (2011). A coupled THC model of the FEBEX "*in situ*" test with bentonite swelling and chemical and thermal osmosis. Journal of Contaminant Hydrology 126(1–2): 45-60.

Zheng, L., Samper, J., Montenegro, L., Fernández, A.M. (2010). A coupled THMC model of a heating and hydration laboratory experiment in unsaturated compacted FEBEX bentonite. Journal of hydrology 386(1-4): 80-94.

Zhou, Y., Rajapakse, R.K.N.D., Graham, J. (1999). Coupled Field in a deformable unsaturated medium. International Journal of Solid and Structures, 36: 4841-4868.

Zuo, L., Ajo-Franklin, J.B., Voltolini, M., Geller, J.T., Benson, S.M. (2016). Pore-scale multiphase flow modeling and imaging of CO_2 exsolution in Sandstone. Journal of Petroleum Science and Engineering.